E-20-618a
#10

STATIC MIXERS IN WATER TREATMENT: EXPERIMENTS AND MODELING OF MIXING FOR COAGULATION AND CRYPTOSPORIDIUM INACTIVATION

Prepared by:

Appiah Amirtharajah, S. Casey Jones, Brian M. Skeens,

Heather L. Heindel, Wei Li, Scott A. Hardy, and Ron Latimer

School of Civil and Environmental Engineering

Georgia Institute of Technology

Atlanta, GA 30332–0512

Sponsored by:

AWWA Research Foundation

6666 West Quincy Avenue

Denver, CO 80235–3098

Published by the

AWWA Research Foundation and

American Water Works Association

DISCLAIMER

This study was funded by the AWWA Research Foundation (AWWARF). AWWARF assumes no responsibility for the content of the research study reported in this publication or for the opinions or statements of fact expressed in the report. The mention of trade names for commercial products does not represent or imply the approval or endorsement of AWWARF. This report is presented solely for informational purposes.

ISBN 0-00000-000-0

CONTENTS

LIST OF TABLES ix

LIST OF FIGURES xi

FOREWORD xvii

ACKNOWLEDGMENTS ix

EXECUTIVE SUMMARY xi

CHAPTER 1: INTRODUCTION AND BACKGROUND 1

Introduction 1

Literature Review 3

Coagulation and Mixing 4

Turbulence, Mixing, and Chemical Reactions 5

Static Mixers 6

Disinfection and Mixing 9

Computational Fluid Dynamics 11

CHAPTER 2: PILOT-SCALE TESTING OF STATIC MIXERS FOR COAGULANT MIXING 13

Introduction and Objectives 13

Methods and Materials 13

Pilot-Plant Description 13

Source Water 16

Experimental Procedure 16

Head Loss Experiments 18

Results and Discussion 18

Comparison of the KMS Mixer and Backmixer 18

Effect of Design Parameters 30

Head Loss Tests 36

Summary and Conclusions 38

KMS Mixer versus the Backmixer 38

Static Mixer Experiments 38

CHAPTER 3: BENCH-SCALE EXPERIMENTS OF THE INACTIVATION OF *CRYPTOSPORIDIUM PARVUM* OOCYSTS WHEN USING STATIC MIXERS 85
Introduction and Background 85
Cryptosporidium Detection Methods 85
Determining Viability 86
Materials and Methods 87
Experimental Apparatus 87
Preparing for the Disinfection Experiments 88
Disinfection Experiments 90
Results and Discussion 95
Dispersion of Oocysts in Carboy 95
Losses in Filtration Step of Experiments 96
Concentration of Oocysts in Samples Collected 96
Concentration of Oocysts in Stock Samples 96
Infectivity Curves 97
Head Losses and *G*-values 98
Chlorine Disinfection Studies 99
Conclusions and Recommendations 105
Recommendations 107
CHAPTER 4: A NEW PHYSICOCHEMICAL MODEL OF DISINFECTANT MIXING INCLUDING THE EFFECTS OF MIXING ON *CRYPTOSPORIDIUM PARVUM* OOCYSTS 133
Introduction 133
Traditional View of the Disinfection Process 133
New View of the Disinfection Process 134
Development of the New Disinfection Model 135
Fluid Transport of the Disinfectant and Pathogens 136
Summary of the Model Derivation 141
Disinfection of *Cryptosporidium* in a Batch Reactor 142
Development of a Batch Reactor Model 142

Initial Validation of Model for Batch Reactor 143
Comparing the New Model to Other Models of Disinfection 144
Disinfection of *Cryptosporidium* in Plug-Flow Dispersion Reactor 149
Development of a Plug-Flow Dispersion Reactor Model 149
Sensitivity Analysis 151
Summary and Conclusion 152
CHAPTER 5: COMPUTATIONAL FLUID DYNAMICS PREDICTIONS OF THE FLOWFIELD IN HELICAL STATIC MIXERS 159
Introduction 159
What is CFD? 159
Previous Applications of CFD in Water Treatment 161
Questions in Water Treatment that CFD can Address 162
Description of the CFD Model 164
Reynolds-Averaged Navier–Stokes Equations 164
Summary of the Numerical Method 168
Validation of the CFD Model 170
Experimental and Computational Details 170
Validation Results 171
Results and Discussion of Static Mixer Predictions 175
Computational Details 175
More Validation 178
Verification 181
Discussion of the Flowfield Physics 182
Applying the CFD Model to Issues in Water Treatment 189
Flowfield Predictions for Water Treatment 189
Rapid Mixing for Coagulation 191
G-value for Static Mixers 192
Conclusions 195
Recommendations for Future Work 197

CHAPTER 6: CONCLUSIONS 219
Overview 219
Static Mixers for Coagulation 219
Inactivation of *Cryptosporidium Parvum* Using Static Mixers 220
A New Model of Mixing and Disinfection of *Cryptosporidium Parvum* 222
Computational Fluid Dynamics and the Flowfield in Helical Static Mixers 223
REFERENCES 227
ABBREVIATIONS 251

TABLES

1.1	Various design criteria for mixing of disinfectants	10
2.1	Raw water data for Series 1—KMS mixer versus backmixer with charge neutralization chemical conditions	19
2.2	Experimental conditions for Series 1—KMS mixer versus the backmixer with charge neutralization chemical conditions	20
2.3	Filtered-water particle counts for Series 1—KMS mixer versus the backmixer (BM) with charge neutralization chemical conditions (anthracite filters only)	22
2.4	Raw water data for Series 2—KMS mixer versus backmixer with sub-optimal chemical conditions	23
2.5	Experimental conditions for Series 2—KMS mixer versus the backmixer (BM) with sub-optimal chemical conditions	23
2.6	Filtered-water particle counts for Series 2—KMS mixer versus the backmixer (BM) with sub-optimal chemical conditions (anthracite filters only)	26
2.7	Raw water data for Series 3—KMS mixer versus the backmixer with sweep coagulation chemical conditions	26
2.8	Experimental conditions for Series 3—KMS mixer versus the backmixer (BM) with sweep coagulation chemical condition	26
2.9	Filtered-water particle counts for Series 3—KMS mixer versus the backmixer (BM) with sweep coagulation chemical conditions	27
2.10	Raw water data for Series 4—KMS mixer versus the backmixer with equal streaming current	28
2.11	Experimental conditions for Series 4—KMS mixer versus the backmixer (BM) with equal streaming current	28
2.12	Summary of results for Series 4—KMS mixer versus the backmixer (BM) with equal streaming current	29
2.13	Static mixers and flow rates in the experiments of Series 5 to 7	31
2.14	Raw water data for Series 5—Comparing the effect of the number of elements	32

2.15 Experimental conditions for Series 5—Comparing the effect of the number of elements 33
2.16 Raw water data for Series 6—Static mixers versus an empty pipe 34
2.17 Experimental conditions for Series 6—Static mixers versus an empty pipe 34
2.18 Raw water data for Series 7—Comparing the effect of diameter 35
2.19 Experimental conditions for Series 7—Comparing the effect of diameter 36
3.1 Inactivation of *Cryptosporidium* by chlorine dioxide at pH 8 and 20 ± 1°C 104
3.2 Inactivation of Cryptosporidium by chlorine followed by monochloramine at pH 8.0 ± 0.1 and 20°C ± 1°C 104
4.1 Comparison of the new model with the IgH model 145
4.2 Comparison of the new model with the data from Ransome, Whitmore, and Carrington (1993) 146
4.3 Comparison of the new model to the Chick–Watson model 147
4.4 Comparison of the new model with the Chick–Watson model 148
5.1 Summary of the CFD model 169
5.2 Summary of computer simulations 179
5.3 Reynolds numbers in drinking water treatment plants. The calculation of the Reynolds number assumes a bulk velocity of 6 feet per second and a temperature of 20°C 189

FIGURES

2.1	Diagram of the pilot plant	40
2.2	Backmixer setup	41
2.3	Static mixer setup	42
2.4	Experimental chemical operating conditions on the alum diagram	43
2.5	Series 1—Streaming current measurements	44
2.6	Series 1—Experiment 1B (2 gpm) settled-water turbidity	45
2.7	Series 1—Experiment 9A (4 gpm) settled-water turbidity	46
2.8	Series 1—Experiment 1B (2 gpm) filtered-water turbidity	47
2.9	Series 1—Experiment 9A (4 gpm) filtered-water turbidity	418
2.10	Series 2—Experiments 3A and 3B (2 gpm) streaming current	49
2.11	Series 2—Experiment 8C (4 gpm) streaming current	50
2.12	Series 2—Experiment 3A (2 gpm) settled-water turbidity	51
2.13	Series 2—Experiment 3B (2 gpm) settled-water turbidity	52
2.14	Series 2—Experiment 8C (4 gpm) settled-water turbidity	53
2.15	Series 2—Experiment 3A (2 gpm) filtered-water turbidity	54
2.16	Series 2—Experiment 3B (2 gpm) filtered-water turbidity	55
2.17	Series 2—Experiment 8C (4 gpm) filtered-water turbidity	56
2.18	Series 3—Experiment 2A (2 gpm) settled-water turbidity	57
2.19	Series 3—Experiment 2A (2 gpm) filtered-water turbidity	58
2.20	Series 5—Experiment 2S (4 gpm) settled-water turbidity	59
2.21	Series 5—Experiment 7S (4 gpm) settled-water turbidity	60
2.22	Series 5—Experiment 10S (2 gpm) settled-water turbidity	61
2.23	Series 5 - Experiment 13S (2 gpm) settled water turbidity	62
2.24	Series 5—Experiment 2S (4 gpm) filtered-water turbidity	63
2.25	Series 5—Experiment 7S (4 gpm) filtered-water turbidity	64
2.26	Series 5—Experiment 10S (2 gpm) filtered-water turbidity	65
2.27	Series 5—Experiment 13S (2 gpm) filtered-water turbidity	66
2.28	Series 6—Alum doses for KMS static mixer versus empty pipe	67
2.29	Series 6—Alum doses for Stata-tube versus empty pipe	68

2.30 Series 6—Alum doses for Spiral static mixer versus empty pipe 69
2.31 Series 6—Experiment 20S settled-water turbidity 70
2.32 Series 6—Experiment 25S settled-water turbidity 71
2.33 Series 6—Experiment 26A settled-water turbidity 72
2.34 Series 6 - Experiment 20S filtered water turbidity 73
2.35 Series 6—Experiment 25S filtered-water turbidity 74
2.36 Series 6—Experiment 30S filtered-water turbidity 75
2.37 Series 6—Experiment 23S filtered-water turbidity 76
2.38 Series 7—Experiment 33S settled-water turbidity 77
2.39 Series 7—Experiment 32S filtered-water turbidity 78
2.40 Reynolds number versus friction factor for KMS static mixers 79
2.41 Reynolds number versus friction factor for spiral static mixer 80
2.42 Reynolds number versus friction factor for Stata-tube static mixer 81
2.43 Reynolds number versus friction factor for SMV static mixer 82
2.44 Reynolds number versus friction factor for all static mixers tested 83
3.1 Experimental apparatus setup 109
3.2 Bench-scale experimental apparatus 110
3.3 Schematic describing the oocyst concentration procedure 111
3.4 Sample infectivity curve for oocysts inoculated onto MDCK cells 112
3.5 Distribution oocysts in the spiked carboy 113
3.6 Oocyst losses in filtration step of experiment 114
3.7 Concentration of oocysts in collected samples through test runs 115
3.8 Concentration profile of purification 19IA9 of the Iowa isolate 116
3.9 Infectivity curve for 3.12.99 purification (9HMAI) of Maine isolate 117
3.10 Comparison of control data infectivity curves 117
3.11 Head loss across 0.5-inch diameter static mixers and 14.4 inches of tubing at 20°C. 118
3.12 Inactivation of Cryptosporidium parvum in batch and jar test experiments with chlorine at pH 6 and 22 ± 2°C 119
3.13 Log inactivated versus CT-value of two element helical mixer, Omega mixer, and empty pipe 120

3.14 Six-element static mixer inactivation data 121
3.15 Comparison of inactivation data of six element helical mixer, two element helical mixer, Omega mixer and empty pipe 122
3.16 Linear trendline of disinfection data for two element mixer, Omega mixer, and empty pipe 123
3.17 Linear trendline of six element mixer disinfection data 124
3.18 Inactivation of *Cryptosporidium parvum* oocysts as a function of *G* values at less than 3 seconds contact time with chlorine at pH 6 and 22 ± 2°C 125
3.19 Inactivation of *Cryptosporidium parvum* oocysts as a function of *G*-value at 30 minute contact time with chlorine at pH 6 and 22 ± 2°C 126
3.20 Hom model constant determination using the natural log of the log inactivated versus the natural log of the disinfectant concentration 127
3.21 Hom model constant determination using the natural log of the log inactivation versus the natural log of the contact time 128
3.22 Hom model for six element helical mixer, 0.25 log inactivated to 4.0 log inactivated at 0.25 log increments 129
3.23 Hom model for six element helical mixer with experimental data points 130
3.24 Inactivation of Cryptosporidium by chlorine at pH 6, 7 and 8 131
3.25 Inactivation of *Cryptosporidium* by monochloramine following 111-132 mg×min/L of chlorine at pH 8 and 20 ± 1°C 132
4.1 Traditional model of the disinfection process 153
4.2 New model of the disinfection process 153
4.3 Interfacial mass transfer model 154
4.4 Finding the model parameters with chlorine as disinfectant 154
4.5 Comparison of the predictions from the new disinfection model and the experimental data from Gyürék, Finch, and Belosvic (1997) with chlorine as the disinfectant 155
4.6 Finding the model parameters with ozone as disinfectant 155
4.7 Comparison of the predictions from the new disinfection model to the experimental data from Ransome, Whitmore, and Carrington (1993) with ozone as the disinfectant 156

4.8 Comparison of the predictions from the new disinfection model to the experimental data from Gyürék (1997) with ozone as disinfectant 156
4.9 Prediction of log removal from the new disinfection model for a plug-flow dispersion reactor and the bench-scale experiments in a static mixer from Chapter 3 157
4.10 Sensitivity analysis of K_p for the completely mixed batch reactor with chlorine as the disinfectant 157
4.11 Sensitivity analysis of K_p for the completely mixed batch reactor with ozone as the disinfectant 158
4.12 Sensitivity analysis of K_p for plug-flow disperion reactor with chlorine as the disinfectant 158
5.1 Predicted and measured pressure coefficient 199
5.2 Velocity profiles within the bend and upstream of it 200
5.3 Velocity profiles downstream of the bend 201
5.4 Contours of the longitudinal velocity u_s with predictions in the top semi-circles and the measurements in the bottom ones 202
5.5 Computational grid for the turbulent flow predictions. The top of the figure shows a longitudinal cross-section that has been untwisted to emphasize the clustered grid near the leading and trailing edge of the elements. The bottom of the figure shows a transverse cross-section to emphasize the clustered grid near the sides of both elements 203
5.6 Three-dimensional picture of the computational grid with only one-half of the domain shown for clarity. The whole domain was used in the simulations 204
5.7 Friction factor comparison of predictions (lines) and experiments (circles) for different numbers of elements 205
5.8 Effect of the outlet length on the skin-friction coefficient C_f at a point near the pipe wall plotted versus the longitudinal coordinate x_1 206

5.9 Effect of grid resolution on the flowfield. All three cross-sections are located at the exit of the two-element mixer at Re=10,000. The top row shows contours of the mean longitudinal velocity; the bottom row shows vectors of the mean transverse velocity 207

5.10 Flowfield upstream of and within the first element for a simulation at Re=10,000 and two elements. The top row shows contours of the mean longitudinal velocity; the middle row shows vector of the mean transverse velocity; and the bottom row shows contours of the mean longitudinal vorticity 208

5.11 Flowfield within the second element for a simulation at Re=10,000 and two elements. The top row shows contours of the mean longitudinal velocity; the middle row shows vector of the mean transverse velocity; and the bottom row shows contours of the mean longitudinal vorticity 209

5.12 Flowfield downstream of the mixer elements for a simulation at Re=10,000 and two elements. The top row shows contours of the mean longitudinal velocity; the middle row shows vector of the mean transverse velocity; and the bottom row shows contours of the mean longitudinal vorticity 210

5.13 Regions of reverse flow in six-element mixer at Re=20,000. The bottom plot (b) is rotated 90° about the longitudinal direction 211

5.14 Effect of the number of elements on the mean longitudinal velocity for a range of Reynolds numbers. Each cross-section is located at the trailing edge of the last element 212

5.15 Effect of the number of elements on the turbulence kinetic energy for a range of Reynolds numbers. The top row of three contours shows the normalized turbulence kinetic energy entering each mixer for each of the three Reynolds numbers. Each of the bottom nine cross-sections is located a the trailing edge of the last element 213

5.16 Flowfield within the second element for a simulation at Re = 100,000 and two elements. The top row shows contours of the mean longitudinal velocity; the middle row shows vector of the mean transverse velocity; and the bottom row shows contours of the mean longitudinal vorticity 214

5.17 Distribution of the turbulence energy dissipation in a two-element, helical static mixer at Re=100,000 215

5.18 Distribution of local G-value in a two-element, helical static mixer at Re=100,000 216

5.19 Average local G-value for Re=100,000 plotted versus the longitudinal coordinate. To obtain G_a in units of s^{-1}, multiply by 36 217

FOREWORD

The AWWA Research Foundation is a nonprofit corporation that is dedicated to the implementation of a research effort to help utilities respond to regulatory requirements and traditional high-priority concerns of the industry. The research agenda is developed through a processes of consultation with subscribers and drinking water professionals. Under the umbrella of a Strategic Research Plan, the Research Advisory Council prioritizes the suggested projects based upon current and future needs, applicability, and past work; the recommendations are forwarded to the Board of Trustees for final selection. The foundation also sponsors research projects through the unsolicited proposal process; the Collaborative Research, Research Applications, and Tailored Collaboration programs; and various joint research efforts with organizations such as the U.S. Environmental Protection Agency, the U.S. Bureau of Reclamation, and the Association of California Water Agencies.

This publication is the result of one of these sponsored studies, and it is hoped that its findings will be applied in communities throughout the world. The following report serves not only as a means of communicating the results of the water industry's centralized research program but also as a tool to enlist the further support of the nonmember utilities and individuals.

Projects are managed closely from their inception to the final report by the foundation's staff and large cadre of volunteers who willingly contribute their time and expertise. The foundation serves a planning and management function and awards contracts to other institutions such as water utilities, universities, and engineering firms. The funding for this research effort comes primarily from the subscription program, through which water utilities subscribe to the research program and make an annual payment proportional to the volume of water they deliver and consultants and manufacturers subscribe based on their annual billings. The program offers a cost-effective and fair method for funding research in the public interest.

A broad spectrum of water supply issues is addressed by the foundation's research agenda: resources, treatment and operations, distribution and storage, water quality and analysis, toxicology, economics, and management. The ultimate purpose of the coordinated effort is to assist water suppliers to provide the highest possible quality of water economically and reliably. The true benefits are realized when the results are implemented at the utility level. The foundation's trustees are pleased to offer this publication as a contribution toward that end.

[Paragraph to be supplied by Kenan Ozekin]

Julius Ciaccia, Jr.
Chair, Board of Trustees
AWWA Research Foundation

James F. Manwaring, P.E.
Executive Director
AWWA Research Foundation

ACKNOWLEDGMENTS

The authors of this report are indebted to the following water utilities, individuals, government agencies, and private businesses for their cooperation and participation in this project:

The Centers for Disease Control and Prevention, Atlanta, Ga., Mike Arrowood, Mark Eberhard, Long-Ti Xie, and Kimberly Donaldson

The City of Atlanta, Atlanta, Ga.

Chemineer, North Andover, Mass.

Koch-Glitsch, Wichita, Kan.

Kemwater North America, Savannah, Ga.

TAH Industries, Robbinsville, N.J.

United Water, Atlanta, Ga

Financial support was provided to Heather L. Heindel by the American Association of University Women (AAUW) Education Foundation. Metcalf & Eddy also provided support to Ron Latimer, Heather L. Heindel, and S. Casey Jones.

In addition, the authors acknowledge the advice and help of the Project Advisory Committee (PAC)—including James Malley, Chandra Mysore and Susumu Kawamura—and the help of Kenan Ozekin, the AWWARF project officer. Fotis Sotiropoulos also provided expert advice for the modeling portions of this project.

The authors also acknowledge Fotis Sotiropoulos, Associate Professor of Civil and Environmental Engineering, and Jill Holder, Administrative Coordinator for the Environmental Engineering Program, who both provided much needed support over the course of this project.

CHAPTER 1
INTRODUCTION AND BACKGROUND

INTRODUCTION

The 1993 outbreak of Cryptosporidiosis in Milwaukee, which caused 400,000 illnesses and over a hundred deaths, emphasizes the importance of controlling microorganisms in drinking water. However, the threat of cancer from long-term exposure to disinfection by-products (DBPs) in chlorinated drinking water complicates the task of providing safe drinking water to the public. In 1994 in response to these two, often conflicting needs, the US Environmental Protection Agency (EPA) proposed the Interim Enhanced Surface Water Treatment Rule (IESWTR) and the Stage I Disinfectant/Disinfection By-Products (D/DBP) Rule. The IESWTR focuses on the threat from microbial pathogens, i.e., *Giardia lamblia*, *Cryptosporidium parvum*, and viruses. The D/DBP rule focuses on disinfection by-products (DBPs) and, in particular, will limit the concentration of DBP precursors in drinking water by requiring enhanced coagulation, in which coagulant doses are optimized for the removal of natural organic matter (NOM), which are the precursors for DBPs. The 1996 Amendments of the Safe Drinking Water Act require the US EPA to promulgate the IESWTR, a final ESWTR, a Stage I D/DBP Rule, and a Stage II D/DBP Rule in accordance with a specific schedule. The first regulations in the Microbial/Disinfection By-Products (M/DBP) cluster were published in the Federal Register on December 16, 1998 and established new Maximum Contaminant Levels (MCLs) for DBPs, emphasized optimizing existing treatment techniques rather than major shifts to alternative technologies, with compliance dates of 2001 and 2003 (Pontius 1998, 2000). To meet the requirements of the current regulations, water utilities must optimize each of their unit operations, especially coagulation and disinfection. Common to each of these processes is the need to add a small volume of chemical quickly and uniformly throughout a large volume of water being treated. Static mixers are increasingly being used to perform this task.

Mixing is a critical component of the conventional, direct, and in-line filtration process trains. A proper optimization of the rapid mixing unit often results in lower chemical dosages and a better final filter effluent quality. In a study of design and operation guidelines for optimization of the high-rate filtration process, Cleasby et al. (1989) concluded that "rapid mixing is an

essential and important unit operation in chemical pretreatment. Various rapid mixing schemes were being used including back-mixed reactors, baffled tanks, in-line static or motor driven mixers, and hydraulic multi-jet injectors. Some plants reported significant chemical savings with improved rapid mixing, but this is not always observed and further observations on this issue would be desirable." The AWWA Research Committee on Coagulation (1989) highlighted many of the important long term research needs for a better understanding of the coagulation process, and two of the specific research needs identified were: (1) An understanding of contaminant destabilization using organic and inorganic coagulants during the first few seconds after coagulant addition and (2) development of scale-up and design relationships for mixing processes from basic concepts. These two research needs assessments indicate that the rapid mixing process for coagulation should be studied both at the fundamental level as well as at the plant-scale level to generate results that are sufficiently general as well as applicable for design and operation of the rapid mix unit.

While the overall process of rapid mixing has a fair volume of literature, it needs to be emphasized that static mixers have little or no information in current textbooks and in the recent literature. Not only does the lack of knowledge apply to what happens within the mixer in quantitative terms, but it also applies to design parameters for practical mixing applications. However, these units are being increasingly used in water treatment plants for initial mixing of chemicals; for dissolution of ozone; and have a significant potential for mixing of chlorine to cause additional inactivation of *Giardia* cysts, *Cryptosporidium* oocysts, and viruses as needed by the proposed ESWTR. Amirtharajah and O'Melia (1990) state that these units are effective but have some constraints since head loss can be significant and mixing efficiency is related to flow rate. There is little literature that specifically examines mixing of alum, polymers, ozone, or chlorine in static mixers.

The overall goal of the research contained within this report was to evaluate static mixers for use in coagulation and disinfection of *Cryptosporidium* and hence to optimize these processes. The project included the following overlapping but distinct sub-projects: (1) Pilot-scale testing of static mixers for coagulant mixing (Chapter 2); (2) Bench-scale disinfection experiments on the inactivation of *Cryptosporidium parvum* oocysts using static mixers (Chapter 3); (3) Development of a new physicochemical model for disinfectant mixing to inactivate *Cryptosporidium parvum* oocysts (Chapter 4); and (5) Development and use of a computational fluid

dynamics (CFD) model to predict the flowfield in helical static mixers (Chapter 5). The specific chapters in this report detail the four topics that were researched, the objectives and conclusions reached in each topic area studies, and Chapter 6 provides a summary and synthesis of the conclusions from the four aspects that were studied. This report incorporates research described in detail in six documents: one doctoral dissertation (Jones 1999), three Master of Science theses (Hardy 1999, Heindel 1999, Skeens 1999), and two Master of Science research reports (Latimer 1998, Li 1999). The reader is directed to these documents for additional information on the project.

LITERATURE REVIEW

The following review highlights some of the important background work related to this research. Literature reviews specific to the following topics are discussed in the six theses and research reports generated as a part of this project.

1. Static Mixers for Water Treatment: A Computational Fluid Dynamics Model (Jones 1999).
2. Effectiveness of Static Mixers for Disinfection of *Cryptosporidium* Oocysts (Hardy 1999).
3. A Bench-Scale Examination of the Effect of Static Mixers on the Disinfection of *Cryptosporidium* (Heindel 1999).
4. Pilot-Scale Studies of Static Mixers for Coagulation (Skeens 1999).
5. Pilot-Scale Comparison of Static Mixers and Backmix Reactors for Coagulation (Latimer 1998).
6. Physicochemical Modeling of the Disinfection Process for *Cryptosporidium parvum* Oocysts (Li 1999).

In the following literature review, the topics addressed are: coagulation and mixing, turbulence and mixing (including a discussion of micromixing models), static mixers, disinfection and mixing, and computational fluid dynamics.

Coagulation and Mixing

Amirtharajah and co-workers have studied rapid mixing over the last twenty years and their publications (Amirtharajah and Mills 1982; Amirtharajah and Trusler 1986; Amirtharajah, Clark, and Trussell 1991) provide a broad coverage of the subject. Conclusions from two papers on rapid mixing, which are an amalgam of fundamentals and practice, are noted as follows. In the first paper, Amirtharajah and Mills (1982) developed the coagulation diagram for alum which is often used to establish the chemical conditions (pH and alum dose) for the mechanisms of coagulation and to determine the appropriate rapid mixing unit. The results of the paper showed that high intensity mixing would benefit particle destabilization for low alum doses and the mechanism of charge neutralization, while sweep coagulation was insensitive to mixing conditions. In the second paper, Amirtharajah and Trusler (1986) provided a rationale for the design of rapid mix units for direct filtration and made a first attempt to design rapid mixers in terms of particle size distributions. They developed a new theory which indicated that minima in destabilization rate occurred at specific ratios of the Kolmogorov microscale (η) to particle diameter (d). For the viscous and inertial subranges of turbulence, these ratios (η/d) were 2.00 and 1.33, respectively. These values corresponded to G-values of 1500 to 3500 s^{-1} which were to be avoided for 3 μm colloidal particles in the raw water. This study provided an underlying conceptual basis for the magnitude of velocity gradients typically provided in rapid mix units used in practice. This study further demonstrated the application of fundamental fluid mechanics information (i.e., the distribution of energy dissipation throughout the standard mixing jar) to the design of rapid mix units. In study described in this report, fundamental fluid mechanics information from CFD is applied to mixing in static mixers.

In 1991, a book, *Mixing in Coagulation and Flocculation,* was published and provided a state of the science review of mixing in drinking water treatment (Amirtharajah, Clark, and Trussell 1991). The book was a review of the literature at that time by internationally recognized authorities in the field. The contents of the book are not reviewed in this report, but the book provided the overall background for the research completed in this project.

Turbulence, Mixing, and Chemical Reactions

Any fundamental approach to the study of rapid mixing must incorporate some ideas about turbulence. The problem of turbulence itself is one of the unsolved problems of classical physics due to the non-closure of the Reynolds Averaged Navier-Stokes (RANS) equations that describe the motion of a fluid. However, the general concepts used in describing turbulence can be used for a study of rapid mixing (Amirtharajah 1981). It is useful in terms of the fundamental physical phenomena to distinguish between macromixing where large and small scale eddies cause a mixing of two components while the eddies themselves are of pure components and micromixing where eddy and Brownian diffusion cause a commingling of the two components at the molecular level so that they cannot be distinguished. Baldyga and Bourne (1984a,b,c) published a three part review on micromixing: Part I discussed the inadequacies of available methods, Part II dealt with micromixing in light of turbulence theory, and Part III provided computational and experimental results for the new micromixing model.

Bourne and Dell'Ava (1987) studied micro- and macromixing in stirred tank reactors of different sizes. They suggested that the mixing modulus, which has a large value in an environment which favors diffusion, may be used as a control parameter to study competitive, consecutive chemical reactions. For example, the mixing modulus is directly proportional to the following:

- the rate constant, k_2, for the slower of two rapid, competitive, consecutive chemical reactions, namely,

$$A + B \xrightarrow{k_1} R$$
$$R + B \xrightarrow{k_2} S\,;$$

- the initial concentration of the limiting reagent; and
- the square of the thickness of the laminae which form each eddy (equal to the Kolmogorov microscale).

A large value of mixing modulus occurs when the rates of reaction of each of two competitive, consecutive reactions become similar; when there are ample supplies of the limiting

reagent; when the mixing intensity is low; and when diffusivities are high. Such a condition will encourage production of the final product of two competitive, consecutive reactions rather than the production of an intermediate product.

Micromixing and Coagulation

The possible application of the above concepts in alum coagulation suggests that precipitation of aluminum hydroxides should be favored over the production of hydrolyzed species under conditions when the mixing modulus is high since that reaction appears to be the slowest. Clark (1986) suggested that the precipitation of aluminum hydroxide could be considered a rapid, competitive, consecutive chemical reaction of this type, and he used this approach to study the effect of mixing on the aluminum speciation in base titrations of aluminum chloride solutions (Clark, Srivastava, and David 1993). In these studies, chemistry and turbulent mixing were coupled using a micromixing model similar to the model by Baldyga and Bourne (1984b).

Distribution of Turbulent Energy Dissipation

In several studies of mixing in turbulent stirred tank reactors (Baldyga and Bourne 1988; Clark, Srivastava, and David 1993; Amirtharajah and Trusler 1986), the volume of the reactor was divided into regions of low, medium, and high turbulence energy dissipation (ε). However, it is likely that these regions do not adequately describe the distribution of ε in the mixers. In the research completed, a CFD model, which predicts the distribution of velocities, vorticity, and ε throughout the flow field in a static mixer is used to address micromixing in such a mixer.

Static Mixers

When using turbulent pipe flow to introduce chemicals into an untreated water, a static mixer can be installed. A static mixer consists of a series of stationary mixing elements inserted end-to-end along the direction of flow in a pipe. Each of the mixing elements is a rigid structure which divides and recombines the flow stream. The fluid is directed through the flow channels provided by the mixing elements. The fluid becomes more homogeneous along the length of the

elements (Mutsakis and Rader 1986). The introduction of static mixing elements not only accelerates radial mixing but also produces a higher and more uniform rate of turbulence energy dissipation, thereby promoting micromixing (Bourne and Maire 1991).

Many types of static mixer elements exist in the market today, each with its own operational characteristics. The actual grouping and division of the flow stream varies with the type of element. For example, the Sulzer-Koch mixing element consists of corrugated metal sheets oriented at 90° to each other. On the other hand, the Kenics element utilizes helices, which increase the interfacial area between the two streams and cause rotational motion of the fluid. Because of the widely varying designs, mixer performance cannot be estimated based on a general equation. Rather, mixer performance is unique to the type of element utilized. Each of the companies manufacturing the elements have gathered performance data for their elements and developed guidelines for design. Many of these specify the length-to-diameter ratio (L/D) required to achieve uniform mixing. The guidelines are nonspecific and tell relatively little about the performance of the mixers with chemical reactions nor their turbulence characteristics. More information about static mixer performance for chemical reactions is needed before a rational basis for design can be developed. Likewise, scale-up information for static mixers is very limited. The scale-up of in-line mixers for coagulation was investigated by Clark et al. (1994), but the results were inconclusive. In general, they showed that, as the diameter of an in-line mixer increased, the level of mixing decreased.

Energy Dissipation in Static Mixers

The energy for mixing in static mixers is derived from pressure losses due to fluid flowing through the elements. The mixers reduce the required contact time to achieve adequate mixing at the cost of increased energy consumption. Pahl and Muschelknautz (1982) presented a pressure drop equation based on the empty pipe and a geometrical correction factor. For Newtonian liquids,

$$\frac{1}{2}\frac{\Delta p}{\rho U^2}\frac{D}{L} = \psi(Re, \text{geometry})$$

where U = mean velocity of empty pipe = $4Q/\pi D^2$

Q = volumetric flow rate

ρ = liquid density

Δp = pressure drop in the mixer

D = pipe diameter

L = the total mixer length

Re = the pipe Reynolds number = UD/ν

ν = the kinematic viscosity

Plotting ψ_D versus Re provides a means of comparing the various static mixer types. The average rate of energy dissipation, Φ, in a static mixer is determined as follows (Bourne and Maire 1991):

$$\Phi = \frac{NeU^3}{eD}$$

where e = ratio of working volume to total internal volume = V_m/V_t

Ne = Newton's drag coefficient

The dissipation rate can be divided into turbulence dissipation, ε, and direct dissipation, E_d. Turbulence dissipation is caused by gradients of the turbulence velocity fluctuations. Direct dissipation is due to gradients of the mean velocity. Both ε and E_d vary widely with position, but Φ is an average over the volume, V_m (Bourne and Maire 1991). A CFD model with an adequate turbulence model can give the variation of ε throughout the mixer.

Coagulation with Static Mixers

Preliminary experiments at the Georgia Institute of Technology, Atlanta, Ga., USA investigated the effectiveness of static mixers for coagulation (Schulgen 1995; Burke 1996). In these bench-scale experiments, a static mixer was studied for the addition of alum to an artificial water made with bentonite clay and Atlanta tap water. In both conventional and direct-filtration schemes, the head loss (i.e., flow rate) through the static mixer had little effect on the settled or filtered water turbidity under a variety of chemical conditions (Schulgen, Amirtharajah, and Jones 1996). Burke (1996) used the same experimental setup but added NOM to the artificial raw

performance; however, as expected, the alum dose required for adequate treatment was higher because of the NOM. An important conclusion from Burke's study (1996) was that organics removal was significantly higher (approximately 25 percent) with the static mixer as compared to the jar test, which is the required testing protocol under the ESWTR. Hence, testing procedures in the regulations may not reflect plant-scale results of maximizing organics removal and minimizing disinfectant by-products.

Schulgen, Amirtharajah, and Jones (1996) also performed a survey of US water treatment plants currently using static mixers. The Water Industry Database (AWWA 1992) was used to identify approximately 65 plants using static mixers for rapid mixing of coagulants. Twenty-three of these plants responded providing information on plant operating data, static mixer design, and operators' comments on the static mixer. The typical static mixer in these plants has between 1 and 4 mixing elements. The pipe diameters vary from 6 to 108 inches, and typical head losses range from 0.5 to 6 feet of water as based on average summer flow rates. While many plants are using static mixers, criteria for their design and their appropriateness for use are not well established.

Disinfection and Mixing

The microbial and disinfection by-products regulations for drinking water focus on the $C \times T$ concept, where C is the residual disinfectant concentration in mg/L and T is the detention time in minutes, to insure that drinking water is properly disinfected. This concept ignores the initial mixing of the disinfectant and includes only the mixing of the disinfectant during the detention time in a contact tank. However, in the wastewater treatment industry, it is widely understood that intense initial mixing of chlorine at the point of addition can cause an increase in the inactivation of microorganisms especially those organisms more resistant to chlorine, such as enteric viruses. A summary of design recommendations is given in Table 1.1, which indicates the variations in the recommended design criteria.

Table 1.1

Various design criteria for mixing of disinfectants

Reference	*G*-value (s^{-1})	Time (s)	Type of Water
White (1978)	1000	—	wastewater
James Montgomery (1985)	400	—	water
WEF/ASCE (1991)	500	3	wastewater
Metcalf and Eddy (1991)	1500-3000	≈1	wastewater

The California State Department of Health suggested that initial mixing is one of the most important factors affecting the efficiency of disinfection of wastewater effluents (White 1972). A pilot study by Longley et al. (1974) concluded that "substantial viral and bacterial removals may be achieved by chlorination of wastewater under highly turbulent, plug flow conditions." Another study showed little effect of initial mixing on coliform inactivation once the bacteria were in contact with the disinfectant for more than ten minutes (Huang, Warriner, and Ni 1985). Virus inactivation increased as initial mixing increased even after a certain contact time was considered (Krusé et al. 1973). In a subsequent pilot-plant study, Longley (1978) found initial mixing to be more important for f_2 bacteriophage virus inactivation than for coliform inactivation. Haas, Longley, and Selfridge (1990) determined the inactivation of total coliform bacteria for the high-rate disinfection of stormwater overflow. An increase in pipe fluid velocity from 1 to 4 ft/s resulted in a decrease of the required $C \times T$ value from 334 to 109.

Cryptosporidium and Mixing

Cryptosporidium oocysts are highly resistant to chlorine disinfection. Based on the studies reviewed above, it is reasonable to suspect that the disinfection of *Cryptosporidium* oocysts may be susceptible to initial mixing. Parker and Smith (1993) recently demonstrated that *Cryptosporidium* oocysts can be inactivated by shaking in a sand-water suspension. After shaking for 5, 90, and 120 minutes, the percent of inactivated oocysts was 50, 99.7, and 100 percent, respectively. Furthermore, when the oocysts were shaken for 5 minutes and then treated with a 1 mg/L dose of chlorine for 5 minutes, 68 percent of the oocysts were inactivated, 18 percent more than

by shaking alone. Thus, the stresses caused by collisions with sand grains rendered the oocysts susceptible to chorine even at a $C \times T$ value of 5. This study indicates the possibility that *Cryptosporidium* oocysts may also be injured or inactivated by the high fluid shear stresses caused by the increased turbulence.

Finch, Black, and Gyürék (1995) have suggested that sequential addition of free chlorine followed by monochloramine is very effective in inactivating *Cryptosporidium* oocysts. The use of two static mixers in series would be an ideal, practical design for feeding dual disinfectants in a plug flow arrangement, especially for existing facilities without significant modification or additional construction for the chlorine contact tanks.

Computational Fluid Dynamics

The simulation of flowfields within static mixers requires the numerical solution of the incompressible RANS equations and the species transport equations together with appropriate models for chemical reactions and turbulence phenomena. The RANS equations in vector form are:

$$\nabla \cdot \mathbf{U} = 0$$

and

$$\frac{\partial \mathbf{U}}{\partial t} + \mathbf{U} \cdot \nabla \mathbf{U} + \frac{1}{\rho} \nabla p - \nabla \cdot \boldsymbol{\tau} = 0$$

where $\mathbf{U}$ = mean velocity vector

p = pressure

$\boldsymbol{\tau}$ = shear stress tensor, which includes both molecular and turbulence stresses

A general equation for transport is given by Patterson and Zipp (1991):

$$\frac{\partial \xi}{\partial t} + \mathbf{U} \cdot \nabla \xi = \nabla \left[\frac{\nu + \nu_t}{\sigma_\xi} \nabla \xi \right] + \mathrm{PROD}_\xi - \mathrm{DISS}_\xi$$

where ξ = species concentration or a turbulence parameter such as turbulence kinetic energy, k, or turbulence energy dissipation, ε

ν, ν_t = kinematic and turbulent viscosity

σ_ξ = diffusion coefficient of ξ

PROD_ξ = production of ξ

DISS_ξ = dissipation of ξ.

The terms that must be modeled are PROD_ξ and DISS_ξ. If no chemical reactions occur (that is, ξ is a scalar), then PROD_ξ and DISS_ξ are zero.

Previously, CFD has been used to study several types of static mixers that are used in fields other than water treatment (Rauline et al. 1998. However, these modeling efforts were limited to very low Reynolds numbers ($Re < 1$), which is appropriate for the mixing of very viscous materials like epoxy or polymers. However, for static mixers used in water treatment plants, the Reynolds numbers are much higher, and the previous models are not applicable. Therefore, a new CFD model was developed for this project. A description of the components of this new CFD model are given in Chapter 5 along with a brief history of CFD.

CHAPTER 2

PILOT-SCALE TESTING OF STATIC MIXERS FOR COAGULANT MIXING

INTRODUCTION AND OBJECTIVES

As discussed in Chapter 1, the purpose of the pilot-scale experiments was to extend the findings of previous bench-scale testing of static mixers for coagulant mixing. The specific objectives were to

- Compare a static mixer with a backmixer
- Investigate the effect of static mixer geometry
- Investigate the effect of design parameters, that is, number of elements and diameter of the mixer
- Compare the various static mixers with an empty-pipe mixer at the pilot-scale
- Investigate the head loss performance of various static mixer designs

METHODS AND MATERIALS

Pilot Plant Description

The pilot-scale experiments were conducted at the City of Atlanta Pilot Plant, which is located on the Chattahoochee River at the raw water intake facility for the City of Atlanta. The pilot plant consists of two, conventional drinking water treatment trains in parallel. Each train includes a rapid-mix module, a three-stage flocculation basin, a sedimentation basin equipped with plate settlers, and two filter columns one with GAC media and the other with anthracite and sand. Each train also includes pre- and post-ozone contact chambers, but these were not used in this study. Figure 2.1 shows a schematic of the pilot plant. The rapid-mix module was modified to provide either a backmixer, a static mixer, or an empty pipe. The two trains have a flow capacity of between 1 and 5 gpm (60 and 300 mL/s) each. For a flow rate of 2 gpm (125 mL/s), flocculation and sedimentation detention times are 30 minutes and 1.6 hours, respectively; at a flow rate of 4 gpm (250 mL/s), the times are 15 minutes and 0.8 hours, respectively.

Raw water was supplied from a tap on the 78-inch (2-m) diameter raw water pipe from the Chattahoochee River and pumped through a fine screen and into an influent basin at the pilot plant. The raw water was pumped to each of the two trains by a centrifugal pump with the flow rate in each train manually controlled by a separate flow meter (Dwyer RMC-6, Dwyer Instruments, Michigan City, Ind.). The water entered either a backmixer, static mixer, or an empty pipe for rapid mixing with the coagulant. Coagulated water flowed into the first of three clear acrylic flocculation tanks. The flocculators used Phipps and Bird stirrers (Phipps and Bird, Richmond, Va.) with 6.8-inch (175-mm) diameter axial flow impellers (Lightnin A 310 Lightnin, Rochester, N.Y.) in each basin. Tapered flocculation was used for all experiments with *G*-values of 60, 40, and 20 s^{-1} in the first, second, and third compartments, respectively. After flocculation, the water entered a plate-settler module. The effluent of the sedimentation basin overflowed into a collection channel. From the collection channel, water was pumped by a peristaltic pump to the filter columns. Two, 4-inch (100-mm) diameter, dual-media, filter columns were operated on each train. One filter consisted of 24 inches (600 mm) of granular activated carbon (GAC) and 12 inches (300 mm) of sand; the other consisted of 24 inches (600 mm) of anthracite coal and 12 inches (300 mm) of sand. The GAC was a 10×20 mesh size bituminous coal carbon (NORIT Americas, Atlanta, Ga.). The anthracite and sand were obtained from the Chattahoochee Water Treatment Plant (WTP). All of the filter media was installed prior to the beginning of the experiments. The filtration rate for each filter was controlled by a variable-speed, positive-displacement pump located on the effluent pipe of the filter column. A constant filtration rate of 4 gpm/ft^2 (2.7 L/m^2/s) was maintained for all experiments. The filtered water flow rate was measured with a flow meter (Model RMC-1, Dwyer Instruments, Michigan City, Ind) on the discharge side of the pump.

Backmixer

The backmixer is shown in Figure 2.2. Two backmixers in series were available; however, only the second compartment was used. The backmixer compartments have stator baffles on all four sides. Coagulant was injected into the backmixer through 1/8-inch (3-mm) diameter flexible tubing approximately one inch above the water surface at the impeller blades. A Phipps and Bird stirrer (Phipps and Bird, Richmond, Va.) was used to drive two, 3.4-inch (85-mm) di-

ameter Lightnin A310 impellers (Lightnin, Rochester, N.Y.) on the shaft. The backmixer was operated at a constant speed of 330 rpm for all experiments, which translates to a *G*-value of 160 s^{-1} at 15°C.

Static Mixers

The setup for the static mixer is shown in Figure 2.3. Alum was injected just upstream of the static mixer through a pipe tee and 1/8-inch (3-mm) diameter flexible tubing. A short length of small diameter pipe (approximately 1/16-inch (1.5-mm) inside diameter) was inserted into the 1/8-inch (3-mm) tubing to allow alum to be injected into the center of the pipe. A pressure transducer (Omega PX154, Omega Engineering, Stamford, Conn.) was connected to the static mixer to measure the head loss across the static mixer. Four different static mixer designs were used in these experiments:

- Kenics helical static mixer provided by Chemineer (Chemineer, North Andover, Mass.)—from now on called the **KMS** mixer (see http://www.chemineer.com).
- Koch SMV series mixer provided by Koch Glitsch (Koch-Glitsch, Wichita, Kan)—from now on called the **SMV** mixer (see http://www.koch-glitsch.com).
- TAH Spiral mixer provided by TAH (TAH Industries, Robbinsville, N.J.)—from now on called the **Spiral** mixer (see http://www.tah.com).
- TAH Stata-tube mixer provided by TAH (TAH Industries, Robbinsville, N.J.)—from now on called the **Stata-tube** mixer.

The Stata-tube mixer was constructed of PVC and housed in a PVC pipe. The other three mixers were constructed of 304 stainless steel and housed in stainless steel pipe.

Empty-Pipe Mixer

The experimental setup for the empty-pipe mixer was the same as for the static mixer, except that the static mixer was replaced by a stainless steel pipe with the same length and di-

ameter of the static mixer. The purpose of this setup was to provide mixing via turbulent pipe flow in the absence of the static mixer.

Source Water

The water source for these experiments was the Chattahoochee River. This water is typically low in organics with a yearly average total organic carbon (TOC) of 2.5 mg/L and typical turbidities of 15–30 ntu. The turbidity of the water is sensitive to precipitation and can quickly rise to 100 ntu during rain events. The turbidity primarily consists of clay particles typical of the clays found in the Piedmont region of Georgia.

Experimental Procedure

Aluminum sulfate (alum) and polyaluminum chloride (PACl) were used as coagulants. A fresh solution of coagulant was prepared for each experiment. Piston pumps (FMI QD-1, Fluid Metering., Oyster Bay, N.Y.) were used to feed the coagulant to the two trains from a common chemical storage tank. Piston pumps were selected to provide a constant coagulant flow rate that is critical for static mixers because they have little if any backmixing. To set the coagulant pump to the desired flow rate, a volumetric flow rate was measured using a 25-mL graduated cylinder and a stopwatch. Measurements were duplicated. The coagulant feed rates were checked at hourly intervals over the course of the experiment to ensure correct dose rates.

The liquid alum stock solution (5.4 lb/gal) was obtained from the Chattahoochee Water Treatment Plant. This stock solution was diluted to either 0.5% (5 g/L) or 1.0% (10 g/L) depending on the raw water flow rate to allow adequate alum flow rates. The liquid PACl stock solution was provided by Kemwater (PAX-XL70, Kemwater North America, Savannah, Ga.). This stock solution was also diluted to either 0.5% (5 g/L) or 1.0% (10 g/L) depending on the raw water flow rate to allow adequate PACl flow rates. When required to obtain a certain coagulated water pH, sodium hydroxide or hydrochloric was used to raise or lower the raw water pH prior to coagulation. These chemicals were added to the raw water at the influent basin. Adding these chemicals to the influent basin allowed adequate detention time for mixing prior to alum addition.

Each experimental run was started with potable water in the rapid mix, flocculation, and sedimentation basins. The experiments were run, with settled water being wasted to the sewer, for a time equal to at least the detention time in the flocculators and sedimentation basins before settled water was diverted to the filters. Samples of the settled water were also taken to verify that the turbidity had become stable. This was done to ensure approximately steady-state settled-water conditions for filtration. The filters were operated for approximately four hours before terminating the run. After each experiment, the filters were backwashed with air-water wash and all the basins were desludged and cleaned.

All instruments were calibrated at regular intervals according to the manufacturer's instructions. The pH meter was calibrated before each experiment. The turbidimeters were calibrated on a bi-weekly basis.

Grab samples for raw water turbidity and pH were taken every hour from the influent basin. Raw water turbidity was measured using a Hach Ratio/XR Turbidimeter and the pH measurements were made with an Orion 720A pH meter (Orion Research, Beverly, Mass.). Grab samples for coagulated-water pH were taken every hour to monitor coagulation conditions. Two taps located on the 1.5-inch (38-mm) PVC pipe between the static mixer and the first flocculation basin were used to sample coagulated water pH and for a sample stream to the streaming current detector (SCD) (Milton Roy, Ivyland, Pa.). Streaming current measurements were made hourly for all experiments to monitor the coagulant feed pump rates. A single SCD was used to measure the streaming current on both trains. For each streaming current measurement, the SCD was allowed to stabilize for a minimum of ten minutes before the reading was recorded.

Settled-water turbidity was monitored through the use of grab samples from the effluent collection channel during the filter operation period. The turbidity for the grab samples was measured on either a Hach 2100N or a Hach Ratio/XR turbidimeter. During the course of this project, two, low-range turbidimeters were installed to monitor settled-water turbidity on each train simultaneously in real-time.

Filtered-water turbidities were recorded continuously during a filter run using a low-range turbidimeter. For most of the experiments, a chart recorder was used to collect the data. For the last few of the experiments, a bitlogger (Logic Beach, La Mesa, Calif.) was installed for continuous monitoring of all instruments. Filtered water particle counts were performed with a particle counting system (Particle Measuring Systems, Boulder, Colo.). The particle counting

system consisted of the following elements: a batch sampler (PMS LBS-100), a volumetric sensor (PMS Model IMOLV), and a particle spectrometer (PMS Model μLPS-16). Grab samples for filtered-water particle counts were taken usually just before shut down and well into the run after the initial ripening period. Samples for the filtered-water particle counts were taken from the overflow of the turbidimeter. The glass sample containers were rinsed five times with deionized water and then rinsed three times with the filtered water that was to be sampled. These sample containers were only used for particle counts.

Head Loss Experiments

To compare the head loss in the various static mixers tested, head loss experiments were performed to measure the head loss across each of the mixers at various flow rates. Using the pressure transducer, the head loss across the static mixer was measured. To provide a fully-developed turbulent flowfield entering the static mixer, a length of pipe greater than 100 diameters was attached upstream of the static mixer. To minimize downstream disturbances, a length of pipe greater than 50 diameters was attached downstream of the mixer. This experimental setup is shown in Figure 2.3. Each of the static mixers was tested at flow rates up to 7 gpm (420 mL/s). The sequence in which different flow rates were measured was randomized. All head loss measurements were performed in triplicate.

RESULTS AND DISCUSSION

Comparison of the KMS Mixer and Backmixer

Four series of experiments compared a 6-element, 1-inch diameter KMS mixer with the backmixer under four different chemical conditions:

Series 1— charge neutralization
Series 2— sub-optimal (low-dose) conditions
Series 3— sweep coagulation conditions
Series 4— equal streaming current conditions

Table 2.1

Raw water data for Series 1—KMS mixer versus backmixer with charge neutralization chemical conditions

Exp. #	Date	Turbidity (ntu)	pH	Temperature (°F)
1B	8/30/97	53-30	6.9	69
1C	1/5/98	4.5-5.0	6.5-6.6	52
1D	2/6/98	79-48	6.9	50
9A	11/15/97	15-12	7.2	55

The chemical operating points for each of these series of experiments are plotted on the alum coagulation diagram in Figure 2.4. Coagulation diagrams for metal salts were developed by Amirtharajah and Mills (1982) to define the regions of coagulant dose and pH for the various coagulation mechanisms. For a the detailed description and case study on the use of these diagrams see also Karr, Amirtharajah, and Jones (1997).

Series 1—Charge Neutralization Conditions

The experiments in Series 1 compared the KMS mixer and backmixer with charge neutralization chemical conditions. Experiments were conducted at 2 gpm (120 mL/s) and 4 gpm (240 mL/s). For each flow rate, a duplicate run was made with the KMS mixer and backmixer on the opposite train as in the previous run to confirm the results. The raw water and experimental conditions for Series 1 are shown in Tables 2.1 and 2.2.

The alum dose for the 2 gpm run, Experiment 1B, was determined from the dose that was being used at the Chattahoochee WTP that day. The alum dose for the 4 gpm run, Experiment 9A, and duplicate optimum dose runs were determined by measuring the alum flow rate required to give a streaming current condition of about zero for the static mixer. The streaming current conditions for Experiments 1B and 9A are shown in Figure 2.5. As shown, the static mixer had a significantly better streaming current than the backmixer for both runs. The less negative streaming current indicates that the static mixer was more effective at charge neutralization than

Table 2.2

Experimental conditions for Series 1—KMS mixer versus the backmixer (BM) with charge neutralization chemical conditions

Exp. #	Alum dose (mg/L)	Flow rate (gpm)	pH	Δh in KMS (in.)	G (s^{-1})		t_d (s)	
					KMS	BM	KMS	BM
1B	9.3	2	6.6–6.7	6.5	1,090	160	1.2	120
1C	7.0	2	6.3–6.4	6.5	1,090	160	1.2	120
1D	17.2	2	5.9–6.0	6.5	1,090	160	1.2	120
9A	9.5	4	6.8–6.9	18	2,560	160	0.6	120

the backmixer. This result is in agreement with the idea of charge neutralization regime conditions requiring fast, intense mixing and dispersion for best results. For the 2-gpm run, the G-value for the static mixer was 1,090 s^{-1} with a detention time of 1.2 seconds, while the G-value for the backmixer was 160 s^{-1} with a detention time of 2 minutes. For the 4-gpm run, the G-value for the static mixer was 2,560 s^{-1} with a detention time of 0.6 seconds, while the G-value for the backmixer was 160 s^{-1} with a detention time of 1 minute.

The settled- and raw-water turbidities for Experiments 1B and 9A are shown in Figures 2.6 and 2.7, respectively. The settled-water turbidity results show that the backmixer outperformed the static mixer by about 1 to 1.5 ntu at 2 gpm and 0.5 to 1 ntu at 4 gpm. This result is not as expected based upon the streaming current since the flocculation basins were operated identically. However, the differences in detention time between the two mixers may explain the improved settled water turbidities. Aluminum hydroxide precipitation begins within 7 seconds after alum addition while the detention time within the backmixer was 1 to 2 minutes (Letterman et al. 1973). At these detention times, it is likely that some high-intensity flocculation occurred in the backmixer. As confirmation, small pinpoint floc were actually observed in the backmixer during several experiments. This high-intensity flocculation in the backmixer most likely promoted the formation of a more dense, settleable floc. In practice, however, the flocculation intensity and detention time can be adjusted or polymer added as a flocculation aid to help promote the formation of a better settling floc when using a static mixer.

Filtered-water turbidities for Experiments 1B and 9A are shown in Figures 2.8 and 2.9, respectively. As shown in Figure 2.8, the static mixer performed better than the backmixer at 2 gpm with respect to filtered-water turbidity, especially during the first three hours of filter operation. This result may be due to the significantly better streaming current condition for the static mixer, since charge neutralization is critical to filter performance. For the 4 gpm run, both mixers performed equally well as shown in Figure 2.9. The filtered-water turbidity for the static mixer was equally good at both 2 and 4 gpm, despite having a less-negative streaming current (-1.0 at 2 gpm and ~0.0 at 4 gpm). However, the backmixer filtered-water turbidity improved for the 4-gpm run. The improved performance of the backmixer at 4 gpm is a result of the better streaming current, -1 versus -2.3 to -4 for the 2 gpm run. Two additional runs at 2 gpm, Experiments 1C and 1D, were conducted using the same method for determining the optimum alum dose as in the 4-gpm run. The results were similar to those obtained in the 4-gpm run indicating that the differences seen between the first 2-gpm run and the 4-gpm run were a result of different chemical conditions (as indicated by the streaming current readings) and not the increased head loss or *G*-value at 4 gpm. A streaming current reading of -1.0 may be better than 0.0. However, the static mixer was able to reach a less negative streaming current at the same alum dose, indicating increased efficiency at charge neutralization. The results for the filtered water particle counts for the experiments in Series 1 are shown in Table 2.3. The particle counts generally followed the trends that were observed for filtered-water turbidity.

Series 2—Underdosed Conditions

Series 2 compared the static mixer and backmixer with underdosed chemical conditions. The alum doses used for Series 2 were approximately half of the required dose for optimum charge neutralization regime conditions. Experiments were conducted at 2 gpm and 4 gpm. The raw-water and experimental conditions for Series 2 are shown in Tables 2.4 and 2.5.

The streaming current for the 2-gpm runs, Experiments 3A and 3B are shown in Figure 2.10. As shown in Figure 2.10, the static mixer had a significantly better streaming current than the backmixer for both of the 2-gpm runs. The less-negative streaming current indicates that the static mixer was more effective at charge neutralization than the backmixer at low alum doses. Similar to the experiments in Series 1, these results reinforce the idea of charge neutralization

Table 2.3

Filtered-water particle counts for Series 1—KMS mixer versus the backmixer (BM) with charge neutralization chemical conditions (anthracite filters only)

Exp. #	Flow rate (gpm)	Turbidity* (ntu)		Particle counts (#/mL)					
				2–15 µm		3–15 µm		20–150 µm	
		KMS	BM	KMS	BM	KMS	BM	KMS	BM
1B	2	0.11	0.31	171	146	81	54	0.9	1.2
1C	2	0.09	0.08	103	89	55	43	0.2	0.7
1D	2	0.09	0.10	52	63	23	27	0.5	0.6
9A	4	0.13	0.12	129	135	73	72	0.2	1.0

*Turbidity measured at the same time as the grab sample was taken for the particle count measurements.

regime conditions requiring fast, intense mixing and dispersion for best results. The streaming current readings for the 4-gpm run, Experiment 8C, are shown in Figure 2.11. As shown in Figure 2.11, the static mixer performed only slightly better (0.2 SCD units) than the backmixer. This was unexpected considering the results of the 2-gpm runs. However, the raw water conditions were quite different than for the 2-gpm runs. The 4-gpm run was conducted on a day with low turbidity (5 ntu) and cold water temperature of 48°F (9°C).

The settled-water and raw-water turbidities for Experiments 3A and 3B are shown in Figures 2.12 and 2.13, respectively. The static mixer performed better (about 1 ntu) for settled-water turbidity for the first 2-gpm run, Experiment 3A. However, in the second 2-gpm run, Experiment 3B, both mixers had the same settled-water turbidity. Settled-water and raw-water turbidities for the 4-gpm run, Experiment 8C are shown in Figure 2.14. As shown in Figure 2.14, both mixers performed about the same for settled-water turbidities. The settled-water turbidities for both mixers were actually higher than the raw-water turbidities for the 4-gpm run. This indicates that virtually no settling occurred due to poor floc formation for both mixers. The settled-water turbidities were higher than the raw-water turbidity because of the solids added by aluminum hydroxide precipitation. The poor settling results are as expected for the 4-gpm run for the following reasons: the low alum dose, poor streaming current for both mixers, low raw-water turbidities (5 ntu), cold water temperature of 48°F (9°C), and short flocculation time (15 minutes).

Table 2.4

Raw water data for Series 2—KMS mixer versus backmixer with sub-optimal chemical conditions

Exp. #	Date	Turbidity (ntu)	pH	Temperature (°F)	Alkalinity (mg/L as $CaCO_3$)	Color (alpha units)	Conductivity (µS/cm)
3A	09/16/97	31–24	6.9–6.5	68	—	—	—
3B	09/18/97	24–19	6.9	67	12.6	78	44
3C	01/03/98	5.0–3.9	6.6–5.5	52	—	—	—
8C	12/08/97	5–6	6.7	48	18.0	57	60
8E	02/09/98	9–10	7.0–7.1	54	—	—	—

Table 2.5

Experimental conditions for Series 2—KMS mixer versus the backmixer (BM) with sub-optimal chemical conditions

Exp. #	Alum dose (mg/L)	Flow rate (gpm)	pH	Δh in KMS (in.)	G (s^{-1})		t_d (s)	
					KMS	BM	KMS	BM
3A	6	2	6.6-6.2	6.5	1,090	160	1.2	120
3B	5	2	6.6-6.7	6.5	1,090	160	1.2	120
3C	4	2	6.4	6.5	1,090	160	1.2	120
8C	4	4	6.4	18	2,560	160	0.6	60
8E	4.6	4	6.9	18	2,560	160	0.6	60

Filtered-water turbidities for the 2-gpm runs, Experiments 3A and 3B are shown in Figures 2.15 and 2.16, respectively. The static mixer performed considerably better than the backmixer for both 2-gpm runs, especially during the first 2 hours of filter operation. In fact, the KMS mixer produced excellent filtered-water turbidities (<0.2 ntu) by the end of both 2-gpm runs, despite the low alum doses. Once again, these results are due to the significantly better streaming current developed by the static mixer which indicates better charge neutralization conditions. The filtered-water turbidity results for the 4-gpm run, shown in Figure 2.17, were quite different than for the 2-gpm runs. The backmixer actually performed slightly better than the static mixer for filtered-water turbidity. The differences between the 2-gpm and 4-gpm run may once again be explained by the significantly different raw water conditions and the streaming current for the static mixer. The streaming current of -4 for the 4-gpm run on the static mixer indicates that very little charge neutralization had occurred. This explains the poor filter performance for the static mixer compared with the 2-gpm run. The slightly better filtered water performance for the backmixer compared to the static mixer for the 4-gpm run may be due to the long detention time (1 minute) in the backmixer compared to 0.6 seconds in the static mixer. This long detention time most likely promotes the formation of aluminum hydroxide precipitates over the species which promote charge neutralization. With the low raw water turbidities and cold water temperature in the 4-gpm run, these additional particles may have improved the flocculation kinetics for the backmixer over the static mixer. Also, it is well known that colder water requires longer flocculation times and higher alum doses compared with warmer waters.

As a result of the significant differences found between the 2-gpm and 4-gpm runs, the 2-gpm run was repeated (Experiment 3C) under raw water conditions similar to the 4-gpm run (see Tables 2.4 and 2.5). The results were quite similar to those found in the 4-gpm run, Experiment 8C. Both mixers had a streaming current of -2.5 and the filtered-water turbidities were approximately equal. This indicates that the differences observed in Experiments 3A and 3B (2 gpm) and Experiment 8C (4 gpm) were mostly due to the substantially different raw water conditions and not the different mixing conditions in the static mixer at 2 and 4 gpm, as alluded to above.

The 4-gpm run was also repeated (Experiment 8E) with higher raw-water turbidities and temperatures. The results of this 4-gpm run were more similar to the first 2-gpm runs. For this 4-gpm run, the static mixer performed better than the backmixer for all measured parameters: streaming current of -2.2 for the static mixer and -3.4 for the backmixer, settled-water turbid-

ity—6.8 for the static mixer and 7.4 for the backmixer, filtered-water turbidity—0.18 for the static mixer and 0.29 for the backmixer.

Filtered water particle counts for Series 2 are shown in Table 2.6. The particle counts generally followed the same trend as the turbidity. The static mixer produced equal or better particle counts than the backmixer for all experiments in Series 2.

Series 3—Sweep Coagulation Conditions

Series 3 compared the static mixer and backmixer with chemical conditions which were in the sweep coagulation regime. The alum doses used for Series 3 were at least twice the required dose for optimum charge neutralization regime conditions and the coagulated water pH range was kept between 7 to 7.5 by adding sodium hydroxide to the raw water. Two duplicate runs, with the static mixer and backmixer on the opposite train as the previous run, at raw water flow rates of 2 gpm were conducted in Series 3. The raw-water and experimental conditions for Series 3 are shown in Tables 2.7 and 2.8 .

The settled-water and raw-water turbidities for Series 3, Experiment 2A, are shown in Figure 2.18. As shown, the two mixers performed approximately the same for settled-water turbidity. However, the duplicate run for this experiment, Experiment 2D, showed that the backmixer performance was slightly better (about 0.5 to 1 ntu lower) than the static mixer. The raw water turbidity for Experiment 2D (5 to 6 ntu) and water temperature were significantly lower than for Experiment 2A. These conditions may have made the settled-water turbidity more sensitive to flocculation conditions for Experiment 2D. The high-energy flocculation occurring in the backmixer, as discussed earlier, may have allowed the backmixer to create a more dense, settleable floc.

Filtered-water turbidities for both mixers were equally good as shown in Figure 2.19. The duplicate run showed similar results. Filtered-water particle counts for Series 3 are shown in Table 2.9. As shown, the particle counts generally followed the same trend as the turbidity. In general, these results are in agreement with the results found by Amirtharajah and Mills (1982) and Clark et al. (1994) who both found that under sweep coagulation conditions, rapid mixing conditions had very little effect on treatment performance.

Table 2.6

Filtered-water particle counts for Series 2—KMS mixer versus the backmixer (BM) with sub-optimal chemical conditions (anthracite filters only)

Exp. #	Flow rate (gpm)	Turbidity* (ntu)		Particle counts (#/mL)					
				2–15 µm		3–15 µm		20–150 µm	
		KMS	BM	KMS	BM	KMS	BM	KMS	BM
3A	2	0.14	0.33	115	173	56	71	0.8	1
3B	2	0.18	0.63	71	211	30	55	0.3	0.7
3C	2	0.18	0.16	203	203	91	97	0.3	0.2
8C	4	0.52	0.41	319	327	163	163	0.6	0.3
8E	4	0.19	0.29	156	200	59	79	0.2	0.3

*Turbidity measured at the same time as the grab sample was taken for the particle count measurements.

Table 2.7

Raw water data for Series 3—KMS mixer versus the backmixer with sweep coagulation chemical conditions

Exp. #	Date	Turbidity (ntu)	pH	Temperature (°F)	Alkalinity (mg/L as $CaCO_3$)	Color (alpha units)	Conductivity (µS/cm)
2A	09/09/97	19–14	7.1	69	13.2	72	50
2D	12/13/97	5.3–5.9	6.8	52	—	—	—

Table 2.8

Experimental conditions for Series 3—KMS mixer versus the backmixer (BM) with sweep coagulation chemical conditions

Exp. #	Alum dose (mg/L)	Flow rate (gpm)	pH	Δh in SM (in.)	G (s^{-1})		t_d (s)	
					KMS	BM	KMS	BM
2A	25	2	7-7.5	6.5	1,090	160	1.2	120
2D	25	2	7-7.2	6.5	1,090	160	1.2	120

Table 2.9

Filtered-water particle counts for Series 3—KMS mixer versus the backmixer (BM) with sweep coagulation chemical conditions

Exp. #	Flow rate (gpm)	Turbidity* (ntu)		Particle counts (#/mL)					
				2–15 µm		3–15 µm		20–150 µm	
		KMS	BM	KMS	BM	KMS	BM	KMS	BM
2A†	2	0.12	0.13	75	66	32	30	2.4	1.8
2D‡	2	0.08	0.11	120	199	54	88	0.6	0.7

*Turbidity measured at the same time as the grab sample was taken for the particle count measurements.
†Antracite filters only
‡GAC filters only because of problem with anthracite filters during this experiment.

Series 4—Equal Streaming Current Conditions

Because the initial experiments showed that using the KMS mixer consistently provided a better (less negative) streaming current than the backmixer at the same alum dose, the experiments in Series 4 were carried out under equal streaming current conditions instead of equal alum doses. The objective for doing this was to show that equivalent treatment performance could be obtained with lower alum doses using the static mixer. Series 4 compared the static mixer and backmixer with chemical conditions that caused the streaming current reading to be between 0 to -0.2. A zero or slightly negative streaming current indicates that charge neutralization conditions exist. Therefore, all of the experiments in Series 4 were conducted with optimum charge neutralization chemical conditions. The alum flow rate was set on each train at the beginning of each run by slowly increasing the alum dose from a low value until the streaming current condition was equal to the desired value. As conditions changed over the course of the run, the alum flow rate was adjusted to maintain the set streaming current measurement on each train. The streaming current of each train was checked and the alum flow rate adjusted, if necessary, every 30 minutes. Alum doses were determined at the beginning and end of each experiment. Experiments with raw-water flow rates from 2 to 5 gpm were conducted. The raw-water and experimental conditions for Series 4 are shown in Tables 2.10 and 2.11.

Table 2.10

Raw water data for Series 4—KMS mixer versus the backmixer with equal streaming current

Exp. #	Date	Turbidity (ntu)	pH	Temperature (°F)	Alkalinity (mg/L as $CaCO_3$)	Color (alpha units)	Conductivity (μS/cm)
4A	09/30/97	71–41	7–6.7	67	14.8	340–280	57
5A	10/09/97	28–46	7–6.7	69	14.8	64–122	60
5B	10/11/97	12–8.5	6.6–7.2	68	—	—	—
6A	10/15/97	10.3–6.7	6.9–7.4	67	—	—	—
6B	10/23/97	24–28	6.4–6.8	64	13.9	68-76	48
7A	10/25/97	25–17	6.9–7.1	64	—	—	—

Table 2.11

Experimental conditions for Series 4—KMS mixer versus the backmixer (BM) with equal streaming current

Exp. #	Alum dose (mg/L)		Flow rate (gpm)	pH	Δh in KMS (in.)	G (s^{-1})		t_d (s)	
	SM	BM				KMS	BM	KMS	BM
4A	14.6	19.9	2	6.0–6.3	6.5	1,090	160	1.2	120
5A	8.0	11.0	3	6.3–6.8	13.5	1,920	160	0.8	80
5B	7.0	10.0	4	6.2–6.7	18	2560	160	0.6	60
6A	9.3	12.5	4	6.4–6.9	18	2560	160	0.6	60
6B	6.9	9.6	5	6.5–6.9	26	3440	160	0.5	48
7A	7.2	9.9	5	6.4–6.8	26	3440	160	0.5	48

Table 2.12

Summary of results for Series 4—KMS mixer versus the backmixer (BM) with equal streaming current

Exp. #	Flow rate (gpm)	Alum dose (mg/L)		Δd^* (%)	Turbidity (ntu)				Particle counts† (#/mL) 2–15μm	
					Settled		Filtered			
		KMS	BM		KMS	BM	KMS	BM	KMS	BM
4A	2	14.6	19.9	27	8.5	7.3	0.13	0.12	92	82
7A	3	8.0	11.0	27	4.4	3.8	0.11	0.11	94	105
5A	4	7.0	10.0	30	9.0	7.0	0.13	0.12	129	104
5B	4	9.3	12.5	26	4.3	3.9	0.14	0.13	111	99
6A	5	6.9	9.6	28	6.0	4.9	0.11	0.10	—	—
6B	5	7.2	9.9	27	7.9	5.3	0.10	0.11	98	120

*Δd is the difference in percent of the backmixer alum dose between the dose required by the static mixer and the backmixer to obtain the same, nearly zero streaming current.
†Particle counts for the anthracite filters only.

The results for Series 4 are shown collectively in Table 2.12. The KMS mixer required significantly less alum than the backmixer to reach the same streaming current condition. For all flow rates, the KMS mixer required 25 to 30% less alum than the backmixer to reach optimum charge neutralization conditions as indicated by the streaming current readings. However, the backmixer produced better settled water turbidities for all of the experiments in Series 4. The better settled-water performance of the backmixer is consistent with the previous experiments and is potentially caused by the high energy flocculation provided by the backmixer. In practice, the flocculation intensity and detention time could be adjusted to promote the formation of a better settling floc when using a KMS mixer. The filtered-water turbidities and particle counts were approximately equal for both mixers for all runs, despite significantly lower alum doses with the KMS mixer. These results indicate that treatment plants could possibly see significant chemical cost savings by using a static mixer over a backmixer. This would be especially true for direct filtration or dissolved air flotation plants where charge neutralization conditions and pin-point floc are desired over a large, settleable floc.

Effect of Design Parameters

Two different series of experiments were performed to investigate the effect of static mixer design parameters on the performance of the pilot plant. In this context, design parameters refers to those parameters that a process engineer (the person designing a water treatment plant) can choose, namely, the number of elements in the static mixer (Series 5) and the diameter of the static mixer (Series 6). For the experiments in both series, the chemical conditions were charge neutralization. The operating points for these experiments are shown on the coagulation diagram in Figure 2.4. Table 2.13 shows the different flow conditions for each static mixer tested.

Series 5—Number of Elements

This series of experiments compared the performance of static mixers with the same configuration but with a different number of elements. For these experiments, KMS 1-inch diameter mixers were used. Experiments were performed with mixers containing 2 and 6 elements. Flow rates of 2 and 4 gpm were used. For each flow rate, duplicate runs were made with the mixers on the opposite trains. Some of these experiments were performed using both alum and PACl. The raw-water and experimental conditions are shown in Tables 2.14 and 2.15.

The chemical dose for each experiment was determined using the streaming current of the coagulated water. In Experiments 2S, 7S, and 13S, the dose was set on each individual mixer to obtain the same streaming current. In experiments 10S and 12S, the dose was set to charge neutralization for the 6-element mixer and then applied to the 2-element mixer. As mentioned previously for charge neutralization, a streaming current reading close to zero was desired (usually -0.03). In the 4-gpm experiments, the coagulant dose required for charge neutralization was identical in both the 2- and 6-element mixer. However, for the 2-gpm runs in experiments 10S and 12S, when the dose was optimized on the 6-element mixer and the same dose was used on the 2-element mixer, a slightly more negative streaming current was observed for the 2-element mixer.

Table 2.13

Static mixers and flow rates in the experiments of Series 5 to 7

Mixer*	Δh (in.)		G (s^{-1})		t_d (s)	
	Q=4 gpm	Q=2 gpm	Q=4 gpm	Q=2 gpm	Q=4 gpm	Q=2 gpm
1–KMS–2	3.14	1.20	2,072	906	0.29	0.59
1–KMS–4	5.76	1.86	2,275	914	0.45	0.89
1–KMS–6	9.37	2.87	2,504	980	0.60	1.20
1.5–KMS–2	0.73	0.40	552	289	0.96	1.92
1.5–KMS–6	2.30	0.74	673	270	2.04	4.07
2–KMS–2	0.60	0.30	341	171	2.07	4.13
2–KMS–4	0.74	0.31	297	136	3.37	6.73
2–KMS–6	1.20	0.58	324	159	4.59	9.18
1–Stata–7	34.24	8.33	4,595	1,603	0.65	1.30
1–Stata–14	52.90	18.01	4,929	2,034	0.87	1.75
2–Stata–5	1.80	0.55	434	170	3.83	7.65
2–Stata–10	3.10	1.00	477	192	5.46	10.92
1–Spiral–6	7.50	2.41	2,240	898	0.60	1.20
2–Spiral–6	0.85	0.47	282	148	4.30	8.60
1–SMV–3	6.63	1.79	2,495	916	0.43	0.85
2–SMV–3	0.45	0.20	238	112	3.20	6.40

*Notation: [mixer diameter]–[mixer type]–[number of mixer elements], e.g., 2–KMS–6 is a 2-inch diameter Kenics helical (KMS) mixer with six elements.

The settled-water and raw-water turbidities for Experiments 2S and 7S are shown in Figures 2.20 and 2.21, respectively. These turbidity readings were obtained using grab samples taken every 30 minutes. The settled-water results show that there is very little difference between the 2- and 6-element KMS mixer at 4 gpm. The settled- and raw-water turbidities for experiments 10S and 13S are shown in Figures 2.22 and 2.23, respectively. These figures show that the settled-water turbidity is lower for the 6-element mixer at 2 gpm. Though the magnitude of this difference is small, a similar difference was observed in the duplicate experiment.

Table 2.14

Raw water data for Series 5—Comparing the effect of the number of elements

Exp. #	Date	Turbidity (ntu)	pH	Temperature (°F)
2S	07/02/98	51–76	7.1	72
7S	08/04/98	6–8	7.1–7.4	75
10S	08/18/98	17–26	7.0–7.3	72
12S	08/25/98	16–19	7.1–7.3	68
13S	08/26/98	11–15	7.1–7.4	68

Filtered-water turbidities for experiments 2S, 7E, 10E, and 13E are shown in Figures 2.24, 2.25, 2.26, and 2.27, respectively. As shown, there was very little difference in filtered-water turbidity on ripening occurred, and all turbidities were 0.2 ntu or lower. These minor differences may have been due to differences in the filter themselves or differences in the turbidimeters. Attempts to remove these differences were unsuccessful. The similarity of filtered-water turbidity is expected because filtration is primarily dependent on the chemical conditions of the water (Amirtharajah 1988). Since in all experiments chemical conditions of the water were charge neutralization, filtration differences were too small to be detected. The particle counts for the anthracite and GAC filter media were similar for all experiments.

From these experiments, very little difference was observed in the performance of the KMS mixers with 2 and 6 elements. This result suggests that the mixing (and consequently the additional head loss) provided by the additional 4 elements did not seem to result in a measurable improvement in performance. The only observed difference was at 2 gpm where the 6-element static mixer had slightly lower settled-water turbidity.

Table 2.15

Experimental conditions for Series 5—Comparing the effect of the number of elements

Exp. #	Coagulant	Average coagulant dose (mg/L)	Average pH
2S	Alum	10.5	6.6
7S	PACl	2.2	7.1
10S	PACl	2.9	7.1
12S	PACl	2.3	7.1
13	Alum	7.9	6.8

Series 6—Mixer Diameter

This series of experiments compared static mixers of the same configuration and number of elements but with different diameters. For all experiments in this series, alum was the coagulant, and the flow rate was 4 gpm. At 2 gpm, experiments in the 2-inch diameter mixers would have approach velocities 0.2 ft/s (6 cm/s)—obviously much too low—thus, experiments were only performed at the higher flow rate. For this series of experiments, duplicates were only performed on selected experiments because of time and other resource constraints. Both the KMS and SMV mixers were tested in this series.

The raw water and experimental conditions for these experiments are shown in Tables 2.16 and 2.17. The chemical dose was optimized for charge neutralization using the SCD for both static mixers. No significant, repeatable differences in the chemical dose required for charge neutralization was observed. The settled- and raw-water turbidities for experiments 23S and 33S are shown in Figures 2.28 and 2.29. The filtered-water turbidity for experiment 32S is shown in Figure 2.30. The settled-water turbidity for experiment 23S was measured from grab samples taken every 30 minutes. The settled-water and filtered-water turbidity for experiments 32S and 33S were measured using the bitlogger at a rate of 1 sample per minute. Although slight differences were observed in the performance of the 1- and 2-inch diameter mixers, none of these differences were consistent from experiment to experiment. Thus, these tests were inconclusive.

Table 2.16

Raw water data for Series 6—Static mixers versus an empty pipe

Exp. #	Date	Turbidity (*ntu*)	pH	Temperature (°F)
20S	07/29/99	8–12	7.3	75
21S	07/30/99	9–12	7.3	75
22S	08/04/99	5–7	7.3	75
26S	08/13/99	8–9	7.3	75
25S	08/09/99	8–11	7.4	72
30S	08/19/99	5–8	7.3	72
27S	08/16/99	5–7	7.3	73
26S	08/11/99	7–11	7.3	75
29S	08/18/99	5–6	7.4	72
31S	08/27/99	19–30	7.2	68

Table 2.17

Experimental conditions for Series 6—Static mixers versus an empty pipe

Exp. #	Static mixer	Diameter (in.)	Alum dose (mg/L)	
			Static mixer	Empty pipe
20S	KMS	1	9.4	9.4
21S	KMS	1.5	9.6	9.9
22S	KMS	2	8.0	8.5
26S	Stata	1	8.4	8.4
25S	Stata-tube	2	9.6	11.0
30S	Stata-tube	1	7.9	8.4
27S	Spiral	1	7.3	7.3
26S	Spiral	2	10.7	11.5
29S	SMV	1	7.5	7.6
31S	SMV	2	9.0	8.9

Table 2.18

Raw water data for Series 7—Comparing the effect of diameter

Exp. #	Date	Turbidity (ntu)	pH	Temperature (°F)
23S	08/05/99	5–7	7.3	72
24S	08/06/99	6–9	7.4	72
32S	08/31/99	8–10	7.3	68
33S	09/08/99	8–12	7.2	68
34S	10/7/99	20–33	7.0	61

Series 7—Comparison of Static and Empty-Pipe Mixer

The experiments in Series 7 compared each of the static mixers to an empty-pipe mixer of the same dimensions. For all experiments, alum was the coagulant, and the flow rate was 4 gpm. Duplicates were only performed for selected tests because of time and other resource constraints. The KMS mixer was compared to the empty pipe at three diameters: 1, 1.5, and 2 inches. The Stata-tube and Spiral mixers were tested at diameters of 1 and 2 inches only.

The raw-water and experimental conditions for Series 7 are shown in Tables 2.18 and 2.19. The chemical dose was determined by optimizing both the static mixer and the empty-pipe mixer for charge neutralization conditions with the SCD. The settled- and raw-water turbidity in experiments 20S, 25S, and 26S are shown in Figures 2.30, 2.31, and 2.32, respectively. These data were obtained using grab samples every 30 minutes. The results for the settled water showed almost no performance difference between the empty-pipe mixer and the static mixer in all cases. This is expected because of the charge neutralization conditions. The filtered-water turbidity for experiments 20S, 25S, and 30S are shown in Figures 2.33, 2.34, and 2.35, respectively. These data were from using the bitogger. Much like the settled-water turbidity data, the filtered-water turbidity data show almost no difference between the empty-pipe and the static mixer for all cases.

Table 2.19

Experimental conditions for Series 7—Comparing the effect of diameter

Exp. #	Static mixer	Diameters (in)	Alum dose (mg/L)	
			Small *d*	Large *d*
23S	KMS	1 v. 2	8.2	8.6
24S	KMS	1.5 v. 2	8.0	8.0
32S	SMV	1 v. 2	7.6	7.1
33S	SMV	1 v. 2	6.8	6.8
34S	SMV	1 v. 2	7.7	7.7

For each static-mixer design, a trend was observed by comparing the optimum alum dose for each diameter of static mixer and empty-pipe mixer tested. Figure 2.36 compares the optimum alum dose for the 1-, 1.5- and 2-inch KMS mixers. For the 1.5- and 2-inch mixers, there is a 3 and 6 percent difference in the coagulant required. Since the raw water conditions vary for each experiment, the important point to note on this graph is the difference in chemical dose. Figure 2.37 shows a similar difference for the Stata-tube mixers, and likewise, Figure 2.38 shows a similar trend for the Spiral static mixers. One possible explanation for this difference is that at the 1- and 2-inch scales, the Reynolds number (*Re*) in the empty-pipe mixer is 10,505 and 5,252, respectively, thus, at the 1-inch scale, the Reynolds number is much further into the fully-developed turbulent region.

Head Loss Tests

The results of the head loss tests were used to calculate a plot of friction factor, *f*, versus Reynolds number, *Re*, for each mixer. From the perspective of the process designer, the head loss represents the operating cost of the mixer. For each flow rate measured on each mixer, a Δh value was recorded. This value was used to calculate the friction factor using the Darcy–Weisbach equation:

$$\Delta h = f \frac{L}{D} \frac{U^2}{2g}$$

where Δh = head loss across the static mixer (inches)

f = friction factor

L = length of the static mixer (inches)

D = nominal diameter of the pipe (inches)

U = bulk (average) velocity in the approach section of the pipe (ft/s)

g = acceleration due to gravity (ft/s^2).

The plots of Reynolds Number, *Re*, versus friction factor, *f*, for the KMS mixer, TAH Spiral mixer, TAH Stata-Tube mixer, and SMV mixer are shown in Figures 2.40, 2.41, 2.42, and 2.43, respectively. For each configuration, all sizes and number of elements were grouped together, except where noted. For the KMS mixers, there were two correlations for all diameters and number of elements tested. First, when the Reynolds number is less than 2,000, or in the laminar region, the trend is linear as shown in Figure 2.40. When the Reynolds number exceeded 2,000, up to almost 20,000, it can be seen that the friction factor is fairly constant. This constant friction factor can be seen as well with the TAH Spiral mixers and Koch SMV mixers in Figures 2.41 and 2.43, respectively. The TAH Stata-Tube mixer showed two correlations, based on the diameter of the mixer. The trends for the 1- and 2-inch diameter mixers were parallel, and not constant. The 2-inch diameter mixer had a consistently higher friction factor than the 1-inch static mixer. The data for all static mixers are plotted in Figure 2.44.

Pahl and Muschelknautz (1982) found the friction factor for various static mixers with Reynolds number greater than 1,000: KMS , $f \sim 0.75$; and SMV, $f \sim 1.0$. Others have also done similar experiments using static mixers with different mixing element configurations (Šír and Lecjaks 1982, Burfoot and Rice 1983).

SUMMARY AND CONCLUSIONS

KMS Mixer versus the Backmixer

The KMS mixer was found to be very effective for rapid mixing in coagulation with alum. Based on streaming current measurements, filtered-water turbidities and filtered-water particle counts, the KMS mixer performed as well or better than the backmixer and empty pipe for almost all raw water, chemical and mixing conditions tested. The KMS mixer performed well over the head loss ranges of 6.5 to 26 in. (G-values of 1,090 s^{-1} to 3,440 s^{-1}) and detention times of 0.5 to 1.2 seconds. The KMS mixer worked very well for both charge neutralization and sweep coagulation mechanisms. Further, the KMS mixer was able to reach charge neutralization conditions and equal treatment performance, with the exception of settled-water turbidity, at alum doses which were 20 to 30% less than required for the backmixer. This indicates that chemical cost savings could be realized with the static mixer over a conventional mechanical backmixer.

However, the results at the pilot-scale indicate that the mechanical backmixer may have an advantage of producing a more settleable floc, under equivalent flocculation basin conditions, due to simultaneous high energy flocculation in the backmixer as a result of the long detention time. In practice, if a more settleable floc is desired, adjustment of the flocculation time and/or energy or addition of a flocculation aid would allow a larger and more settable floc to form when using the static mixer.

Overall, the static mixer would be very effective for both conventional or direct filtration. However, the static mixer seems ideal for direct filtration or flotation plants where charge neutralization conditions and pinpoint floc are desired.

Static Mixer Experiments

The various static mixers tested were found to be very effective for rapid mixing in coagulation with alum and PACl, based on settled-water turbidity, filtered-water turbidity, and filtered-water particle counts.

For the KMS mixer, at flow rates of 4 gpm, a two element mixer at 1-inch diameter performs as well as the 6-element mixer, based on streaming current readings, settled-water turbidity, filtered-water turbidity, and filtered water particle counts. While at 2 gpm, this same comparison showed that the 6 element mixer performed better based on streaming current readings alone. This supports the idea that there is a minimum mixing intensity required for adequate treatment, and that additional mixing elements increase the detention time and head loss to an unnecessary level.

At the 1-inch diameter, empty pipes with a Reynolds number of 10,505 perform as well as the static mixer for all static mixer geometries tested. However, as the scale increases to 2-inches in diameter, the Reynolds number drops to 5,252 and the static mixer maintains effective mixing of the coagulant, while the empty pipe does not perform as well at the same coagulant dose based on streaming current readings. The empty pipe at the 2-inch diameter required as much as 15 percent more coagulant to achieve the same streaming current condition. This suggests that at higher pipe diameters, the static mixer is necessary to create the mixing for coagulation that empty pipes cannot provide. This effect was seen in all mixer geometries tested.

When static mixers of similar mixer geometries and number of elements but different diameters were compared, the mixing intensity was adequate at the 1-inch diameter as well as the 2-inch diameter based on streaming current readings. This result occurred in all mixer geometries tested, which suggests that the minimum mixing intensity required for adequate mixing of the coagulant was exceeded by the 1 and 2-inch diameter mixers.

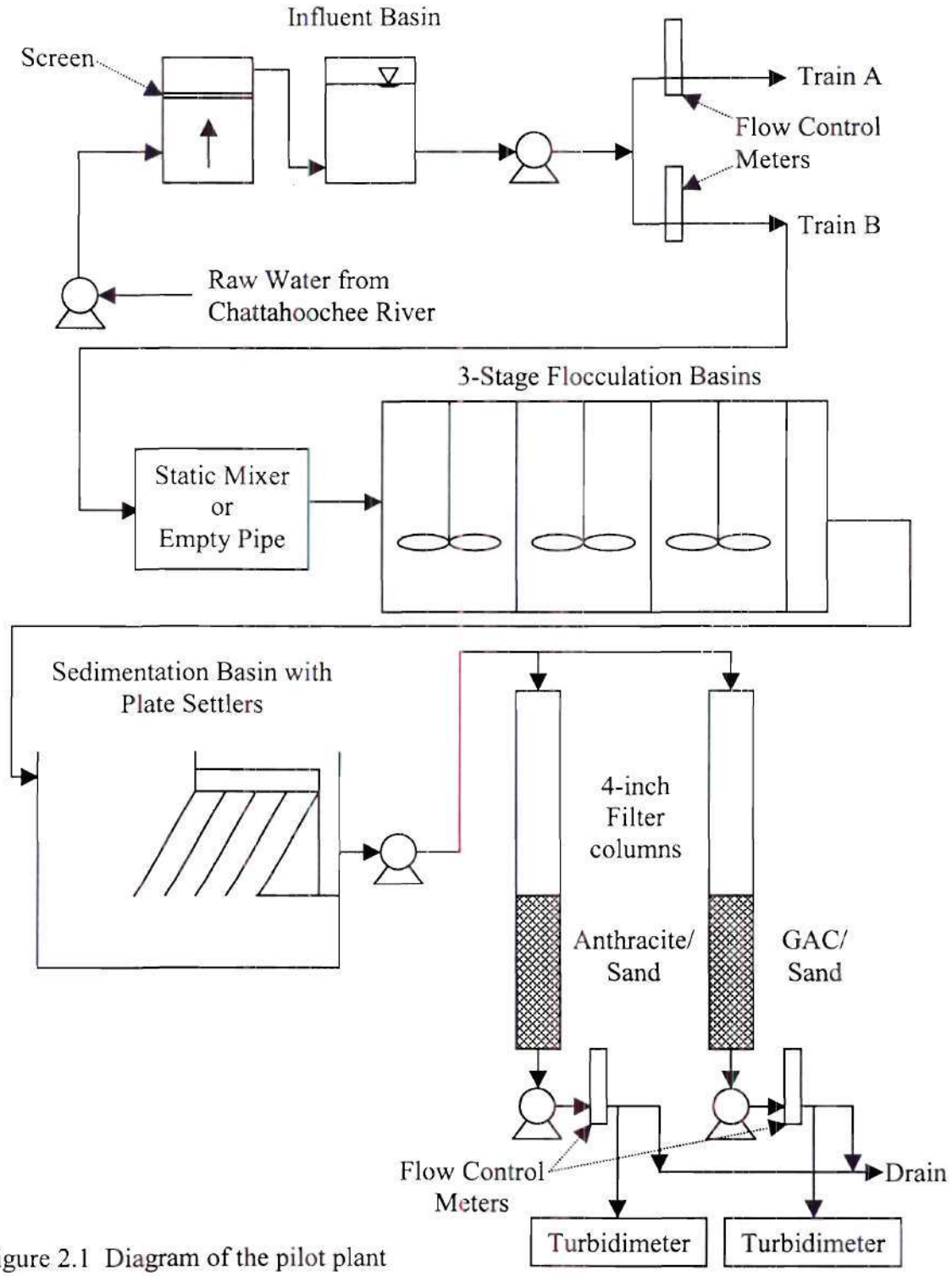

Figure 2.1 Diagram of the pilot plant

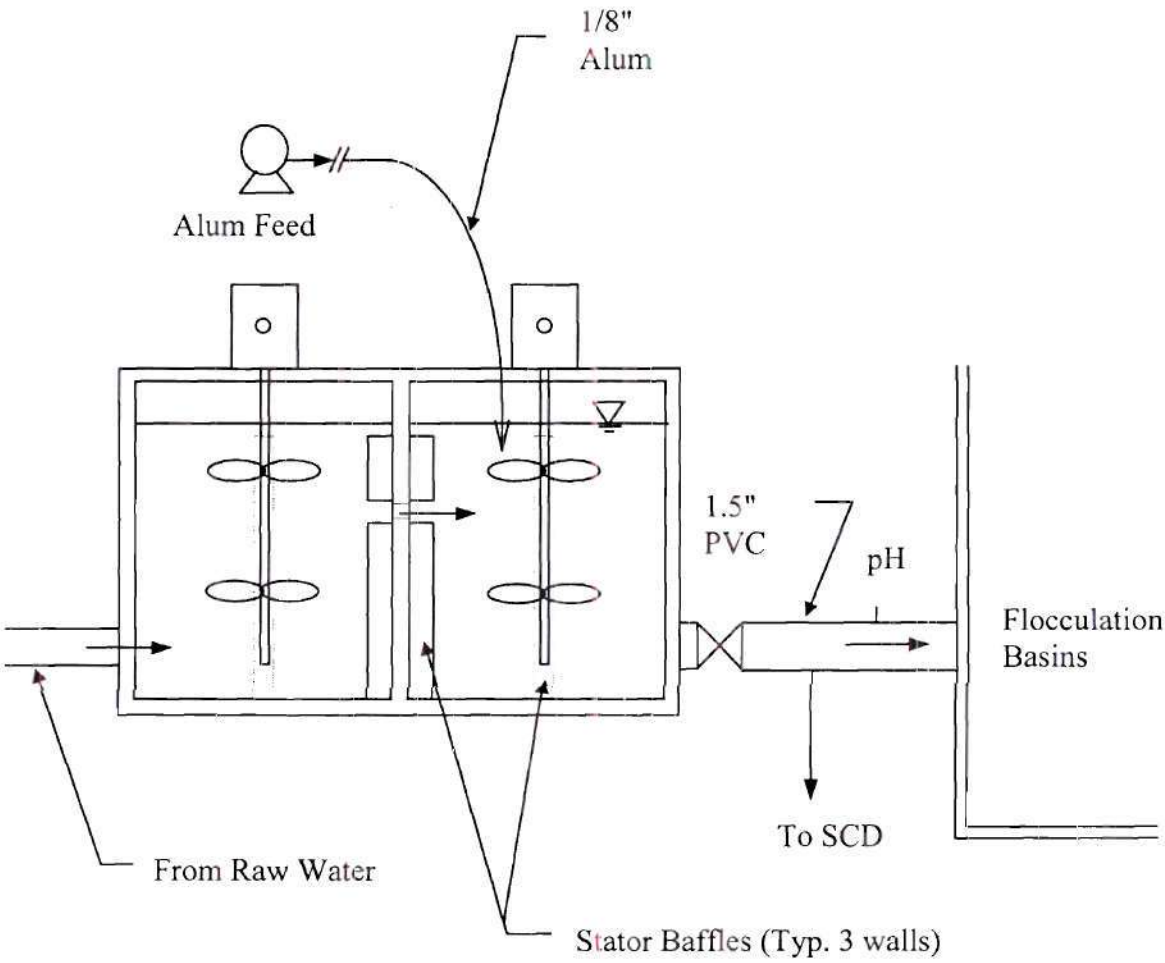

Note: Two Backmixers available, only the downstream mixer was used.

Figure 2.2 Backmixer setup

Head Loss Measurement Setup:

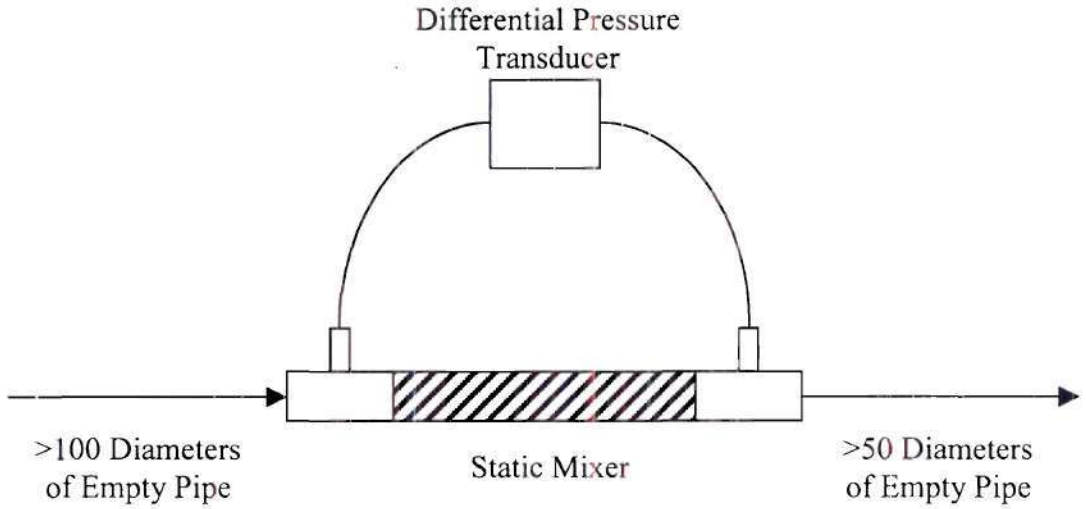

Experimental Setup:

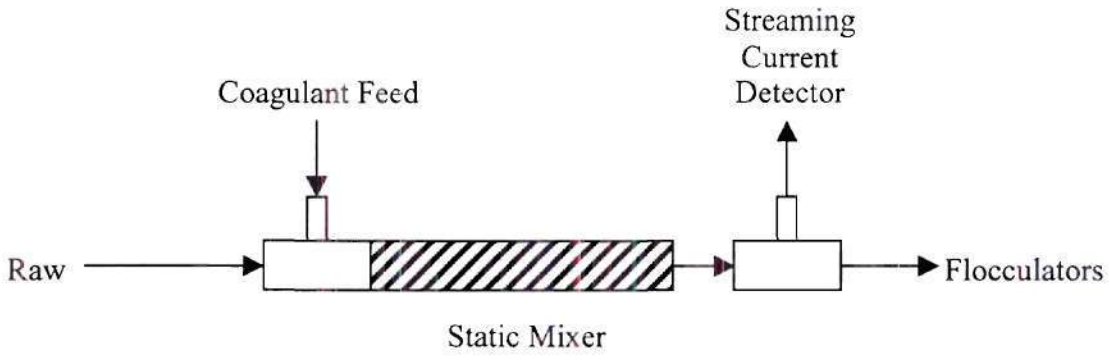

Figure 2.3 Static mixer setup

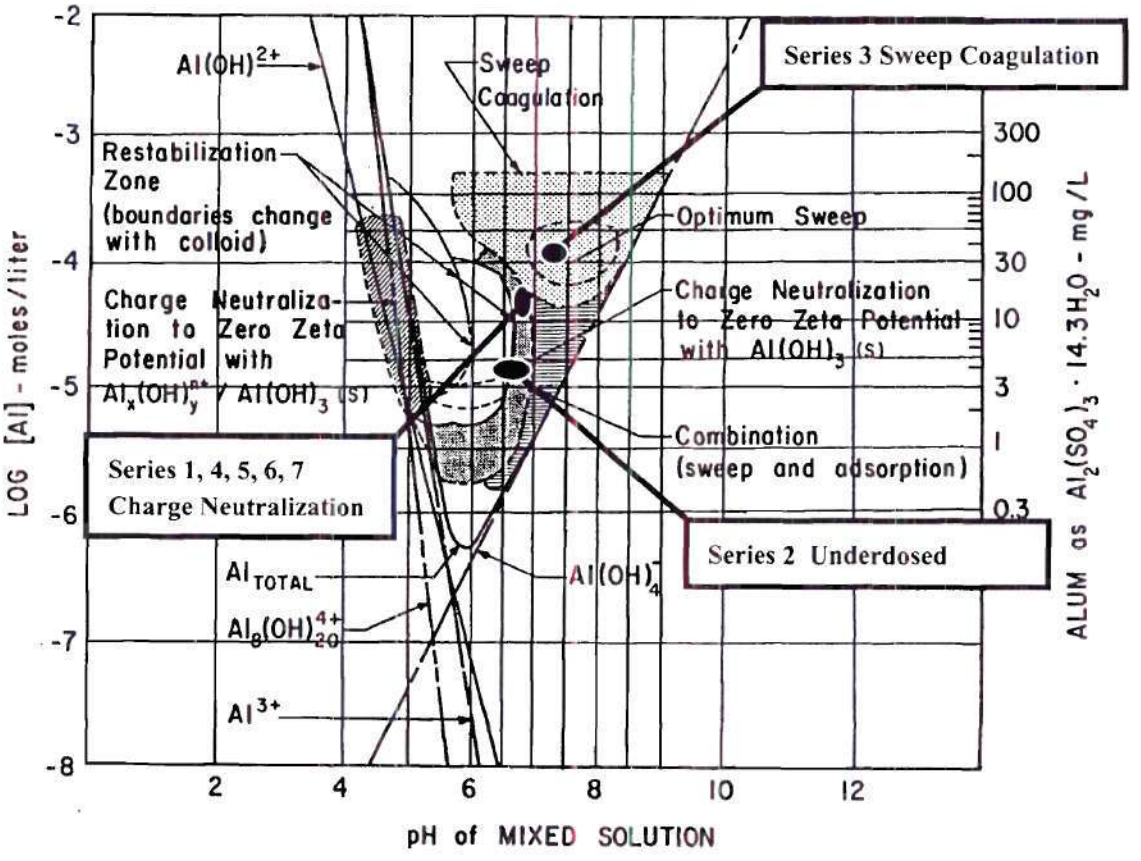

Source: Amirtharajah and Mills 1982

Figure 2.4 Experimental chemical operating conditions on the alum coagulation diagram

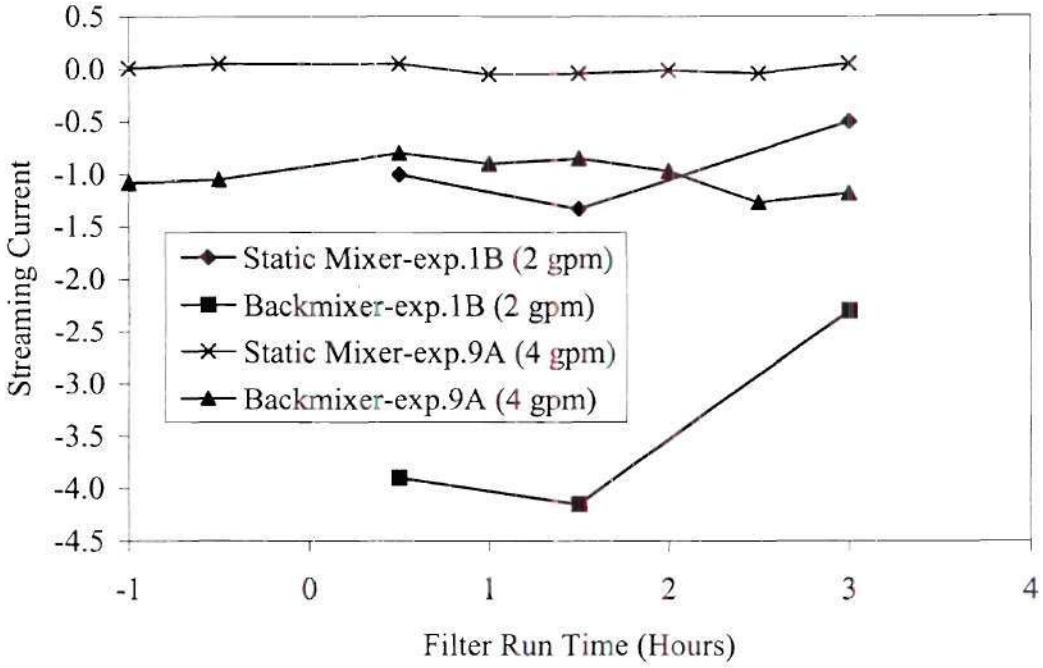

Figure 2.5 Series 1—Streaming current measurements

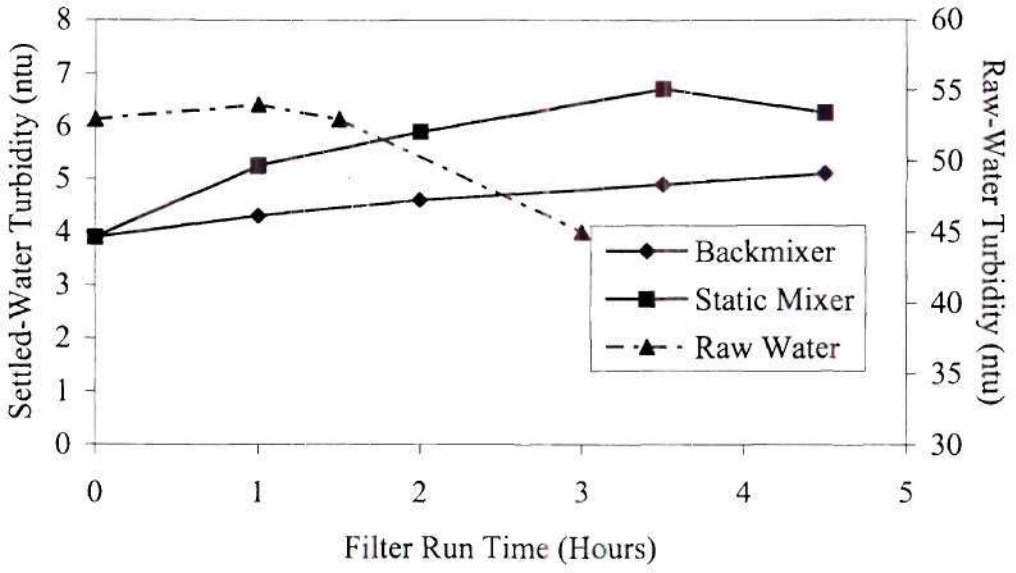

Figure 2.6 Series 1—Experiment 1B (2 gpm) settled-water turbidity

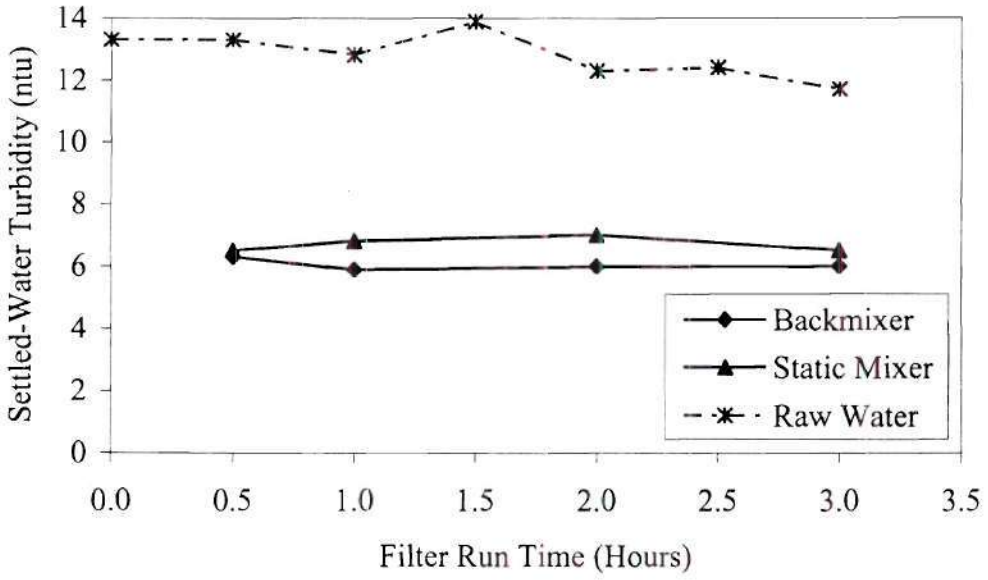

Figure 2.7 Series 1—Experiment 9A (4 gpm) settled-water turbidity

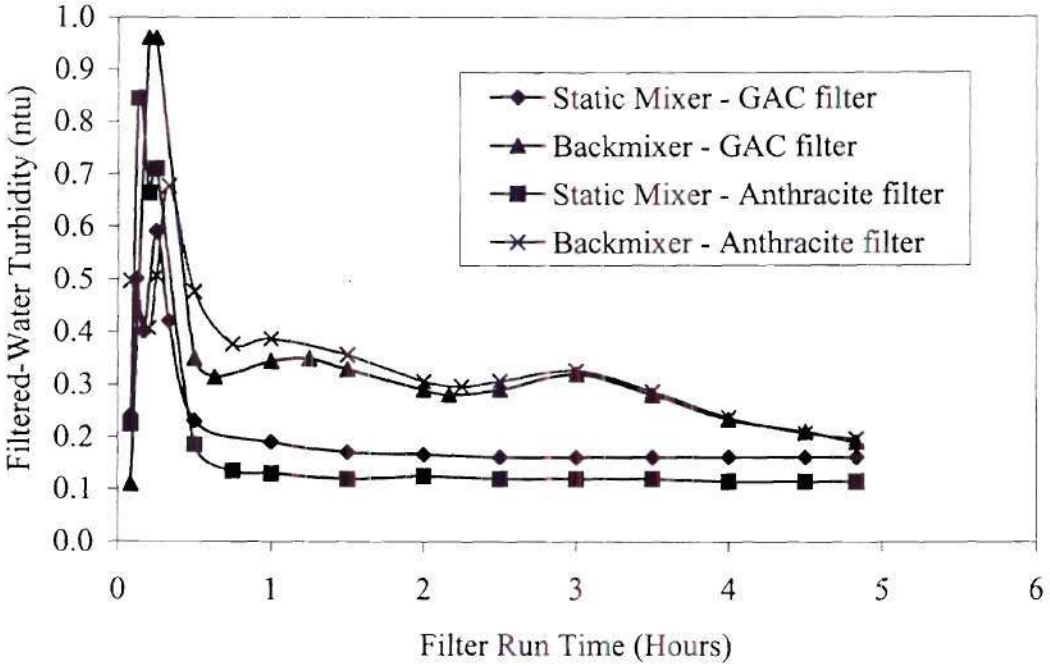

Figure 2.8 Series 1—Experiment 1B (2 gpm) filtered-water turbidity

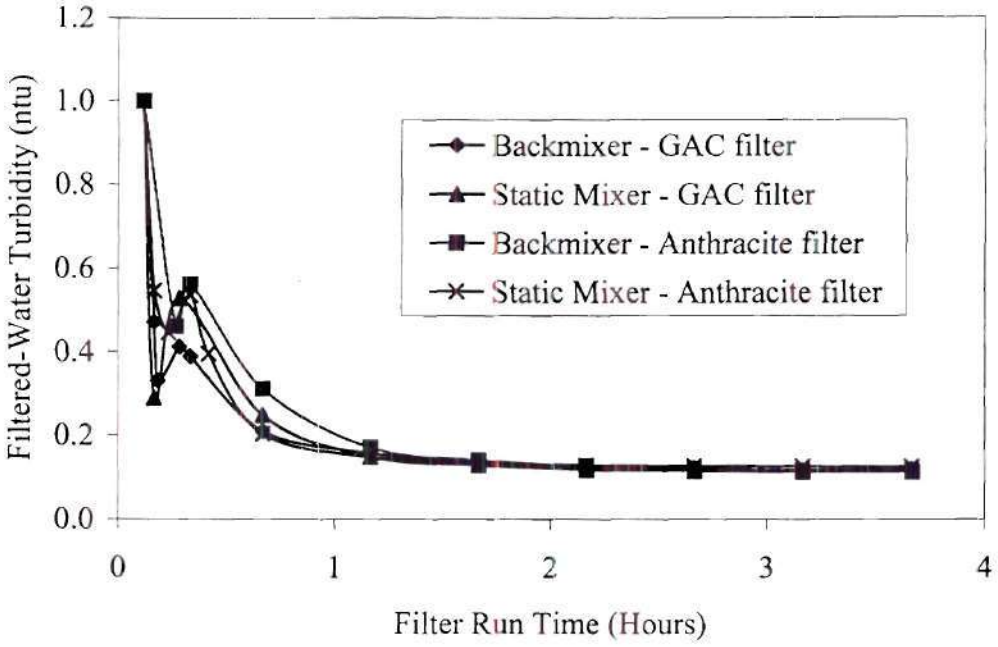

Figure 2.9 Series 1—Experiment 9A (4 gpm) filtered-water turbidity

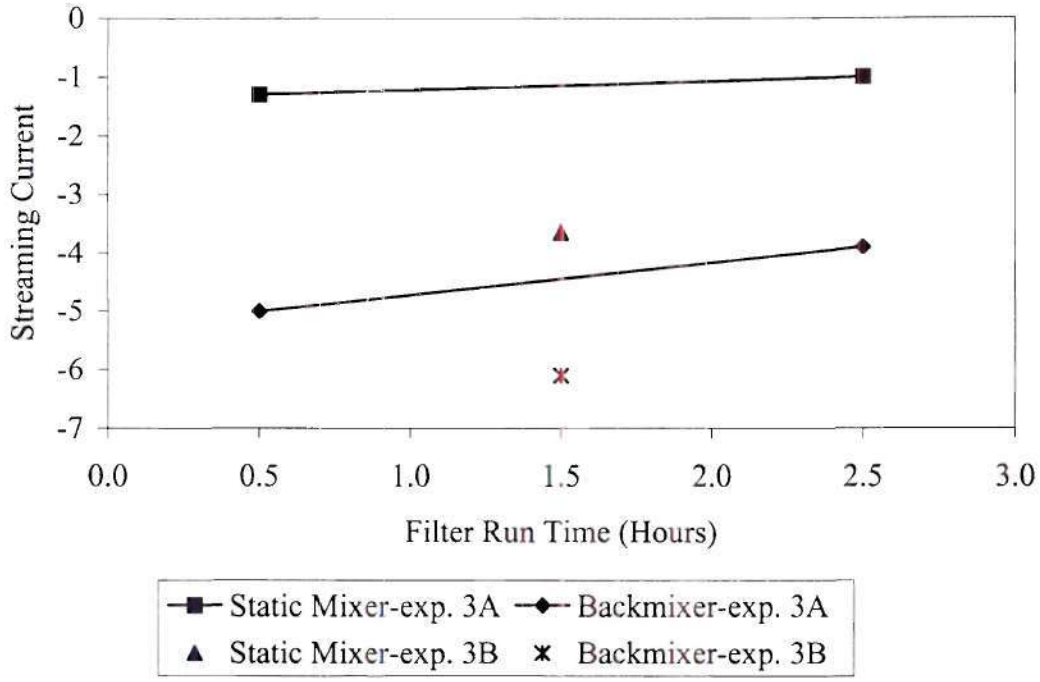

Figure 2.10 Series 2—Experiments 3A and 3B (2 gpm) streaming current

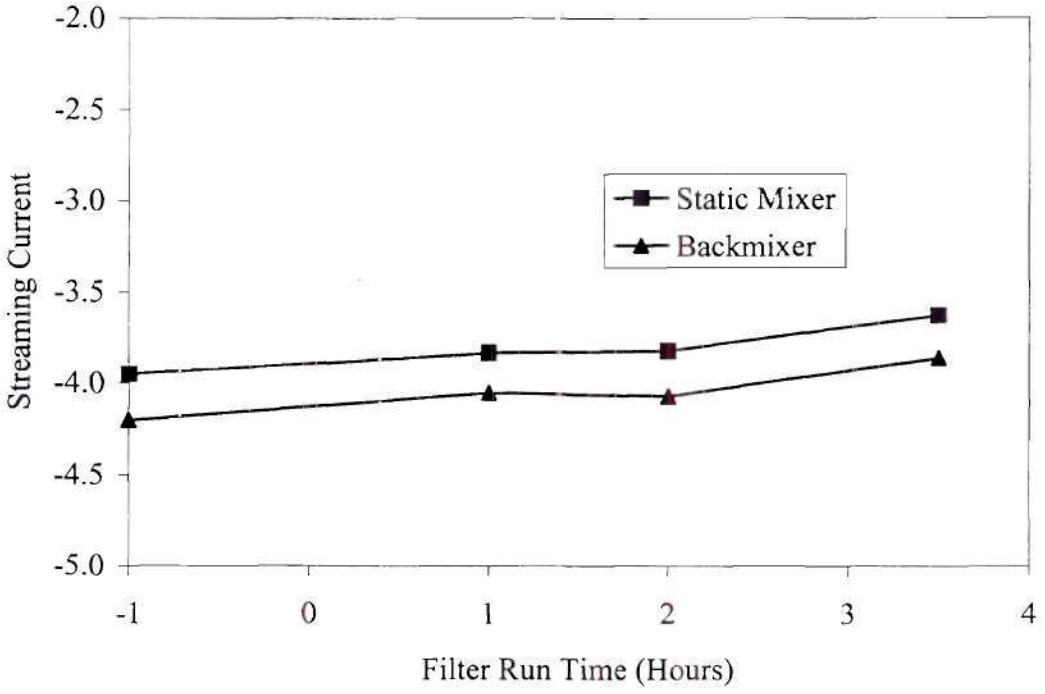

Figure 2.11 Series 2—Experiment 8C (4 gpm) streaming current

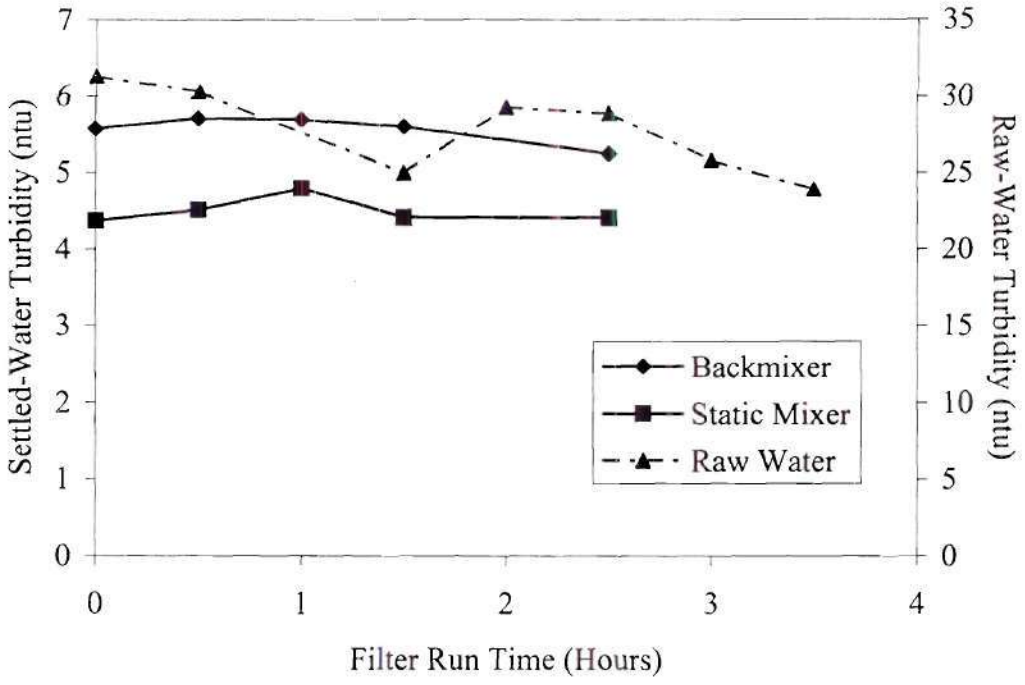

Figure 2.12 Series 2—Experiment 3A (2 gpm) settled-water turbidity

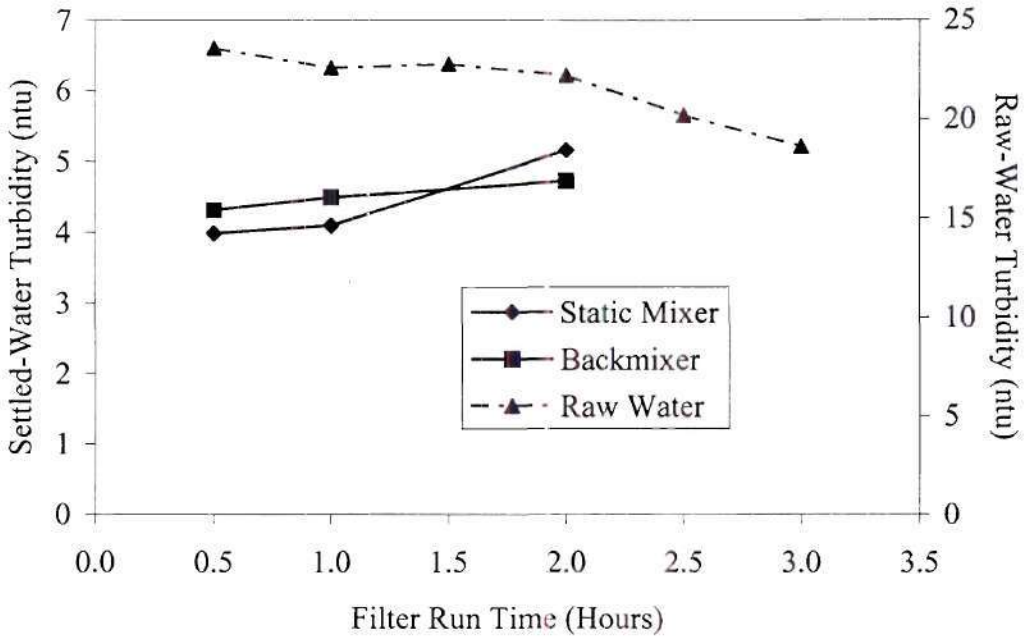

Figure 2.13 Series 2—Experiment 3B (2 gpm) settled-water turbidity

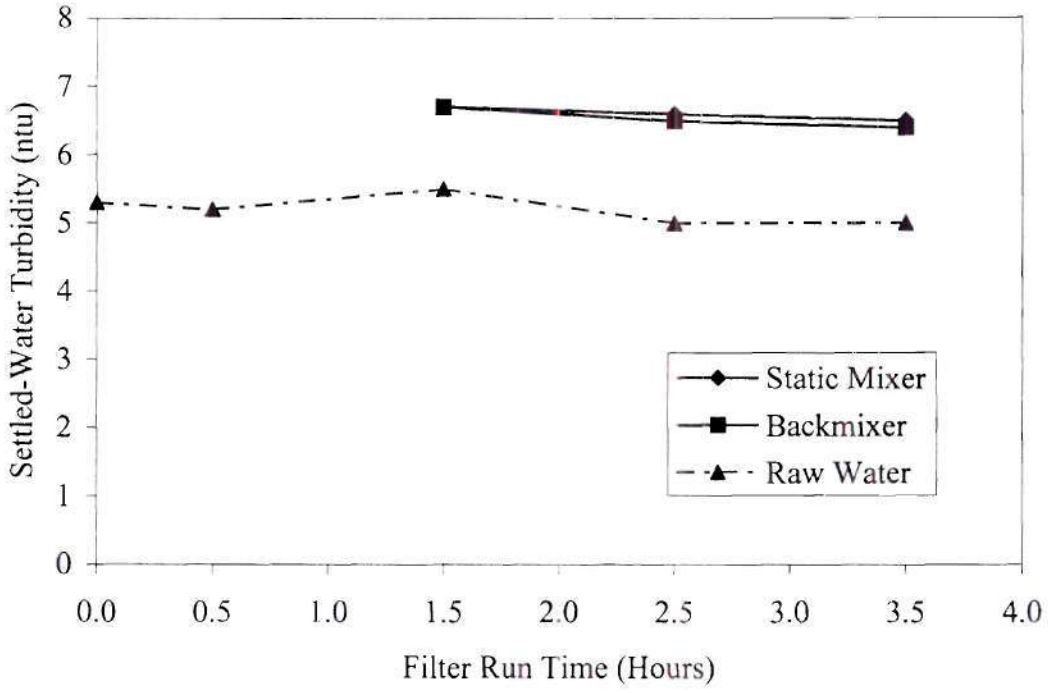

Figure 2.14 Series 2—Experiment 8C (4 gpm) settled-water turbidity

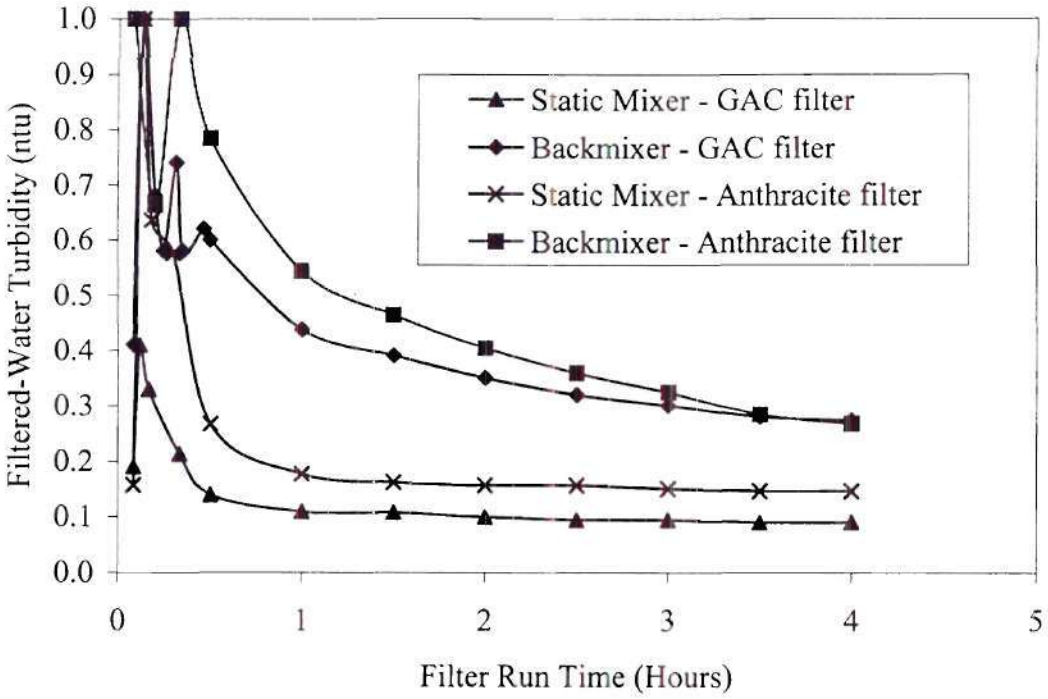

Figure 2.15 Series 2—Experiment 3A (2 gpm) filtered-water turbidity

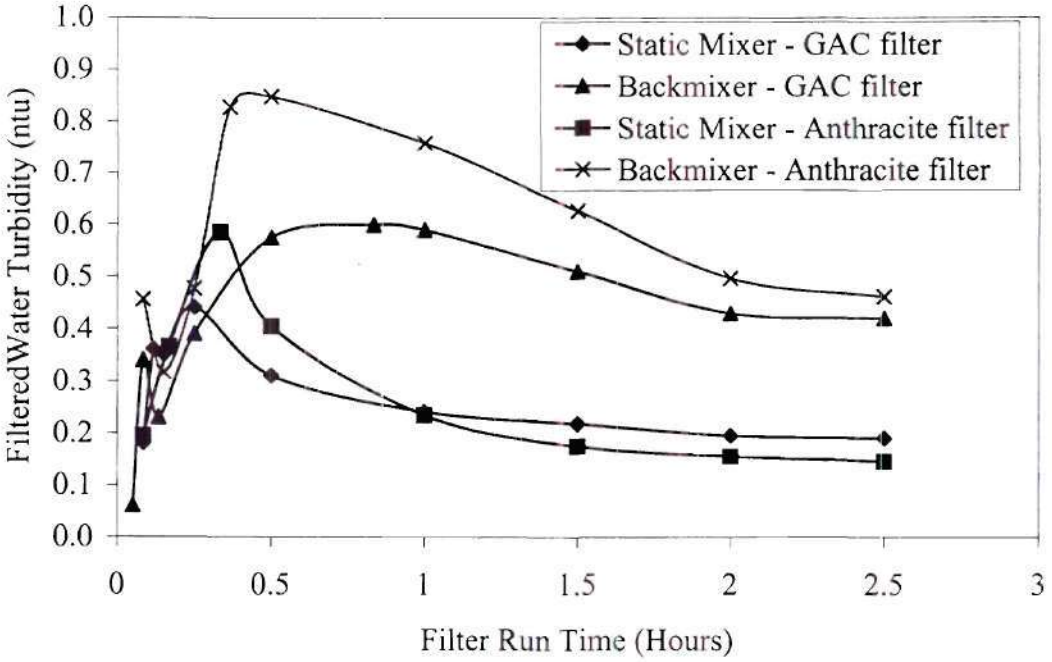

Figure 2.16 Series 2—Experiment 3B (2 gpm) filtered-water turbidity

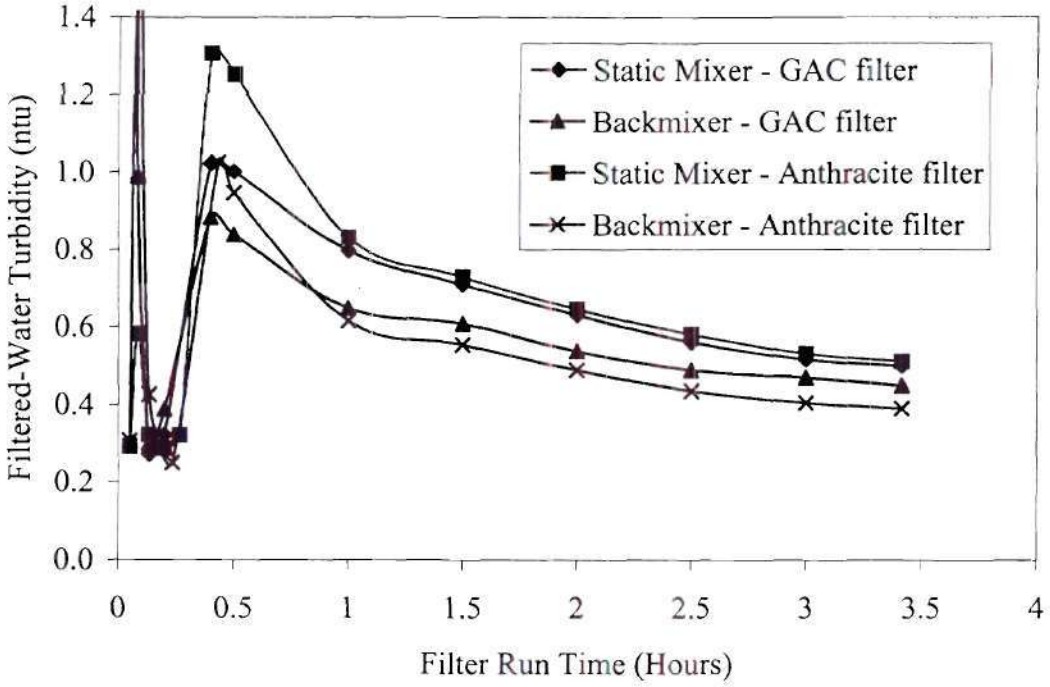

Figure 2.17 Series 2—Experiment 8C (4 gpm) filtered-water turbidity

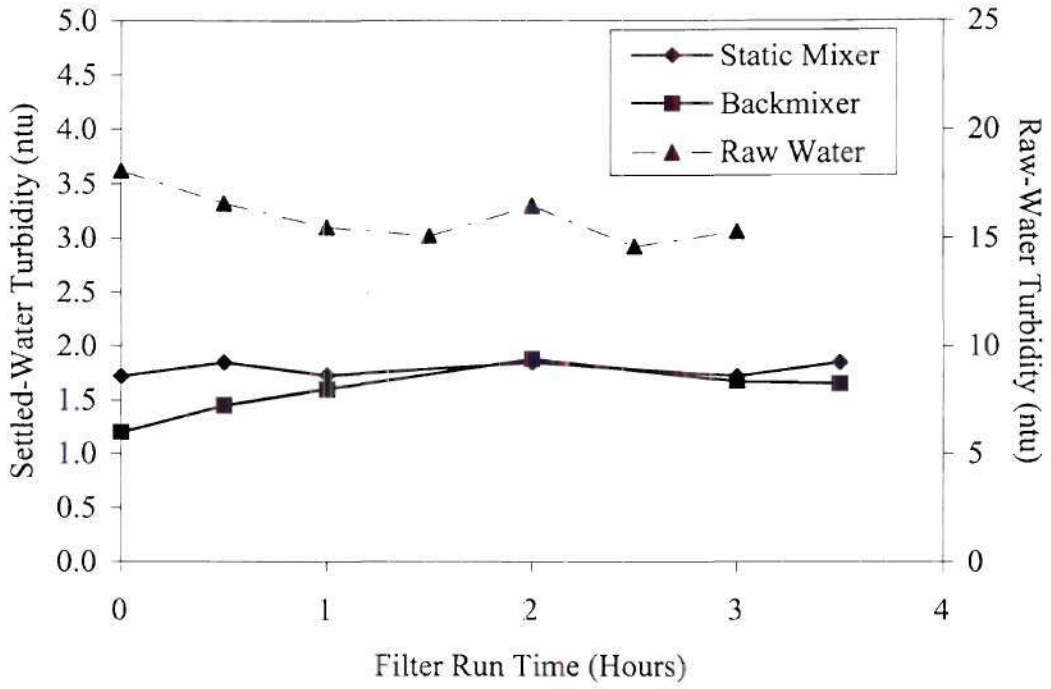

Figure 2.18 Series 3—Experiment 2A (2 gpm) settled-water turbidity

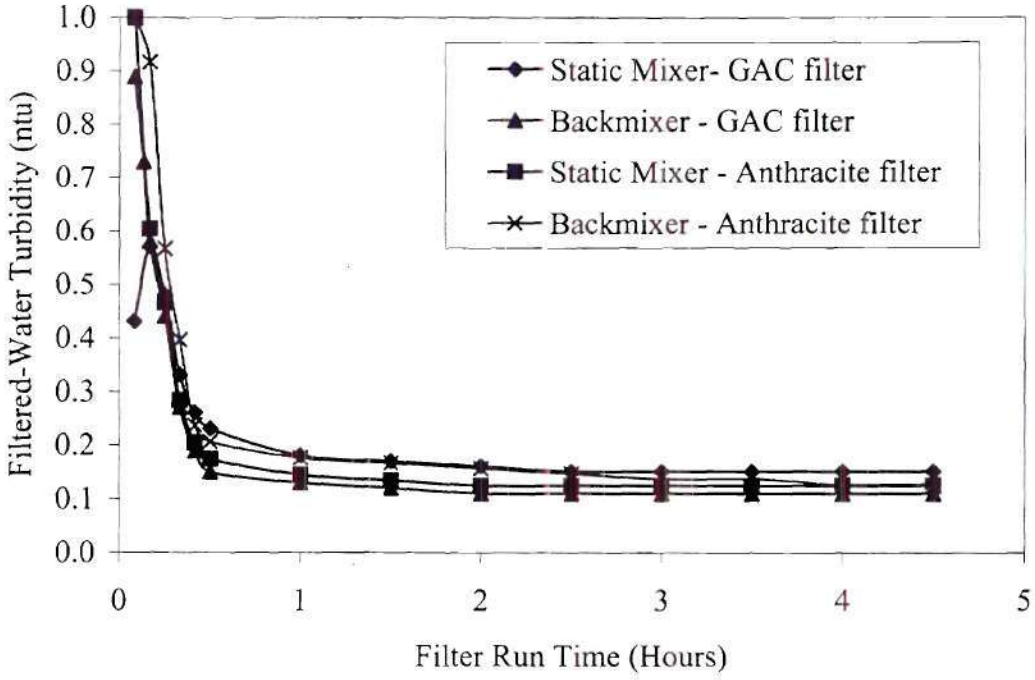

Figure 2.19 Series 3—Experiment 2A (2 gpm) filtered-water turbidity

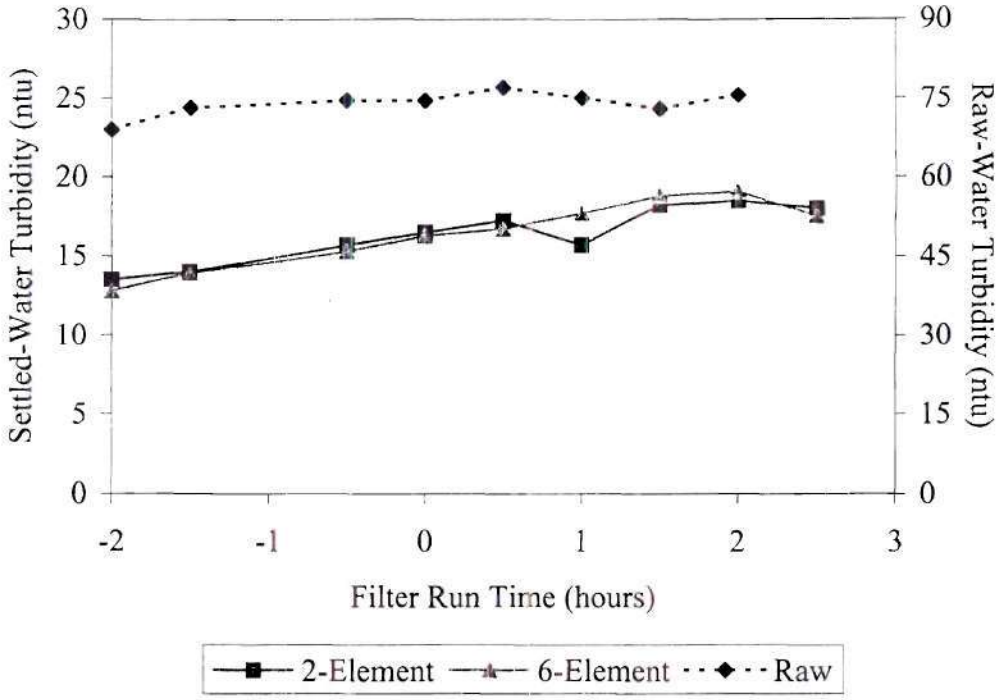

Figure 2.20 Series 5—Experiment 2S (4 gpm) settled-water turbidity

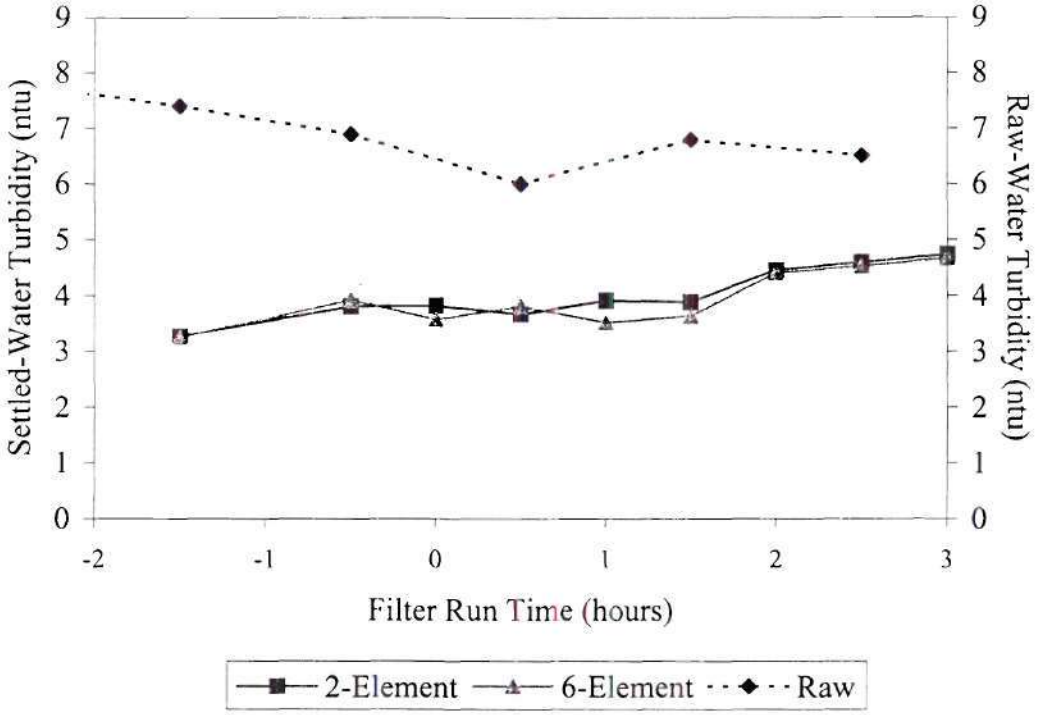

Figure 2.21 Series 5—Experiment 7S (4 gpm) settled-water turbidity

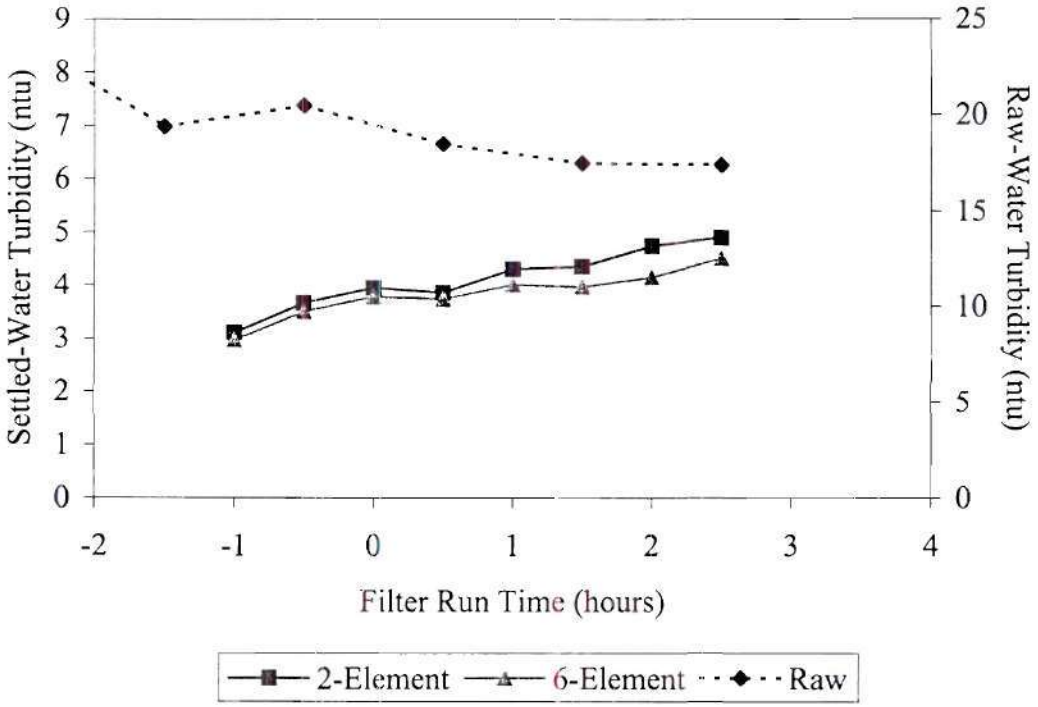

Figure 2.22 Series 5—Experiment 10S (2 gpm) settled-water turbidity

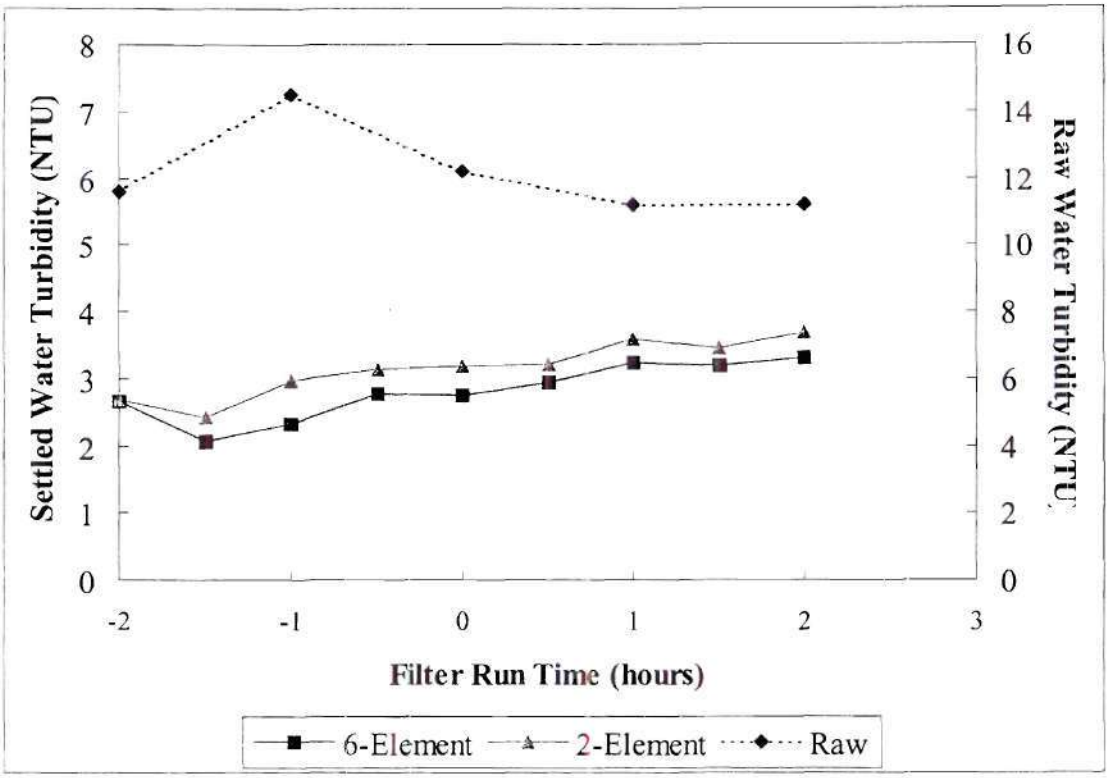

Figure 2.23 Series 5 - Experiment 13S (2 gpm) settled water turbidity

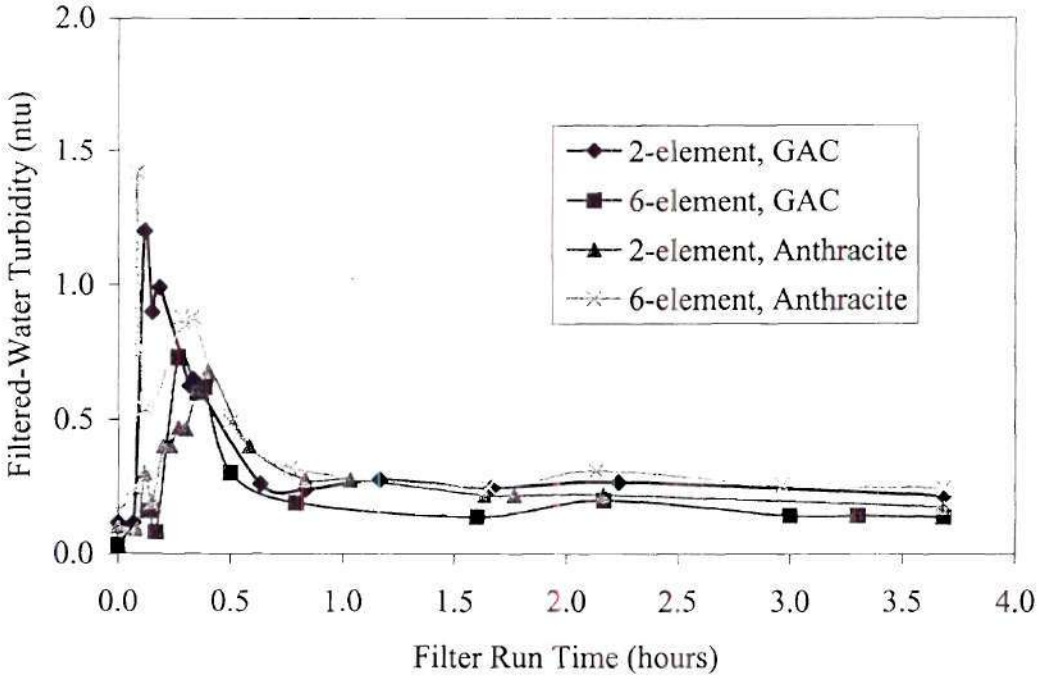

Figure 2.24 Series 5—Experiment 2S (4 gpm) filtered-water turbidity

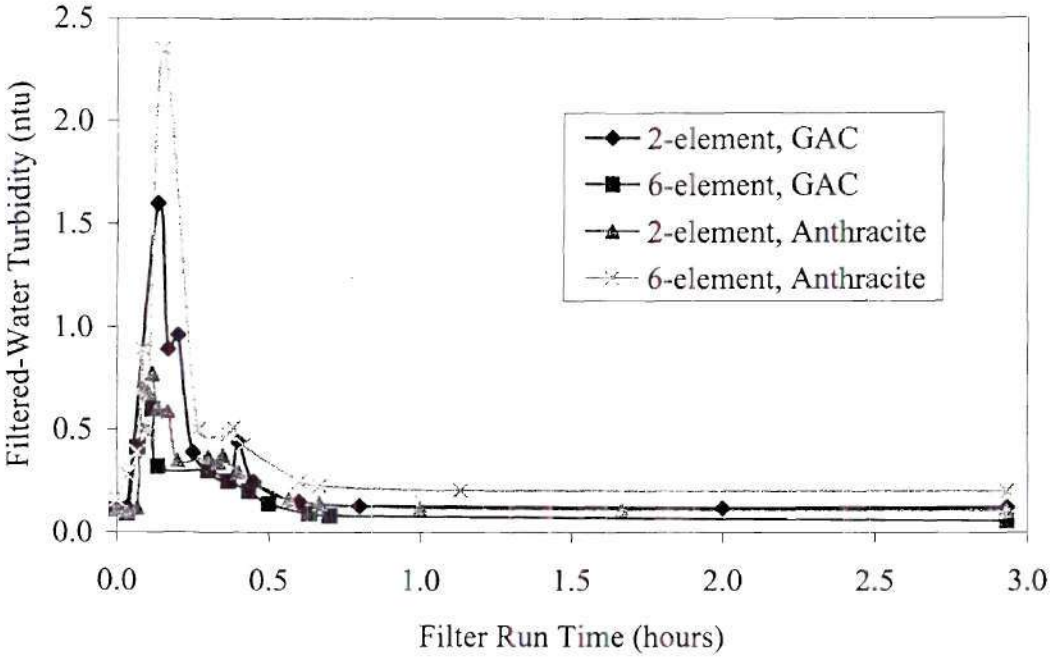

Figure 2.25 Series 5—Experiment 7S (4 gpm) filtered-water turbidity

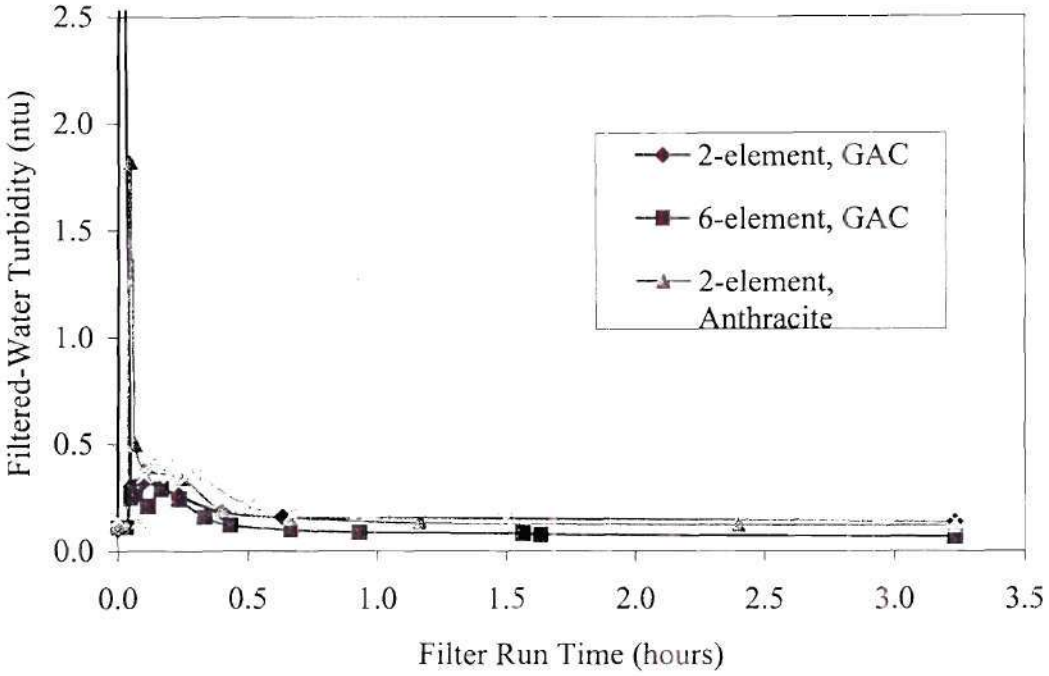

Figure 2.26 Series 5—Experiment 10S (2 gpm) filtered-water turbidity

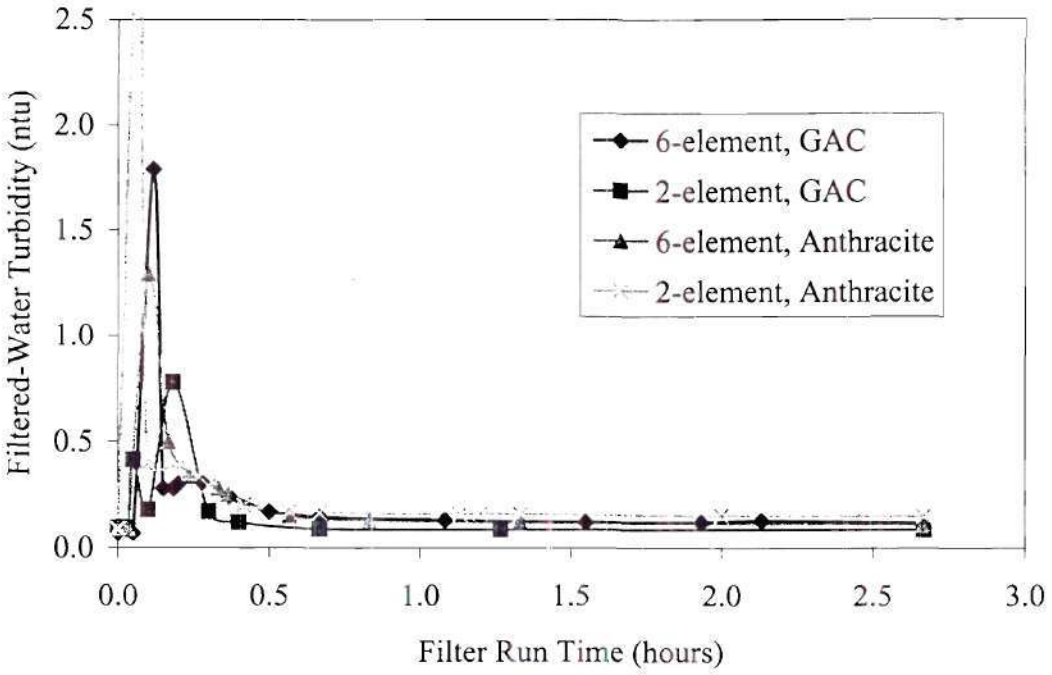

Figure 2.27 Series 5—Experiment 13S (2 gpm) filtered-water turbidity

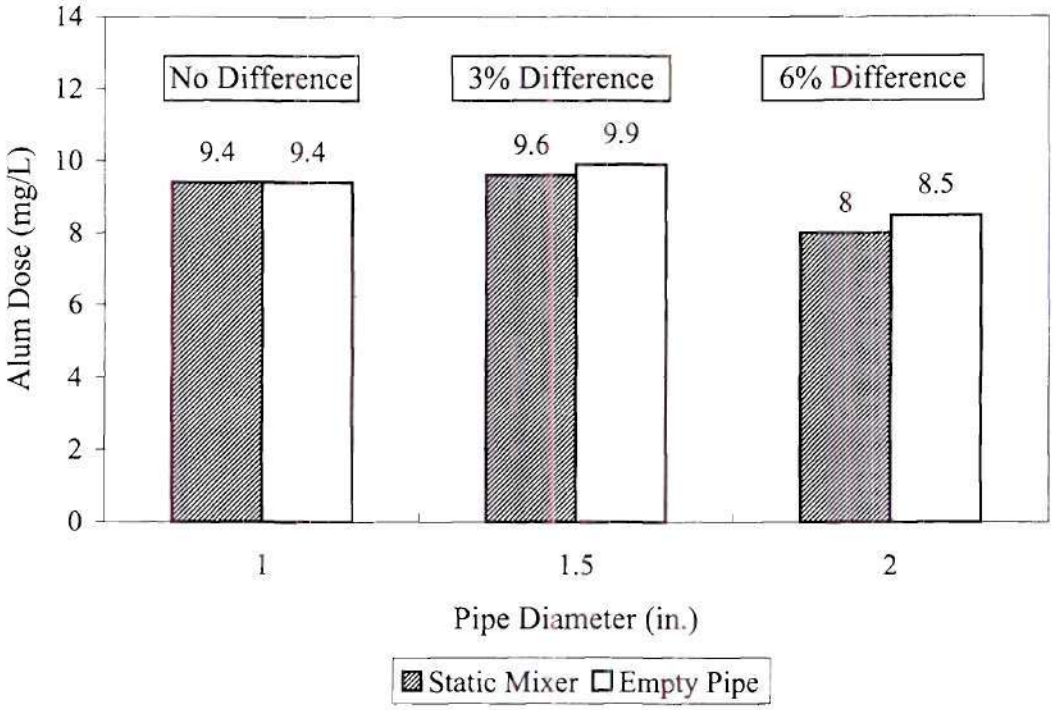

Figure 2.28 Series 6—Alum doses for KMS static mixer versus empty pipe

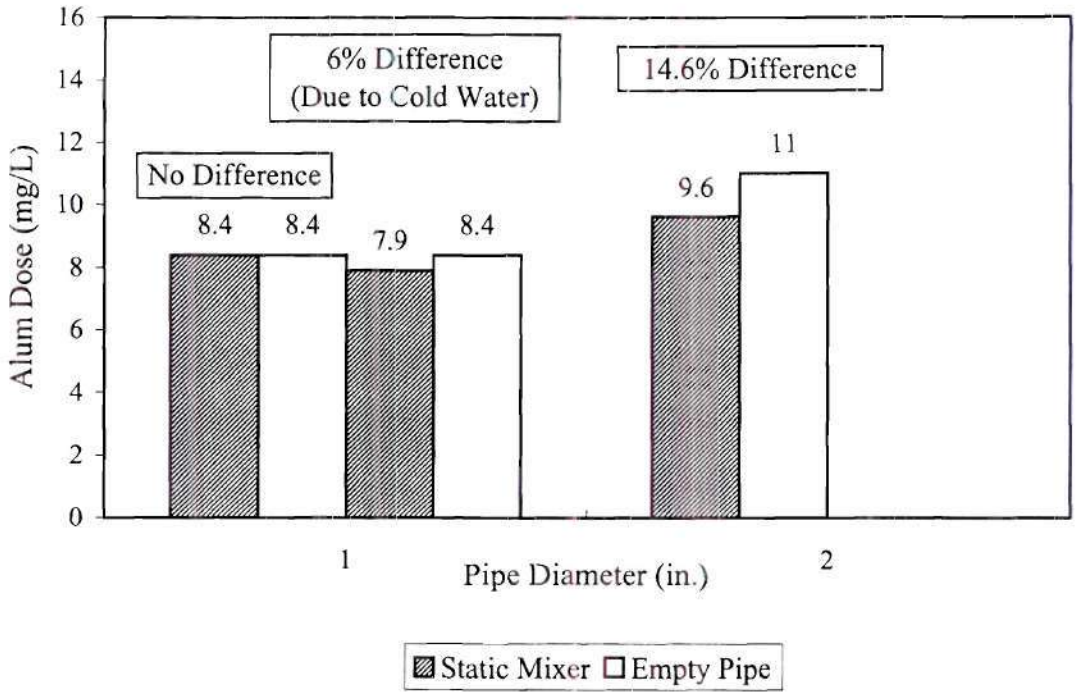

Figure 2.29 Series 6—Alum doses for Stata-tube versus empty pipe

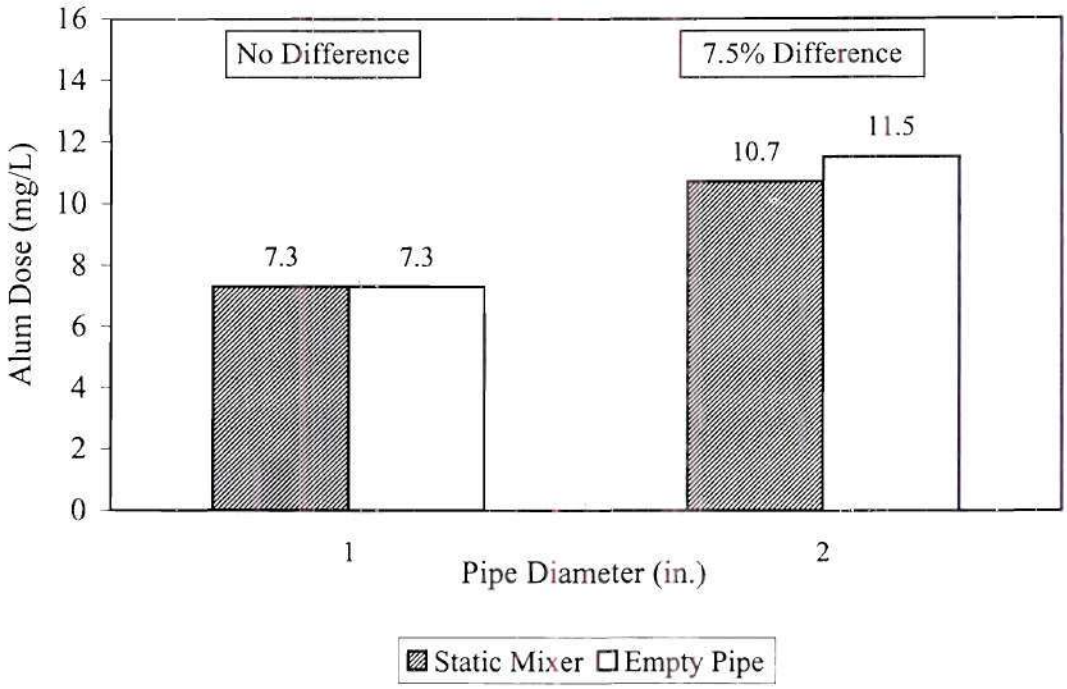

Figure 2.30 Series 6—Alum doses for Spiral static mixer versus empty pipe

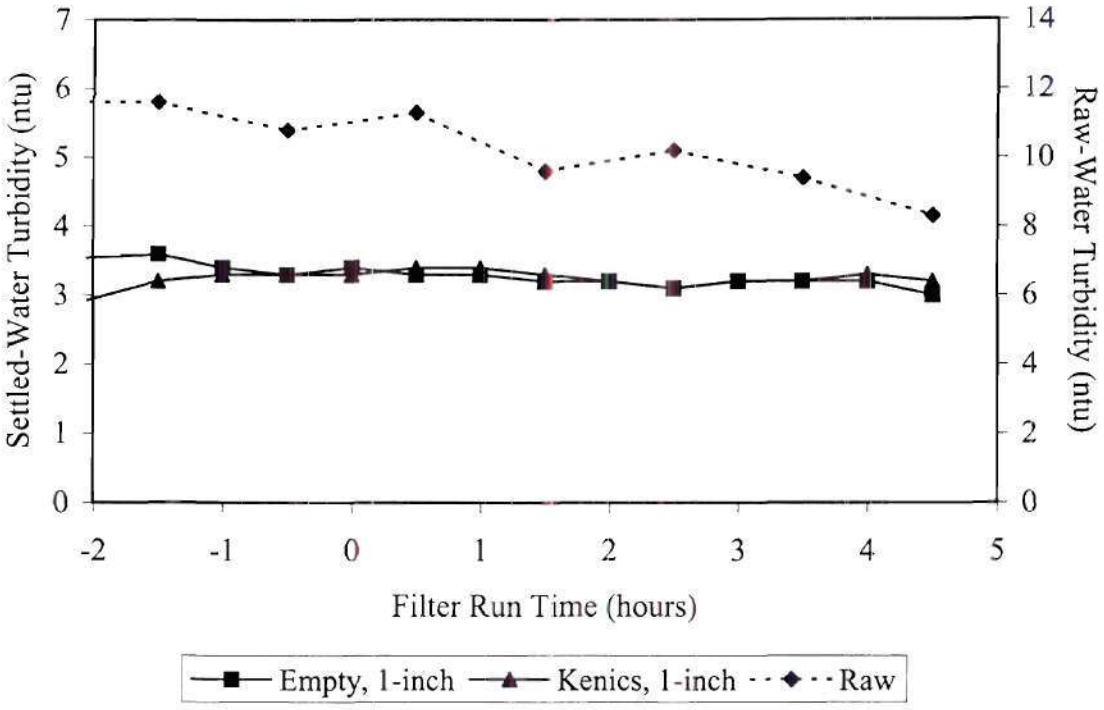

Figure 2.31 Series 6—Experiment 20S settled-water turbidity

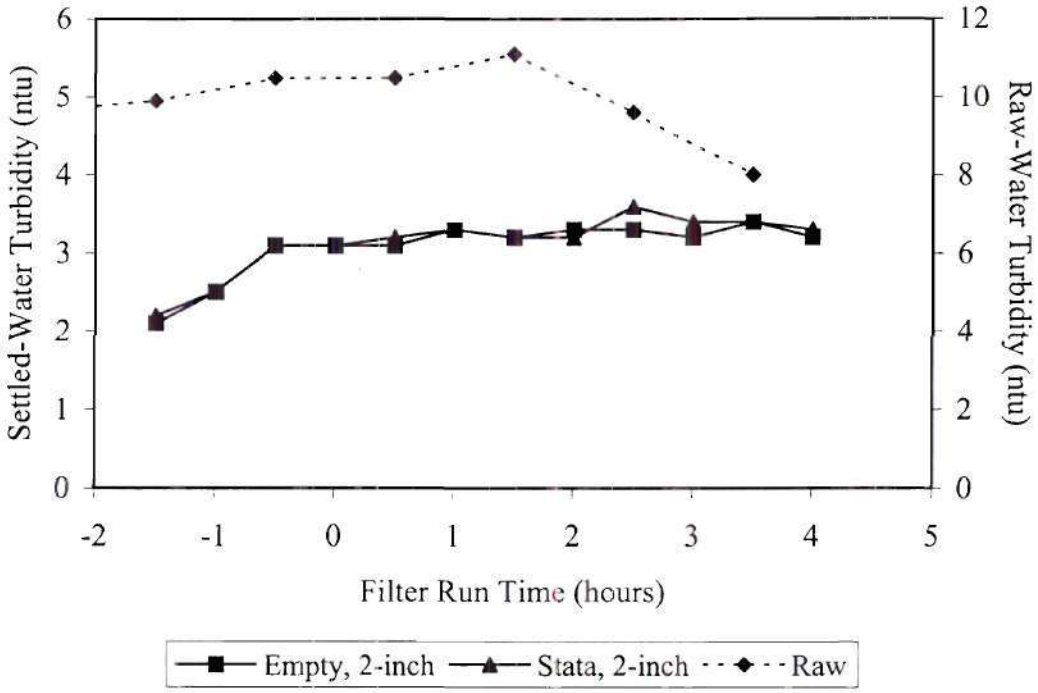

Figure 2.32 Series 6—Experiment 25S settled-water turbidity

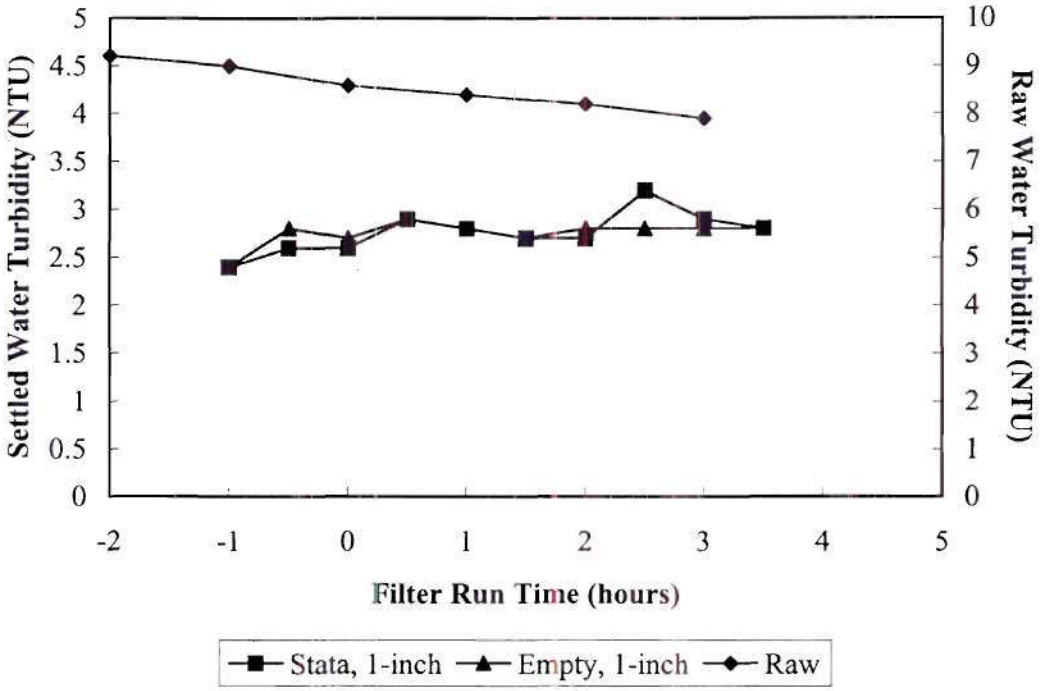

Figure 2.33 Series 6—Experiment 26A settled-water turbidity

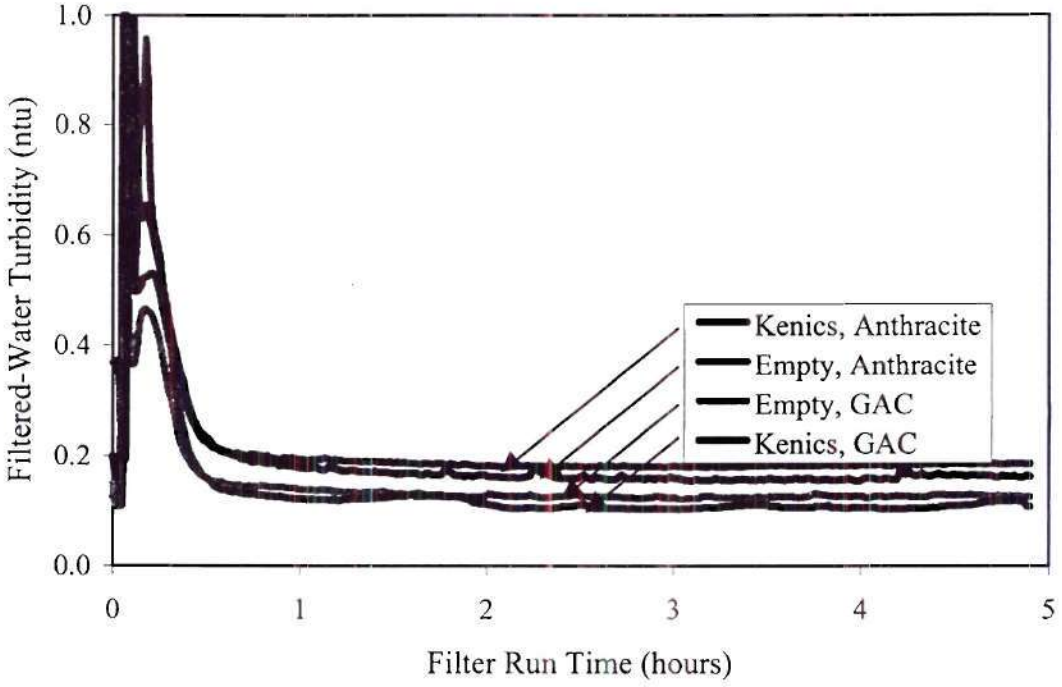

Figure 2.34 Series 6 - Experiment 20S filtered water turbidity

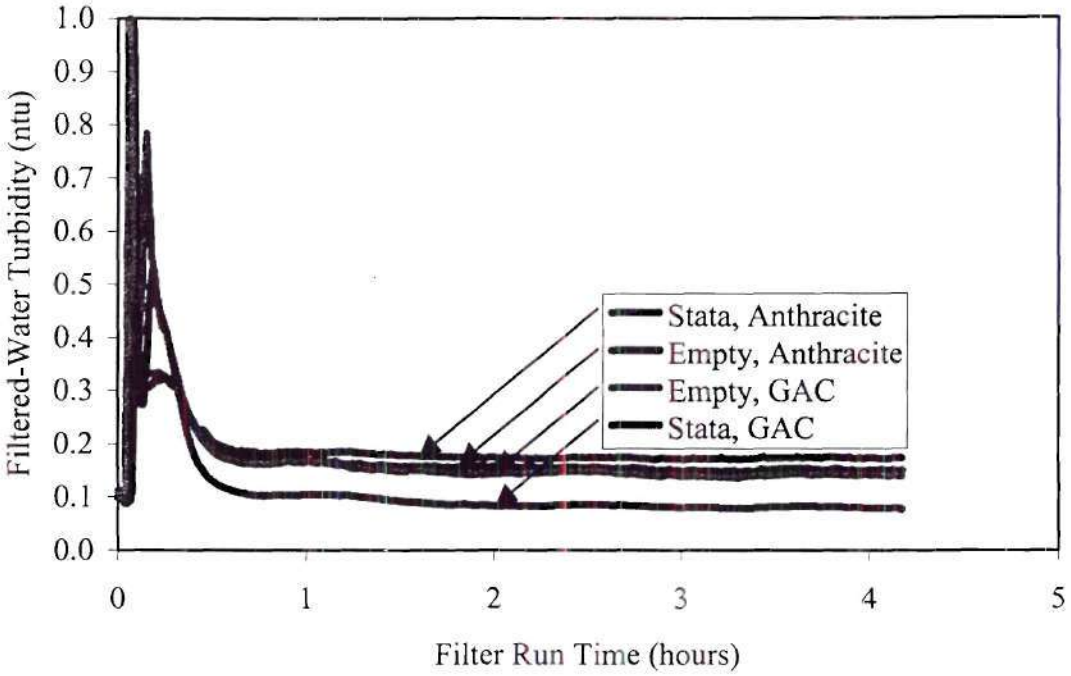

Figure 2.35 Series 6—Experiment 25S filtered-water turbidity

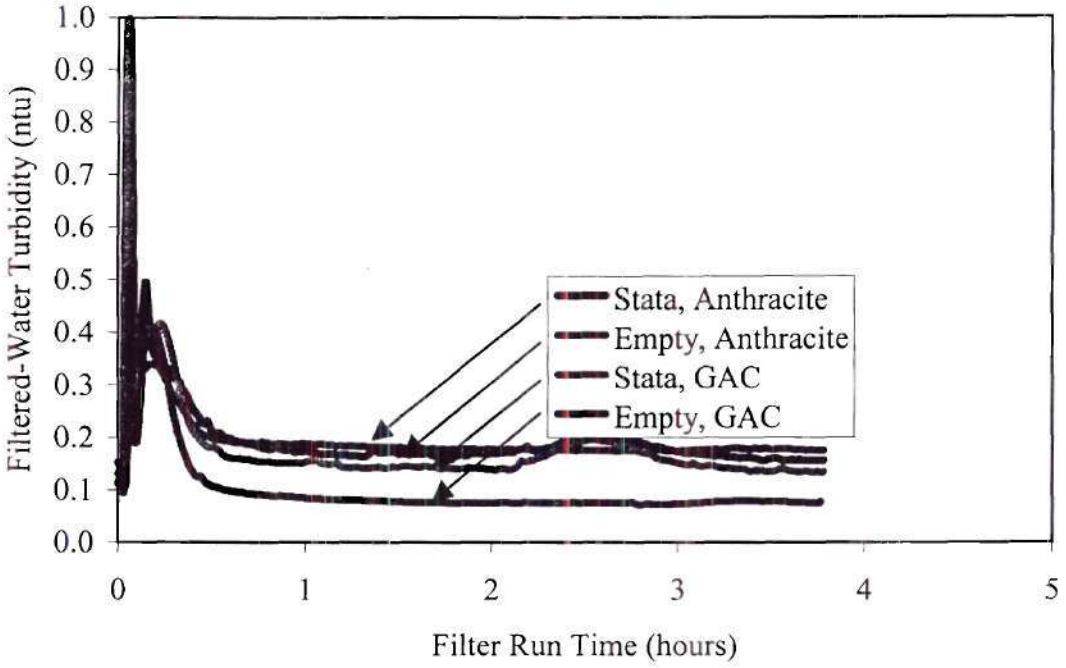

Figure 2.36 Series 6—Experiment 30S filtered-water turbidity

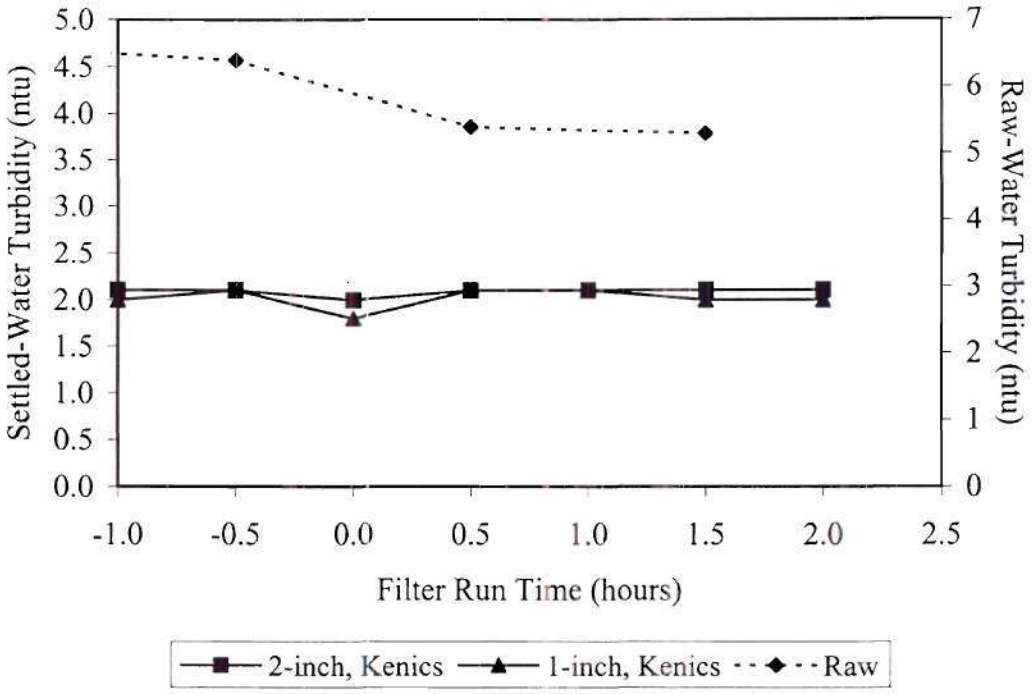

Figure 2.37 Series 6—Experiment 23S filtered-water turbidity

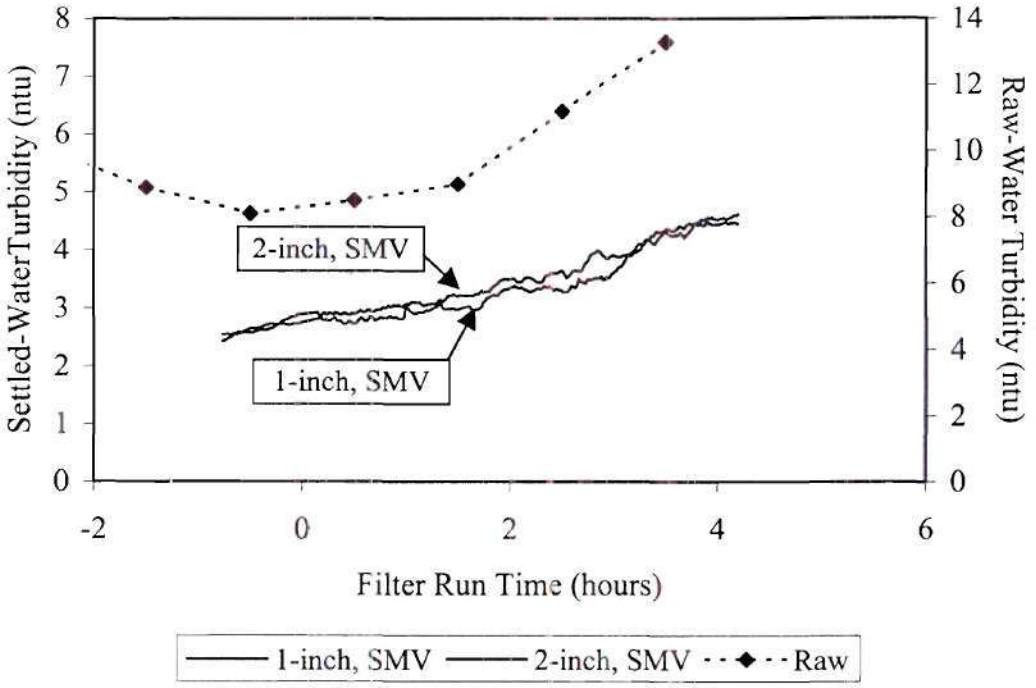

Figure 2.38 Series 7—Experiment 33S settled-water turbidity

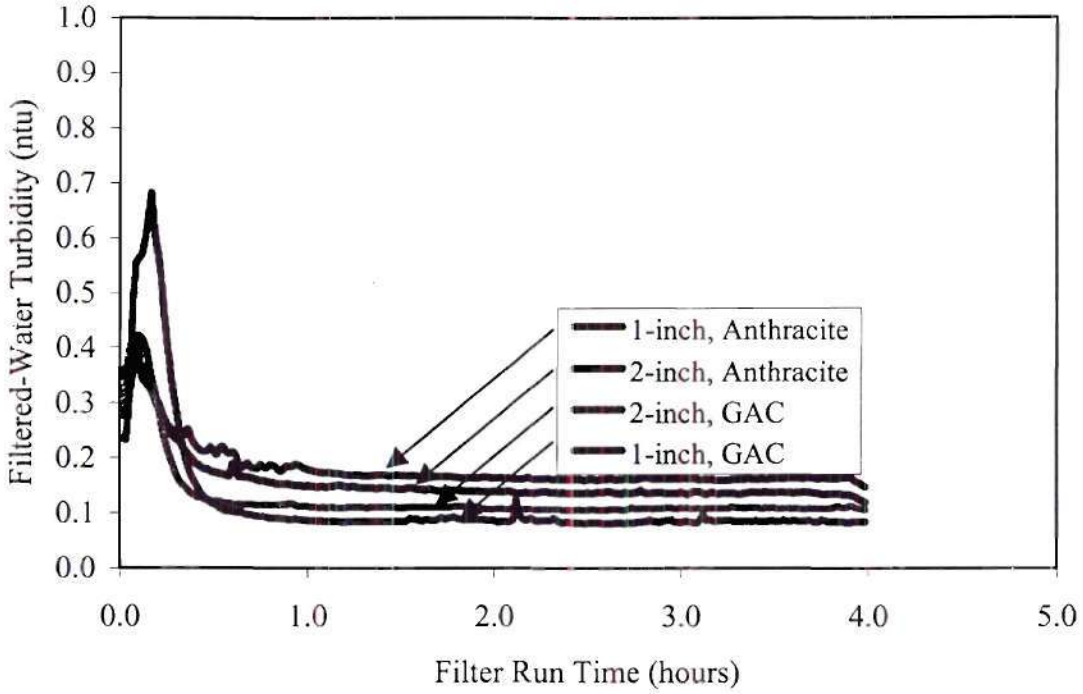

Figure 2.39 Series 7—Experiment 32S filtered-water turbidity

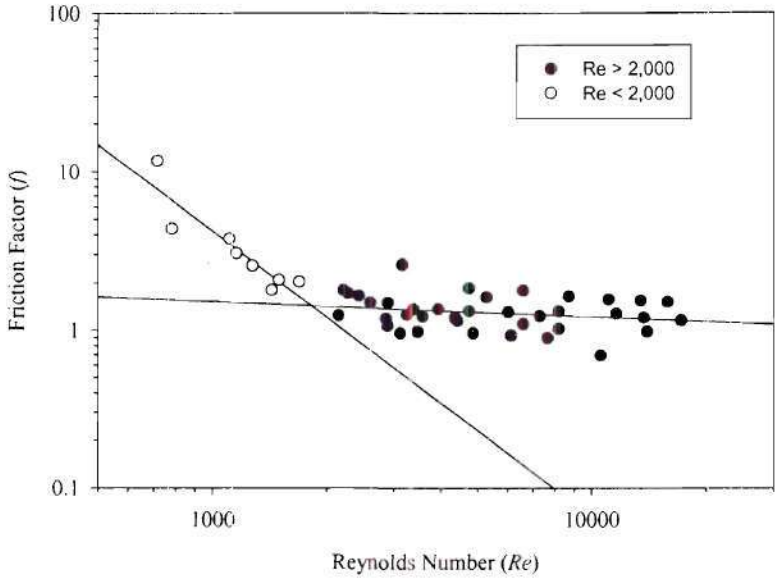

Figure 2.40 Reynolds number versus friction factor for KMS static mixers

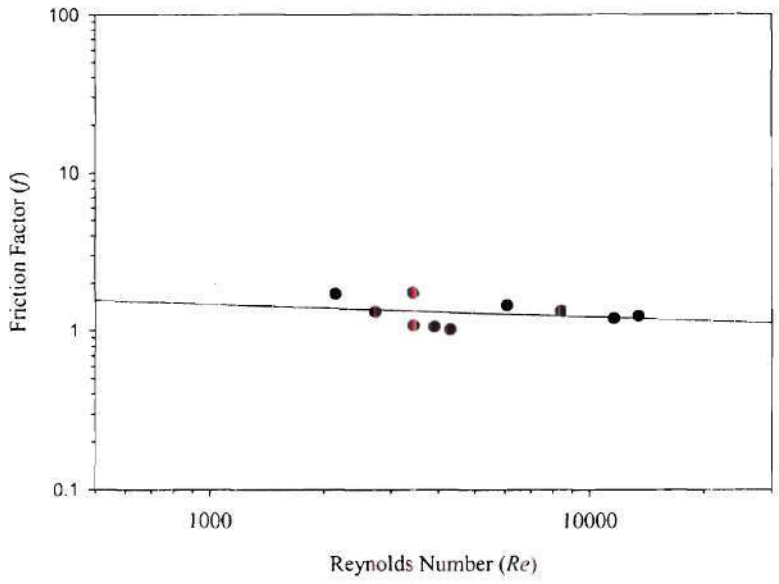

Figure 2.41 Reynolds number versus friction factor for spiral static mixer

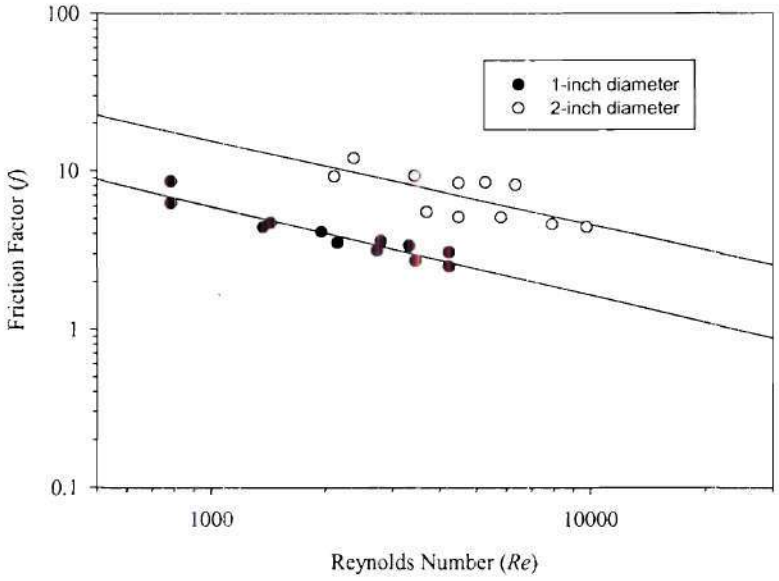

Figure 2.42 Reynolds number versus friction factor for Stata-tube static mixer

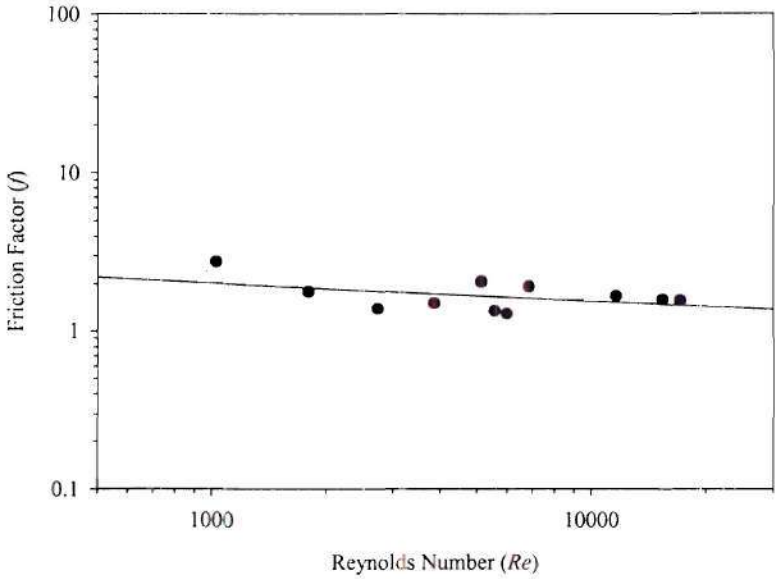

Figure 2.43 Reynolds number versus friction factor for SMV static mixer

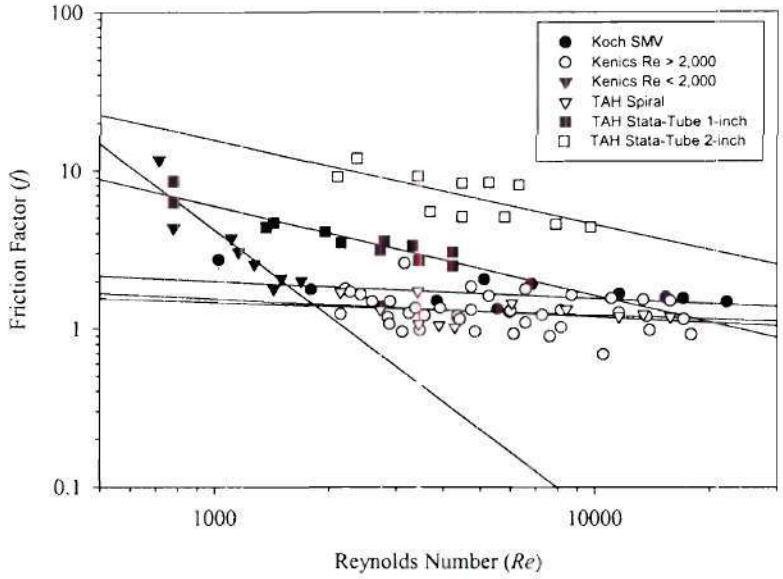

Figure 2.44 Reynolds number versus friction factor for all static mixers tested

Page missing from thesis

CHAPTER 3

BENCH-SCALE EXPERIMENTS ON THE INACTIVATION OF *CRYPTOSPORIDIUM PARVUM* OOCYSTS WHEN USING STATIC MIXERS

INTRODUCTION AND BACKGROUND

The purpose of the experiments reported in this chapter is twofold: (1) to explore the use of a new technique for measuring the inactivation (viability) of *Cryptosporidium parvum* oocysts and apply this technique in bench-scale mixing studies; and (2) to determine if the initial mixing of chlorine-based disinfectants in static mixers improves the ability of these disinfectants to inactivate *Cryptosporidium* oocysts. The remaining sections of this introduction discuss the various methods currently available to detect *Cryptosporidium* and provide a reference in which to place the current work.

Cryptosporidium Detection Methods

Perhaps one of the greatest difficulties encountered in *Cryptosporidium* research is the detection of the organisms and the subsequent determination of the ability of the organisms to infect. Microscopic counts with a phase contrast microscope and a hemacytometer are useful to enumerate oocysts in a sample. However, this method does not indicate if the oocysts are able to infect a host and relies on the ability of the individual lab technician to correctly identify oocysts in a given sample. Currently, three methods are commonly used to detect the viability of oocysts. In the United States, the most common method of detection in an environmental sample is an antibody based immunofluorescence assay. Identification is based on an oocyst that luminesces under an ultraviolet (UV) light source. The object is identified positively by visible light microscopy and at least one sporozoite in the oocyst structure. Positively identified oocysts may be viable or nonviable. Viable oocysts may be infective or non-infective. The strain may be able to infect various species. Currently there are two known genotypes of *Cryptosporidium*. Genotype 1 is anthroporotic, it is promulgated through a human to human transmission cycle. Genotype 2 is zoonotic, it is passed from species to species (Chappell et al. 1999).

Determining viability

The first method of determining viability is in-vitro excystation. The oocysts are inoculated into a solution that simulates epigastric conditions. The premise of this method is to mimic the conditions within the host's body that promote the release of infective sporozoites from oocysts. The solution is typically reductive/acidic with elevated temperatures and contains bile salts. There are advantages and disadvantages to in-vitro excystation. Advantages are the ease of use, relatively low cost, and it resembles the pathogenesis process. Disadvantages are that samples need to be concentrated and purified, long incubation times are necessary, the variability within different strains of oocysts are not quantified, and different environmental stresses may affect the viability. In-vitro excystation is not useful in environmental samples because of the large number of oocysts needed (Jakubowski et al. 1996).

The second method of viability determination commonly used is vital dye staining. More than twenty commercial dyes have been developed to determine viability. The ability of vital dyes to determine viability is dependent upon may factors including environmental stresses, the concentration method employed, and differences in strains (Jakubowski et al. 1996).

The third method of viability determination currently in use is a multitude of infectivity assays. Animal infectivity studies are quite popular, although there has been no definite correlation between animal and human infectivity. Animal infectivity is commonly used to determine the effectiveness of disinfectants in water treatment. One of the greatest drawbacks to animal infectivity is the cost involved. The facilities needed for these tests are expensive to maintain nad operate, and a typical test involves many duplicates (animals to infect) in order to achieve the appropriate statistical significance. The ethical debate regarding the use of animals in scientific studies when other options are available must also be considered. Another popular infectivity assay is the cell culture infectivity method. In the cell culture infectivity method, a monolayer of cells is studied for infectivity. Cells typically used are Buffalo Green Monkey Kidney cells (BGMK), Madine Darby Canine Kidney cells (MDCK), and Human Enterocyte cells (HCT-8). The advantage to cell culture is a lower cost (versus animal infectivity), a less complex system (cell monolayer versus entire animal), and ability to reproduce results. Some disadvantages to all infectivity assays are the need to have a relatively clean sample to inoculate, and the biological variance in the infected subjects (whether they are animals or cell lines).

MATERIAL AND METHODS

The experiments performed in this study were completed at the bench scale at the Centers for Disease Control and Prevention, Atlanta, Ga. The effect of the static mixer in the disinfection process was studied in a test apparatus that included a raw water reservoir, a contact area, and an area for disinfectant contact time. The infectivity studies were designed to test the efficiency of the disinfectant. To enhance reproducibility in infectivity analysis, cell culture studies were used.

Experimental Apparatus

The test apparatus used in this study was modeled after an apparatus used in the coagulation study of Schulgen (1995). The apparatus is shown in Figure 3.1 and a photograph of the apparatus is shown in Figure 3.2. The raw water reservoir was a 5.28-gal(20-L) autoclavable carboy (Nalgene, Rochester, N.Y.). The carboy rested on a magnetic stir plate and contained a magnetic stir bar to provide a uniform distribution of the oocysts in the carboy. The carboy was connected to the stationary test apparatus via a three-way valve. The valve allowed raw water, hot water, or chlorinated water to be cycled through the apparatus. The addition of the valve allowed sterile conditions to be maintained within the apparatus during different stages of the experiments.

The valve was connected via 0.5-inch (1.27-cm) tubing to a metering pump (QD-3, Fluid Metering, Oyster Bay, N.Y.). The pump had a maximum flow rate of 0.61 gpm (2.3 L/min). The next point in the apparatus was the point of disinfectant addition. The disinfectant was stored in a 0.26-gal (1-L) flask and entered the flow stream by a different pump, (RP-D, Fluid Metering, Oyster Bay, N.Y.). The disinfectant entered the flow stream immediately upstream of the static mixer via a 0.125-inch (0.5-mm) diameter tube. The flow of the disinfectant was adjusted so that it was continuous (as opposed to drip). The combination of the raw water and disinfectant then entered the static mixer. The water was then collected in a sterile sample bottle to allow for the disinfectant contact time.

Two different static mixer configurations were initially used in this study. The first mixer used was a helical static mixer (Cole-Parmer, Vernon Hills, Ill.). The length of one element is $1.5d$ where d is the diameter of the element. The static mixer is designed with twelve elements.

The design of the mixer allows for the removal of elements. For these experiments, two- and six-element mixers were used. The second type of mixer was a more complex design (Omega Engineering, Stamford, Conn.). It will be referred to as the Omega mixer in this chapter. The Omega mixer was a fixed length. The head loss across the mixers was measured by a pressure transducer (Model PX 154, Omega Engineering, Stamford, Conn.). Tees were added immediately upstream and downstream of the mixer to measure the head loss. Hot water was used to inactivate the *Cryptosporidium* oocysts that may have remained in the apparatus after the completion of a round of experiments. The water was stored in a 2.5-gal (10-L) carboy, which was placed to allow static head to drive the water through the water heater.

Preparing for the Disinfection Experiments

Four days prior to the experiment

Four days prior to the day of the experiment the Madine Darby Canine Kidney (MDCK) cells were split by a CDC lab technician. This was the preparation of the cells to be inoculated with the *Cryptosporidium* for infectivity testing. The cells were maintained in 2-well Lab-Tek Chambered Slides (Nunc, Naperville, Ill.). Ultraculture media (Bio Whittaker, Walkersville, Md.) was used as a nutrient source for the cells. The four days of growth allowed the cell monolayer to properly attach to the cell chamber and reach confluency. The media was changed every other day during the growth phase.

One day prior to the experiment

Prior to conducting disinfection experiments, the test apparatus was disinfected overnight with chorine bleach to destroy any microbes that could influence the test or potentially harm the MDCK cells. It was necessary to kill any bacteria or fungi that would exert a chlorine demand. The 5.28-gal (20-L) carboy was filled with 2.91 gal (11 L) of deionized water. The water was buffered to pH 6 with 50 g of KH_2PO_4 and 4.73 g of Na_2HPO_4. The water was 0.05 M phosphate buffered after the addition of KH_2PO_4 and Na_2HPO_4. The buffered water was autoclaved to kill any microbes present in the water. The carboy was then allowed to reach room temperature. The

water used in preparing the chlorine dilution of any chlorine demand that may have existed prior to the experiment. The mixers and carboy spigot were also placed in chlorinated water to kill any microbes that may have attached to them. The collection bottles were received from the central glass storage area at the CDC. The bottles were autoclaved prior to arrival at the test location.

The Day of the Experiment

Disinfectant and pump preparation. The stock disinfection concentration was determined on the day of the experiment using the appropriate method from Standard Methods (APHA, AWWA, WEF 1995). For chlorine, the DPD Ferrous Titrimetric Method was used. In this method, N,N-diethyl-p-phenylenediamine (DPD) is used as an indicator with ferrous ammonium sulfate (FAS). The DPD Ferrous method is able to detect residual chlorine concentrations of up to 5 mg/L. In cases where the residual chlorine was higher, a dilution step with chlorine demand free deionized water was added. The pumps were warmed up by circulating the chlorinated water through the apparatus. Once the pumps were warm, the flow rates were measured. The flow rates were determined by collecting water in graduated cylinders over a given time and determining the rate of flow. Flow meters were not used due to the possible contamination and additional loses of oocysts that may be encountered during the experiments. The flow rates were set to appropriately dose the disinfectant into the spiked water. The lower constraint on the flow rate was that the disinfectant was flowing at a constant stream, that is, not dripping.

Cryptosporidium oocyst preparation. While the process pumps were warming up, the oocysts were prepared. Iowa and Maine isolates were used for the disinfection experiments. These zoonotic isolates are known to be more resilient than other isolates. The oocysts were purified from calf feces using the discontinuous sucrose gradient and a cesium chloride gradient as described in You et al. (1996) and Arrowood and Donaldson (1996). Laboratory technicians at the CDC performed the purification. The oocysts were stored in a 2.5% potassium dichromate solution at 4°C. The oocysts were used within three months of processing due to the decreased infectivity that occurs in older oocysts.

Laboratory technicians also determined the concentration of the stock solution. From this value, the volume of oocysts required for one day's experiment was determined. Typically, 150 µL of concentrated oocysts was transferred with a micropipetter to a 1.7-mL siliconized mi-

crotube (Phenix Research Products, Haywood, Calif.). The oocysts were washed with 1 mL of tissue culture phosphate buffer saline (T-PBS) at pH 7.2. The samples were mixed in a vortex to insure complete dispersion of the T-PBS. The oocysts/T-PBS/dichromate solution was centrifuged at 13,000 rpm (16,000 *g*) for 3 minutes. The T-PBS/dichromate solution was aseptically aspirated in a biological safety cabinet (NuAire, Plymouth, Mich.). This washing procedure was repeated two additional times. Upon the final washing, the volume was raised to 0.5 mL and the concentration of oocysts was determined. The number of oocysts in the suspension was determined with a phase hemacytometer (American Scientific Products, McGaw, Ill.) under a bright field microscope (Leitz Laborlux 12, Ernst Leitz, Wetzlar, Germany). The number of oocysts in the suspension was typically 1.1×10^7 oocysts. The goal was to achieve a final concentration in the carboy of 1×10^6 oocysts/L.

The carboy was then fully assembled and placed on the mixer plate. The carboy was inoculated with the washed oocysts, and the solution was mixed via a magnetic stir bar for 15 minutes prior to the beginning of the experiment to assure that complete mixing in the carboy. Two, sterile 5-mL pipettes were placed in the lid of the carboy to keep the contents of the carboy sterile. The pipettes contained a filter-like material that prohibited unwanted microbial material from entering the carboy.

Disinfection experiments

After 15 minutes of mixing, the three-way valve was adjusted so that the carboy was feeding the spiked, *Cryptosporidium*-containing water into the apparatus. The first run was a control run. The first 500 mL of water was wasted to insure that no chlorine was in the control sample. The approximate total volume in the apparatus was 250 mL. Approximately 500 mL of water was collected for the control in an autoclaved collection bottle (Wheaton, Wheaton, IL). After the collection of the control, one of the static mixers was placed in the apparatus. The pumps were once again started and again 500 mL of water was wasted. The next 300 mL of water was collected to test for the chlorine residual, conductivity (Model 840039, SPER Scientific, Scottsdale, Ariz.), and temperature. Later, the pH was measured when the oocysts had been recovered from the water. An additional 500 mL of water was collected to achieve a disinfection contact time. For the 0-minute contact time samples, 1 mL of sterile 0.1 N sodium thiosulfate

was added to the bottle prior to the addition of the water to the bottle. The sodium thiosulfate was added to neutralize the chlorine in the sample. For each of the other samples after the desired contact time was met (30, 60, or 90 minutes), sodium thiosulfate was added, and the bottle was mixed to insure complete mixing. All contaminated wastewater was collected and subsequently heated to 80°C to inactivate any *Cryptosporidium* present. Also upon completion of a battery of experiments, hot water was run through the apparatus and collected to inactivate any oocysts in the apparatus. The hot water was followed with chlorinated water, which was left in the apparatus.

After the required contact time was achieved, the process of concentrating the oocysts began. Samples were aseptically filtered in the biological safety cabinet (NuAire, Plymouth, Mich.) with 115 mL disposable 0.2 µm cellulose nitrate membrane filters (Nalgene, Rochester, N.Y.). Each sample was shaken and mixed prior to filtration to release oocysts that adhering glass bottle. The filter membrane was not allowed to dry, and to insure this, approximately 5 mL of the solution was left on top of the membrane. To efficiently remove the oocysts adhering to the membrane, 5 mL of 0.1% Tween 80 (polyoxyethylene sorbitan monooleate) was added as an eluting agent. The membrane was washed by vacuuming the surface with a sterile pipette. The oocysts/Tween 80 solution was then removed from the filter apparatus and placed in a sterile 15 mL centrifuge tube. The filtered water was collected and the pH was measured with a pH meter using a combination probe (Model 340 pH meter, Corning, Corning, N.Y.). After the pH was measured, the filtered water was discarded. The solution was centrifuged for 10 minutes at 4,000 rpm (3,290 *g*) and 4°C by a swing bucket centrifuge (Model CR422, Jouan, Winchester, Va.). The supernate was aspirated, and the oocyst pellet was dispersed into the solution with a volume of approximately 100 µL. The solution was then transferred into a 1.7 mL siliconized microtube. The volume was raised to 0.3 mL with sterile T-PBS. The number of oocysts in the solution was determined using a phase contrast hemacytometer. A minimum of 423 oocysts was counted in order for the number of oocysts counted to be within 10% of the actual number present with a 95% confidence interval (Krane and Sutter 1962). Figure 3.3 summarizes this process.

From the concentration of each of the samples, the volume to be inoculated into the MDCK cells for the viability tests was determined. The volume of the inoculum was desired to be between 50 µL and 250 µL, the upper bound existing because of potential cell washout. Sterile T-PBS was used to dilute samples as necessary. The number of oocysts inoculated per well

was typically $10^{4.7}$. Infectivity-curve data indicated that when approximately $10^{4.7}$ oocysts were inoculated the infectivity curve was relatively linear, indicating less variability in the data. For the control samples, a positive control of 2×10^5 was inoculated along with $10^{4.7}$ and two other concentrations to appropriately develop an infectivity curve. The infectivity curve represented the level of infection expected on the day of the experiment given a known number of untreated oocysts inoculated into the sample. The growth media (Ultraculture) was changed on each of the wells prior to the time of inoculation. The temperature of the growth media was raised in a water bath so that the cells were not shocked by the temperature differential. For the control wells, antibiotics were added to the Ultraculture to assure no microbial contamination. Antibiotic supplemental Ultraculture was prepared by adding 100 µL of a mixture of penicillin and streptomycin and 100 µL of fungizone to 100 mL of Ultraculture. The appropriate volume of oocyst solution was added to each well after the Ultraculture was changed. The cells were incubated at 37°C and 5% CO_2 for 46 to 48 hours in an incubator (Forma Scientific, Marietta, Ohio) maintained by microbiologists at the CDC.

Fixing and Staining MDCK Cells

After the incubation period, the cells were fixed and stained. The cells were washed three times with T-PBS. The cells were fixed with 500 µL of Bouin's solution (Sigma Diagnostics, St. Louis, Mo.) for one hour at 4°C. After one hour, the Bouin's solution was removed with a micropipette. The cells were washed with 70% ethanol for ten minutes on a rocker table. This process continued until the yellow color of the Bouin's solution disappeared. The cells were washed again three times with T-PBS, and then incubated in 500 µL of T-PBS enriched with 0.1% bovine serum albumin (BSA) for 30 minutes at room temperature on a rocker table.

After 30 minutes, the T-PBS/BSA was removed and replaced with 300 µL of fluorochrome-labeled monoclonal antibody solution. Two solutions were used: (1) a 1/400 dilution of monoclonal antibody C3C3-Cy3 in T-PBS/BSA and (2) a 1/100 dilution of less concentrated monoclonal antibody C3C3-Cy3 in T-PBS/BSA. The monoclonal antibody C3C3 is an antibody directed against *Cryptosporidium* cytoplasmic antigens found in the sporozoites, meront, and gamont life-cycle stages. The C3C3 antibody was produced at the CDC in a Cell-Pharm mini bioreactor system (UniSyn Fibertec, San Diego, Calif.). The antibody was labeled with Fluoro-

link Cy3 reactive dye (Research Organics Inc., Cleveland, OH). The C3C3-Cy3 remained on the cells for 90 minutes on a rocker platform in the dark. The C3C3-Cy3 was removed from the cells and the cells were washed three times with T-PBS. The fluorescence labeling was checked under the microscope, and if the signal was acceptable, then the slides were mounted. To protect the cells from ultra-violet light degradation and to mount the coverslips onto the cells, 2 or 3 drops of PVA II/DABCO was added to each well. The cells were covered with 18 mm^2 coverslips (Corning Glass Works, Corning, N.Y.). Entrapped air was carefully removed. Excess PVA II/DABCO was aspirated. The slides were stored inverted at 4°C. The stain remained bright and readable for up to three months.

The slides were read using a Carl Zeiss epi-fluorescense microscope with an HBO 100W/2 high pressure mercury lamp with an exciter filter of 546 nm (green). The barrier filter allows 590 nm and greater wavelengths (red) to pass. A chromatic beam splitter of 580 nm also is present (Carl Zeiss, Oberkochen, Germany). The cryptosporidial sexual and asexual life cycle stages were stained bright red against a dark red background. Five hundred microscope fields were read at 40× magnification. Each of the fields was identified as positive or negative for the presence of the labeled *Cryptosporidium* using a laboratory counter (Clay Adams, Parsippany, N.J.).

From the control data, an infectivity curve for the oocysts on the day of the study was produced. The data was fit to a 5-parameter sigmoidal equation using nonlinear regression software (Sigma Plot, Jandel, San Rafael, Calif.). A sample infectivity curve is presented in Figure 3.4. The 5-parameter sigmodial equation is

$$y = y_0 + a\left[1+\exp\left(\frac{-(x-x_0)}{b}\right)\right]^{-d}$$

where y = fraction of views positive for *Cryptosporidium*

x = log inoculated

a = model parameter

b = model parameter

y_0 = model parameter

x_0 = model parameter

d = model parameter.

In addition to the data collected, end points were added to obtain a realistic fit. The end-points were no fields positive with 100 oocysts inoculated and all fields positive with 10^6 oocysts inoculated. These endpoints were determined by the parasitologists at the CDC. For each sample collected and slide read, the percent of fields reported positive was related to the infectivity curve. This curve gave the expected number of oocysts inoculated for that particular level of fields positive. The difference between the expected number of oocysts inoculated and the actual number of oocysts inoculated was the $\log_{10}$ inactivated.

Experiments for Losses in Apparatus

To determine losses of oocysts that may have occurred within the test apparatus and the subsequent filtration steps, additional tests were developed. The first test examined the losses within the test apparatus. The preparation of the experiment was very similar to that of the disinfection experiments. The two major differences were that no disinfectant was needed and no MDCK cells were needed. The carboy volume was recorded and fifteen minutes after the carboy was inoculated, the experiment began. The spigot was detached from the apparatus to collect the first sample. The first 300 mL of process water was discarded. The next 500 mL was collected in a sterile sample bottle and labeled DIST1. This sample was to determine the distribution of the oocysts in the carboy prior to entering the apparatus. The spigot was then reattached to the test apparatus. The next point of testing was directly downstream of the process pump, which was directly upstream of the static mixer. This sample also consisted of 500 mL of process water. It was labeled PUMP1. PUMP1 was collected to determine if any losses were occurring in the pump. The third sample was collected directly downstream of the mixer and was labeled MIX1. At the end of the first run the carboy volume was recorded and the process was repeated until the process water in the carboy was exhausted. The apparatus was disinfected and the samples were processed using the same methods discussed above. However, since viability was not tested, the procedure was complete when the samples were counted with the hemacytometer.

Experiments for Losses in Filtration

There was concern that the filtration step for the concentration of samples may have led to losses during the experiments. To test this concern, an experiment was designed to determine what losses were occurring within the filtration step. A series of dilutions of oocysts in deionized water were prepared. The number of oocysts in the dilutions was determined prior to dilution with a phase hemacytometer (as previously discussed). The dilutions were filtered and centrifuged as discussed previously. The concentrated samples were counted using the phase hemacytometer.

RESULTS AND DISCUSSION

The purpose of the experiments described in this chapter was to determine if static mixers affect the disinfection of *Cryptosporidium*. The following results focus on the static mixer and the ability of the disinfectant to perform better under the influence of the static mixer.

Dispersion of Oocysts in Carboy

One of the first physical parameters investigated was the dispersion of oocysts in the carboy. Due to the nature of the disinfection experiments it was desired that the oocysts be completely dispersed in the carboy that served as the spiked water source. Figure 3.5 shows the results. The ±10% counting error introduced with the hemacytometer is represented by the error bars on the data. The data points above and below the error bars represent the standard deviation of the data set. From this data it is concluded that there is very little if any difference between the concentration of oocysts measured at different depths within the carboy. The conclusion derived is that the carboy is well mixed and the oocysts are evenly dispersed within the ±10% counting error. These samples were drawn fifteen minutes after the carboy was inoculated with oocysts. Because of these results, prior to all experiments, the carboy was allowed to mix for fifteen minutes.

Losses in Filtration Step of Experiments

There is a great deal of concern in research on *Cryptosporidium* that oocysts are lost in experiments due to their physical characteristics. Because of surface charge characteristics oocysts are known to stick to surfaces such as glass. Many oocyst recovery methods prescribing a filtration step have been known to achieve relatively low recovery efficiencies in spiked samples. The filtration step of the experiments was examined more closely to determine the loss of oocysts in this step. The results of the filtration experiments are shown in Figure 3.6. The data are presented as bar graphs. The bars on the left represent the samples spiked with oocysts prior to filtration. The bars on the right represent the samples after the filtration step. The error bars represent the ±10% counting error introduced by the hemacytometer. The difference between the number of oocysts inoculated and recovered can be accounted for within the counting error. The filtration experiments indicated that there was no appreciable loss of oocysts through the filtration step of the disinfection experiments.

Concentration of Oocysts in Samples Collected

The concentration of oocysts in the samples collected in each experiment was also recorded. The concentrations are shown in Figure 3.7. The samples are reported in the order in which they were collected. During some days there were more samples collected than others. The error bars on the data represent the ±10% counting error introduced by the hemacytometer. The target concentration for the sampling was 500,000 oocysts per 500-mL sample or 10^6 oocysts/L, the average concentration of the samples was 1.26×10^6.

Concentration of Oocysts in Stock Samples

The stock sample oocysts were stored in a laboratory refrigerator at 4°C in potassium dichromate. The viability of oocysts is known to decrease with age. For these experiments the concentration was also monitored to determine if there was any significant change in concentration through the course of a series of experiments. In most cases the oocysts were used within two months or sixty days of purification to be sure that no losses in viability occurred. For the major-

ity of the experiments the variation in the stock concentration determined was within the ±10% counting error. The data is presented in Figure 3.8. However there are two outliers, with concentrations significantly higher than the remainder of the test dates. The concentrations for the outlier data points were calculated from very small volumes (~15μL). Typically 150 μL was removed from the stock solution on days when disinfection experiments were performed. Smaller volumes were used for infectivity curves and quality control experiments. The higher concentrations found in the two small samples are most likely attributed to the volume removed not being representative of the concentration of the entire sample.

Infectivity Curves

Prior to the use of a new isolate/purification of an oocyst suspension, an infectivity curve was prepared. This was a very important step since viability (or ability to infect) varies not only with oocyst age, but also within each isolate passage. There are two types of variability, between strains (Louisiana, Maine, Iowa, etc.) and within strains (different passages). An infectivity curve is presented in Figure 3.9 from April 23, 1999 for the Maine strain. The sample was purified on March 12, 1999 and the oocysts were already one month old. There is a considerable difference between the infectivity curve of the Iowa and Maine isolates. The Maine isolate was not used extensively in this study, primarily due to supply. The Iowa isolate is thought to be a more environmentally resilient strain. The use of the more resilient strain in the disinfection studies was desired to better gauge the effectiveness of the static mixers. The difference between the strains is quite large. For example, the Maine isolate had 167 views positive (0.333) when 4 log oocysts were inoculated. An Iowa isolate purified on June 10, 1999 had 10 views positive (0.02) when 4 log oocysts were inoculated. This is a significant difference. Because of this the experimenter must be sure to use the correct infectivity curve for each isolate and the daily controls to interpret the data. Because of the large variations in viability from strain to strain, the Iowa strain was used primarily in these experiments.

For each experiment control experiments were performed in the empty pipe with no disinfectant. From the controls an infectivity curve for that day's experiments was developed. The infectivity curve had to be derived for each day an experiment was run because of the changing

viability of the oocysts. A comparison of the infectivity curves for various testing dates is presented in Figure 3.10. The curves show the variability in viability on different test dates.

Head loss and *G*-values

The pressure drop across the Omega mixer, six element helical mixer and two element helical mixer was measured for different flow rates used in the experiments. The head loss measurements were used to determine the *G*-values. The head loss (Δh) data for the three mixers and 14.4 in. (36.6 cm) of tubing are presented in Figure 3.11 as a function of velocity head $U^2/2g$. The six element helical mixer had the greatest head loss followed by the Omega mixer, the two-element helical mixer, and the empty pipe. The calculated Reynolds number for the empty pipe ranged from 880 to 2,300. The head loss for the mixers without the additional tubing can be found in Hardy (1999). The *G*-values were calculated for the mixers by the following equations:

$$\Phi = \frac{gU\Delta h}{L}$$

and

$$G = \sqrt{\frac{\Phi}{\nu}}$$

where Φ = total energy dissipation rate per unit volume in the static mixer
g = acceleration due to gravity
U = bulk (average) velocity
Δh = head loss across static mixer
L = length of static mixer
G = average or mean velocity gradient
ν = kinematic viscosity.

The *G*-values are presented in Figure 3.11. For a flow rate of 0.53 gpm (2 L/min), the *G*-values were 357 s^{-1} for the empty pipe, 2,840 s^{-1} for the two element helical mixer, 3,200 s^{-1} for the six element helical mixer, and 3,890 s^{-1} for the Omega mixer.

Chlorine Disinfection Studies

Batch reactor chlorine experiments were performed at pH 6 by inverting a 1-L glass bottle three times after the disinfectant was added. The mixing in the jar tests was at *G*-values of 500 s^{-1} and 1000 s^{-1} for approximately one second after the disinfectant was added. The batch experiments at low contact times produced log inactivation between -0.07 and 0.15. At longer contact times, the batch experiments produced log inactivation between 0.15 and 0.17. The jar test experiments at both *G*-values showed similar results. The results are presented in Figure 3.12.

Preliminary disinfection studies showed very little difference between the two element helical mixer, the Omega, the Stata-tube mixer, and the empty pipe data. The empty pipe had an average velocity of 1900 mL/min and a Reynolds number between 3,000 and 3,500. The results are presented in Figure 3.13. With the exception of a few outliers, the general trend of the data is a slight increase in inactivation with an increase in $C \times T$ (concentration × time) value. This result is to be expected. The significance of this data is that the empty pipe performed the same as the two-element helical mixer, the Omega, and the Stata-tube mixer. In other words, the two-element and Omega mixers did not significantly affect the disinfection of *Cryptosporidium*.

The error bars presented in Figure 3.13 represent a combination of two types of error. The first is the ±10% error that is introduced during the counting step with the phase hemacytometer. In all disinfection studies, $10^{4.7}$ (50,119) oocysts were inoculated into the cells. The 95% confidence interval range at $10^{4.7}$ is [45,107 to 55,131]. The log range is [4.65 to 4.74]. The corresponding error bar lengths are -0.05 log and +0.04 log. This is the error on the log inoculation introduced strictly in the counting step. The second error type accounted for is the variability within the cell culture method. Because the system is biological there is natural variability that will be encountered. The difference between cells was determined to be one standard deviation 0.003 log with a 95% confidence interval of [0.0023 to 0.0047]. The confidence interval ranges were added to the error bars determined by the counting. These combined error bars are shown in Figure 3.13. The six-element helical mixer was found to achieve a greater level of inactivation when compared to the empty pipe in preliminary tests, consequently, subsequent experiments focused on the six-element mixer. The results from the six element disinfection experiments are

shown in Figure 3.14. At a $C \times T$ of 945 mg·min/L, 1.85 log inactivation was observed. This is a significant reduction in oocyst viability at this $C \times T$. At these water conditions (pH 6, 22°C), this level of inactivation has not been seen in previously published research. There is some scatter in the data, but the general trend is a more dramatic increase in inactivation with increasing $C \times T$ than seen in the empty pipe, two element mixer, or the Omega mixer. Figure 3.15 shows the six-element data in addition to the two-element data, the Omega mixer data and the empty-pipe data. Typically a linear trend line can be fit to disinfection data that is plotted on a log inactivated versus $C \times T$ graph. The linear fit of the two-element mixer, Omega mixer, and empty pipe is shown in Figure 3.16. The linear fit of the six-element disinfection data is presented in Figure 3.17. From the linear regression of the data, the introduction of the six-element mixer produces a 0.5 log increase in inactivation of *Cryptosporidium* at a $C \times T$ of approximately 400 mg·min/L. At a $C \times T$ of approximately 1050 mg·min/L, a 1.0-log increase in inactivation was observed. These increases are the difference between the empty pipe flow and the six-element mixer. By determining the difference between the empty pipe and the six-element mixer the performance of the six-element mixer is more truly represented.

Figures 3.18 and 3.19 show the inactivation of *Cryptosporidium* oocysts as a function of G-value for contact times less than 3 seconds and 30 minutes, respectively. The data presented is limited to the series called 2 in the previous disinfection graphs. The general trend for both contact times is an increase in inactivation with an increase in G-value.

The Hom model was used to fit the data from the 6-element experiments. To determine the appropriate constants for the Hom model the following transformations were performed. The Hom model is represented in a steady-state plug flow regime as:

$$\log\left(\frac{N_o}{N}\right) = kc^n t^m$$

where N_0 = initial concentration of organisms
N = final concentration of organisms
k = model parameter
n = model parameter
m = model parameter

c = disinfectant concentration

t = contact time

The equation was linearized twice to determine each of the model parameters constants. The linearization procedure is shown in Figures 3.20 and 3.21. The Hom model equation becomes

$$\log\left(\frac{No}{N}\right) = 3.28\times10^{-6} c^{3.2629} t^{1.2265} \tag{3.1}$$

In Figure 3.22, the Hom model was graphed using Equation 3.1 at 0.25-log intervals. Each curve represents a different level of inactivation (log (*No*/*N*)). The *x*-axis is the contact time in minutes and the *y*-axis is the concentration of the chlorine. At the larger contact times, where chlorine degradation would begin to take place, the concentration of chlorine would be an average concentration relating to the degradation kinetics. This model is useful to predict what level of inactivation will occur in this system at a given concentration and time.

To test the validity of the empirical constants derived in the method previously discussed, the Hom model was used to calculated the log inactivation of each concentration and contact time for all of the experiments. The calculated values and the experimental values were compared. The difference between the two values was examined using a hypothesis test. The two values were not determined to be different at the $\alpha = 0.01$ level, or a 99% confidence interval. For illustrative purposes, Figure 3.23 shows a portion of the experimental data points on the Hom model curves for 0.5-log inactivation and 1.0-log inactivation. The graph is similar to the other Hom model curves in that the *x*-axis is contact time and the *y*-axis is the chlorine concentration. The data points are accompanied by labels that indicate the experimental log inactivation measured at that point. The graph visually indicates what the hypothesis testing had previously concluded.

Inactivation of Cryptosporidium *by Chlorine at pH 7 and 8*

The effects of increasing the pH to 7 and 8 can be seen in Figure 3.24. The six-element helical mixer showed a noticeable decrease in inactivation as pH increased at the high and low

contact times. At low contact times, the six-element helical mixer inactivated between -0.22 to 0.05 log at pH 8, 0.07 to 0.08 log at pH 7, and 0.33 log at pH 6. At higher contact times with the six-element static mixer, 0.11 log of oocysts were inactivated at pH 8, 0.08 at pH 7, and between 0.28 to 0.39 log inactivation at pH 6. The two-element static mixer inactivated 0.08 log at pH 7 and between 0.22 and 0.31 log inactivation at pH 6 at low contact times. At high contact times, similar inactivation was observed; however, at pH 8 the $C \times T$ was 50 mg·min/L greater. The empty pipe showed little difference in inactivation at the low contact times between pH 6 and 7 except for one data point that showed -0.19-log inactivation. At the higher $C \times T$, inactivation was 0.19 at pH 7 and between 0.26 to 0.38 at pH 6.

For both short and long contact times, chlorine at pH 6 was more effective at inactivating the oocysts than at pH 7 or 8. At pH 6, greater than 97% of the chlorine is in the hypochlorous acid phase; whereas for pH 7 and pH 8, the percent drops to 79% and 33% hypochlorous acid. These results support the generally accepted hypothesis than HOCl is more effective that OCl^- at inactivating *Cryptosporidium* oocysts because the neutral HOCl molecule has a greater ability to diffuse through the oocyst wall and membranes than the charged OCl^- species. The relative effectiveness of HOCl as contrasted with OCl^- has long been established for other organisms.

The results from this current research agree with many with other studies. Gyürék, Finch, and Belosevic (1997) report that essentially no inactivation is observed at pH 8 with free chlorine. To complement this study, Gyürék, Finch, and Belosevic (1998) showed that all of the inactivation data at pH 8, except for an extremely high $C \times T$, could not be discerned from zero inactivation due to the uncertainty of animal infectivity data. Liyanage et al. (1997) showed that 0.1-log inactivation was observed at a chlorine dose of 4 mg/L and a contact time of 240 minutes at pH 8. Ransome, Whitmore, and Carrington (1993), using excystation, showed -0.2-log inactivation with a dose of 1.5 mg/L chlorine and a contact time of 1,440 minutes at pH 7. Overall, this study reinforces the finding that little inactivation of *Cryptosporidium* oocysts occurs at pH 7 and above.

Inactivation of Cryptosporidium *by Chlorine Dioxide*

The results from the chlorine dioxide inactivation of *Cryptosporidium* oocysts at pH 8 is presented in Table 3.1. At the low contact times, the batch experiment inactivated 0.03 log and

the empty pipe inactivated 0.18 log of oocysts. The 6-element helical static mixer produced 0.23 log inactivation and the Stata-tube 0.28 log inactivation. At the higher $C \times T$, the batch, empty pipe, and six-element helical experiments produced log inactivation between 0.41 to 0.43. The data for the Stata-tube experiment with chlorine dioxide was discarded because of atypical *Cryptosporidium* infection of the MDCK cell monolayer.

Mixing appeared to be an important factor for the short contact time with chlorine dioxide as with the chlorine experiments. However, at the 30-minute contact time, the effects of mixing were not seen. Chlorine dioxide produced a noticeable increase in inactivation over the 30-minute contact time, whereas, chlorine did not. Chlorine dioxide appeared less dependent on initial mixing than chlorine. Chlorine dioxide at different mixing intensities produced the same inactivation at the 30-minute contact time. Chlorine produced greater inactivation at the higher mixing intensities.

The results with chlorine dioxide show less inactivation than indicated in other studies. LeChevallier et al. (1996) showed 1.4 mg/L of chlorine dioxide with 30 minutes contact produced 1-log inactivation by excystation. Liyanage et al. (1997) showed 1-log inactivation using mouse infectivity counts for a chlorine dioxide dose of 2.0 mg/L and contact time of 30 minutes. Chlorine dioxide was added to pH 8 water in both studies.

Inactivation of Cryptosporidium *by Chlorine Followed by Monochloramine*

The results of the batch and six-element helical mixer inactivation experiments of chlorine and monochloramine added in series at pH 8 are summarized in Table 3.2. The chlorine pretreatment for all of the experiments had $C \times T$ between 111 and 141 mg·min/L and the contact time for the monochloramine was varied. Batch experiments of just chlorine and formed monochloramine produced between 0.15 to 0.38 and -0.02 to 0.19 log inactivation respectively. The batch experiment of chlorine followed by monochloramine at the 110-minute contact time

Table 3.1

Inactivation of *Cryptosporidium* by chlorine dioxide at pH 8 and 20 ± 1°C

Mixer	*C* (mg/L as ClO_2)	*T* (min)	*C*×*T* (mg·min/L)	*G*-value (s^{-1})	Log inactivation
Batch	2.3	0.076	0.17	—	0.03
	2.3–1.8	30.	61.5		0.41
Empty pipe	1.7	0.005	0.008	357	0.18
	1.7	30.	51.		0.43
Six-element helical	1.9	0.005	0.010	3,200	0.23
	1.9–1.3	30.	48.5		0.41
Stata-tube	1.7	0.005	0.009	3,890	0.28
	1.7	30.	51.		—

Table 3.2

Inactivation of *Cryptosporidium* by chlorine followed by monochloramine at pH 8.0 ± 0.1 and 20°C ± 1°C

Mixer	*C* (mg/L as Cl_2)	*T* (min)	Cl_2–*C*×*T* (mg·min/L)	*C* (mg/L as NH_2Cl)	*T* (min)	NH_2Cl–*C*×*T* (mg·min/L)	Inactivation log_{10}
Batch	3.8	30	114	–	–	–	0.38
	4.3	30	129	–	–	–	0.15
	–	–	–	3.9	110	429	-0.02
	–	–	–	4.4	110	484	0.19
	4.4	30	132	4.7	110	517	0.39
Six-element helical	3.7	30	111	3.6	0.005	0.02	0.37
	3.7	30	111	3.6	30	108	0.09
	4.7	30	141	4.7	30	141	0.10
	3.7	30	111	3.6	110	396	0.30
	4.7	30	141	4.7	110	517	0.39

with monochloramine produced 0.39 log inactivation. The six-element helical mixer for a contact time of 0.05, 30, and 110 minutes produced 0.37, 0.10 - 0.09, and 0.30-0.39 log inactivation, respectively.

Because of the great difference between the chlorine batch tests at pH 8, the log inactivation of chlorine at pH 7 and 8 from the static mixer were included in the analysis. The rationale being that the static mixers would represent an upper limit of inactivation, based on the results of chlorine at pH 6. As can be seen in Figure 3.25, the chlorine batch experiment at pH 8 showed 0.38 log inactivation, which is much greater than the static mixers and empty pipe inactivation at pH 7 and 8. In the same manner, the 0.37 log inactivation by the six-element helical mixer with 0.02 mg·min/L of monochloramine after pretreatment with chlorine (combined $C \times T$ of 111.2 mg·min/L) appeared to be out of the expected range.

To evaluate if dual disinfectants caused synergism in disinfection, the average of all the chlorine data at the 30-minute contact time, including the static mixer and empty pipe experiments, was added to the average inactivation of monochloramine at approximately 4 mg/L for 110 minutes. The average inactivation by chlorine with $C \times T$ ranging from 114 to 198 was 0.18 log inactivation. The mean value of inactivation due to monochloramine at $C \times T$ ranging from 429 to 484 was 0.09 log. Adding together these results causes a combined inactivation of 0.27 log. Following 111 to 132 produced 0.30 log inactivation at the 110 minute contact time. The results indicate a 0.12 log inactivation due to synergism. In comparing the monochloramine results to Gyürék, Finch, and Belosevic (1997), a difference must be noted. Gyürék, Finch, and Belosevic (1997) used preformed monochloramine and this study used chlorine with post ammoniation, which gave the oocysts a short contact time with free chlorine.

CONCLUSIONS AND RECOMMENDATIONS

Results from this research indicate that the introduction of a six-element static mixer into a flow stream where disinfection with chlorine is occurring has a positive effect on the effectiveness of the disinfectant. This effect can be seen at the bench-scale at high $C \times T$. Because of the high and impractical $C \times T$ used, the practical usefulness of these findings seem limited. However, fundamentally these findings may turn out to be quite important.

The conclusions of this research were derived through a series of disinfection experiments. There were six sets of experiments from which the sum total of the data was derived. From the experiments the conclusion was drawn that there was no discernible difference between the two element helical mixer, the Omega mixer, and the empty pipe. For all three mixers, less than 0.8 log inactivation was observed at a $C \times T$ of approximately 1000 mg·min/L. The six-element helical mixer, however, showed a greater level of inactivation. The six-element mixer was able to achieve 0.8-log inactivation at a $C \times T$ between 300 and 700 mg·min/L. At a $C \times T$ of 1000 mg·min/L 2-log inactivation was observed. Using linear regression, the following improvements in disinfection were observed with the introduction of a static mixer into the flow regime; at a $C \times T$ of approximately 400 mg·min/L produces a 0.5-log increase in inactivation and at a $C \times T$ of approximately 1050 mg·min/L a 1.0-log increase in inactivation was observed.

The $C \times T$ values at which chlorine is able to inactivate *Cryptosporidium* are beyond values that can practically be obtained in most utilities. Some utilities, through a series of long distribution systems can reach these values. An example of this is the New York City water supply system. The aqueduct system bringing water into the city is approximately 125 miles (201 km) long (Freud 1999). If the velocity of the water in the aqueduct system is assumed to be 3 ft/s (0.9 m/s), the time the water remains in the aqueduct is 3,722 minutes. New York City has a city wide chlorine residual goal of 1.2 mg/L as a goal (Freud 1999). The $C \times T$ achieved by that system given these parameters is theoretically 4,470 mg·min/L. This value is well beyond any $C \times T$ tested in these experiments; however, substituting into the trend lines presented in Figures 3.16 and 3.17, an increase of 3.74-log inactivation from an empty pipe to a six-element mixer could be calculated. Caution should be used in interpreting this calculation and result since there is no data that validates the linear regression at $C \times T$ values greater than 1100 mg·min/L.

Since these $C \times T$ are not practical for most utilities and the New York aqueduct system is very unique, there are other implications of this research that should be discussed. To date the disinfection mechanism for *Cryptosporidium* is unknown. The idea that a static mixer can increase the effect chlorine has on *Cryptosporidium* has fundamental significance. Something that is occurring when the static mixer is introduced in the disinfection process is increasing inactivation. This could be increased turbulence that occurs when the static mixer is introduced into the flow stream, or perhaps better dispersion of the disinfectant into the flow stream. In the end this could mean less disinfectant is needed to achieve the same level of inactivation previously only

seen with more chemicals. This could result in potential cost savings on chemicals and upgrades to stronger disinfectants. Another potential implication of this is less disinfection by-products formation. This would not be the case at the high $C \times T$ of chlorine. However, perhaps with ozone, one of the most promising disinfectants against *Cryptosporidium*, this could be the case.

This research suggests that static mixers may potentially be used to optimize disinfection. The six-element helical mixer has been shown to be particularly effective at the bench-scale. However, caution in interpreting the data should be exercised. The completed experiments were performed using laboratory grade water buffered to pH 6 with a controlled temperature. Natural waters were not examined, due to the cell culture method of infectivity measurement. Because natural waters were not examined, chemical interactions, biological interactions, and particle interactions are not accounted for in this research. All of these interactions would have a significant effect on any disinfection regime. If the increase in inactivation is due to increased turbulence, additional particles may further enhance the disinfection. If the increase in inactivation relates to the dispersion of the chlorine, additional microbes in the system will also be inactivated with the enhanced disinfection. Another item that must be noted is the difficulty in scaling up mixing. Caution should be observed when using this data for design, analysis, or operation of larger mixers. Historically, scale-up of mixing has been difficult.

The experiments showed that the mixer alone with no disinfectant did not significantly change the infectivity of the oocysts. However, the addition of chlorine did change the infectivity. The MDCK cell culture method for testing infectivity is a useful method. It is reproducible and gives an accurate measure of oocyst infectivity.

Recommendations

Mixing may play a significant role in disinfection kinetics. This phenomenon was seen at the bench-scale with laboratory grade water. More research on the role of mixing in disinfection kinetics in natural systems is needed. This study focused on chlorine disinfection, future studies could focus on stronger disinfectants. Additional research should also focus on the mode of action of the chlorine against the oocyst. There has been little research done on this and by understanding the mode of action, perhaps disinfection systems could be better designed. Additionally, coliforms or other less resilient microbes could be studied in this disinfection regime.

The physical condition of the oocysts is also an important aspect of disinfection studies. For research purposes oocysts that are fresh, that is, recently purified and stored in a preservative were used. In real water treatment plants, oocysts that enter the system have typically been exposed to a variety of environmental conditions and could be significantly older than those studied here. Clumping of oocysts and protection from disinfects in flocs may also occur. Future research could investigate the oocysts that have been exposed to environmental conditions, to simulate a real system.

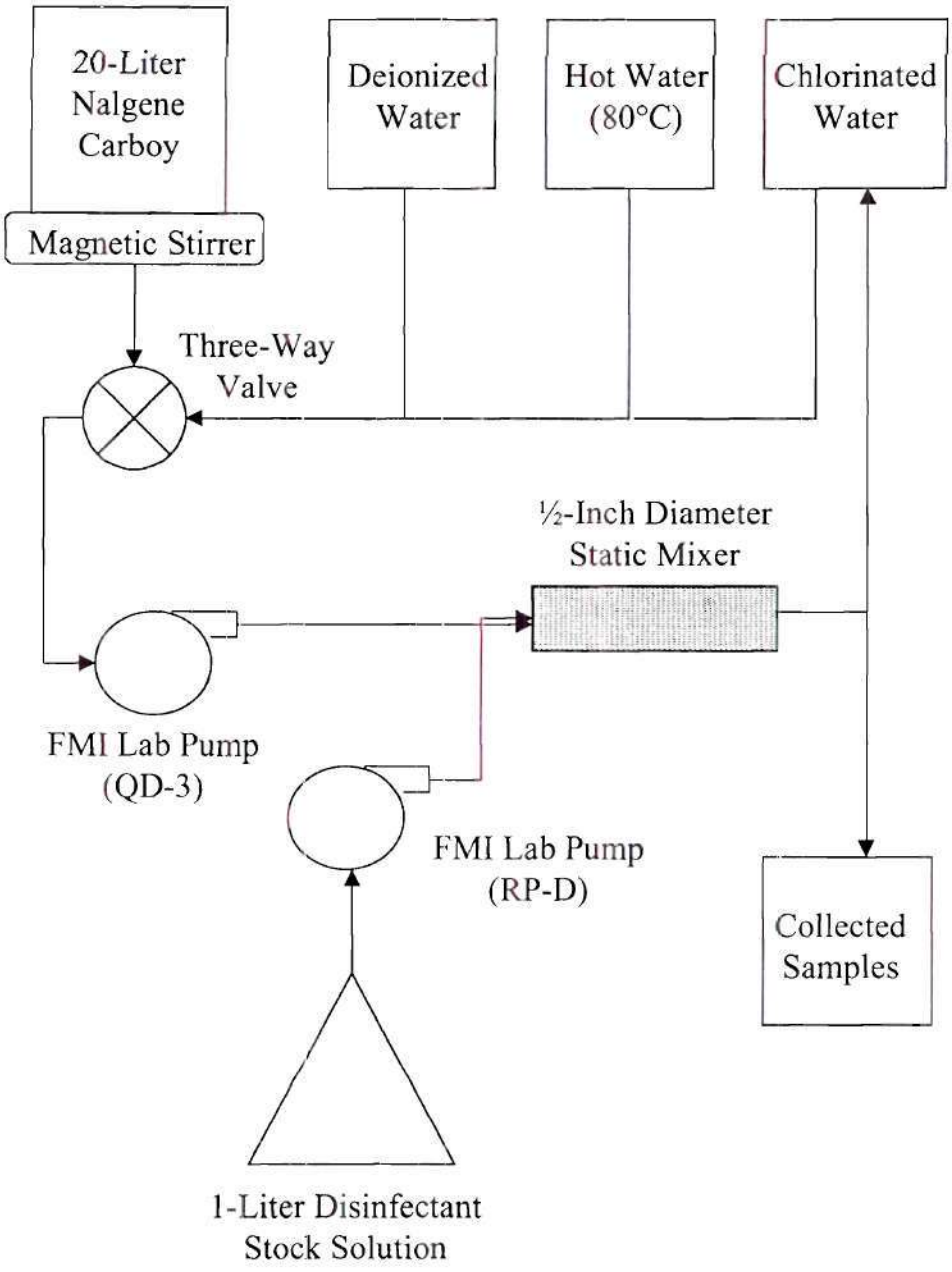

Figure 3.1 Experimental apparatus setup

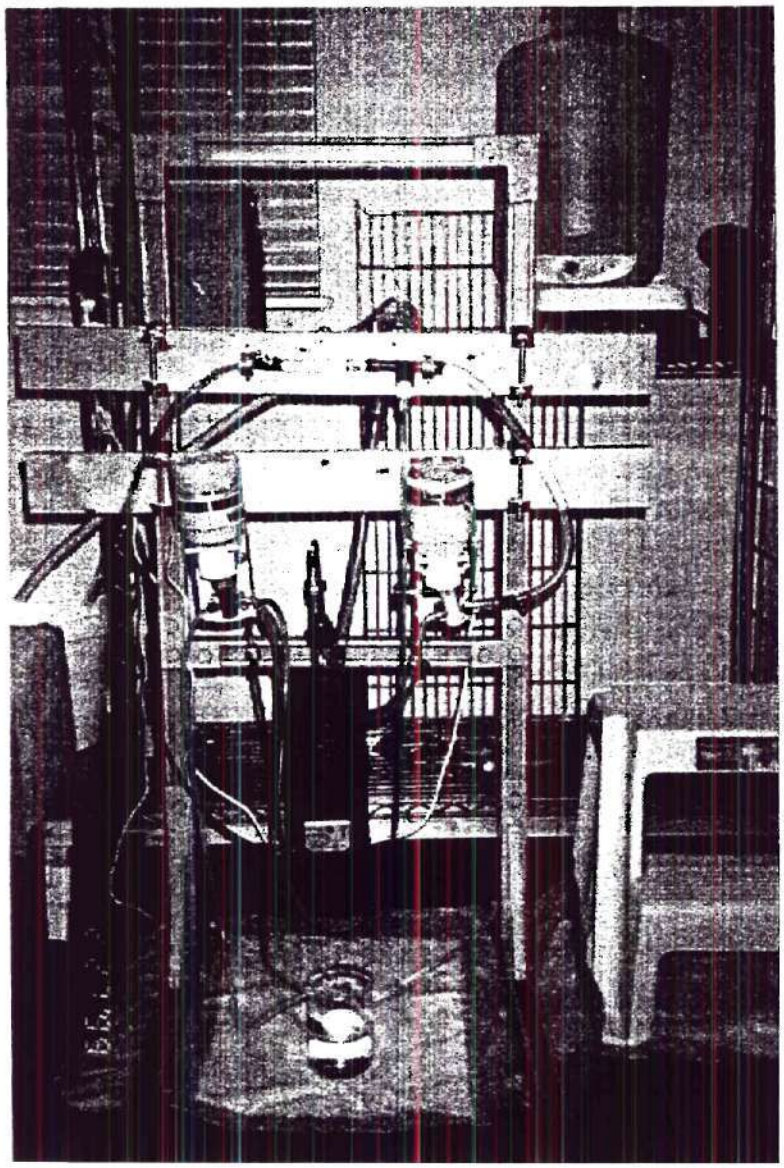

Figure 3.2 Bench scale experimental apparatus

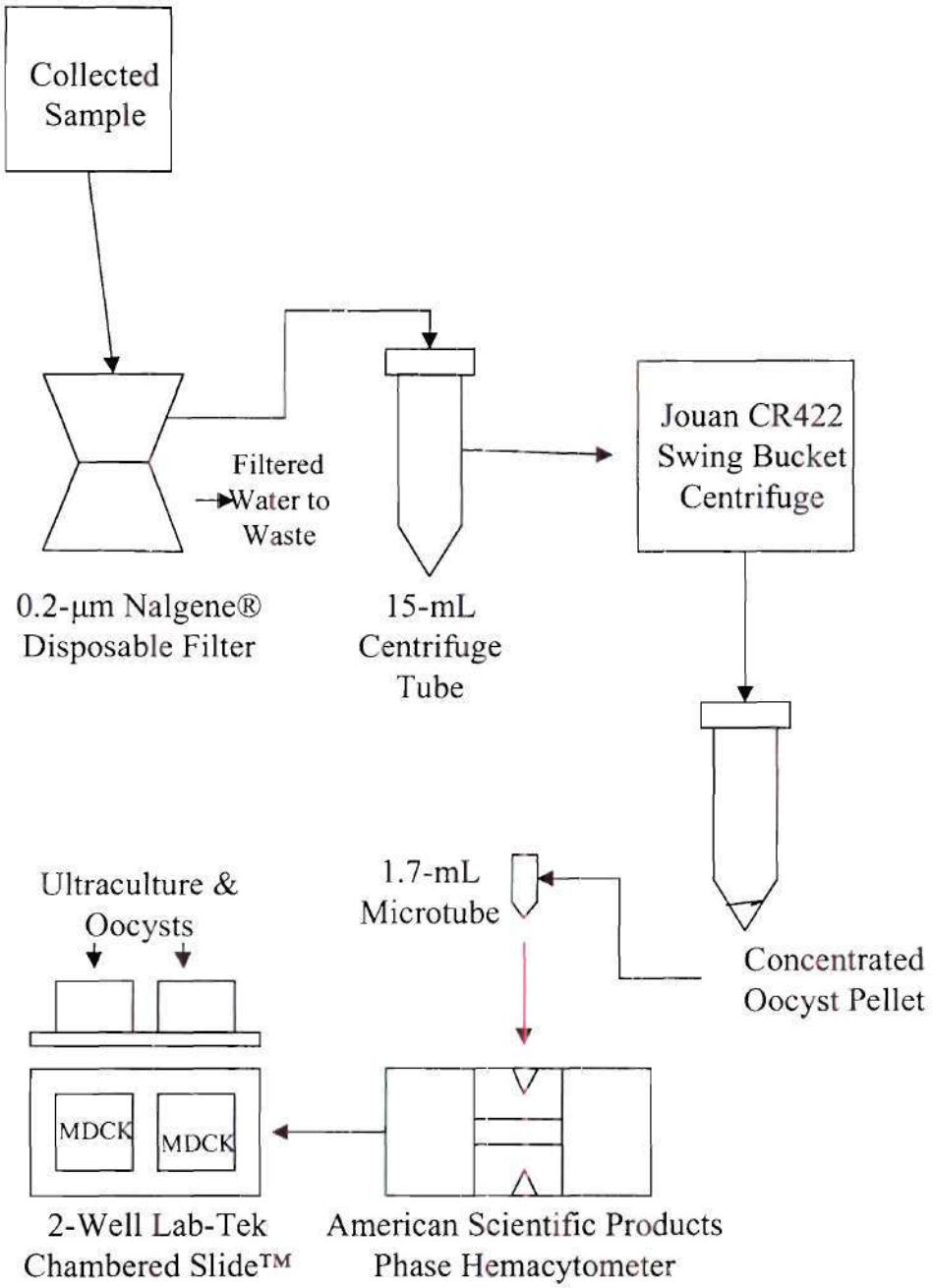

Figure 3.3 Schematic describing the oocyst concentration procedure

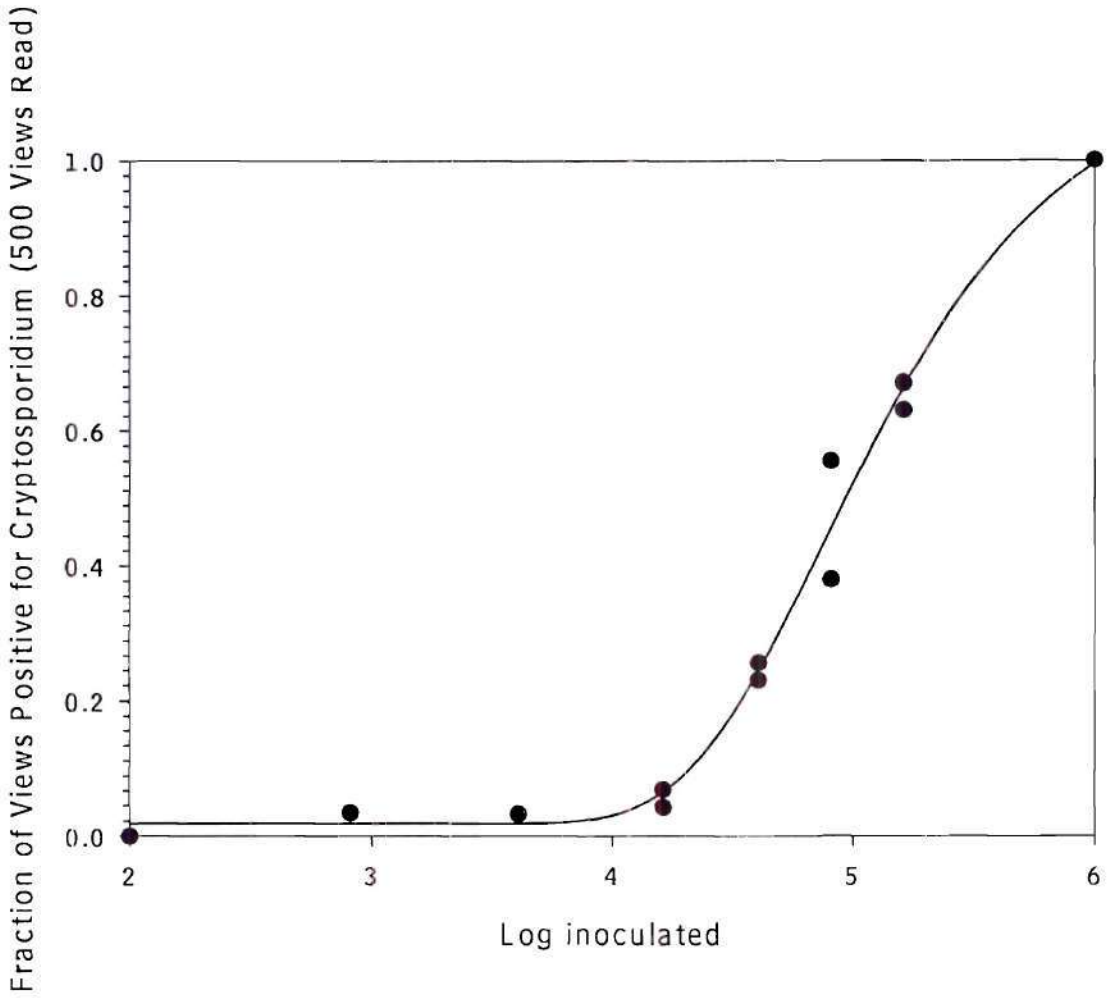

Figure 3.4 Sample infectivity curve for oocysts inoculated onto MDCK cells

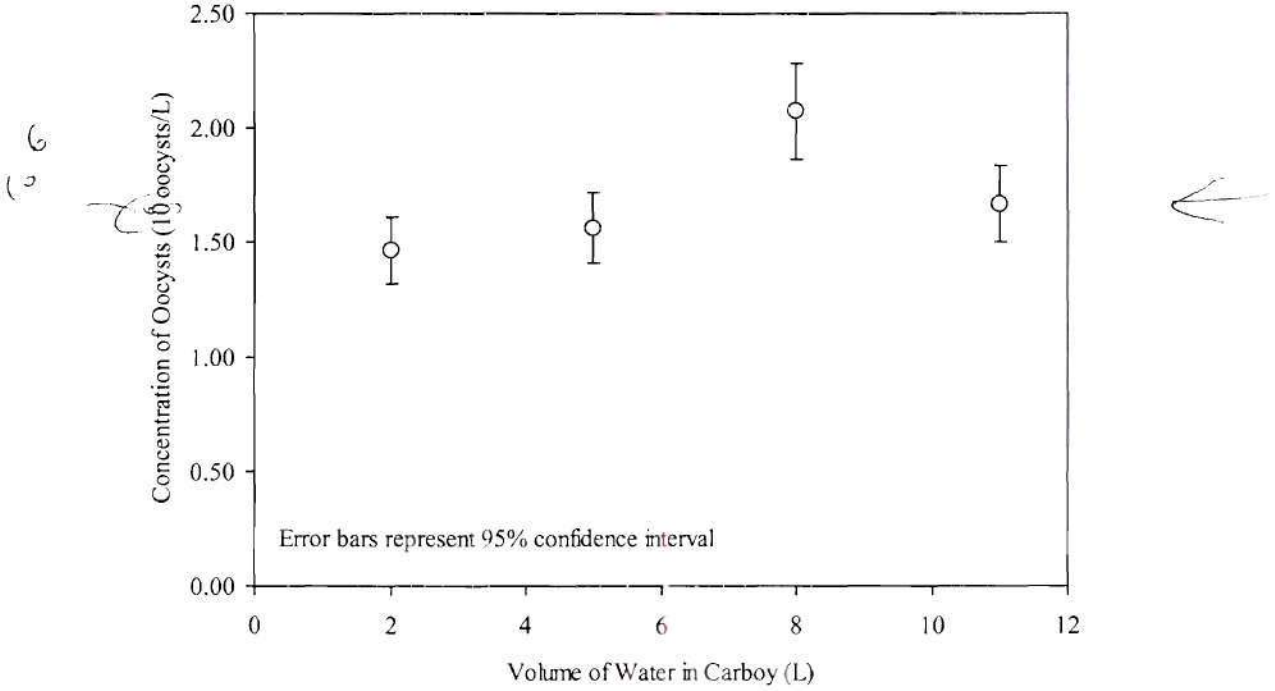

Figure 3.5 Distribution oocysts in the spiked carboy

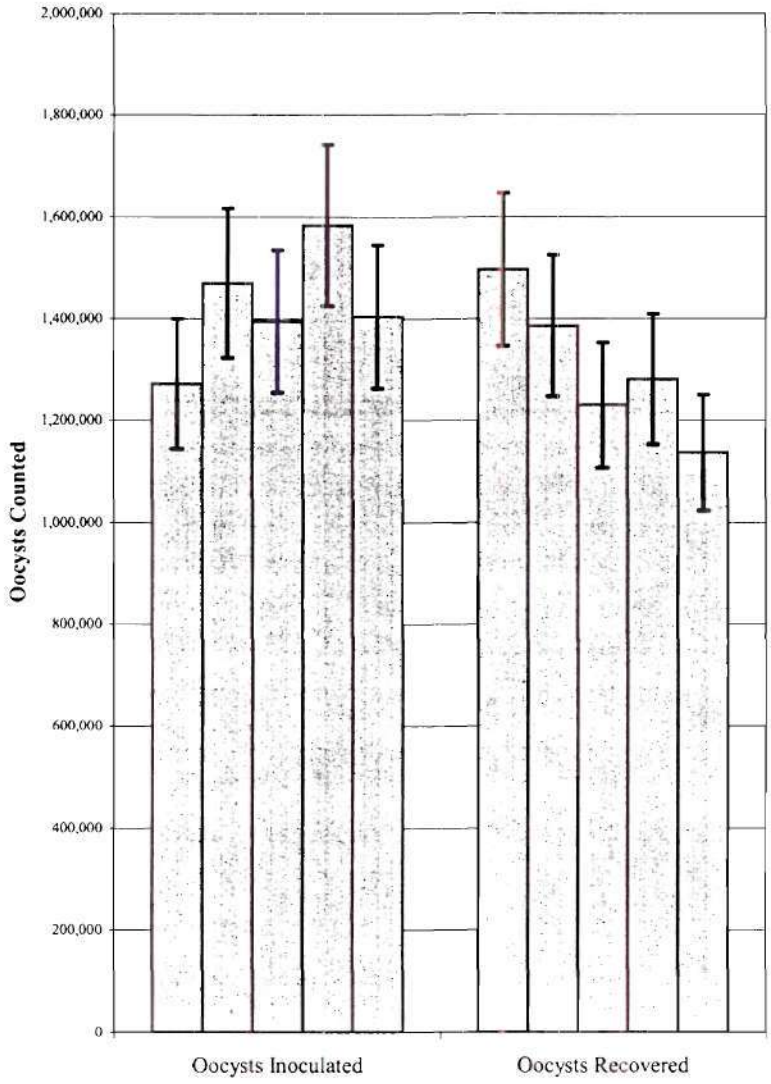

Figure 3.6 Oocyst losses in filtration step of experiment

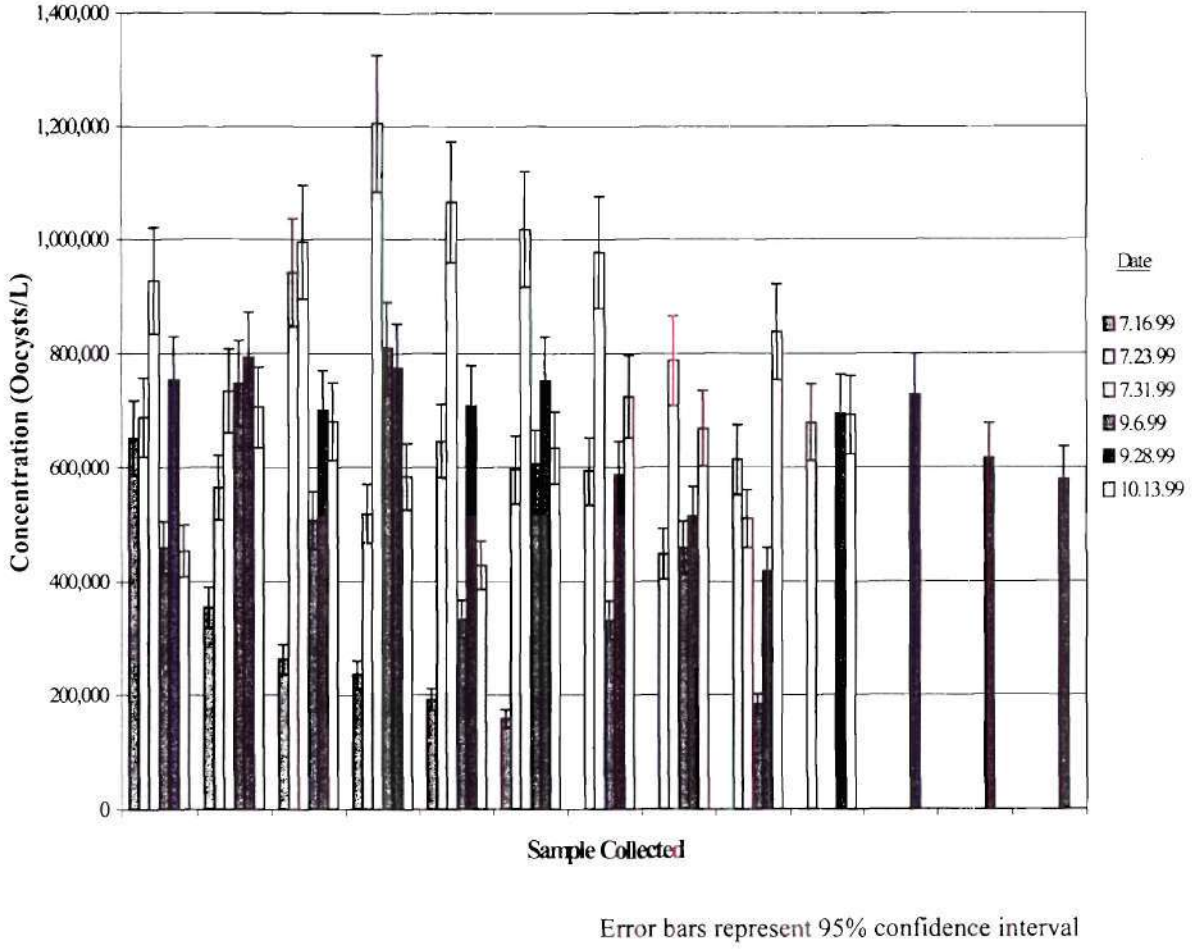

Figure 3.7 Concentration of oocysts in collected samples through test runs

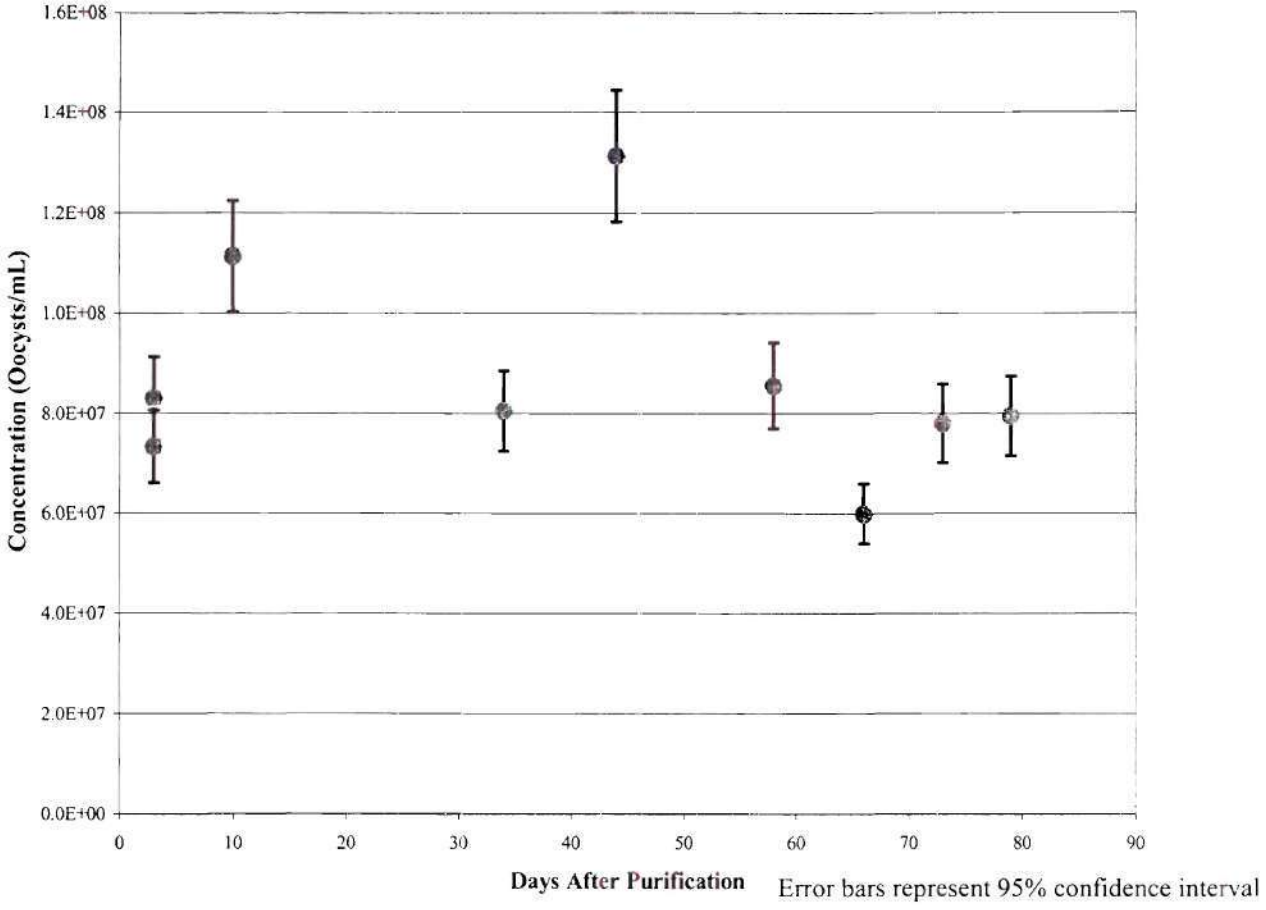

Figure 3.8 Concentration profile of purification 19IA9 of the Iowa isolate

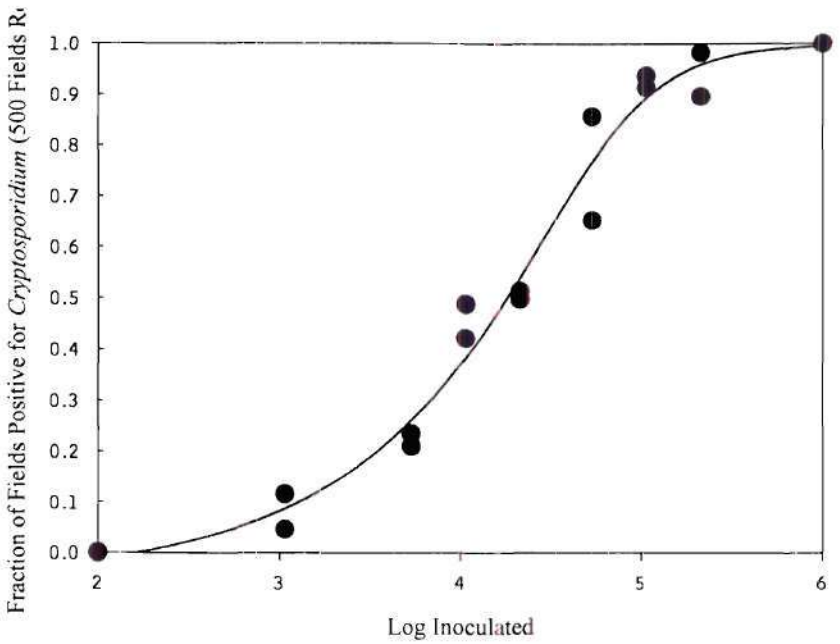

Figure 3.9 Infectivity curve for 3.12.99 purification (9HMAI) of Maine isolate

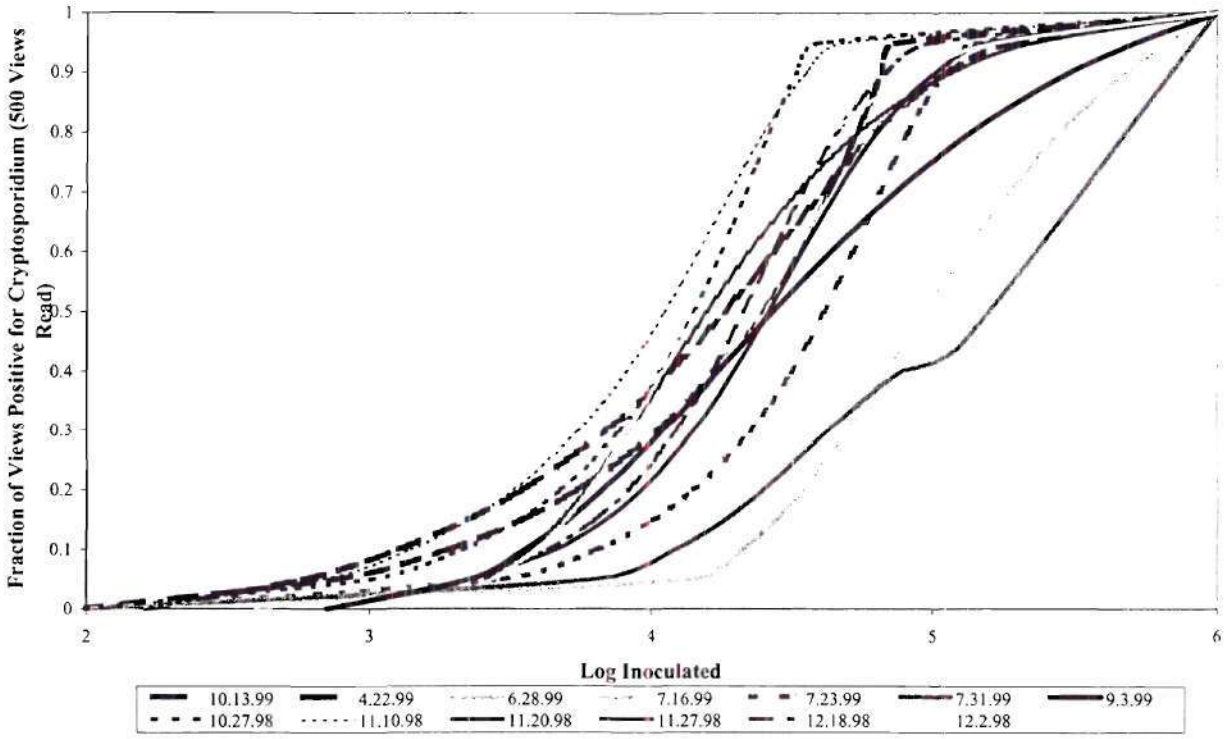

Figure 3.10 Comparison of control data infectivity curves

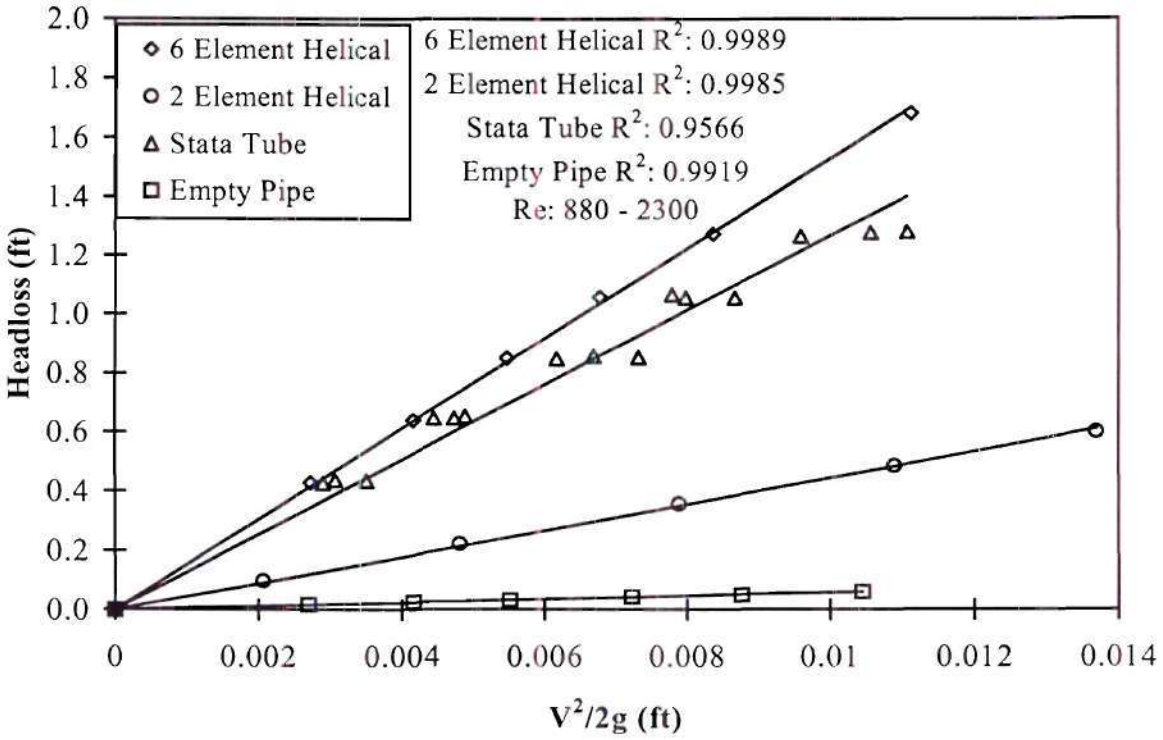

Figure 3.11 Head loss across 0.5-inch diameter static mixers and 14.4 inches of tubing at 20°C.

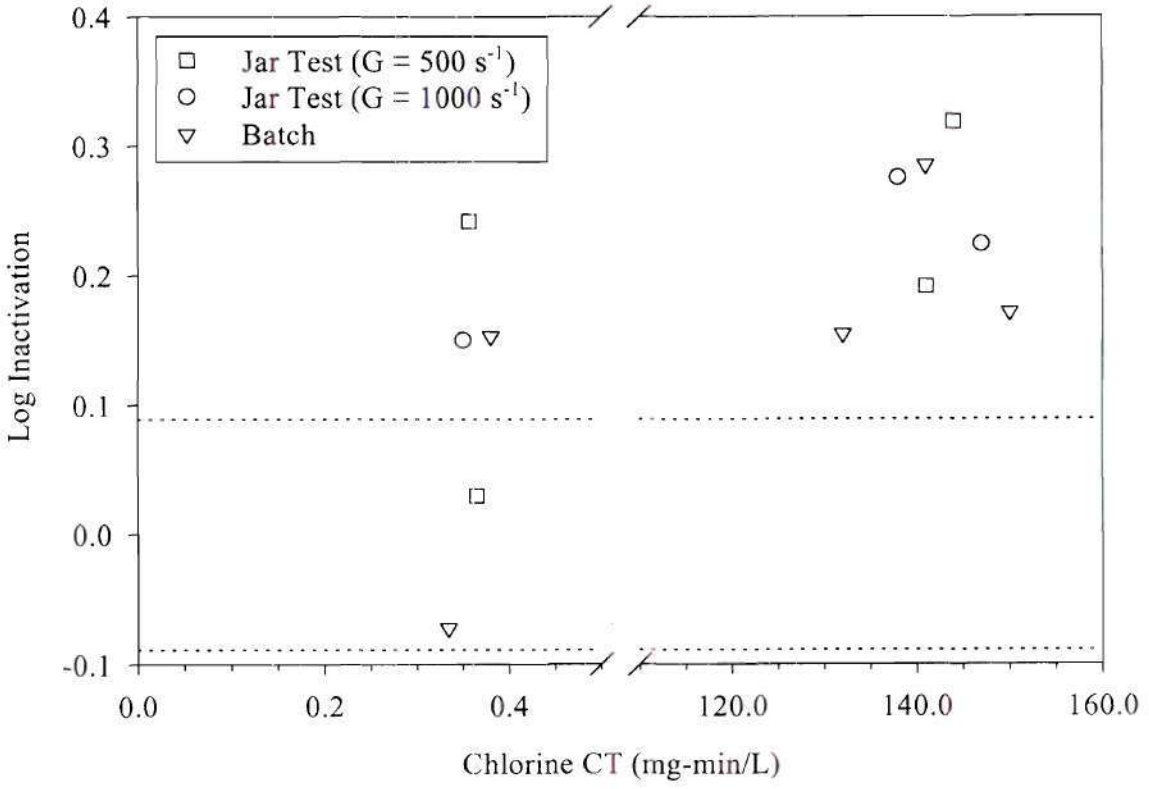

Figure 3.12 Inactivation of *Cryptosporidium parvum* in batch and jar test experiments with chlorine at pH 6 and 22 ± 2°C

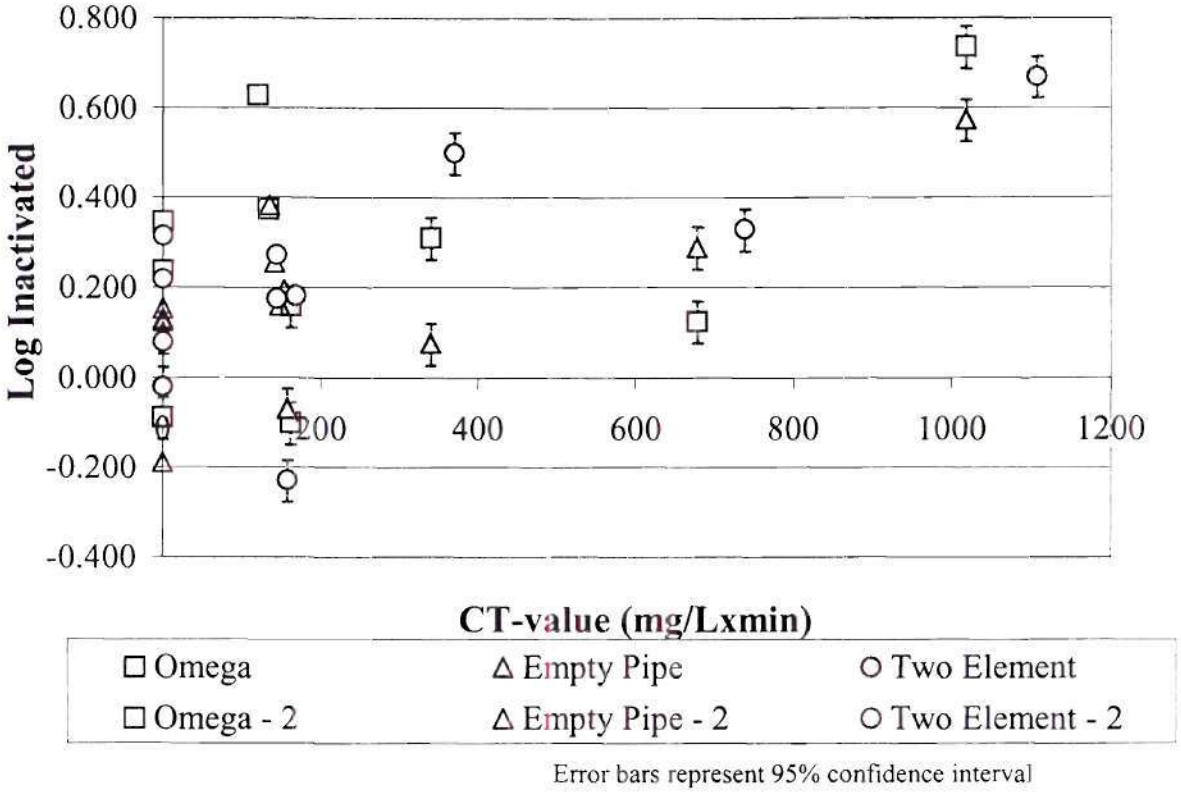

Figure 3.13 Log inactivated versus $C \times T$ value of two element helical mixer, Omega mixer, and empty pipe

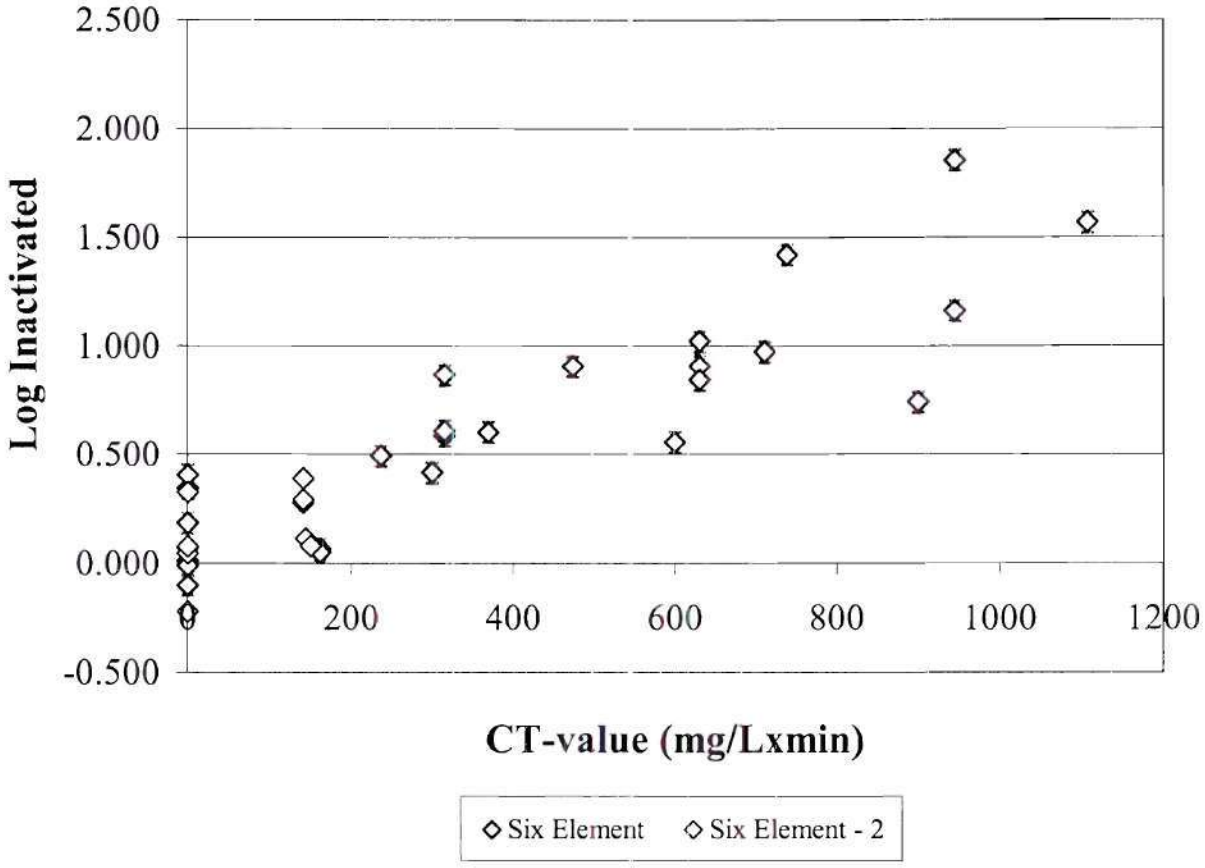

Figure 3.14 Six element static mixer inactivation data

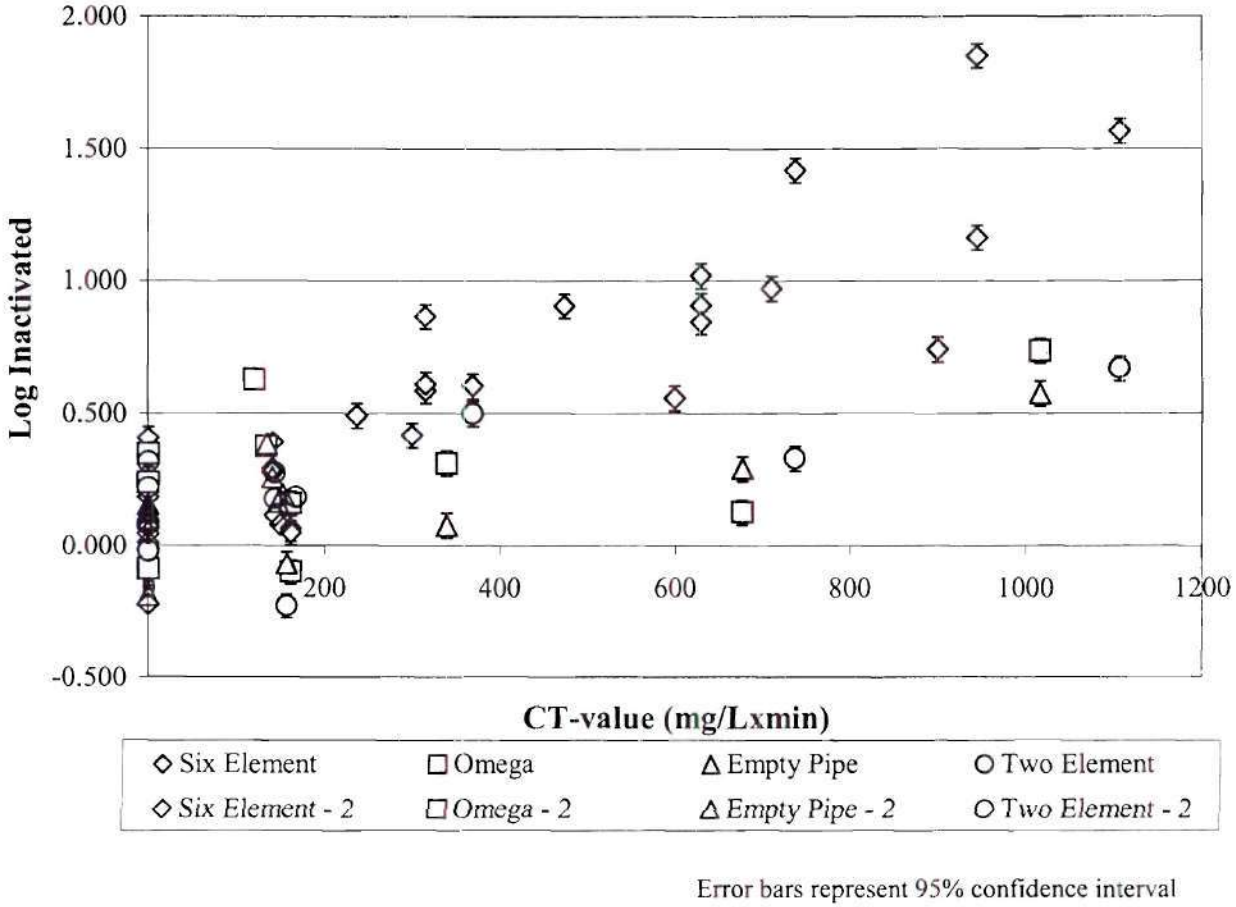

Figure 3.15 Comparison of inactivation data of six element helical mixer, two element helical mixer, Omega mixer and empty pipe

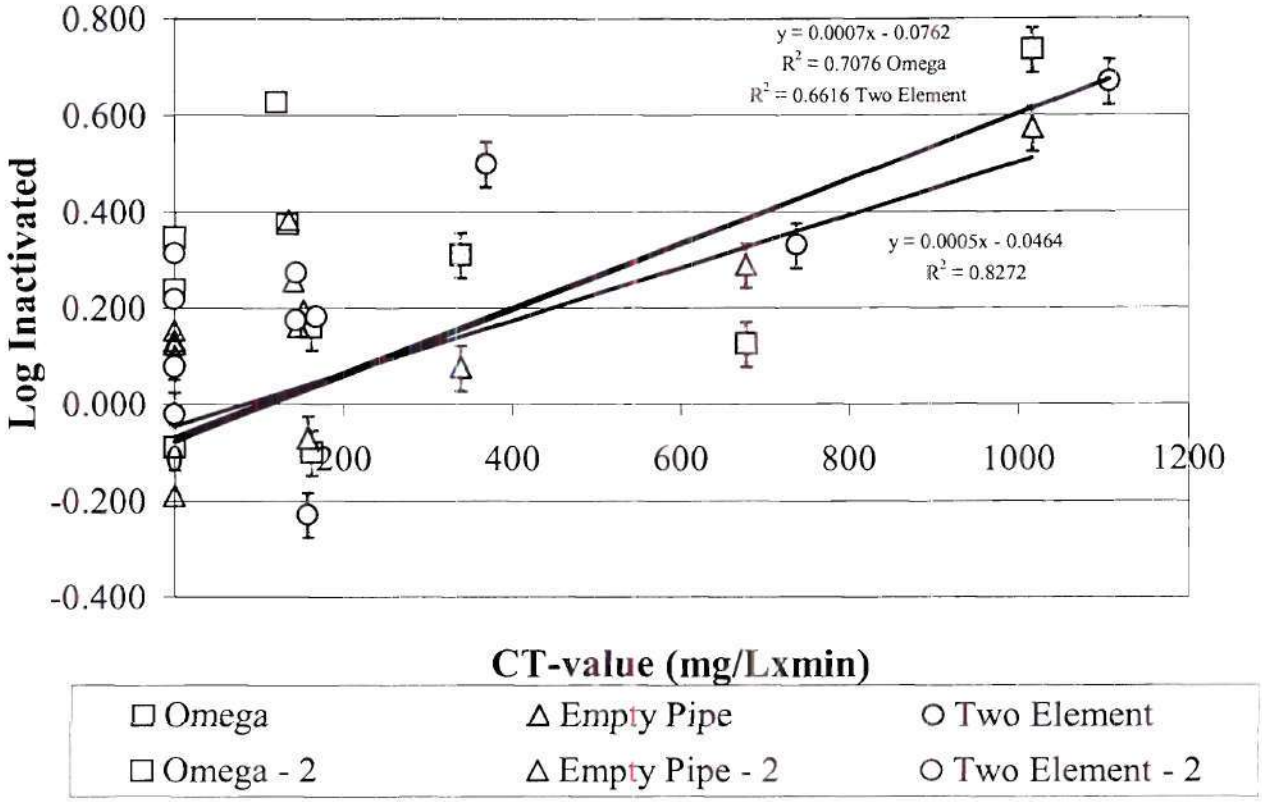

Error bars represent 95% confidence interval

Figure 3.16 Linear trendline of disinfection data for two element mixer, Omega mixer, and empty pipe

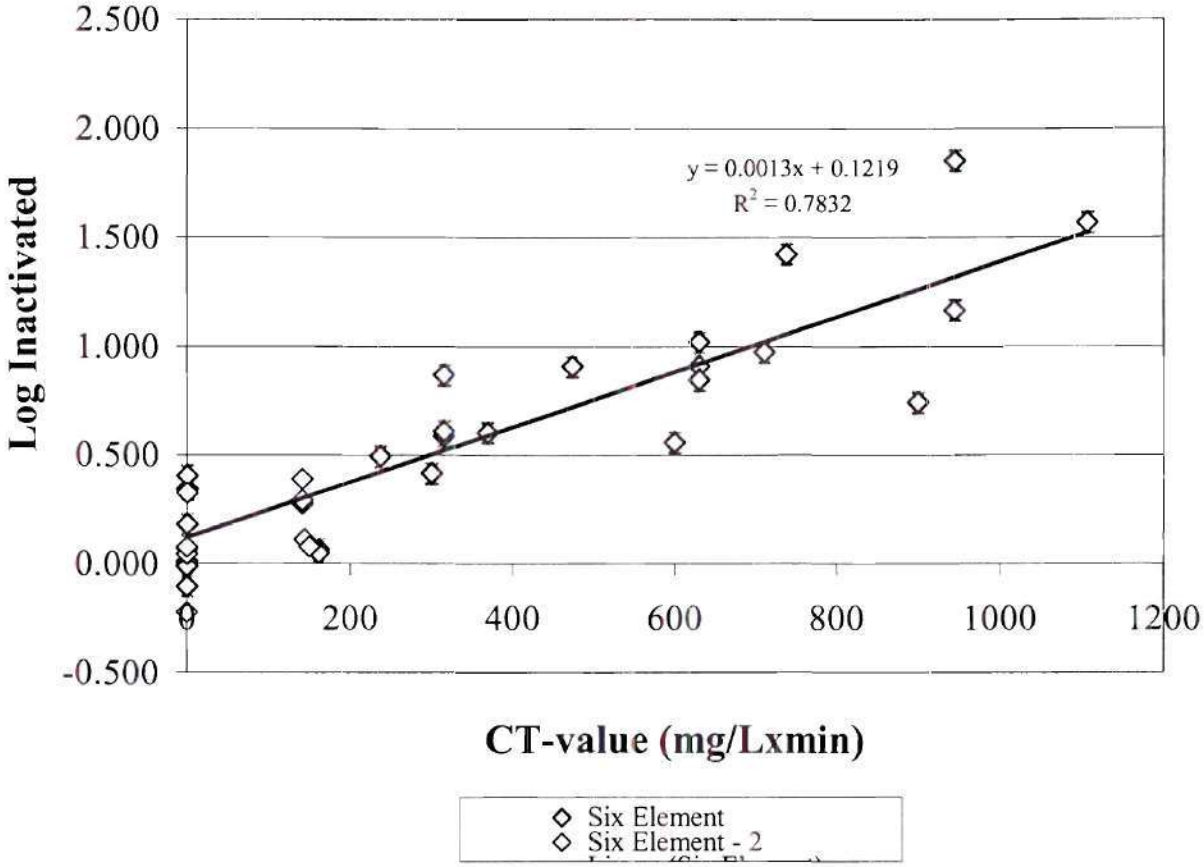

Figure 3.17 Linear trendline of six element mixer disinfection data

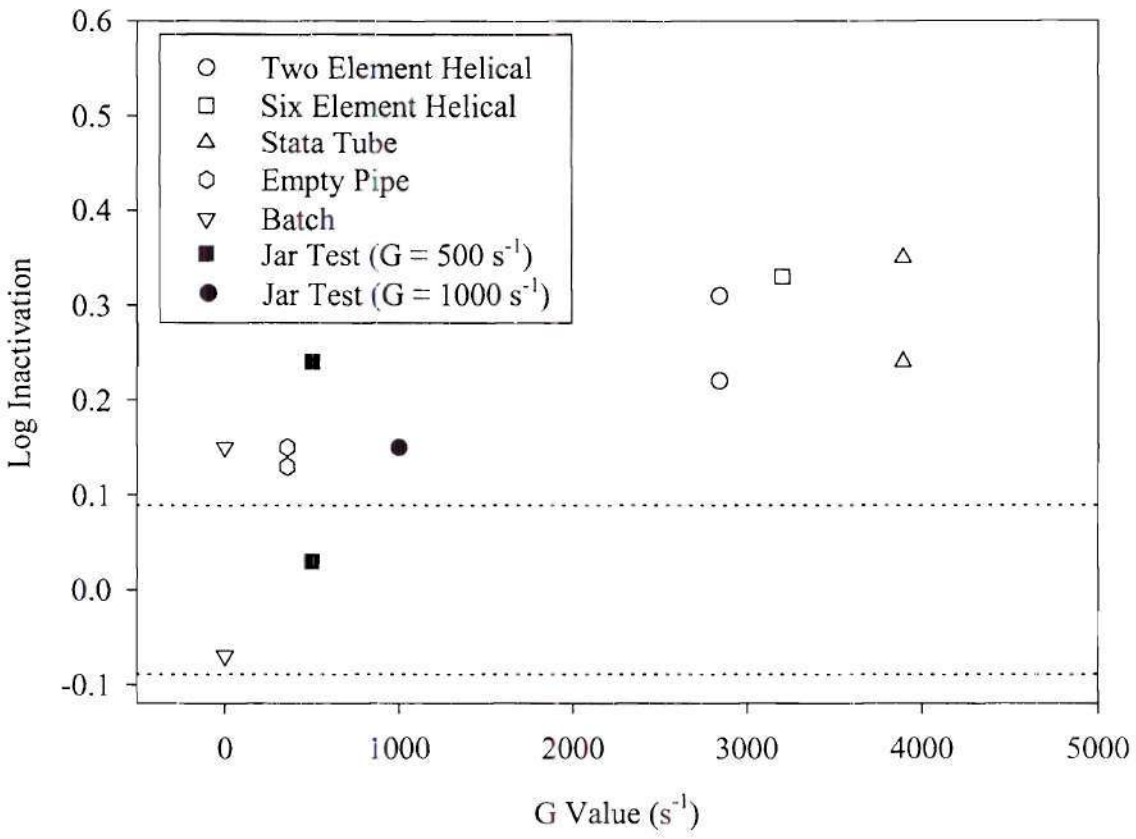

Figure 3.18 Inactivation of *Cryptosporidium parvum* oocysts as a function of *G* values at less than 3 seconds contact time with chlorine at pH 6 and 22 ± 2°C

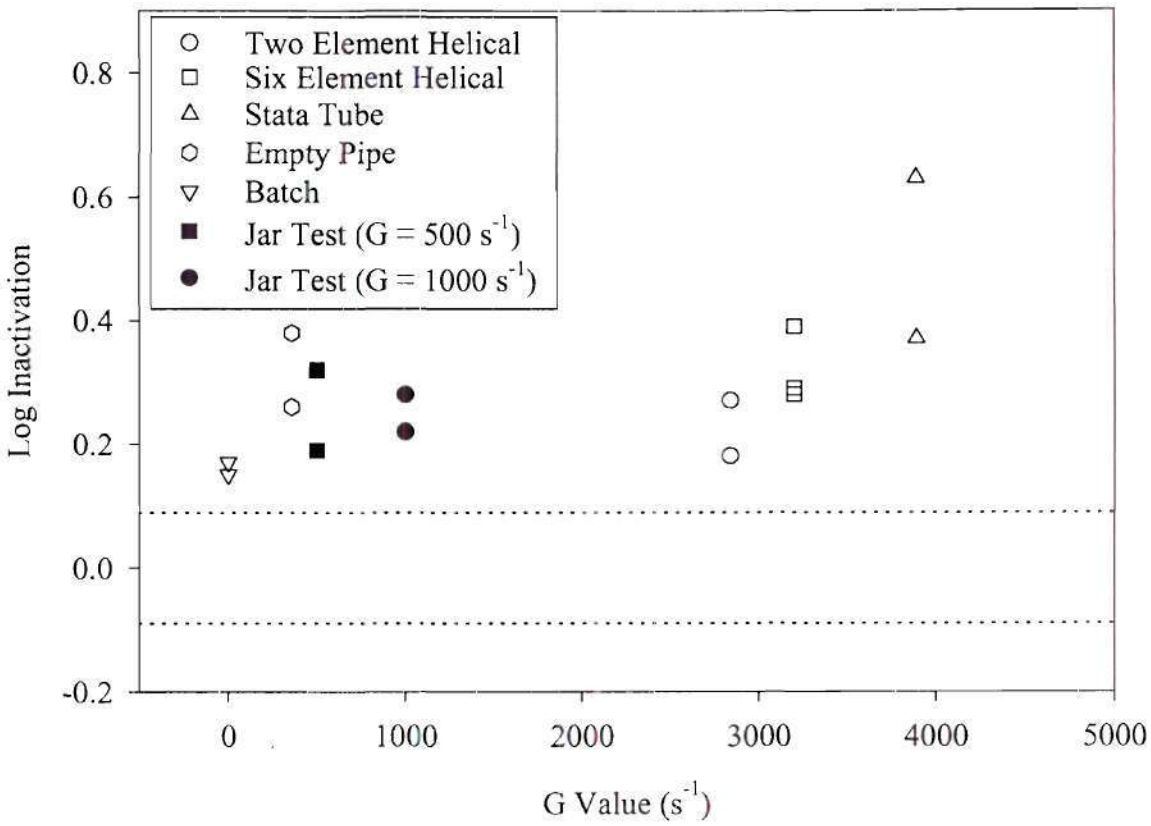

Figure 3.19 Inactivation of *Cryptosporidium parvum* oocysts as a function of *G*-value at 30 minute contact time with chlorine at pH 6 and 22 ± 2°C

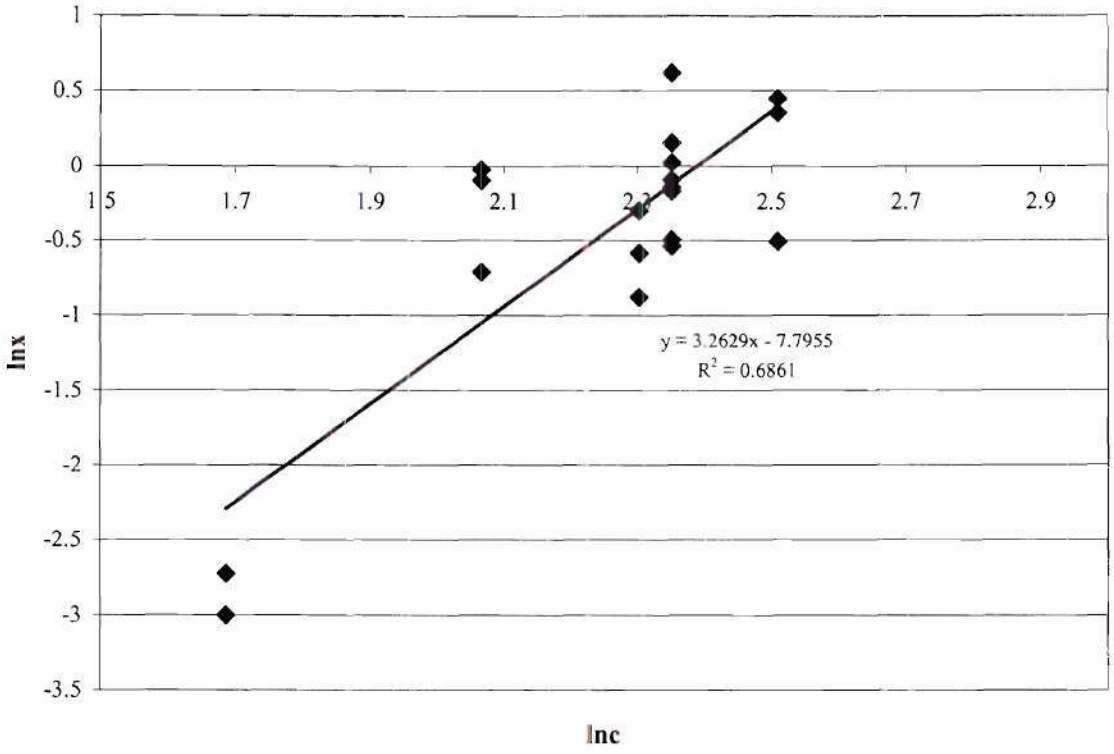

Figure 3.20 Hom model constant determination using the natural log of the log inactivated versus the natural log of the disinfectant concentration

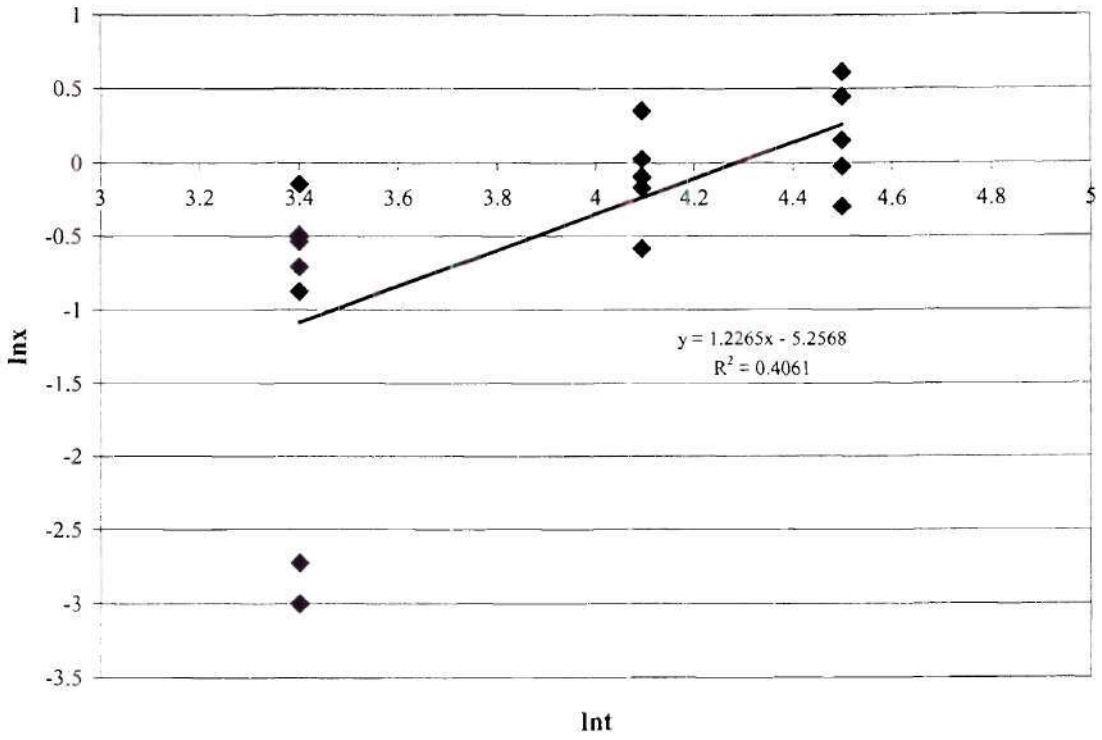

Figure 3.21 Hom model constant determination using the natural log of the log inactivation versus the natural log of the contact time

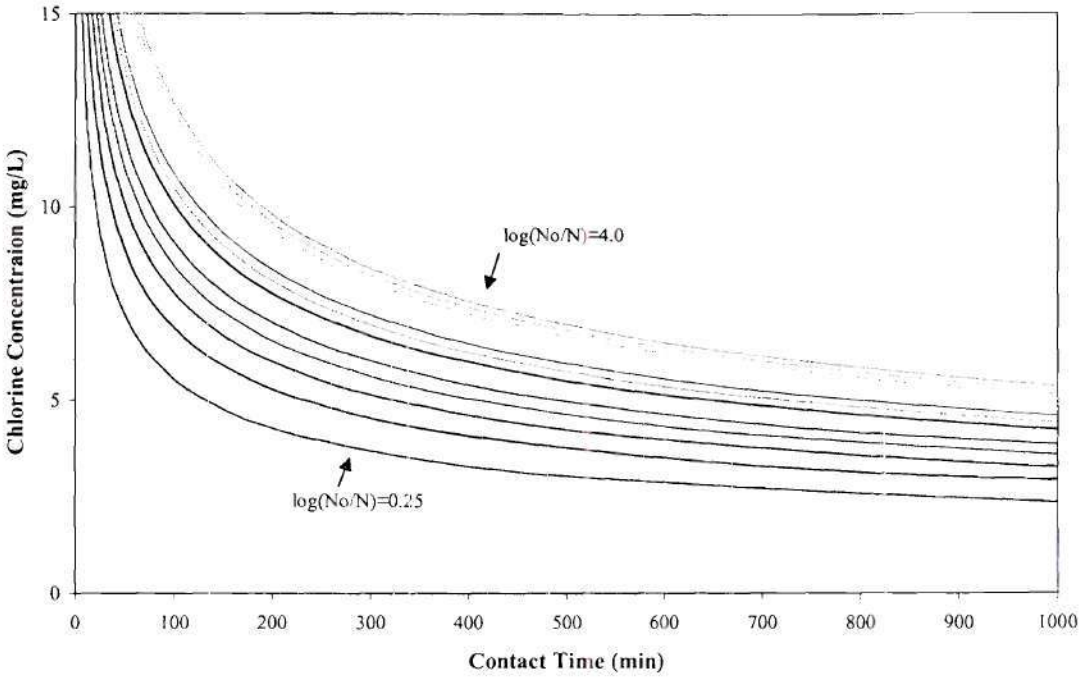

Figure 3.22 Hom model for six element helical mixer, 0.25 log inactivated to 4.0 log inactivated at 0.25 log increments

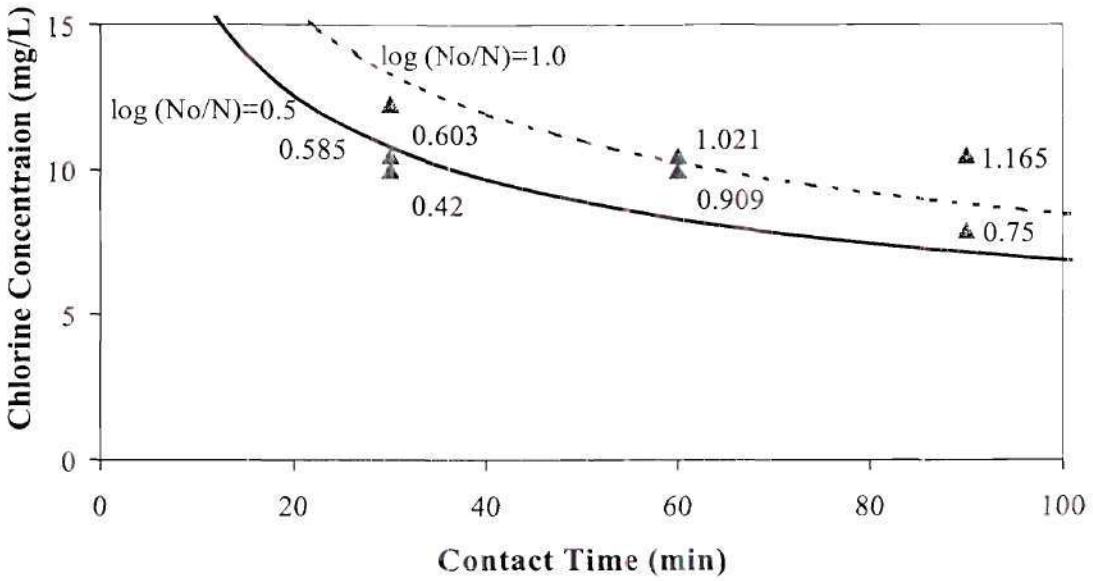

Figure 3.23 Hom model for six element helical mixer with experimental data points

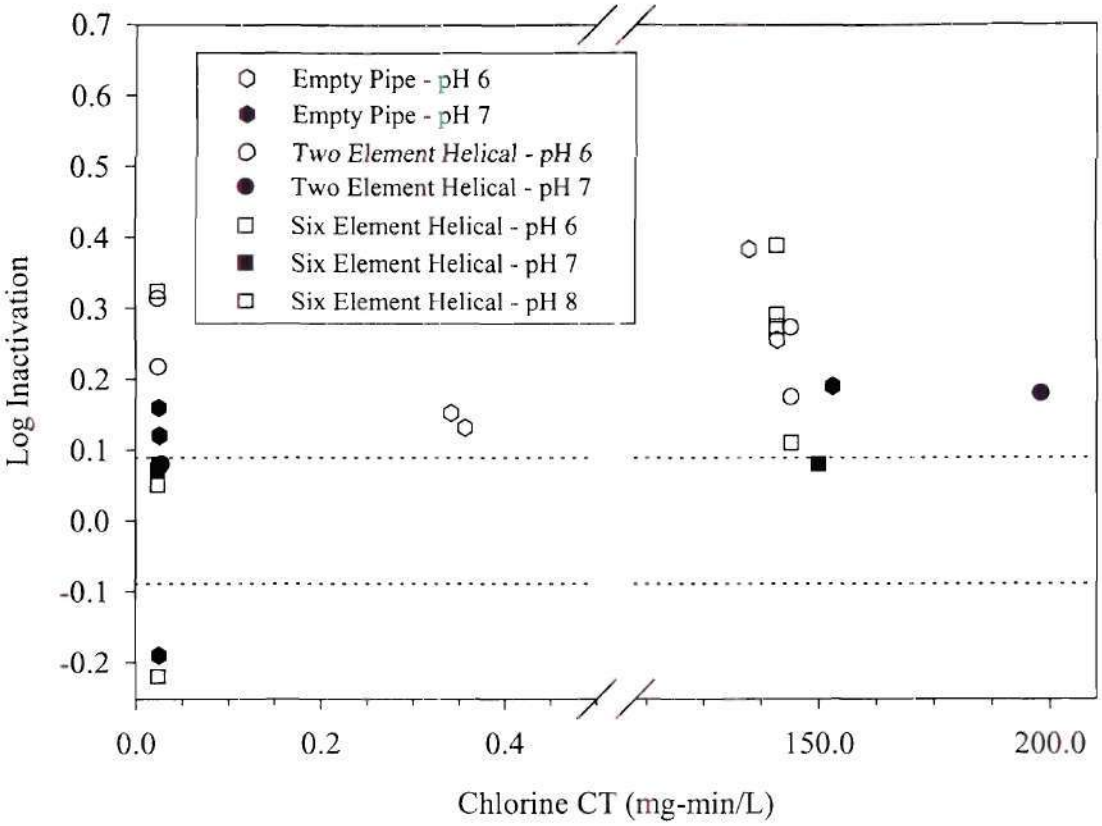

Figure 3.24 Inactivation of Cryptosporidium by chlorine at pH 6, 7 and 8

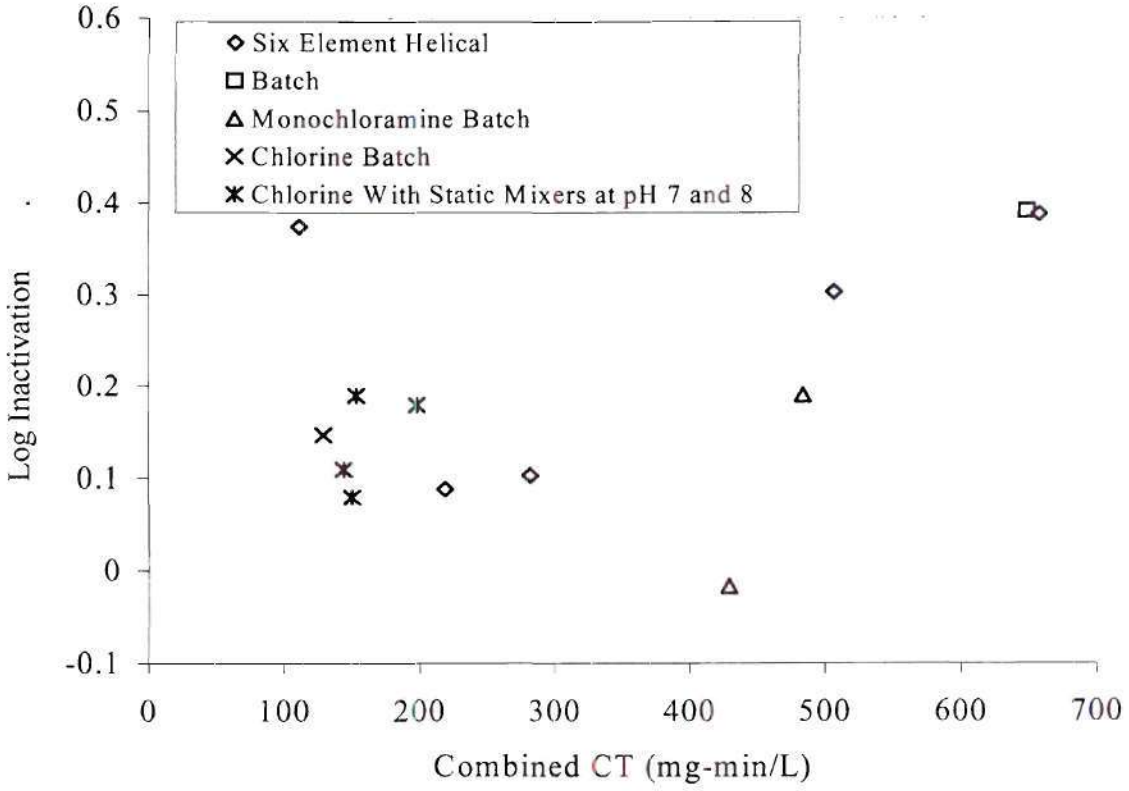

Figure 3.25 Inactivation of *Cryptosporidium* by monochloramine following 111-132 mg×min/L of chlorine at pH 8 and 20 ± 1°C

CHAPTER 4

A NEW PHYSICOCHEMICAL MODEL OF DISINFECTANT MIXING INCLUDING THE EFFECTS OF MIXING ON *CRYPTOSPORIDIUM PARVUM* OOCYSTS

INTRODUCTION

Before discussing the new physicochemical model of the disinfection process, a basic assumption has to be introduced. All the processes, including the chemical speciation, disinfectant distribution, pathogen distribution as well as the pathogen inactivation reaction, which occur during the disinfection process, will be affected by the hydraulic mixing process, but none of these processes affect, at least in a significant way, the hydraulic mixing. On the basis of this fundamental assumption, the model of the disinfection process can be divided into two distinct parts, the computation of the hydraulic velocity field and the computation of the disinfection efficiency using physicochemical models of disinfection. The former is addressed in the next chapter; the latter is addressed in this chapter.

The model development given here also implicitly assumes that the inactivation "reaction" occurs inside the pathogenic organism. This assumption is reasonable for *Giardia lamblia* cysts and *Cryptosporidium parvum* oocysts because both protozoa are in an inactive state in the environment. For bacterial organisms, this assumption may be invalid because the inactivation reaction may occur on the surface of the cell.

Traditional View of the Disinfection Process

Traditionally, the entire disinfection process is divided into three major steps, which are, sequentially, the chemical speciation of the disinfectants, the diffusion of the disinfecting agents to the surface of the pathogens (Morris 1970), and the inactivation "reaction" of the pathogens (Chang 1970). This description of the disinfection process is shown in Figure 4.1.

From this conventional point of view, it is believed that the chemical speciation process, that is, a thermodynamic process which determines the active disinfecting agent, and the inactivation "reaction" of the pathogens, i.e., a kinetic process which is probably the rate-limiting step in the entire disinfection process, are the key steps. The diffusion of the disinfectant, under the

complete-mixing assumption, is very fast so that it will not affect the overall disinfection efficiency.

Based on this idea, several disinfection kinetic models, such as Chick's Law, Chick–Watson Law, and Hom's alteration (Haas et al. 1996), have been developed. All of the above models have a similar form due to the similar assumption of the inactivation process of the pathogens, i.e., the survival of pathogens is approximately log-linear with respect to contact time or a certain power of the contact time.

New View of the Disinfection Process

Several studies have measured an improvement of disinfection efficiency for environments with intense mixing, that is, with intense solid and fluid applied forces (Geisser and Garver 1977, Longley 1978, and Parker and Smith 1993). Apparently in these studies the more intense mixing improved the disinfection efficiency, sometimes to a great extent. Based on the discussion presented above, a description of the disinfection process that can only explain mixing-induced improvements in disinfection efficiency is needed. The purpose of this chapter is to provide such a description through the development of a new mathematical model of the disinfection process.

The basic idea of this new description is to divide the entire process of disinfection into a series of steps, which may no longer be sequentially independent, but are interactive. The overall disinfection process is divided into five steps:

(1) chemical speciation of the disinfecting agents
(2) distribution of the disinfecting agents
(3) distribution of pathogenic organisms
(4) mass transfer through the surface of the disinfecting agents into the pathogens
(5) "inactivation reaction" taking place within the organism.

These steps are shown schematically in Figure 4.2.

DEVELOPMENT OF THE NEW DISINFECTION MODEL

The chemical speciation of disinfectants is a very fast thermodynamic process, which is assumed to have reached equilibrium. For simplicity, chlorine (Cl_2) is used as the disinfectant in the following model development; a similar analysis can be made for ozone (O_3). For chlorine, the speciation process involves two reactions:

$$Cl_2(aq) + H_2O \overset{K_1}{\rightleftharpoons} Cl^- + HOCl(aq) + H^+$$

and

$$HOCl(aq) \overset{K_2}{\rightleftharpoons} H^+ + OCl^-$$

The concentration of the most effective disinfectant species [HOCl] can be calculated by solving the following equations:

$$C_{Cl} = [Cl^-] + [HOCl] + [Cl_2(aq)] + [OCl^-]$$

$$K_1 = \frac{[Cl^-][HOCl][H^+]}{[Cl_2(aq)]}$$

and

$$K_2 = \frac{[OCl^-][H^+]}{[HOCl]}$$

where C_{Cl} = total concentration of chlorine species

$[Cl^-]$ = concentration of chloride ion

$[HOCl]$ = concentration of hypochlorous acid

$[Cl(aq)]$ = concentration of aqueous chlorine

$[OCl^-]$ = concentration of hypochlorite ion

$[H^+]$ = concentration of hydrogen ion

Fluid Transport of the Disinfectant and Pathogens

The transport of disinfectant within a reactor and ultimately to the surface of a pathogen is a typical mass transfer process. For any generic control volume, the change in the disinfectant concentration with time is calculated as follows:

$$\frac{\partial C_d}{\partial t} = -\nabla \bullet \mathbf{N}_d + R_d \tag{4.1}$$

where C_d = concentration of the disinfectant where $C_d = C_d(\mathbf{x}, t)$ (M L^{-3})

$\mathbf{x}$ = position vector (x, y, z) in Cartesian coordinates (L)

t = time (T)

∇ = del operator, which in Cartesian coordinates is $\left(\tilde{i}_x \frac{\partial}{\partial x} + \tilde{i}_y \frac{\partial}{\partial y} + \tilde{i}_z \frac{\partial}{\partial z}\right)$

$\mathbf{N}_d$ = mass flux of the disinfectant relative to a fixed coordinate system (M $L^{-2} T^{-1}$)

R_d = reaction rate of the disinfectant in the *inactivation* reaction (M $L^{-3} T^{-1}$)

The mass flux of the disinfectant $\mathbf{N}_d$ is calculated as

$$\mathbf{N}_d = \mathbf{J}_d + C_d \mathbf{U}$$

where $\mathbf{J}_d$ = mass flux of disinfectant relative to the mass average velocity ($M\ L^{-2}\ T^{-1}$)

$\mathbf{U}$ = fluid velocity vector (u, v, w) in Cartesian coordinates ($L\ T^{-1}$)

The transport of the each pathogen is more complicated than that of the disinfectant. Conceptually pathogen transport can be divided into two simultaneously occurring processes: (1) the transport of clumps of pathogens and (2) the growth and breakup of these pathogen clumps. In the present model, only the first step is considered. However, the second step is mentioned because, ultimately, it must also be included if the model is to accurately predict the effect of mixing on disinfection efficiency.

The transport of the pathogen clumps is a mass transfer process and is modeled in the same way as the transport of the disinfectant. To simplify the later analysis, the transport of concentration of pathogen clumps is written in terms of the number concentration of individual pathogens.

$$\frac{\partial C_p}{\partial t} = -\nabla \bullet \mathbf{N}_p + R_p \tag{4.2}$$

where C_p = number concentration of the pathogens where $C_p = C_p(\mathbf{x}, t)$ (L^{-3})

$\mathbf{N}_p$ = mass flux of the pathogen clumps relative to a fixed coordinate system ($L^{-2}T^{-1}$)

R_p = reaction rate of the pathogen clumps in the inactivation reaction ($L^{-3}\ T^{-1}$)

The mass flux of the pathogens $\mathbf{N}_p$ is calculated as

$$\mathbf{N}_p = \mathbf{J}_p + C_p \mathbf{U}$$

where $\mathbf{J}_p$ = mass flux of the pathogens relative to the average mass velocity ($L^{-2}\ T^{-1}$)

$\mathbf{U}$ = fluid velocity ($L\ T^{-1}$)

Referring to Figure 4.3, once the disinfectant reaches the surface of the pathogen clump it must penetrate through that surface before the *inactivation* reaction occurs. Here, the surface of the clump consists of three layers: (1) an outer boundary layer, (2) the clump wall, and (3) a layer within the clump. The transport of the disinfectant from the bulk fluid to an individual cyst located within a clump is an interfacial mass transfer problem. Problems of this type are typically solved in one of two ways: (1) if the relative time of transport through each layer is known, then only the slowest or rate-limiting step is used; or (2) the layers are combined and considered as a whole. Because no detailed information on the nature of the pathogen clumps is available, the latter, more empirical method is chosen. For any interface, the flux through the interface is

$$N_f = \frac{K_f \Delta C}{\delta} \tag{4.3}$$

where N_f = flux through the interface (M L^{-2} T^{-1})

K_f = interfacial mass transfer coefficient (L^2 T^{-1})

ΔC = concentration difference across the interface (M L^{-3})

δ = thickness of the interface (L)

Writing Equation 4.3 for the disinfectant gives

$$N_{f,d} = \frac{K_{f,d}\left(C_{\text{bulk}} - C_{\text{inner}}\right)}{\delta_{\text{outer}} + \delta_{\text{surface}} + \delta_{\text{inner}}} = \frac{K_{f,d}\left(C_d - C_{\text{inner}}\right)}{\delta_{\text{outer}} + \delta_{\text{surface}} + \delta_{\text{inner}}} \tag{4.4}$$

where $N_{f,d}$ = flux of the disinfectant through the interface (M L^{-2} T^{-1})

$K_{f,d}$ = interfacial mass transfer coefficient of the disinfectant(L^2 T^{-1})

C_{bulk} = concentration of the disinfectant in the bulk fluid (M L^{-3})

C_{inner} = concentration of the disinfectant on the inside of the pathogen clump (M L^{-3})

δ = thickness of the outer layer, surface layer, or inner layer (L)

The term C_{inner} is a constant determined by the characteristics of the inactivation reaction that occurs within the pathogen clump. This inactivation reaction is the last step in the new conceptual model of the disinfection process. The inactivation reaction is assumed to be instantaneous, and thus, the rate of the reaction is governed by the rate at which reactants are provided to the inside of the clump. This rate is written as

$$R_r = K_r N_{f,d} A_f \tag{4.5}$$

where R_r = rate of the inactivation reaction (M L^{-3} T^{-1})

K_r = dimensionless rate constant for the inactivation reaction

A_f = surface area of the pathogen clumps (L^2)

The surface area of the pathogen clumps, A_f is derived as follows. Suppose the mass concentration of *Cryptosporidium* is C_p^m, which is the mass of *Cryptosporidium* per unit volume and suppose that the average diameter of the *Cryptosporidium* "clumps" is η. Thus, C_p^c, the number of the *Cryptosporidium* "clumps" per unit volume, is as follows:

$$C_p^c = \frac{C_p^m}{\frac{\pi}{6}\rho_p \eta^3} = \frac{6C_p^m}{\pi \rho_p \eta^3}$$

where ρ_p = density of the *Cryptosporidium* oocyst (M L^{-3})

The specific surface area of *Cryptosporidium* clumps becomes

$$A_f = C_p^c \pi \eta^2 = \frac{6C_p^m}{\pi \rho_p \eta^3} \pi \eta^2 = \frac{6C_p^m}{\rho_p \eta}$$

Since number concentration of individual *Cryptosporidium*, that is, C_p, not *Cryptosporidium* clumps, is usually used in experiments, it is convenient to use C_p instead of using C_p^m. Assuming that the mass of an individual *Cryptosporidium* oocyst is m_{crypto}, a simple relationship exists between these two concentrations:

$$C_p^m = m_{crypto} C_p$$

The specific surface area of the clumps is

$$A_f = \frac{6C_p^m}{\rho_p \eta} = \frac{6m_{crypto} C_p}{\rho_p \eta} \tag{4.6}$$

Combing Equations 4.4, 4.5, and 4.6, the following expression for the rate of the inactivation reaction is obtained.

$$R_r = \frac{K_r K_f (C_d - C_{inner})}{\delta_{outer} + \delta_{inner} + \delta_{surface}} A_f = \frac{K_r K_f (C_d - C_{inner})}{\delta_{outer} + \delta_{inner} + \delta_{surface}} \left(\frac{6m_{crypto} C_p}{\rho_p \eta} \right) = K_5 (C_d - C_{inner}) C_p$$

where K_5 = a comprehensive coefficient that characterizes the overall five-phase process model

This hypothetical inactivation reaction can be exploited further to provide a stochiometric relationship between rate of decrease of the disinfectant concentration and the concentration of the pathogens. Such a reaction can be defined as

$$D[\text{disinfectant}] + P[\text{pathogen}] \rightleftharpoons I[\text{inactivated pathogen}] + B[\text{by-products}]$$

where D, P, I, B = are stoichiometric coefficients

Thus, the overall reaction rate is related to the rate of disappearance of the disinfectant and pathogens as

$$R_r = -\frac{R_d}{D} = -\frac{R_p}{P}$$

Finally, this provides an expression for both of the reaction rates that appear in the original transport equations (Equation 4.1 and 4.2).

That is,

$$R_d = -K_5 D\left(C_d - C_{inner}\right)C_p \quad \text{and} \quad R_p = -K_5 P\left(C_d - C_{inner}\right)C_p \tag{4.7}$$

Summary of the Model Derivation

With these expressions for the reaction rate of the hypothetical inactivation reaction, the initial derivation of the new disinfection process is complete. The new model is composed of essentially four equations (or two pairs of equations) that describe the mass transfer of the disinfectant and the pathogen (Equations 4.1 to 4.4 and 4.7). It is important to note that these equations are general and are not limited to a particular reactor geometry, a particular disinfectant, or a particular pathogen. Conceptually, however, the model was developed for pathogens which tend to clump together and whose clumping is significant for the disinfection process as has been theorized to be the case with *Cryptosporidium*. For this reason, the model can easily be extended to include the formation and destruction of these clumps by including aggregation and breakup terms into the expressions for the reaction rates of the pathogens. In this chapter, however, the existing model will be applied to two ideal reactors: the completely mixed batch reactor (that is, an idealized backmixer) and a plug-flow dispersion reactor (that is, an idealized static mixer).

DISINFECTION OF *CRYPTOSPORIDIUM* IN BATCH REACTOR

Development of a Batch Reactor Model

For a completely mixed batch reactor, the mass flux for both the distribution of disinfectants and pathogens can be neglected. Thus, transport equations in Equation 4.1 and 4.3 simplify to kinetic expressions

$$\frac{dC_d}{dt} = -K_5 D\left(C_d - C_{inner}\right)C_p$$

and

$$\frac{dC_p}{dt} = -K_5 P\left(C_d - C_{inner}\right)C_p$$

An analytical solution to this system of equations is

$$C_p(t) = \frac{\left(PC_d^0 - PC_{inner} - DC_p^0\right)C_p^0}{P\left(C_d^0 - C_{inner}\right)\exp\left[\left(PC_d^0 - PC_{inner} - DC_p^0\right)K_5 t\right] - DC_p^0} \tag{4.8}$$

where C_p^0 = the initial number concentration of pathogens

C_d^0 = the initial disinfectant concentration

To make the solution easier to compare with existing literature data, Equation 4.8 is transformed to

$$C_p(t) = \frac{\left(C_d^0 - C_{inner} - \alpha C_p^0\right)C_p^0}{\left(C_d^0 - C_{inner}\right)\exp\left[\left(C_d^0 - C_{inner} - \alpha C_p^0\right)K_p t\right] - \alpha C_p^0}$$

where $\alpha = D/P$

$K_p = K_S P$

To apply linear regression analysis on literature data based on this model, a further transformation of the solution is needed. Let

$$y = \frac{C_p(t)}{C_p^0}$$

which yields

$$Y = \ln\left[\frac{1}{y} + \frac{\alpha C_p^0}{C_d^0 - C_{inner}}\left(\frac{y-1}{y}\right)\right]\left[C_d^0 - C_{inner} - DAPC_p^0\right]^{-1}$$

where $Y = K_p t$

Using linear regression, by adjusting C_{inner} and α, the term K_p can be determined from the slope. The adjustment of these two parameters assumes that there is a linear relationship between Y and t and that the regression line goes through the origin.

Initial Validation of Model for Batch Reactor

Chlorine as Disinfectants

In this section, all of the data is derived from Gyürék, Finch, and Belosevic (1997), unless otherwise noted. By adjusting C_{inner} (0.85 mg/L) and α (3×10^{-7} mg), K_p (0.0013 L/mg min) can be determined from the slope of the regression line. These results are shown in Figure 4.4. Figure 4.5, compares the log removal obtained from the experiments (Gyürék, Finch, and Belosevic 1997) with the estimated log removal obtained from the new model for a completely mixed batch reactor. It should be noted that all the parameters in the new model are derived from

analysis of the same data set (Gyürék, Finch, and Belosevic 1997), therefore, the previous comparisons serve as a check of the consistency of the model but not of its predictive capability.

Ozone as Disinfectant

To test the generality of the new model the same analysis can be applied for ozone as the disinfectant. All of the data used in this section is from Ransome, Whitmore, and Carrington (1993) unless otherwise noted. By adjusting the C_{inner} (0.34 mg/L) and α (3×10^{-7} mg), K_p (0.3991 L/mg min) is obtained as shown in Figure 4.6. In Figure 4.7, the log removals obtained from the experiments of Ransome, Whitmore, and Carrington (1993) are compared with the log removals predicted by the new model for a completely mixed batch reactor. Again, the comparison shown in Figure 4.7 only tests the consistency of the model. To check the predictive ability of the model, the model predictions are compared to the experimental data of Gyürék (1997) with model constants obtained from the experiments of Ransome, Whitmore, and Carrington (1993). This comparison is shown in Figure 4.8, and the comparison indicates that the model successfully reproduces the measured log removals.

Comparing the New Model to Other Models of Disinfection

Chlorine as Disinfectant

The new model of the disinfection process is also compared to the IgH model for different experimental data sets. Table 4.1 shows a comparison between these two models based on data from Gyürék, Finch, and Belosevic (1997); whereas, Table 4.2 shows a comparison based on data from Ransome, Whitmore, and Carrington (1993).

All the parameters for the new model are obtained from the analysis of data from Gyürék, Finch, and Belosevic (1997). All the parameters for the IgH model are also obtained from Gyürék, Finch, and Belosevic (1997). The average difference of log removal between the experimental data and the model estimate are 0.65 and 0.57, for the IgH model (Gyürék, Finch, and Belosevic 1997) and the new model, respectively, indicating that these two models are comparable.

Table 4.1

Comparison of the new model with the IgH model

Time (min.)	Concentration (oocysts/mL)	Applied chlorine (mg/L)	Log_{10} removal		
			Experiment	New model	IgH Model
60	2.20×10^4	11.6	0.6	0.36	0.25
60	2.00×10^5	13.9	0.1	0.44	0.30
60	2.00×10^5	16	0	0.51	0.33
120	2.00×10^5	73.3	3	4.91	1.57
160	2.00×10^5	14.2	1	1.21	0.48
160	2.00×10^5	16.9	0	1.45	0.56
240	2.20×10^4	3.5	0.6	0.36	0.19
240	2.00×10^5	10.9	0.9	1.36	0.47
240	2.00×10^5	11	0.6	1.38	0.47
240	2.00×10^4	14	1.8	1.78	0.57
245	2.00×10^5	3.9	0.7	0.42	0.21
1032	1.58×10^4	1.73	0.5	0.52	0.18

The comparison of the predictions from both the new model and the IgH model shows that neither model is very good in predicting the experimental results of Ransome, Whitmore, and Carrington (1993). The reason for this incompatibility is probably because of the different experimental conditions for these two data sets and the errors intrinsic to current methods used to measure inactivation of *Cryptosporidium*. In Ransome, Whitmore, and Carrington (1993), a much wider range of initial chlorine concentrations and contact times were used, which might also give the data set a larger variation. Conversely, Gyürék, Finch, and Belosevic (1997) used a narrower range of both variables, which can be expected to give more consistent results.

Table 4.2

Comparison of the new model with the data from Ransome, Whitmore, and Carrington (1993)

Initial chlorine concentration (mg/L)	Contact time (min.)	Log_{10} removal		
		Experiment	New model	IgH model
0.099	60	-0.0000652	-0.02	0.00573
0.98	60	0.03	0.00	0.04
0.062	300	-0.02	-0.12	0.01
0.067	300	0.00	-0.12	0.01
0.995	300	0.02	0.02	0.07
0.054	1440	-0.02	-0.43	0.01
0.123	1440	-0.01	-0.40	0.02
0.95	1440	-0.06	0.07	0.12
0.981	1440	0.02	0.09	0.13
1.15	1440	-0.14	0.20	0.14
928	1440	0.56	—	30.85
968	1440	0.83	—	31.91
1557	1440	0.38	—	46.67
1620	1440	0.30	—	48.17
5118	1440	0.92	—	120.91

Table 4.3

Comparison of the new model to the Chick–Watson model

Initial ozone concentration (mg/L)	Contact time (min.)	Log_{10} removal		
		Experiment	New model	Chick–Watson
1.84	5	0.60	1.13	1.06
1.38	10	1.48	1.42	1.54
1.75	10	1.38	2.02	1.70
0.7	15	1.20	0.55	1.44
0.83	15	1.14	0.81	1.55
1.1	15	1.33	1.40	1.75
1	15	1.24	1.17	1.68
1.52	15	1.52	2.41	2.02
1.67	15	1.85	2.78	2.10
0.77	30	1.19	1.12	1.92
0.83	30	1.11	1.36	1.98

Ozone as Disinfectant

Predictions with the new model can also be compared to those made with the Chick–Watson model for ozone as a disinfectant. Table 4.3 shows a comparison between these two models based on data from Ransome, Whitmore, and Carrington (1993). Table 4.4 shows a comparison based on data from Finch et al. (1993). In Table 4.3, the average difference of log removal between the experimental data and the model estimate are 0.42 and 0.41, for Chick–Watson model and the new model, respectively, which shows that these two models are comparable. Also in Table 4.4, the average difference of log removal between the experimental data and the model estimate are 1.22 and 1.06, for the Chick–Watson model and the new model, respectively, which again shows that the two models are comparable.

Table 4.4

Comparison of the new model with the Chick–Watson model

Contact time	Applied ozone dose	Log_{10} removal		
(min.)	(mg/L)	Experiment	New model	Chick–Watson
5	1.6	2.5	0.88	0.99
5	0.7	2.6	0.08	0.70
5	2.6	2.4	1.73	1.22
5	1.8	2.1	1.05	1.05
5	2.1	0.8	1.30	1.12
5	2.8	2.5	1.90	1.26
5	2.4	3.7	1.56	1.18
5	1.4	1.2	0.71	0.94
5	0.8	1.9	0.19	0.74
10	2.9	2.5	3.94	2.12
10	1.6	1.5	1.71	1.64
10	1.7	3.6	1.88	1.68
10	1.7	2.5	1.88	1.68
10	2.6	4.2	3.42	2.02
10	1.6	3.5	1.71	1.64
15	2.4	4.7	4.67	2.45
15	1.4	1.9	2.04	1.95

Development of a Plug-Flow Dispersion Reactor Model

In contrast to the completely mixed batch reactor, the mass flux term in the distribution of the disinfectants and the pathogens cannot be neglected for the plug-flow dispersion reactor. Thus for the plug-flow reactor, the transport equations (Equations 4.1 and 4.2) become

$$\frac{\partial C_d}{\partial t} = \varepsilon_d \frac{\partial^2 C_d}{\partial x^2} - v\frac{\partial C_d}{\partial x} - K_S D\left(C_d - C_{inner}\right)C_p = 0 \tag{4.9}$$

and

$$\frac{\partial C_p}{\partial t} = \varepsilon_p \frac{\partial^2 C_p}{\partial x^2} - v\frac{\partial C_p}{\partial x} - K_S P\left(C_p - C_{inner}\right)C_p = 0 \tag{4.10}$$

where ε_d = the apparent eddy diffusivity of the disinfectant ($L^2\,T^{-1}$)

ε_p = the apparent eddy diffusivity of the pathogens ($L^2\,T^{-1}$)

The procedure that was followed for the completely mixed batch reactor can be followed again for the plug-flow dispersion reactor, namely, the reactor is assumed to be steady state and the same substitutions made (α and k_p). Moreover, Equations 4.9 and 4.10 can be non-dimensionalized to give the following two ordinary differential equations.

$$\frac{\mathrm{d}^2 E_d}{\mathrm{d}\theta^2} - \mathrm{Pe}_d \frac{dE_d}{d\theta} - k_d\left(E_d - E_{inner}\right)E_p = 0 \tag{4.11}$$

and

$$\frac{\mathrm{d}^2 E_p}{\mathrm{d}\theta^2} - \mathrm{Pe}_p \frac{dE_p}{d\theta} - k_p\left(E_d - E_{inner}\right)E_p = 0 \tag{4.12}$$

where θ = dimensionless length along the plug-flow reactor (x/L)

E_d = dimensionless concentration of disinfectant $\left(C_d/C_d^0\right)$

E_p = dimensionless concentration of pathogens $\left(C_p/C_p^0\right)$

E_{inner} = dimensionless inner concentration of disinfectant $\left(C_{inner}/C_d^0\right)$

Pe_d = Peclet number for the disinfectant (vL/ε_d)

Pe_p = Peclet number for the pathogens $\left(vL/\varepsilon_p\right)$

k_d = disinfectant constant $\left(K_p DAPL^2 C_p^0/\varepsilon_d\right)$

k_p = pathogen constant $\left(K_p L^2 C_d^0/\varepsilon_p\right)$

L = length of the plug-flow dispersion reactor

Note that diffusivities calculated using the Stokes–Einstein equation are not applicable in these reactors because of the turbulence and size of the Kolmogorov microscale (and even less applicable in static mixers), thus, the use of apparent eddy diffusivities in the model development for a plug flow dispersion reactor. Also, since it is difficult to calculate the apparent eddy diffusivity, an approximation is used based on the experimental data from the static mixer configurations, which is given in Chapter 3. No analytical solution is available for Equations 4.11 and 4.12; therefore, a numerical method from the software package MATLAB (Mathworks, Natick, Mass.) is used to solve this system of equations.

Initial Validation of Models by Comparison with Experimental Data

A comparison was made between experimental data of disinfection of *Cryptosporidium* in static mixers from Chapter 3 with the estimated log removal calculated from the new disinfection model. An approximate eddy diffusivity was used in this comparison. From Figure 4.9, the new model appears to be compatible with experimental data for low detention times. However for longer detention times, the disinfection efficiency calculated from the new model is lower, than the experimental data.

SENSITIVITY ANALYSIS

Based on the conceptual development of the new disinfection model, one of the most important parameters that influences the disinfection efficiency is the size of the *Cryptosporidium* clumps. The specific surface area of the *Cryptosporidium* clumps is the major part of the driving force for the inactivation reaction. In general, intense turbulence would be expected to breakup clumps thus reducing the effective diameter and consequently increasing the effective surface area. A sensitivity analysis on the average clump diameter can be performed to further investigate the new disinfection model.

An inverse relationship exists between the average clump diameter η and the model parameter K_p. This relationship is shown by rearranging Equations 4.5 and 4.9 to yield

$$K_p = K_5 P = \frac{6 m_{crypto} K_r K_f}{\rho_p \eta \left(\delta_{outer} + \delta_{inner} + \delta_{surface}\right)} P, \quad \text{i.e.,} \quad K_p \propto \frac{1}{\eta} \tag{4.13}$$

Thus, a sensitivity analysis on K_p is also a sensitivity analysis on the diameter of the *Cryptosporidium* clumps. A study of the breakup mechanism for *Cryptosporidium* clumps is beyond the scope of this chapter, a sensitivity analysis is done directly on K_p, which is shown in Figures 4.10 to 4.12 for the completely mixed reactor and for the plug-flow dispersion reactor. However, it should be noted that the new disinfection model can easily be extended to include the aggregation and breakup of *Cryptosporidium* clumps by adding aggregation and breakup terms to the reaction terms in Equation 4.3

The sensitivity analysis for the completely mixed batch reactor with both chlorine and ozone as disinfectants is shown Figures 4.10 and 4.11. Figures 4.10 and 4.11 clearly show that an increase of K_p yields a corresponding increase in disinfection efficiency. The figures also show longer contact times have a greater effect on K_p resulting in improvement of disinfection efficiency. This translates to the concept that the smaller the size of the clumps η (see Equation 4.13), the better the disinfection efficiency. Ozone also shows a better disinfecting ability over chlorine, which is expected. The sensitivity analysis of K_p for the plug-flow dispersion re-

actor is shown in Figure 4.12. An increase in disinfection efficiency results from an increase of K_p, but the increase is not as significant as it was for the completely mixed batch reactor. The estimated log removals seem to be reaching an asymptotic value. These predictions need to be confirmed with a well designed experimental program.

SUMMARY AND CONCLUSION

A new physicochemical model of the disinfection process was developed from a description of the inactivation of *Cryptosporidium* oocysts by a disinfectant based on five separate but interrelated steps or phases: (1) the chemical speciation of the disinfectant; (2) the distribution of disinfectants; (3) the distribution of pathogens; (4) the mass transfer of the disinfectant through the surface of the pathogen; and (5) the inactivation within the pathogenic organism. The new model is applied to two ideal reactors: a completely mixed batch reactor, which is an idealization of the traditional backmixer, and a plug-flow dispersion reactor, which is an idealization of static mixers. Parameters for the new model were determined by fitting the model using the existing experimental data for both types of reactors and for two disinfectants—chlorine and ozone. Predictions from the new model are consistent with the available experiments and with the existing Chick–Watson and Incomplete Gamma Hom (IgH) model. Using the new model, disinfection efficiency was predicted for a different set of experiments for the completely mixed batch reactor and for the inactivation data for *Cryptosporidium* in static mixers described in Chapter 3. The results of these comparison are encouraging.

At present, the development of the new disinfection model is still in its early stages. The usefulness of the new model is that it provides a conceptual basis, which can be coupled with a computational fluid dynamics model to predict disinfection efficiency in a real-world disinfection reactor. Moreover, the new model can easily be extended to incorporate the formation and breakup of pathogen clumps—thus, allowing the effect of mixing on the inactivation of *Cryptosporidium* and other difficult-to-disinfect pathogens to be investigated using a fundamentals-based model.

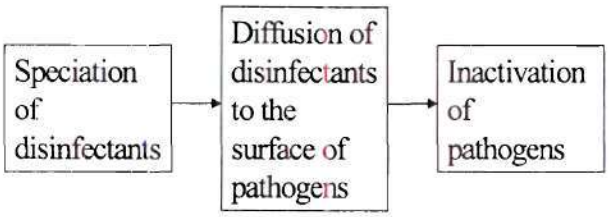

Figure 4.1 Traditional model of the disinfection process

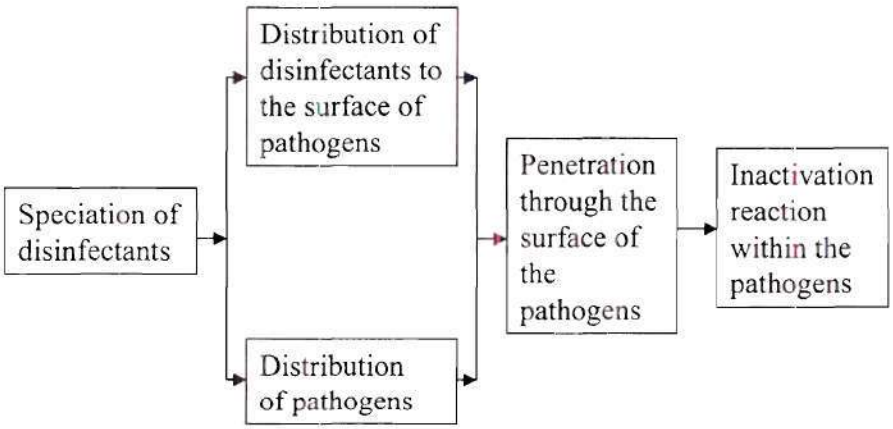

Figure 4.2 New model of the disinfection process

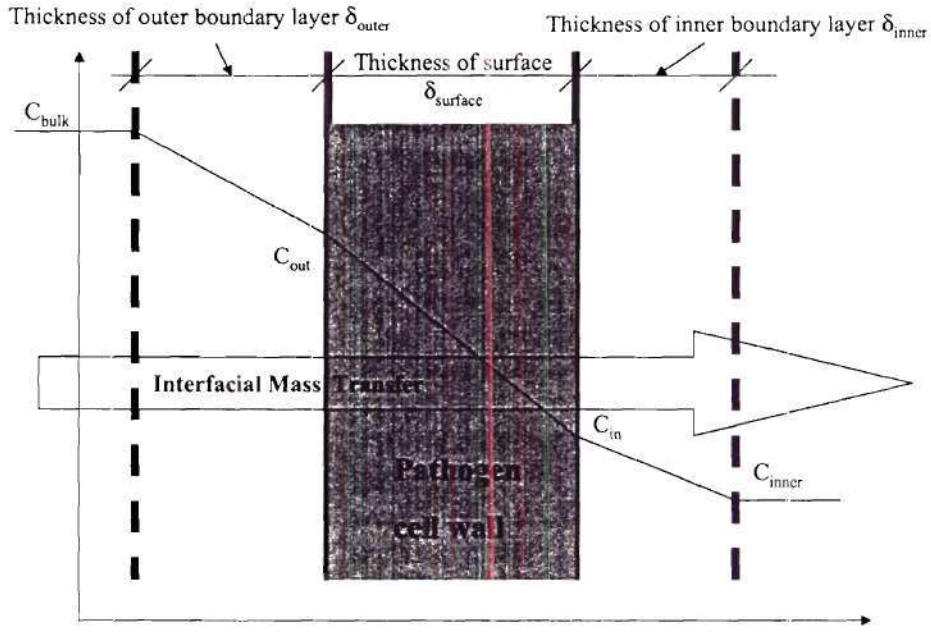

Figure 4.3 Interfacial mass transfer model

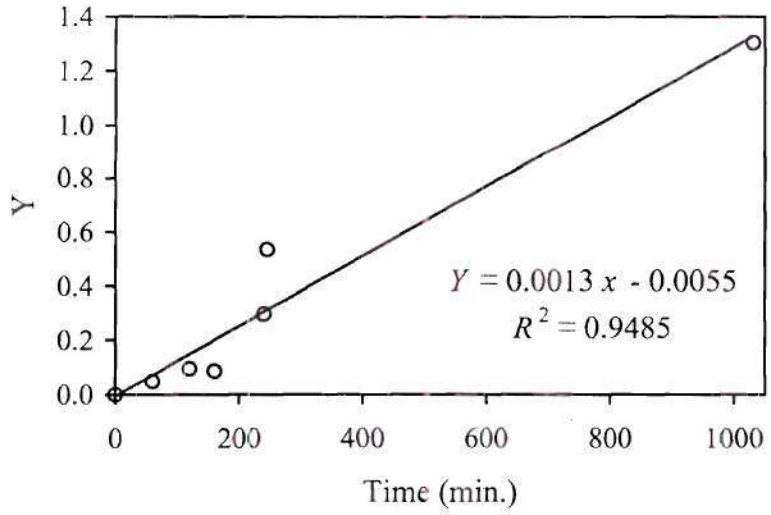

Figure 4.4 Finding the model parameters with chlorine as disinfectant

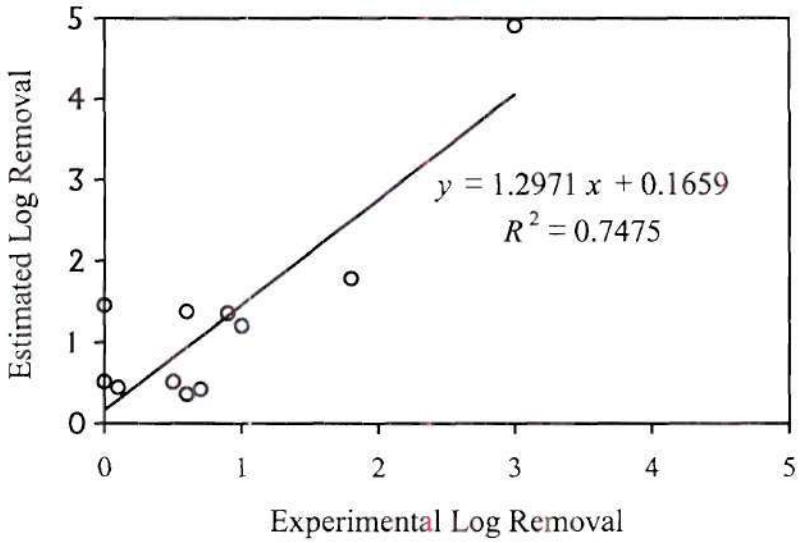

Figure 4.5 Comparison of the predictions from the new disinfection model and the experimental data from Gyürék, Finch, and Belosevic (1997) with chlorine as the disinfectant

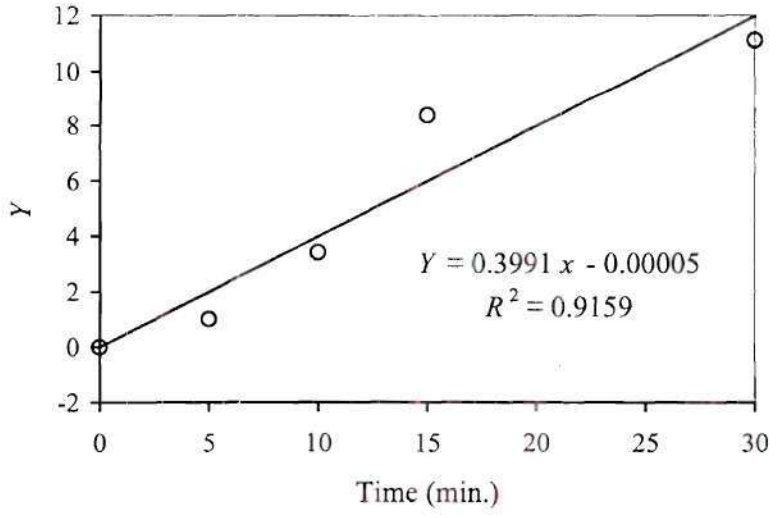

Figure 4.6 Finding the model parameters with ozone as disinfectant

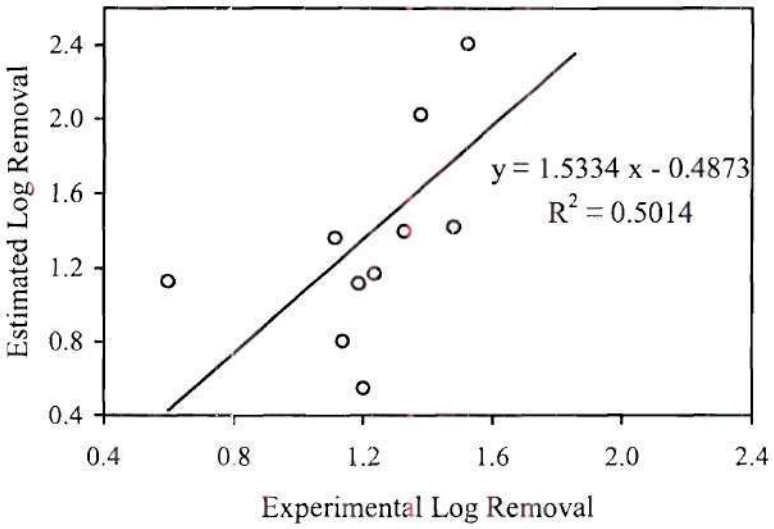

Figure 4.7 Comparison of the predictions from the new disinfection model to the experimental data from Ransome, Whitmore, and Carrington (1993) with ozone as the disinfectant

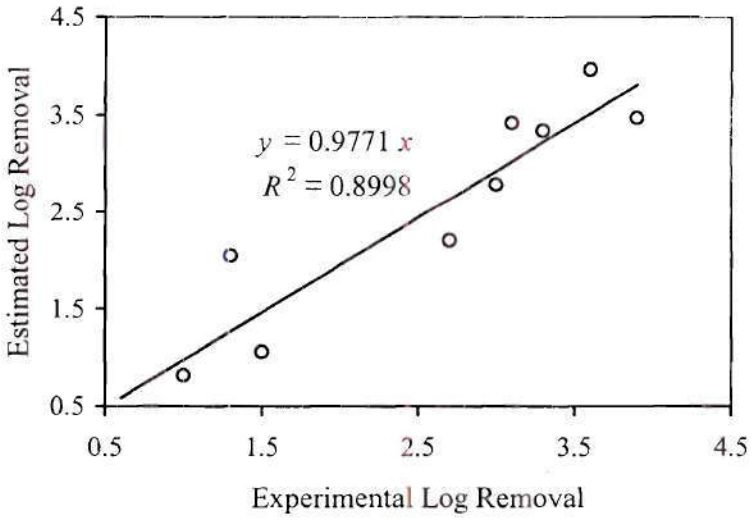

Figure 4.8 Comparison of the predictions from the new disinfection model to the experimental data from Gyürék (1997) with ozone as disinfectant

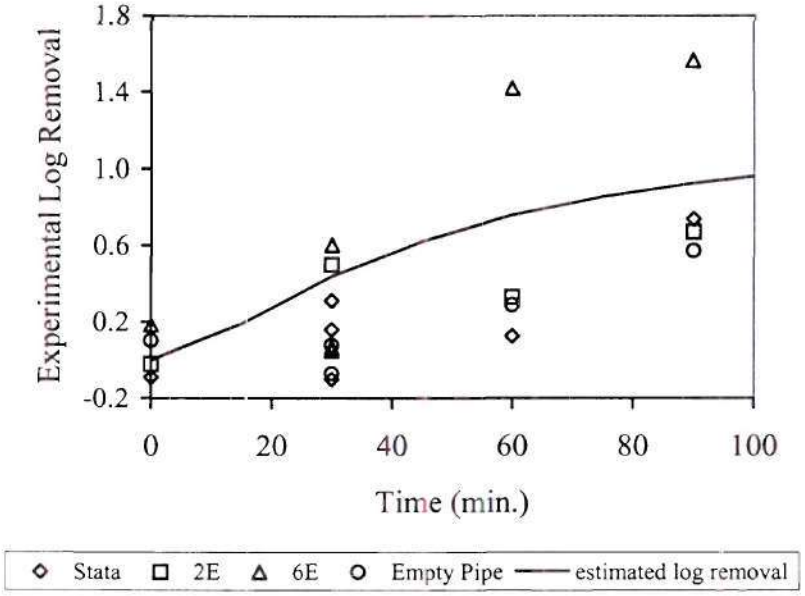

Figure 4.9 Prediction of log removal from the new disinfection model for a plug-flow dispersion reactor and the bench-scale experiments in a static mixer from Chapter 3

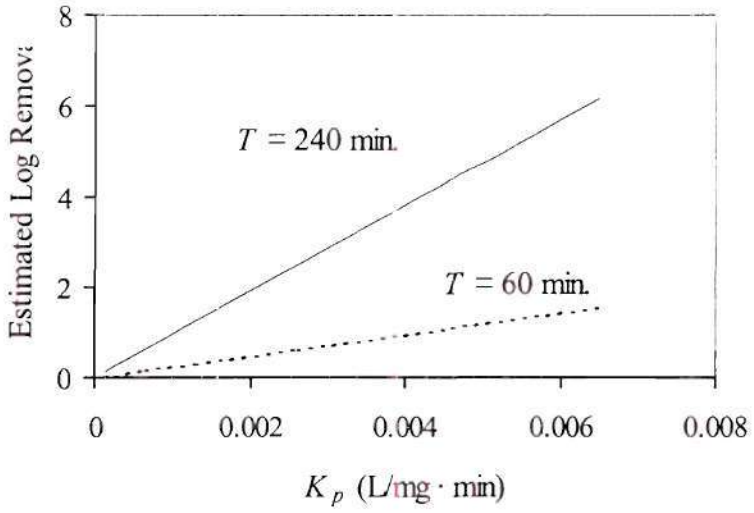

Figure 4.10 Sensitivity analysis of K_p for the completely mixed batch reactor with chlorine as the disinfectant

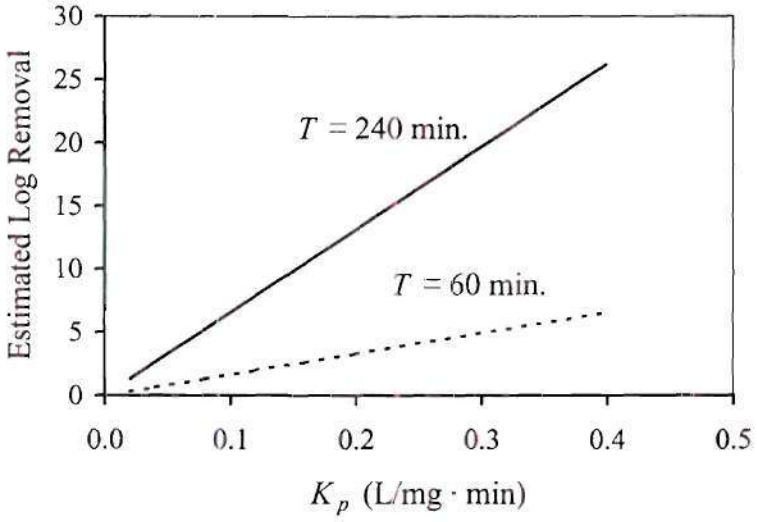

Figure 4.11 Sensitivity analysis of K_p for the completely mixed batch reactor with ozone as the disinfectant

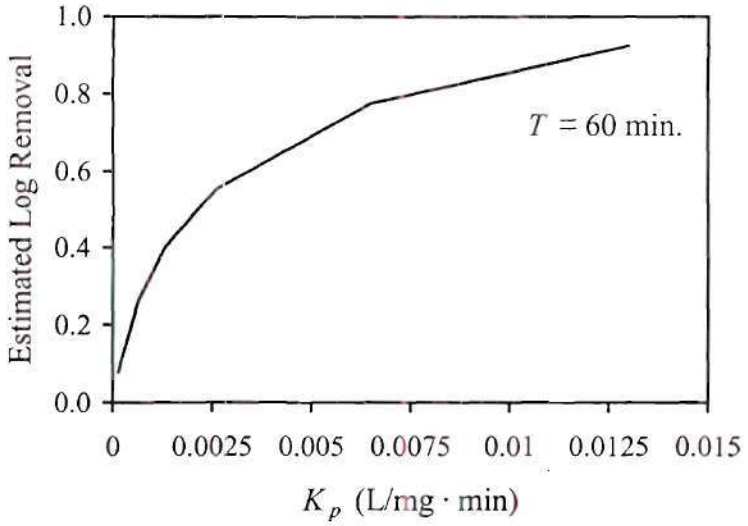

Figure 4.12 Sensitivity analysis of K_p for plug-flow dispersion reactor with chlorine as the disinfectant

CHAPTER 5
COMPUTATIONAL FLUID DYNAMICS PREDICTIONS OF THE FLOWFIELD IN HELICAL STATIC MIXERS

INTRODUCTION

In the drinking water field, the underlying goal of much academic research is to obtain a fundamental understanding of the processes used in water treatment that is based on the laws of chemistry and physics. The desire is that such an understanding will ultimately allow the industry to provide society with clean drinking water far into the future. The work described in this chapter represents a small step toward such an understanding through the development of a physics-based model that provides a fundamental tool for studying the role of mixing in the processes of coagulation and disinfection. More specifically, a three-dimensional, computational fluid dynamics (CFD) model is developed to simulate the flow of water in helical static mixers. This model is then applied to study the physics of this flow in various helical static mixer configurations over a range of flow rates.

What is CFD?

CFD is a relatively new field of fluid mechanics, which deals with the numerical solution of the fundamental equations of fluid motion: the unsteady, three-dimensional, Navier–Stokes equations. Readers interested in a more popular account of CFD should consult a recent *Scientific American* article, which provides an excellent, general introduction to CFD (Moin and Kim 1997). The emergence of CFD in the 1970s, its subsequent rapid growth in the 1980s, and its coming of age in the 1990s were all driven by the advent and evolution of high-performance supercomputers. In fact, the link between CFD and supercomputers was so strong that the sophistication of the numerical models and the complexity of the problems these models could tackle was almost entirely dictated by the available computational speed and memory. Early applications of CFD focused almost exclusively on simple flow for problems in Aerospace Engineering. Today, CFD methods are routinely used to simulate three-dimensional, laminar and turbulent flows in practically every area of engineering where fluid mechanics problems arise.

The most appealing attribute of a CFD model is that it can, at least in principle, provide unique insights into the physics of complex engineering flows at a level of detail not accessible by laboratory experiments. The following requirements are critical prerequisites for constructing such a CFD model:

- the mathematical equations that describe the flowfield are known
- discrete approximations of these equations can be formulated that faithfully represent the underlying physical processes
- a computational grid discretizing the geometrical domain of interest with sufficient spatial resolution can be constructed
- iterative numerical methods for solving the discrete equations on this computational mesh can be developed and implemented

Assuming that these requirements can be met, solutions of the discrete governing equations can be obtained. Such solutions completely define the flowfield at discrete points (the computational nodes) in space and time in terms of instantaneous pressure and velocity components.

In spite of rapid advances in computational power and significant strides in the development of numerical algorithms, the prediction of complex, three-dimensional, turbulent flows continues to challenge modern CFD. Such flows take place at high Reynolds numbers in and around complex geometries. These flows are characterized by a wide range of fluid mechanics phenomena including strong streamline curvature, induced pressure gradients, three-dimensional separation and vortex formation, large-scale unsteadiness, and surface roughness. These complicated effects, which in most real-life flows co-exist simultaneously, cause very complex turbulent flows with fluid motion occurring over a wide range of scales. These motions range in size from meters for the large-scale, coherent structures to micrometers for motion at the smallest, Kolmogorov scales, where molecular viscosity acts. This large disparity in scales, which increases with increasing Reynolds number, makes the numerical simulation of turbulent flows of engineering interest—which occur at high Reynolds numbers—very challenging even with today's supercomputers.

The time-dependent, three-dimensional, Navier–Stokes equations describe the complex fluid motions over this wide range of scales. However, the accurate numerical solution of these

equations (the so-called Direct Numerical Simulation approach or DNS) at realistic Reynolds numbers requires spatial and temporal resolutions that are beyond the capabilities of today's and tomorrow's supercomputers. For this reason, the DNS approach is applicable only to low Reynolds number flows in relatively simple geometries (Kim, Moin, and Moser 1987; Le, Moin, and Kim 1997; Moser, Kim, and Mansour 1999). In spite of this limitation, DNS provides important databases of instantaneous turbulence fields that guide the refinement and development of turbulence models. A more practical alternative for simulating turbulent flows is the so-called Large-Eddy Simulation (LES) approach. In this approach, the Navier–Stokes equations are filtered in space so that only those scales that are larger than the grid resolution are resolved. All other scales, the so-called subgrid eddies, are modeled. Although LES has attracted considerable attention during the past decade, it has not, in general, lived up to initial expectations (Speziale 1998). Some encouraging results for complex flows at moderate Reynolds numbers have been reported in the literature (Kaltenbach et al. 1999, Wu and Squires 1998), but meaningful LES simulations at Reynolds numbers of engineering interest would still require grid resolutions that are beyond the capabilities of existing and projected computer capacity.

Because of the enormous computational requirements of DNS and LES, the most promising alternative for practical engineering computations are those methods that rely on the Reynolds-averaged Navier–Stokes (RANS) equations. The RANS equations are derived by averaging in time the instantaneous Navier–Stokes equations so that only the largest scales of turbulence (the mean flow) are resolved directly. The averaging process produces six new unknowns, the Reynolds stresses, which need to be modeled via a suitable turbulence model to obtain a closed system of equations.

In the past decade, several successful applications of RANS models to complex, three-dimensional flows have demonstrated the potential of this approach as a powerful engineering tool for quantitatively accurate predictions at high Reynolds numbers (Lin and Sotiropoulos 1997b; Sotiropoulos and Patel 1992, 1994, 1995; Sotiropoulos and Ventikos 1998).

Previous Applications of CFD in Water Treatment

Compared to the popularity and wide use of CFD in areas such as aerodynamics, ship hydrodynamics, and hydraulics, there have been relatively few applications of CFD to problems in

the water treatment industry. A few studies are beginning to appear, and these are reviewed in this section. In separate studies, Krebs, Fischer, and Gujer (1995) and Brouchaert, Fortmann, and Buckley (1998) both used the commercial CFD code Phoenics (CHAM, London, United Kingdom) to suggest modifications to the inlet structure of a full-scale, circular clarifier. Van der Walt (1998a) used a different code (Flo++, Softflow, Potchefstroom, South Africa) to predict the flow in a rectangular sedimentation basin. He also used the same code to compute local *G*-values in a hydraulic flocculator (Van der Walt 1998b). The fluid mechanics of a stirred tank flocculator have also been studied with the FIDAP code (Fluent, Lebanon, N.H.) by Ducoste (1996), Ducoste and Clark (1998, 1999), and Luo (1997).

Lyn, Chiu, and Blatchley (1999b) developed a two-dimensional CFD code to predict the fluid flow and disinfection efficiency of ultraviolet-disinfection contactors. They compared the model predictions with laser-Doppler velocimeter measurements in a pilot-scale contactor (Chiu et al. 1999). Grayman et al. (1996) used the Phoenics code to model the mixing in a clearwell. And later, the results were used in combination with laboratory model studies to optimize the detention time in a clearwell as part of a plant renovation (Hannoun, Boulos, and List 1998). Quite a few other CFD studies of clearwell flow patterns have also been reported (Brocard et al. 1998, Engler et al. 1998, Grayman et al. 1998, Hagstrom et al. 1998, Reddy et al. 1998, Ta 1998). CFD studies of the flow patterns and mass transfer characteristics of ozonation contactors have also been reported (Cockx et al. 1997, Cockx et al. 1999, Do-Quang and Lainé 1997, Reddy et al. 1998).

Questions in Water Treatment that CFD can Address

The following paragraphs list several of the issues surrounding static mixers and water treatment and suggest how the in-depth understanding of the flow physics in a static mixer, gained by a three-dimensional CFD model, will help to resolve them.

Mixing a Function of Flow Rate

One widely-claimed (Amirtharajah and O'Melia 1990, Kawamura 1991) disadvantage of the static mixer is that mixing performance is a function of the flow rate. Accordingly, there is

some flow rate below which sufficient mixing is not provided. However, some researchers (Klute and Amirtharajah 1991) have stated that the mixing quality is not a strong function of the flow rate, and the relationship between mixing quality and flow rate is not understood.

Theories of Mixing and Coagulation

Several competing theories of the role of mixing in coagulation exist (Amirtharajah and Trusler 1986; Clark, Srivastava, and David 1993). However, experimental tests of these theories are difficult to perform. Conceivably, the models could be compared using numerical studies. Before this can happen, a detailed characterization of the flow field in a mixing reactor is required. CFD modeling can provide this characterization. A CFD model characterizing the flow in a static mixer would be a first step toward comparing these mathematical models of the coagulation process.

Moreover, the theories of mixing and coagulation were developed, in part, to explain the experimental observations of Amirtharajah and Mills (1982). These observations showed that for some combinations of coagulant dose and pH, mixing has no effect; whereas, for other combinations, mixing has a positive effect. With this evidence and the knowledge of fast kinetics of the coagulation reactions, Clark (1986) suggested that this dependence of coagulation performance on mixing rate may indicate that the coagulation reactions belong to a special class of chemical reactions called fast, competitive, consecutive chemical reactions. In these reactions, *micromix*ing or mixing at the molecular level is important.

Bourne and co-workers developed a theory of micromixing (Baldyga and Bourne 1984a, 1984b, 1984c, 1989a, 1989b) and applied that theory to static mixers (Bourne and Maire 1990; Bourne, Lenzner, and Petrozzi 1992; Baldyga, Bourne, and Hearn 1997). Their results showed that a prevalent assumption in water treatment—that head loss or *G*-value (mean velocity gradient) is directly proportional to the energy useful for mixing—does not apply for these types of reactions in static mixers. The mixer with the lower head loss performed better for the particular set of reactions that they studied. However, to further apply Bourne's model to coagulation and static mixers requires detailed information about the fluid flow in the mixer.

Appropriateness of the G-value

There has been considerable controversy in the Environmental Engineering literature about the concept of the *G*-value. However, it continues to be a widely used parameter in design to compare different mixers. CFD models provide an excellent tool to investigate the *G*-value for static mixers and other in-line type mixers.

Designers Must Rely on Manufacturer

The other widely claimed disadvantage of specifying static mixers for a water treatment plant is that plant designers must depend solely on the information provided by the mixer manufacturers. Godfrey (1992) succinctly summarized the situation as follows: "However, at the moment the only way a buyer can judge what is the best choice [of static mixer] for his process is to balance the cost of the quotation and the reputation of the manufacturer." A knowledge of the physics of the flow in a static mixer and how it affects the mixing would help to eventually eliminate this disadvantage. In particular, it would provide a fundamental basis on which the claims of various manufacturers could be evaluated.

DESCRIPTION OF THE CFD MODEL

This section describes in brief, general terms the CFD model that is used to simulate the turbulent, incompressible flows in a helical static mixer. Only an overview of the CFD model is provided here. Jones (1999) should be referenced for all of the details. The section titled "Results and Discussion" later in this chapter provides the details of the model specific to the static mixer geometry including a description of the computational grid.

Reynolds-Averaged Navier–Stokes Equations

As mentioned above the Reynolds-Averaged Navier–Stokes (RANS) equations describe the motion of turbulent flows. The RANS equations are written in terms of the *mean* velocity after the instantaneous velocity vector is decomposed into a mean and fluctuating components as

$$\widetilde{\mathbf{U}} = \mathbf{U} + \mathbf{u}'$$

where $\widetilde{\mathbf{U}}$ = instantaneous velocity vector

$\mathbf{U}$ = mean part of the velocity vector

$\mathbf{u}'$ = fluctuating part of the velocity

The continuity equation in terms of the mean velocity is

$$\nabla \cdot \mathbf{U} = 0 \tag{5.1}$$

where ∇ = the vector operator *del*, which can be written as $(\partial_x, \partial_y, \partial_z)$

The momentum equation is

$$\frac{\partial \mathbf{U}}{\partial t} + (\mathbf{U} \cdot \nabla)\mathbf{U} + \nabla p + \nabla \times \left(\frac{1}{Re} \nabla \times \mathbf{U} \right) + \nabla \cdot \overline{\mathbf{u}'\mathbf{u}'} = 0 \tag{5.2}$$

where t = time

p = pressure

$\times$ = is the cross-product between two vectors

Re = Reynolds number

$\overline{\mathbf{u}'\mathbf{u}'}$ = Reynolds stresses

Equations 5.1 and 5.2 are collectively called the RANS equations. However, by themselves the RANS equations cannot be solved because they are unclosed—there are ten unknowns but only four equations. For this reason, a turbulence-closure model is required to express some of the unknowns (Reynolds stresses) in terms of the other variables (mean quantities or their derivatives). The most common class of models is based on the Boussinesq assumption that the Reynolds stresses are linearly dependent on the mean strain-rate tensor, that is,

$$\overline{\mathbf{u}'\mathbf{u}'} = \frac{2}{3}\mathbf{I}k + \frac{1}{2}\nu_t\left[\nabla\mathbf{U} + (\nabla\mathbf{U})^T\right]$$

where $\mathbf{I}$ = the identity matrix

k = turbulence kinetic energy

ν_t = eddy viscosity

$(\cdot)^T$ = indicates the transpose of the matrix $(\cdot)$

Closure models that rely on the Boussinesq assumption—known as isotropic (or linear) eddy-viscosity models—are widely used in engineering calculations today due to their relative simplicity and computational expedience. For an extensive discussion of other classes of turbulence-closure models, including more general, non-isotropic models, and their performance in predictions of complex, three-dimensional flows, the reader is referred to Sotiropoulos (2000). Since this is the first attempt to develop a method for simulating turbulent flows in helical static mixers, only a two-equation, isotropic, eddy-viscosity model is considered. It is important to note, however, that more general modeling approaches—including non-linear, two-equation models and full Reynolds-stress transport models—are available in the present methodology, but these have not yet been tested in static mixer configurations.

To calculate the eddy viscosity, the two-equation, low-Reynolds number k–ω turbulence-closure model of Wilcox (1994) is used. Before proceeding with the description of the model, note that the term "low-Reynolds number" indicates that the model equations are valid all the way to the wall, that is, the near-wall buffer layer and the viscous sublayer where the turbulence Reynolds number approaches zero. This term is used to differentiate turbulence models that resolve the near wall flow from the so-called high Reynolds number models that rely on the wall functions approach to bridge the gap between the logarithmic layer and the near-wall sublayer. Although high-Reynolds number models are computationally more expedient (since they require considerably coarser computational meshes), they fail to predict even broad qualitative features of complex three-dimensional flows with intense large-scale vortices (Sotiropoulos and Patel 1995, Sotiropoulos 2000). Since the flow in a helical static mixer is anticipated to be dominated by such vortices, the use of a low-Reynolds number (or near-wall) turbulence model is a critical

prerequisite for developing a reliable, predictive method. The k–ω turbulence model was chosen over other two-equation closure models because it can be easily integrated through the viscous sublayer and because it can be readily extended to non-isotropic turbulence models (Sotiropoulos and Ventikos 1998).

The k–ω model includes two additional partial differential equations: one for the turbulence kinetic energy and one for the specific dissipation ω. Model developers give various interpretations for ω but the most obvious one follows from its definition, namely,

$$\omega \propto \frac{\varepsilon}{k}$$

where ε = the rate of turbulence energy dissipation

In other words, ω is the rate of dissipation of turbulence energy per unit of turbulence kinetic energy. The equations for the closure model are

$$\frac{\partial k}{\partial t} + (\mathbf{U}\bullet\nabla)k - \nabla\bullet\left[\left(\sigma^{*}\nu_t + \frac{1}{Re}\right)\nabla k\right] + P_d - \beta^{*}k\omega = 0 \tag{5.3}$$

and

$$\frac{\partial \omega}{\partial t} + (\mathbf{U}\bullet\nabla)\omega - \nabla\bullet\left[\left(\sigma\nu_t + \frac{1}{Re}\right)\nabla\omega\right] + \alpha\frac{\omega}{k}P_d - \beta_1\omega^2 = 0 \tag{5.4}$$

where P_d = $\frac{1}{8}\nu_t\left[\nabla\mathbf{U} + (\nabla\mathbf{U})^T\right]^2$

σ^{*} = closure coefficient = 1/2

σ = closure coefficient = 1/2

β^{*} = closure coefficient = $\frac{9}{100}\cdot\frac{5/18 + (Re_t/8)^4}{1 + (Re_t/8)^4}$

α = closure coefficient = $\frac{5}{9} \cdot \frac{1/10 + Re_t/2.7}{1 + Re_t/2.7} \cdot (\alpha^*)^{-1}$

α^* = closure coefficient = $\frac{1/40 + Re_t/6}{1 + Re_t/6}$

β_1 = closure coefficient = $\frac{3}{40}$

Re_t = turbulent Reynolds number = $Re\frac{k}{\omega}$

The eddy viscosity is calculated from the turbulence kinetic energy and the specific dissipation as

$$\nu_t = \alpha^* \frac{k}{\omega}$$

Summary of the Numerical Methods

To be solved numerically, Equations 5.1 to 5.4 must be transformed into discrete equations that are defined only on the nodes of the computational grid. The grid divides the geometry of the flow domain, in this case the static mixer, into discrete points and Equations 5.1 to 5.4 are solved at each node. Each of the terms in the governing equations are treated individually and the value of any given variable at any given node is described in terms of that variable at the surrounding nodes. This description is loosely called discretization. Table 5.1 lists each group of terms from the governing equations and how they are discretized. Once the equations are discretized, they form a large system of coupled algebraic equations that must be solved as efficiently as possible. In the present CFD model, a four-stage, point-implicit Runge–Kutta scheme is used. The convergence of the scheme is enhanced by the use of local time-stepping, implicit residual smoothing, and multigrid acceleration.

Table 5.1

Summary of the CFD model

Governing equations	RANS equations
	k-ω turbulence closure model
Coordinate system	Generalized curvilinear, non-orthogonal
Spatial discretization	Finite-volume
Convective terms	Second-order central differencing
Metric terms	Second-order central differencing
Viscous terms	Second-order central differencing
Source terms	Second-order central differencing
Artificial dissipation terms	Flux-difference splitting upwind
	Martix dissipation
	Scalar dissipation
Pressure-velocity coupling	Artificial compressibility
Temporal integration	Point-wise implicit, four-stage Runge-Kutta
Convergence acceleration	Local time-stepping
	Implicit residual smoothing
	Multigrid acceleration
Multigrid acceleration	V-cycle
	Semi-coarsening

VALIDATION OF THE CFD MODEL

No experimental measurement have been reported in the literature for the turbulent flow through helical static mixers. For this reason, the recently published experimental data of the flow in a pipe bend by Sudo, Sumida, and Hibara (1998) was used to validate the method. The flow in a pipe bend is a good substitute for the flow in a static mixer because both flow are complex, three-dimensional, internal, shear flows that have strong secondary (transverse) motions.

Experimental and Computational Details

The experiments were performed in a 90° pipe bend for a Reynolds number (*Re*) 60,000, where $Re = Ud/\nu$ and U is the bulk velocity, d is the diameters of the pipe, and ν is the kinematic viscosity of the fluid flowing through the bend. The radius of curvature R_c of the bend was $2d$. One hundred diameters of pipe were provided upstream of the bend and 40~diameters were provided downstream. The longitudinal, radial, and circumferential components of the instantaneous velocity were measured at 17~cross-sections in the pipe between $1d$ upstream of the bend and $10d$ downstream. At each cross-section, velocity components were measured at 266~points. The points were unevenly distributed over the cross-section---with points clustered near the pipe walls. The spacing nearest the wall was $0.029d$. All measurements were made using hot-wire anemometry. Incidentally, laser Doppler velocimetry (LDV) was not used in this study because for circular cross-sections LDV can only measure the longitudinal component of the velocity.

The same numerical method was used to predict the flow in the bend as was used to predict the flow in the helical static mixer. The pipe bend is located within a Cartesian coordinate system (x_1, x_2, x_3) with corresponding velocity components (u_1, u_2, u_3). The longitudinal velocity component within the entire pipe is denoted as u_s, where s is the coordinate along the pipe centerline. Transverse velocity components are defined in terms of local cross-sectional polar coordinates, r and θ as u_r and u_θ. The inlet and outlet straight sections of the pipe are $3d$ and $8d$ long, respectively. These lengths were chosen based on previous computations in pipe bends (Lin and Sotiropoulos 1997b). Thus, the extent of the computational domain is $-3 < s < \pi + 8$, where the centerline coordinate s is measured from the start of curvature.

The plane-of-symmetry in the pipe is located at $x_3 = 0$. Because the inflow conditions are axisymmetric, only one-half of the domain is simulated. The number of computational nodes in the grid is $151 \times 81 \times 41$ or 501,471, which represents a moderately fine computational grid. The nominal, near-wall spacing is $0.00033d$, which places 3 or 4 nodes within the viscous sublayer. No attempt was made to study the effect of grid resolution for this particular case. But based on the results of previous studies (Lin and Sotiropoulos 1997a), the number of grid nodes used should be adequate to obtain grid-insensitive solutions.

Validation Results

As an introduction to the results, brief review of the physics of bend flows is given. Regardless of the shape of the bend cross-section (circular or rectangular), bend flows are dominated by the interaction of the longitudinal or main flow, which occurs in the direction of the bend axis, and the secondary flow, which occurs in the transverse plane. As fluid enters the bend, both longitudinal and transverse pressure gradients develop (see Figure 5.1). A favorable longitudinal pressure gradient develops on the inside wall and causes fluid near the inside wall to accelerate. Conversely, an adverse gradient along the outer wall causes the fluid near the outer wall to decelerate. The resulting transverse pressure gradients cause a secondary motion along the pipe wall from the outer toward the inner bend. The intensity of the secondary motion strongly depends on the radius of curvature of the bend because this determines the magnitude of the transverse pressure gradients. The secondary motion transports low-streamwise-momentum boundary layer fluid along the circumferential direction from the outer to the inner bend. Consequently, pockets of low streamwise velocity develop near the inner wall causing the maximum of the velocity profile to shift toward the outer bend, thus, reversing the previously described action of the longitudinal pressure gradients. The growth of the secondary motion and the resulting redistribution of the mean streamwise momentum within the bend cross-section cause regions of intense mean-velocity gradients to form away from the pipe wall, which leads to the production of turbulence stresses by mean shear. The structure of turbulence is further complicated by the presence of both convex and concave streamline curvature, which are known to suppress and enhance, respectively, turbulent fluctuations. By the end of the bend, a very complex, three-dimensional, turbulent flow has developed, which subsequently recovers toward fully developed

turbulent pipe flow in the straight pipe section following the bend. The relaxation process within this region is dominated by viscous diffusion and the anisotropy of the Reynolds stresses generated within the bend. For more information, several reviews of bend flows and turbulent secondary flows exist (Bradshaw 1987; Sotiropoulos and Patel 1992)

Mean Pressure

Figure 5.1 shows the measured (data points) and predicted (lines from the CFD model) pressure coefficients along the axis of the pipe. The (static) pressure coefficient C_p is

$$C_p = \frac{p - p_{ref}}{\frac{1}{2}\rho U^2}$$

where p = pressure

p_{ref} = reference pressure

ρ = density

The agreement between the predicted and measured pressure coefficients is excellent. In particular, the CFD predictions capture both the magnitude and location of the longitudinal and transverse pressure gradients.

Mean Velocity

Profiles of the predicted and measured axial (u_s) and circumferential (u_θ) velocity are shown in Figures 5.2 and 5.3 for 16 cross-sections along the length of the bend. A more global view of the flow within the bend can be obtained by comparing measured and computed contours of the mean longitudinal velocity at several cross-sections as shown in Figure 5.4. As this figure shows, the computations capture the measured trends. In keeping with the previous discussion on the physics of bend flows, the velocity maximum shifts initially toward the inner bend and the boundary layers along the outer and inner walls thicken and thin, respectively Figures 5.4 b and c. Approximately halfway through the bend, the pressure-driven secondary motion begins to interact with and distort the streamwise flow forming a small pocket of low streamwise momen-

tum near the inner wall (Figure 5.4 d). At the end of curvature (Figure 5.4 e), this pocket has grown in size and has been transported by the secondary motion toward the center of the cross-section. The streamwise velocity contours have acquired a distinct S-shape structure and a very thin boundary layer has emerged along the outer bend. The computations reproduce all these trends, but they underpredict the magnitude of the streamwise velocity within the pocket of low momentum near the inner bend. This discrepancy between experiments and computations is clearly evident in the comparisons of the mean velocity profiles shown in Figures 5.2 and 5.3. Its origin should be traced to small errors in the prediction of the secondary motion, which causes the distortion of the mean flow. The comparisons of the circumferential velocity component shown in Figure 5.2 support this argument. The predictions capture all experimental trends, including the sign reversal of the circumferential velocity from the wall to the plane of symmetry, but underpredict the magnitude of this secondary velocity component in the vicinity of the symmetry plane.

Downstream of the bend (Figures 5.3 and 5.4 f to h), the measurements indicate a rather rapid recovery of the mean flow towards a fully developed turbulent pipe flow. Just seven diameters after the end of curvature, the circumferential velocity component has decayed to approximately one-third of its magnitude at the end of curvature (Figure 5.4 c) and the streamwise velocity profiles have recovered to an almost uniform distribution across the horizontal and vertical centerlines (Figure 5.4 a). The computations exhibit similar qualitative trends but show a more sluggish rate of recovery. This discrepancy is especially pronounced near the inner wall where the predicted streamwise velocity component are consistently lower than the measurements within most of the bend. Note, however, that the recovery of a rapidly strained turbulent flow toward equilibrium is a very complex and not fully understood process, which is dominated by the interaction of the Reynolds stresses with the mean flow. Similar discrepancies between experiments and computations have also been reported and discussed in previous numerical studies—even those that used more advanced non-isotropic, multi-equation turbulence models (Sotiropoulos and Patel 1995). These discrepancies not withstanding, the overall agreement between computations and experiments is satisfactory given the complexity of the flow.

Note that the comparisons between the experiments and computations are obscured by a significant discrepancy between the measured flow at the entrance of the bend and the inlet boundary conditions specified in the calculations. Sudo, Sumida, and Hibara (1998) reported that

one diameter upstream of the start of curvature, the measured flow exhibited all the features of a fully developed turbulent pipe flow. The $100d$ length of straight pipe in the upstream section of their experimental apparatus should have been more than sufficient to reach fully developed conditions. In the computations, the inlet conditions were specified by performing a separate calculation for fully developed pipe flow at Re=60,000 and prescribing the calculated mean velocity and turbulence quantities as boundary conditions $3d$ upstream of the start of curvature. The computed, fully developed solution is in excellent agreement with the benchmark experimental data of Laufer (1954); see Wilcox (1994, page 135). Yet, the comparisons between these inlet conditions and the measurements of Sudo et al., shown in Figure 5.4 a, reveal significant discrepancies. In fact, the measurements indicate a larger centerline velocity and a thinner boundary layer, attributes which are consistent with a developing, rather than fully developed, pipe flow (Bradshaw 1971, p. 166). Furthermore, if the velocity profile shown in Figure 5.2 at $s = -1$ is assumed to be axisymmetric (which is consistent with Figures 5.2 a and 5.4 a), then the calculated, nondimensional, bulk velocity through the experimental pipe is 1.28 instead of 1, which would indicate a higher than reported Re. However, this is inconsistent with the higher velocity on the centerline because in turbulent pipe flows, centerline velocity decreases with increasing Re. The reasons for these discrepancies in the inlet conditions are unclear and cannot be explained without more detailed information about the experiments. Most importantly, their possible impact on the flow development within the bend and, thus, the uncertainty they introduce when validating the model cannot be quantified. Although one would anticipate these uncertainties to obscure the conclusions reached in this section, the general trends discussed above are thought to be valid because they are generally consistent with previous validation studies of earlier versions of the present model.

RESULTS AND DISCUSSION OF STATIC MIXER PREDICTIONS

Computational Details

Grid Details

Two-dimensional views of the computational grid are shown in Figure 5.5. The Cartesian coordinates are (x_1, x_2, x_3) with corresponding velocity components (u_1, u_2, u_3). The longitudinal coordinate x_1 is measured from the leading edge of the first element. The origin of the other two coordinates is located at the centerline of the pipe. Velocity component u_1 is called the longitudinal velocity; the other components are called transverse velocities. The term transverse is used instead of the more common term secondary because, as shown later in this chapter, the magnitude of the transverse velocities can become very large---with a magnitude at some points larger than the bulk velocity in the mean flow. All distances in Figure 5.5 are normalized by the pipe diameter d.

The elements are formed by rotating the cross-section shown in Figure 5.5 through a twist angle of 180°. For the top grid in Figure 5.5 the mixer elements have been unfolded to illustrate the clustering of the grid nodes in the x_1 direction. A three-dimensional picture of the grid is shown in Figure 5.6 a. Only one-half of the grid is shown to highlight the details of the grid on the elements. However, the full three-dimensional domain is used in all simulations—no symmetry planes are used—unlike the simulations in the 90° bend discussed in the previous section. Figure 5.6 b shows a close-up of the mixer elements. The two elements twist in opposite directions. Notice that the trailing edge of the first element forms an angle of 90° with the leading edge of the second element. The length L_e and width of each element is 1.5 and 0, respectively, for all of the simulations performed.

The specified length of the inlet or outlet section of pipe depended on the purpose of each simulation. A typical inlet length was $6d$; a typical outlet length was $20d$. The lengths were chosen based on the verification studies, which are discussed below. In the x_1 direction, grid nodes are clustered near the leading and trailing edge of each element. Nodes are also clustered on both sides of the elements. The nominal, near-wall spacing is equivalent in all three coordi-

nate directions for the pipe walls and the element surfaces. For most simulations, the near-wall spacing was chosen so that $y^+ \sim 1$ where y^+ is the normal distance from the wall in wall coordinates. such a fine grid spacing is necessary because the turbulence model is valid all the way to the wall, and, thus, the computational mesh should resolve the near-wall, viscous sublayer. Typically 3~to~5 grid nodes were placed in the region $y^+ < 10$. The total number of grid nodes varied, again depending on the purpose of the simulation, from approximately 370,000 or 155×49×49 to 2,590,000 or 275×97×97.

CFD Model Details

The CFD model described in the previous section was used to predict the turbulent flow in helical static mixers. The k–ω turbulence closure model was used for all calculations. The artificial-dissipation flux was calculated with a flux-difference splitting upwind scheme (FDS). In particular, a first-order accurate scheme was used. For implicit residual smoothing, variable residual-smoothing coefficients were used in the x_1 direction. All simulations reported in this chapter used the first-order accurate flux-difference splitting scheme FDS1. Many schemes of higher-order accuracy were attempted including several total-variation diminishing or TVD schemes. In short, TVD schemes provide second-order or higher accuracy in smooth regions of the flow but reduce to first-order accuracy in regions of steep flow gradients. None of these attempts, however, yielded converged solutions of higher-order spatial accuracy. The reasons for this failure are not entirely clear, but two possible explanations exist. First, it could simply be that the appropriate high-order scheme has not been tried. Example of others that have not been tried include schemes which weight the dissipation coefficients based on a three-dimensional interpolation (Turkel et al 1991).

Second, a possible explanation is that at sufficiently high Reynolds numbers the flow through helical static mixers exhibits mean-flow unsteadiness. Two recent experiences suggest this explanation. First, the behavior of the CFD model for laminar flow as the Re was increased on suggesting that the failure of the numerical method to yield converged solutions with a second-order accurate scheme could be due to the onset of unsteadiness—converged solutions could only be obtained with the first-order scheme for $Re \leq 600$. Second, Sotiropoulos, Chrisochoides, and Sturm (1999) reported similar trends, to those found here, for a simulation of the turbulent

flows around a bridge abutment using a numerical method similar to the one developed here with the k–ω turbulence model. More specifically, they too failed to obtain converged solutions using the second-order accurate artificial-dissipation scheme, but rapid convergence was achieved when a first-order accurate flux-difference splitting scheme was used. These numerical difficulties, however, were eliminated when Sotiropoulos, Chrisochoides, and Sturm (1999) solved the RANS equations in a time-accurate fashion. The second-order numerical scheme was able to yield physically meaningful, time-accurate solutions. These solutions exhibited strong, unsteady vortices and time-varying zones of flow reversal. This finding suggests that for complex, three-dimensional flows the RANS equations may not always have steady solutions. The large-scale flow structures that are resolved by the RANS equations could be time-dependent and, therefore, could only be predicted numerically by carrying out time-dependent calculations. The excessive dissipation introduced by first-order accurate schemes damps out these large-scale, time-dependent flow structures, thus, allowing steady solutions.

Physically, the first-order solutions can be thought as representing what one would obtain in the laboratory if the measurements were averaged over time intervals that are much longer than the characteristic period of the large-scale unsteadiness (assuming it exists). For abutment-type flows, that is flows near the juncture of a solid obstacle with a wall, experimental evidence suggests that mean-flow unsteadiness is present (Devenport and Simpson 1990). Although, the flows in helical static mixers are also characterized by strong longitudinal vortices and regions of flow reversal, features that could potentially lead to unsteady, large-scale structures in the flow, the lack of any comprehensive experimental study for such flows prevents any definitive conclusions from being drawn. This issue can only be resolved by a combined experimental and computational effort, the latter focusing on time-dependent, three-dimensional, RANS computations. Such an undertaking, however, is beyond the scope of the present work and will be left as an important subject for future research. This chapter uses the first-order accurate scheme to study steady-in-the-mean turbulent flows in helical static mixers. In spite of the first-order spatial accuracy, the simulations presented here are very useful and should guide future research. Not only do they provide important, qualitative information, concerning the effect of Reynolds number and mixer geometry on the flow, but the predicted pressure drop (friction factor) agrees well with the measurements of friction factor taken at the pilot plant and reported in Chapter 2.

The inlet velocity profile is the turbulent profile in fully developed flow for a pipe with a bulk velocity of one. For each *Re*, this velocity profile was obtained using the program given in Wilcox (1994). The outlet boundary condition for pressure is $p = 0$ on the centerline. For all other nodes in the outlet cross-section, the pressure was extrapolated from the interior of the computational domain. On the solid walls and on the pipe elements, the no-slip boundary condition (zero velocity) was used. On the elements, two values of the pressure were stored—one value for each side of the element. On the leading and trailing edges of the element, the mean pressure P and specific dissipation ω were calculated by averaging their values among interior nodes surrounding the edge under consideration.

Scope of CFD Simulations

A total of 22 different simulations (or runs) were performed for this chapter. Table 5.2 shows each run and gives the *Re*, the number of elements N_e, and the total number of grid nodes N_{tot}. The Reynolds number is defined using the empty-pipe diameter and bulk velocity. No adjustment is made for the volume occupied by the mixing elements. The 21 simulations performed for this chapter required approximately 4000 hours of CPU time on a R10000 SGI Origin~2000 computer (SGI, Mountain View, Calif.). Typically, a simulation ran in parallel on six processors significantly reducing the actual time required. The largest computation (Run~13) required approximately 1~gigabyte of computer memory.

More Validation

The validation of a CFD model requires that the numerical predictions be compared to experimental data. In the previous section, an extensive validation of the present CFD model was presented using published experimental measurements of the turbulent flow in a 90° pipe bend at $Re = 60{,}000$. However, experimental data of such detail are not available for helical static mixers. The friction factor experiments reported in Chapter 2 of this report, which were performed at the pilot plant, can be used to carry out a preliminary validation of the CFD model. In those experiments, the pressure drop was measured across the helical static mixer with a pressure transducer. The static mixers were manufactured out of and housed in stainless steel pipe.

Table 5.2

Summary of computer simulations

Run	Re	N_e	$N_{tot} \times 10^{-6}$	Notes
1	10,000	2	0.65	Loosely coupled
2	10,000	2	0.65	Strongly coupled
3	5,000	2	0.37	Inlet length
4	5,000	2	0.37	Inlet length
5	5,000	2	0.37	Inlet length
6	10,000	2	0.65	Boundary conditions
7	10,000	2	0.65	Boundary conditions
8	10,000	2	0.65	Boundary conditions
9	10,000	2	0.65	Boundary conditions; outlet length
10	10,000	2	0.65	Outlet length
11	10,000	2	0.78	Outlet length, grid independence; N_e and Re
12	10,000	2	1.54	Grid independence
13	10,000	2	2.59	Grid independence
14	10,000	6	1.63	N_e and Re
15	10,000	4	1.17	N_e and Re
16	5,000	2	0.78	N_e and Re
17	5,000	4	1.17	N_e and Re
18	5,000	6	1.63	N_e and Re
19	20,000	2	0.78	N_e and Re
20	20,000	4	1.17	N_e and Re
21	20,000	6	1.63	N_e and Re
22	100,000	2	1.04	Re

The number of elements was 2, 4, and 6. The nominal pipe diameters were 1, 1.5, and 2 inches (25, 38, and 51 mm). Care was taken to isolate the mixer and measure only the pressure drop across the mixer. He also ensured that fully developed pipe flow entered the mixer by providing 50 to100 diameters of pipe upstream of the static mixer. The measurements cover the range $3,000 < Re < 19,000$. In generic, dimensional terms, the pressure drop Δp^* in a pipe is

$$\Delta p^* = f\left(\frac{L^*}{d^*}\right)\left(\frac{\rho^* U_o^{*2}}{2}\right)$$

where d = the nominal pipe diameter

L^* = the length over which the pressure drop occurs

ρ^* = density of water

U_o^* = the bulk velocity

Rearranging the equation above and substituting for some terms with values appropriate to static mixers, the friction factor f is

$$f = 2\frac{\Delta p^*}{\rho^*}\left[\frac{d^*}{N_e\left(L_e^*\right)}\right]\left(\frac{1}{U_o^*}\right)^2$$

Our in the non-dimensional terms of the CFD model, the definition of f is

$$f = 2\frac{\Delta p}{N_e L_e}$$

Comparisons of the predicted to the measured friction factor for 2, 4, and 6 elements are shown in Figure 5.7. The predictions correspond very well to the measured pressure drop especially given that the numerical model does not take into account both the thickness of the element and

the roughness of the pipe wall. This comparison, although encouraging, should only be considered a preliminary step in the validation of the model. Detailed mean-flow and turbulence-statistics measurements will be needed for more comprehensive validation studies.

Verification

Verification examines whether the discrete, CFD model faithfully represents the continuous governing equations (in this case, the RANS and the k–ω turbulence-closure equations). Thus, verification includes issues like iterative convergence, discretization error, and the size of the computational domain. In this study, the following issues were addressed : (1) iterative convergence by ensuring that a fully converged solution is obtained; (2) discretization errors by examining the sensitivity of the computed solutions to mesh refinement; and (3) sensitivity to the size of the computational domain by investigating how the solution changes as the outlet length varies. For a discussion of each of these issues in detail, consult Jones (1999); for brevity, only discretization error is discussed here.

Discretization Error

To determine the effect of discretization error, that is, the sensitivity of the computed solutions to mesh refinement, simulations were performed on three different grids for a two-element mixer at $Re = 10{,}000$. The coarse grid contained 780,000; (185×65×65) nodes, the medium grid 1,541,000; (235×81×81), and the fine grid 2,587,000; (275×97×97).

Figure 5.8 shows the skin-friction coefficient computed on the three different grids. The most significant discrepancies between the three grids are observed downstream of the second element, where the skin-friction coefficient appears to increase continuously as the grid is refined. To investigate the effect of grid-dependence further, Figure 5.9 shows the mean longitudinal velocity contours u_1 and vectors of the mean transverse velocity components u_2 and u_3. The cross-sections are shown at the exit of the last element. This location is used because it represents one of the more complex regions of flow within the mixer and, thus, is more likely to show any differences that exist.

The predicted flowfields on the three grids are broadly similar, but several distinct differences exist. These differences are especially pronounced between the solution on the coarse grid (Figure 5.9 a) and the fine grid (Figure 5.9 c). The predicted flowfield on the fine grid is more complex as indicated by the large distortion of the mean longitudinal velocity contours and the stronger transverse motion. On the other hand, the flowfield on the coarse grid is more diffused. The mean velocity gradients are considerably more smeared and the predicted longitudinal vortices weaker. These differences, and the apparent sensitivity of the computed solutions to grid refinement, should be attributed to the first-order accurate scheme that is used. In spite of the obvious inadequacy of the coarse grid to capture the intensity of the various flow phenomena, this grid was chosen to carry out all the simulations for the parametric studies reported in this chapter. The main reason for this choice is that simulations on the finer grids would require computational resources well beyond those currently available. Moreover, since no detailed measurements are currently available for model validation, the objective of the present, parametric study is to identify general trends in the computed flowfields and need for focused future experiments. The coarse grid simulations, although they cannot be relied upon for quantitative predictions, certainly capture the general features of the flow as revealed by the comparisons with the simulations on the finest mesh. The grid-dependency studies show that an even finer mesh may be necessary for grid-insensitive solutions. Whether the accuracy of the mean flow features predicted on the present finest mesh is adequate for engineering purposes, cannot be established, however, without experimental data for model validation. Of course, if the conjecture regarding the existence of mean flow unsteadiness is correct, further grid refinement could lead, even with the first-order accurate scheme, to the onset of unsteady flow and numerical difficulties similar to those encountered with the second-order accurate schemes. These are all very important issues, critical for further progress in modeling the flows in helical static mixers, and will be left as the subject for future work.

Discussion of the Flowfield Physics

This section discusses the physics of the predicted turbulent flowfield in the helical static mixer. The results presented are for a two-element mixer and were obtained on the fine grid at Re=10,000. The discussion begins with an overview of the flowfield in the mixer. Then, some of

the specific features are investigated in more detail. To obtain an overall view of the flowfield in the static mixer, the mean-velocity field at several longitudinal cross-sections is presented. Figures 5.10 to 5.12 show contours of the mean longitudinal velocity u_1, transverse velocity vectors u_2 and u_3, and contours of the mean longitudinal vorticity Ω_{x_1} (hereafter, called the mean vorticity). This component of the mean vorticity is

$$\Omega_{x_1} = \frac{\partial u_3}{\partial x_2} - \frac{\partial u_2}{\partial x_3}$$

According to the right-hand-rule, $\Omega_{x_1} > 0$ indicates counterclockwise rotation; $\Omega_{x_1} < 0$ indicates a clockwise rotation. Two points about the vector plots should be noted:

- The vectors are drawn relative to the fixed Cartesian coordinates (x_2, x_3). The fact that the element is also twisting relative to the Cartesian coordinates can obscure transverse flow relative to the elements.
- The absence of an obvious vortex core at those points of high longitudinal vorticity in the contour plots does not mean that a vortex is not present. If such a vortex is imbedded in (and transported by) a transverse flow of comparable or larger magnitude, it would not be visible in the vector plots. Hence, the combined use of the vector plots and the longitudinal vorticity contours to visualize the complex transverse flow patterns that arise in the helical mixer.

The three figures show cross-sections located in the three sections of the computational domain. Figure 5.10 shows the flow in the inlet and in the first mixer element; Figure 5.11 shows the flow within the second element; Figure 5.12 shows the flow in the outlet section or downstream of the second element. For all of the figures shown, the flow is directed out of the page. The first element twists in a counter-clockwise direction; the second element in the opposite or clockwise direction.

First element

The first cross-section (Figure 5.10 a) is located approximately one-quarter of a diameter upstream of the first element. The distorted contours of mean longitudinal velocity clearly show that the influence of the mixer elements is already being felt by the approach flow—as expected due the elliptic nature of incompressible flows. On the leading edge of the first element, Figure 5.10 b shows the element splitting the flow into two regions of high-momentum fluid and an extremely thin boundary layer developing along each side of the element. At the same location, the vector plot reveals that a weak, albeit rather complex, mean transverse flow pattern has already formed due to the element-induced, transverse pressure gradients. The mean vorticity contours indicate small regions of large positive and negative mean vorticity at the intersection of the element and the pipe wall. In the same location as the positive mean vorticity, small pockets of negative longitudinal velocity exist suggesting the presence of regions of reversed flow. Figure 5.10 c shows that further downstream the regions of reversed flow have grown larger. At the end of the first element, these regions are still present but have become much smaller (Figure 5.10 d). The three-dimensional structure of these regions are clarified in one the sections below.

Figures 5.10 c and d shows the flowfield at 10% and 90% along the length of the first element. The high-momentum regions of mean longitudinal velocity show a very complex structure with several local peaks. Clockwise (negative) mean vorticity is generated on both sides of the element. These vortices are shown on either side of the element by the vector plot in Figure 5.10 c. The mean transverse flow quickly convects this negative mean vorticity away from the element. More negative mean vorticity is created on the pipe walls. Further into the element, counterclockwise (positive) mean vorticity is created on the element. This mean vorticity rotates in the same (counterclockwise) direction as the twist of the first element.

Second Element

Figure 5.11 shows the details of the flowfield within the second element. The second element twists in a clockwise direction and the element begins at an angle of 90° to the trailing edge of the first element. In the first set of cross-sections, the element is oriented vertically. The

first location shown Figure 5.11 a is the intersection of the two elements. The second element splits the mean longitudinal velocity into four regions of high-momentum fluid. Like the leading edge of the first element, a region of negative mean longitudinal velocity also forms on the second element. The area occupied by this separated region is a much larger percentage of the total cross-section than the corresponding region on the first element. See especially the contour of mean longitudinal velocity in Figure 5.11 c.

The vector plots in Figure 5.11 a,b show very strong, clearly defined vortices in the wake of the first element. Note that the vortices rotate in the direction opposite of the clockwise-twisting elements. These vortices were formed within the first-element section of pipe. Within the first $0.5L_e$ of the second element, they are transported away from the center of the cross-section to the pipe wall. The creation of mean vorticity at the surface of the element and on the pipe wall occurs in the same manner as it did in the first element. However, the mean vorticity created here rotates in the opposite direction because the second element twists in the opposite direction. Positive mean vorticity is produced on the pipe wall, and negative mean vorticity is produced on either side of the elements. The mean vorticity contours in Figure 5.11 c,d show a collection of positive and negative mean-flow vortices that suggests a very complicated pattern of vortex transport and interaction.

Outlet Section

Figure 5.12 shows the flow in the outlet section of the pipe. The cross-sections shown start from an axial location just downstream of the second element (Figure 5.12 a) and continue up to approximately $3.1d$ downstream (Figure 5.12 d). The flow in this outlet section should recover gradually toward a fully developed, turbulent pipe flow as the mean longitudinal vorticity created by the mixer decays to zero due to viscous effects. As seen in the figure, however, the complex three-dimensional structure of the flow persists for several diameters downstream of the second element.

The regions of high momentum leaving the second element are still present $3.1d$ into to the outlet. The flow patterns in the wake of the element suggest a very complex, three-dimensional interaction between the longitudinal flow and the transverse motion. It is evident, for instance, that the three-dimensional wake is being rotated by the mean transverse flow in the

clockwise direction. Figure 5.12 c clearly shows that two diameters downstream of the second element the continuously thickening wake has rotated 90° from the orientation of the trailing edge of the last element. Three diameters downstream of the element (Figure 5.12 *d*) two pockets of high momentum exist. Their existence suggests that the interaction of the longitudinal flow and the swirling motion established downstream of the element still dominate the evolution of the flow, which is far from approaching a fully developed state. The mean transverse flow in the outlet section is nearly as complicated as the flow in the second element. The negative-rotating mean vorticity that was produced on the surface of the element shows the same behavior as the positive-rotating mean vorticity from the first element did in the second element (compare Figure 5.12 a,b to Figures 5.11 a to d). However, this negative mean vorticity persists in the center of the pipe for a much longer interval, see Figure 5.12 c, which is one L_e beyond the second element. Approximately $2L_e$ beyond the second element, the mean transverse flow has decayed considerably, although the single clockwise-rotating cell is still present, and as discussed above, it dominates the evolution of the mean longitudinal flow. Also note the thick (red) layer of positive mean vorticity on the pipe wall. This layer covers almost all of the pipe wall in Figure 5.12 b and in Figure 5.12 c,d grows gradually thicker.

Three-Dimensional Structure of the Reversed-Flow Regions

The presence of pockets of reversed mean longitudinal flow near the leading and trailing edges of the elements underscores the complexity of the flow within a helical static mixer. The objective of this section is to illustrate the three-dimensional structure of these pockets of flow reversal.

Figure 5.10 to 5.12 indicate that regions of separation occur in the vicinity of the intersection of the two elements. For that reason, the six-element simulation (and, arbitrarily, at $Re = 20,000$) was used to visualize the structure of the reversed flow regions. Figure 5.13 shows the (black) regions of negative mean longitudinal velocity in relation to the (red) surfaces of the six elements. In the figure, the flow is from right to left. In Figure 5.13 a, the coordinate axes have the same orientation as the cross-sections in Figures 5.10 to 5.12. The vertical coordinate is x_3 (or z in Figure 5.13 a; the horizontal coordinate is x_2 (y in Figure 5.13 a). In Figure 5.13 b,

the coordinate axes are rotated 90° in the clockwise direction to show a different view of the separated regions.

By far, the largest regions of reversed flow occur in the first element. These reversed-flow regions have a spiral shape and extend through the whole first element and intersect with the regions occurring on the leading edge of the next element.

Reynolds Number and Number of Element Effects

This section summarizes the results of an investigation of the physics of the predicted mean flowfields and turbulence characteristics for mixers with different numbers of elements N_e over the range $5{,}000 \le Re \le 20{,}000$. Fig 5.14 shows a matrix of nine contour plots where each plot corresponds to a different simulation. As Figure 5.14 clearly shows, the predicted flowfields change very little for this number of elements in this range of *Re*. At the exit of the mixer, the only difference in the mean longitudinal velocity is that the regions of high momentum are organized into a more distinct 'L' shape for more elements at higher *Re*.

To compare the turbulence quantities at different *Re*, a normalized turbulence kinetic energy $\hat{k}$ is used

$$\hat{k} = \frac{k}{(k_a)_i}$$

where the average turbulence kinetic energy at the inlet of the computational domain $(k_a)_i$ is

$$(k_a)_i = \frac{4}{\pi}\int_{-\frac{1}{2}}^{\frac{1}{2}}\int_{-\frac{1}{2}}^{\frac{1}{2}} k\,dx_2 dx_3$$

The top row of contours in Figure 5.15 shows the distribution of the normalized turbulence kinetic energy $\hat{k}$ for each of the *Re*. (From these contours, the relative thickness of the turbulent boundary layer on the wall of the pipe clearly decreases with increasing *Re* as expected. The bottom matrix of nine contours corresponds to the same simulations and locations as the

contours in Figure 5.14. These plots clearly show a surprisingly strong effect of the number of elements on the turbulence kinetic energy leaving the mixer. For all three Reynolds numbers, the turbulence kinetic energy diminishes rapidly as the number of elements increases. This effect is especially pronounced for the two lower Reynolds numbers and suggests that a range of Reynolds numbers exists within which increasing the number of mixing elements tends to *laminarize* the flow. This observation is even more striking given that the (non-dimensional) turbulence kinetic energy, defined as , decreases with increasing *Re*. That is, the average turbulence kinetic energy at the inlet $(k_a)_i$ for *Re* of 5,000, 10,000, and 20,000 is 0.014, 0.011, and 0.08, respectively.

It is important to note that this is the first time that such a complex flow phenomenon has been suggested for helical static mixers. Some caution is required. No experimental evidence has been reported in the literature to support (or question) the present finding—recall, however, that all available experiments have focused on pressure drop and mixing measurements. Moreover, the first-order accuracy of the numerical method along with the rather coarse-grid resolution used for the parametric studies urge caution when interpreting the physics of the computed flows. Due to these numerical uncertainties, the present findings should be considered of qualitative nature only. For example, it is unlikely that the present simulations can be used to draw quantitative conclusions regarding the number of elements required to fully laminarize the flow for a given Reynolds number. These uncertainties not withstanding, the stabilizing effect of the mixer elements on the structure of turbulence appears to be a real, physical effect rather than a numerical artifact. Similar laminarization phenomena have been shown to occur in other flow in pipes with helical geometries, that is, the flow in a helical coil. Sreenivasan and Strykowski (1983) reported that for certain *Re* fully developed turbulent flow entered the coil and a laminar flow left the coil. More remarkable is the fact that this laminar flow persisted for $\mathcal{O}(1000)$ diameters downstream of the coil at a *Re* substantially above the critical *Re* for a normal turbulent pipe flow. It has been conjectured that the coil filters many of the perturbations that could cause re-transition to turbulence downstream of the coil. The laminarization effect of helical coils was first studied in the 1920s (Taylor 1929; White 1929). But, in spite of several recent studies on the general problem of the turbulent flow in and downstream of the helical coils (Webster and Humphrey 1993 a; Webster 1994; Hon, Humphrey, and Champagne 1999), the underlying physics of the phenomenon are still not understood (Webster and Humphrey 1993 b).

Table 5.3

Reynolds numbers in drinking water treatment plants. The calculation of the Reynolds number assumes a bulk velocity of 6 feet per second and a temperature of 20°C

Pipe diameter		Flow rate		
(mm)	(in.)	(10^6 L/d)	(mgd)	*Re*
100	4	1.2	0.34	200,000
500	20	31	8.5	1,000,000
1000	40	124	34	2,000,000
1500	60	279	75	3,000,000

The occurrence of laminarization phenomena in a related geometry provides qualitative evidence in support of the present findings. However, exploring this fascinating feature of the flow in helical static mixers further will require focused laboratory experiments in conjunction with more refined numerical simulations.

APPLYING THE CFD MODEL TO ISSUES IN WATER TREATMENT

This chapter began with a discussion of drinking water treatment and suggested that a fundamental understanding—coming in part from a fundamental, numerical model of the coagulation and disinfection processes—could help water suppliers ensure the safety and desirability of the drinking water they provide. The purpose of this section is to present some flowfield predictions in helical static mixers that are more relevant to the water treatment industry and to use these predictions to explore issues specific to drinking water treatment.

Flowfield Predictions for Water Treatment

The previous section provided predictions of the turbulent flow in helical static mixers with up to six elements for *Re* as large as 20,000. However, the *Re* in a typical, full-scale, water treatment plant is much higher than 20,000. To get an idea of the range, Table 5.3 shows the range of *Re* that can be expected for a static mixer functioning as a rapid mixer. Assuming a bulk velocity of 6 ft/s (1.8 m/s) for a raw water pipeline (Kawamura 1991), the flow rates and *Re* as-

sociated with a range of pipe diameters can be calculated directly. This calculation assumes that all the flow entering the plant would pass through one static mixer. The flow would not be split into parallel trains of treatment processes until after the rapid mixing step. For example, the calculation shows that a pipe diameter of 20 inches (500 mm) would give a flow rate of 8.5 mgd (31 ML/d) and $Re = 10^6$. For reference, this rate of water production, 8.5 mgd (31 ML/d), would fulfill the average daily needs of a city with a population of 55,000.

To address the issue of Reynolds number, calculations were performed for a two-element, helical static mixer with *Re*=100,000. The details of the CFD model are the same as those given previously. The number of grid nodes used was 1,035,125 or (245×65×65), and the first grid node off the wall was placed at $y^+ \approx 3$. This provides a resolution consistent with the coarse grid used for the lower-*Re* calculations. Also consistent with those calculations, the first-order accurate dissipation flux scheme was used.

This first section compares the results of the *Re*=100,000 to those obtained for the lower *Re* calculations. Figure 5.16 shows the predicted flowfield at *Re*=100,000 in the same manner as used in 5.10 to 5.12. That is, the figures show contours of the mean longitudinal velocity u_1, vector plots of the mean transverse velocity components u_2 and u_3, and contours of the mean longitudinal vorticity Ω_{x_1}. Figure 5.16 shows only the flowfield in the second element, which corresponds to Figure 5.11 for the *Re*=10,000.

Comparisons of the predicted flowfield at *Re*=100,000 with those at *Re*=10,000 show differences consistent with what is anticipated when increasing the *Re* in a turbulent flow. In particular, the velocity profiles are flatter. The regions of mean longitudinal vorticity are thinner. The boundary layers (especially in the outlet) are also thinner; compare. The reader should note that some of the more dramatic differences, especially for the mean longitudinal velocity, between the *Re* for this set of figures are due to differences in the grid resolution.

Similar to the predictions for the lower *Re*, the CFD model also predicts regions of reversed mean longitudinal velocity for *Re*=100,000. Although not shown here, the reversed-flow regions for the higher *Re* are smaller. The regions associated with the leading edge of the first element is larger than those on the second element. But, unlike the lower *Re* (Figure 5.13) those regions on the first element do not span the entire element.

Rapid Mixing for Coagulation

Over the past fifteen years, two theories of rapid mixing for coagulation have been developed. They are both motivated by the experimental observation that the intensity of mixing affects the outcome of coagulation for certain chemical conditions and not for others (Mills and Amirtharajah 1982). The second observation was that the reactions to produce the coagulant species are very fast, which suggests that the coagulation reactions fall into a class of reactions that are widely studied in Chemical Engineering, namely, fast, competitive-consecutive reactions (Clark 1986, 1987). The significance of this class of reactions is that the product distribution is affected by the micromixing or mixing on the molecular level, which is a function of the properties of the flowfield where the reactions take place.

Amirtharajah and Trusler (1986) extended existing theories (Saffman and Turner 1956; and Delichatsois and Probstein 1975) of particle (or cloud droplet) collisions in turbulent flowfields to rapid mixing for coagulation. They assumed that one of the particles in the existing theories could be replaced by coagulant-containing eddies. These eddies correspond to the small-scale eddies, which have a size of the same scale as the Kolmogorov microscale. A key part of both models is the ability to account for regions with differing levels of turbulence energy dissipation ε. To apply their model to a stirred-tank reactor, they divided the reactor into three zones of different ε based on the existing literature data. In developing another rapid-mixing theory, Clark, Strivastava, and David (1993) applied an existing theory for micromixing called the Interaction by Exchange with the Mean or IEM model to the base neutralization of aluminum chloride—roughly the opposite of the coagulation reactions, which are addition of acid (aluminum sulfate or alum) to water. This model also depends on the distribution of turbulence energy dissipation within the reactor.

Both of these theories are in the beginning stages of development. To further apply and test these models requires the ability to characterize the flowfield and more specifically the turbulence energy dissipation in the mixer. The potential of the CFD model to provide this information is demonstrated in Figure 5.17. Figure 5.17 shows the distribution of the (non-dimensional) rate of dissipation of turbulence kinetic energy ε at three locations within the mixer at a Re=100,000. The cross-sections are located just upstream of the first element, just downstream of the intersection of the two elements, and just downstream of the second and last ele-

ment. From the figure, the regions of the highest ε occurs near the leading and trailing edges of the elements with by far the largest region occurring at the intersection of the two elements (Figure 5.17 b). A simplistic view of both rapid mixing theories suggests that destabilization increases with increasing turbulence energy dissipation. Moreover, the coagulation reactions occur on a time scale faster than the detention time of the static mixer. These considerations together with Figure 5.17 b suggest that the intersection of the two elements might be a good location to inject the coagulant.

G-value for Static Mixers

The purpose of this section is to calculate the predicted mean *G*-value in the two-element static mixer and to compute a local *G*-value that is sometimes also suggested. Camp and Stein (1942) developed the root-mean-squared *G*-value to characterize mixing in flocculation basins. The theoretical development was an extension of the role of the velocity gradient in orthokinetic flocculation in pure shear flows. Essentially, Camp and Stein derived the *G*-value to represent the equivalent velocity gradient for a three-dimensional, turbulent flow. During the ensuing decades, the concept of the *G*-value has permeated Environmental Engineering to the point where it is included in nearly all textbooks. The *G*-value has been extended to characterize a variety of flowfield-induced mixing processes including the rapid mixing of coagulants, floc breakup, hydraulic flocculation, air and water induced-circulation in channels, short-circuiting in tanks, and filter cleaning during backwash (Graber 1994).

Numerous authors (Amirtharajah 1978, Clark 1985, Cleasby 1984, Kramer 1997, Karmer and Clark 1997, Graber 1997, 1998) have discussed the inadequacies of the *G*-value. There is no need to go into a detailed discussion of the *G*-value here; the references listed above can be consulted instead. In short, several problems with the original derivation exist. These inadequacies can be summarized by saying that the *G*-value reduces the process of mixing in extremely complex, turbulent flowfields to one number—a reduction that is unlikely to be successful regardless of the theoretical assumptions. The predictions shown previously in this chapter illustrate the complexity of the flowfields in helical static mixers and thus the futility of the *G*-value approach.

Nonetheless, the *G*-value is thoroughly entrenched in the Environmental Engineering literature. Therefore, the predictions of the flowfield in a helical static mixer at Re=100,000 are

used to compute both a global mean and a local G-value and to compare the results. The mean $\overline{G}$ -value is traditionally defined as follows (an asterisk indicates that the quantity is dimensional)

$$\overline{G}^{*} = \sqrt{\frac{Po^{*}}{\mu^{*} V^{*}}} \tag{5.5}$$

where Po^{*} = the power dissipated by the mixer,

μ^{*} = the dynamic viscosity

V^{*} = the volume of the mixer.

For a static mixer, Equation 5.5 can be written as

$$\overline{G}^{*} = \sqrt{\frac{\gamma^{*} Q^{*} \Delta h^{*}}{\mu^{*} V^{*}}} = \sqrt{\frac{Q^{*} \Delta p^{*}}{\mu^{*} V^{*}}}$$

where Δh^{*} = the head loss across the mixer,

Δp^{*} = the pressure drop.

Expanding the volume and the flow rate in terms of the cross-sectional area (which cancels) yields

$$\overline{G}^{*} = \sqrt{\frac{U_{o}^{*} \Delta p^{*}}{\mu^{*} N_{e} (L_{e})^{*}}} \tag{5.6}$$

The definition of the friction factor f is

$$f = 2 \frac{\Delta p^{*}}{N_{e} (L_{e})^{*}} \tag{5.7}$$

Substituting Equation 5.7 into Equation 5.6 yields

$$\bar{G}^{*} = \sqrt{\frac{U_o^{*} f}{2\mu^{*}}} \tag{5.8}$$

Converting to a non-dimensional $\bar{G}$ value with $U_o = 1$ and $\mu^{*} = 1/Re$ yields

$$\bar{G} = \sqrt{\frac{1}{2} f Re}$$

Using Equation 5.7 together with the two-element simulation at Re=100,000 gives a friction factor of 0.98 and, thus, Equation 5.8 yields a non-dimensional $\bar{G}$-value of 220. To obtain a dimensional $\bar{G}$-value, simply multiply the non-dimensional one by U_o^{*}/L_o^{*}. Using values consistent with Table 5.3, that is, $U_o^{*} = 6$ ft/s (1.8 m/s) and $L^{*} = d^{*} = 2$ inches (51 mm), gives a $\bar{G}$-value of 7,920 s^{-1}. This $\bar{G}$-value corresponds to a flow of 60 gpm (3.8 L/s) and a predicted head loss Δh^{*} of 1.6 feet (0.5 m).

Following other authors (Amirtharajah and Trusler 1986, Luo 1997), a local G-value (no overbar) can also be defined that depends on the local turbulence energy dissipation ε.

$$G = \sqrt{\frac{\varepsilon}{\nu}} \tag{5.9}$$

Figure 5.18 shows contours of the local G-value for the same three cross-sections as in Figure 5.17. Note that the largest contour level is $G = 200$ (7,200 s^{-1}), which is smaller than the mean $\bar{G}$-value of 220 (7,920 s^{-1}) computed from Equation 5.8. To explore this issue further, an average local G-value is computed by averaging the local G-value over each cross-section to obtain G_a. It is defined in the same manner as the cross-sectional average of the turbulence kinetic energy that was defined in previous sections.

$$G_a = \frac{4}{\pi}\int_{-\frac{1}{2}}^{\frac{1}{2}}\int_{-\frac{1}{2}}^{\frac{1}{2}} G\,dx_1\,dx_2$$

Figure 5.19 shows the local G-value averaged over each cross-section for the entire computational domain. From this figure, its clear that the G_a-value never reaches $\overline{G}$=220 (7,200 s^{-1}) that was calculated based on the pressure drop across the mixer.

Comparing Figure 5.19 to $\overline{G}$=220 (7200 s^{-1}) suggests that the local G-value in Equation 5.9 is not the same as the mean $\overline{G}$ calculated from the pressure drop. Following Bourne, Kut, and Lenzner (1992), the total energy dissipated in a turbulent flow is the sum of two quantities: the turbulence energy dissipation ε and the dissipation due to the mean flow. From Figure 5.19, this local G-value only includes the portion of energy dissipation due to turbulence.

CONCLUSIONS

1. The numerical model developed in this chapter is capable of predicting the mean-flow characteristics of complex three-dimensional flows with accuracy sufficient for engineering simulations. Comparisons with detailed mean-flow measurements for flow through a strongly curved pipe bend demonstrated the ability of the model to capture the strength of the secondary motion and its impact on the streamwise flow with satisfactory accuracy.
2. The flow in helical static mixers is highly three-dimensional and dominated by intense, counter-rotating, longitudinal vortices. These vortices originate (at least in part) via the transverse pressure gradients induced by the twisting elements. The vortices have a significant impact on the distribution of longitudinal momentum within a given cross-section in the mixer. Downstream of the last element, the vortices exiting the mixer merge to form a single-cell of swirling flow. This swirling, three-dimensional wake persists for several diameters downstream of the mixer (the actual distance depends on the Reynolds number) and dominates the asymptotic recovery of the flow toward fully developed pipe flow.
3. A previously unknown feature of the flow in helical static mixers is the presence of pockets of reversed flow near the leading and trailing edges of the mixer elements.

These pockets appear at the junction of the element and the pipe wall, presumably due to locally-induced adverse pressure gradients. These reversed-flow regions were for all *Re* simulated, but their size depends strongly on the Reynolds number. In fact, the size of these reversed-flow pockets was found to shrink substantially, compared to lower Reynolds number flowfields, at *Re*=100,000. These regions of reversed flow could significantly affect mixing efficiency because such regions can prevent transport across the mixer cross-section. Given the complexity of the flowfield in a helical static mixer, however, the precise effect of these regions cannot be understood without comprehensive Lagrangian particle tracking studies and more advanced numerical studies.

4. A study of the effect of the number of elements on the flowfield and turbulence quantities for a range of Reynolds numbers showed that the number of elements has only a small effect on the mean flowfield. However, the number of elements has a dramatic effect on the turbulence kinetic energy leaving the mixer. More specifically, these computations suggest that there exists a range of Reynolds numbers within which increasing the number of mixer elements has a stabilizing effect on the flow, causing the incoming turbulence to collapse by the time it exits the mixer. The intensity of the laminarization appears to decrease with increasing Reynolds number. Although no experimental data exist to support or refute the occurrence of this phenomenon in helical static mixers, this finding is supported by experiments in helical coils, a geometry closely related to a helical static mixer, that have reported similar laminarization phenomena.
5. The stabilizing effect of the elements on the incoming turbulent flow could have obvious significant implications on the overall mixing efficiency of helical static mixers. In fact if flow laminarization occurs within the range of Reynolds numbers suggested by the model (experiments must be carried out to confirm this effect with certainty), great care must be exercised when interpreting the results from experiments with static mixers in pilot plants. The Reynolds numbers encountered in pilot plants are much closer to the range of Reynolds numbers where laminarization occurs in the CFD model predictions. Full-scale plants have much larger Reynolds numbers, $\mathcal{O}\left(10^6\right)$, where laminarization would be unlikely to occur. This further emphasizes

the complexity of the mixing process in helical static mixers and the complicated dependence of mixing on the Reynolds number.

6. The CFD model can be used to obtain reliable predictions of pressure drop across the mixer as a function of Reynolds number and the number of mixer elements. The model's predictions can also provide information that can be used to extended the existing theories of rapid mixing for coagulation or mixing for disinfection in water treatment.

RECOMMENDATIONS FOR FUTURE WORK

The modeling study described in this chapter helps identify several important areas for future research. These areas are critical prerequisites for enhancing the understanding of the physics of the flow in helical static mixers and for identifying the role various flow phenomena play in the mixing process. Specific recommendations are listed below.

1. The structure of the flow in helical static mixers emerging from the numerical simulations is far more complicated than what could be deduced from the few available experiments. To make further progress, sophisticated experiments must be carried out to provide detailed information to validate and further refine the present numerical model. First, simple flow visualization experiments, conducted by injecting dye upstream and downstream of the mixer elements, can be carried out to determine whether flow laminarization takes place within the range of Reynolds numbers suggested by the model. Second, detailed mean-flow and turbulence-statistics measurements should be obtained to provide a thorough model validation. The present numerical model can be used to guide such experiments by identifying the regions where complex phenomena are likely to occur and where high experimental resolution is required. Given the preliminary findings concerning the existence of possible mean-flow unsteadiness, such experiments should be carried out with great care and should attempt to detect the existence of large-scale coherent structures in the flow by detailed statistical analysis of measured instantaneous time records of various flow quantities.

2. The numerical model developed in this thesis should be extended to unsteady flows and applied, in conjunction with high-resolution numerical schemes, to simulate both laminar and turbulent flows in helical static mixers. This will eliminate the numerical uncertainties identified in this work and help, along with the experiments, to obtain a more comprehensive understanding of the various flow phenomena. Note that the current CFD model can be readily extended to unsteady flow through the use of the dual time-stepping procedure.
3. It will be very useful to investigate in detail the role of turbulence modeling on the predictive capabilities of the CFD model. Recent studies (Sotiropoulos and Ventikos 1998) with steady-in-the-mean turbulent flows with strong vortices suggest that non-linear eddy-viscosity models can dramatically improve the prediction of both the mean flow and turbulence statistics. Extrapolating from these studies, applying such models to helical static mixers in conjunction with unsteady RANS simulations could result in predicted flow that are considerably more complex. The availability of detailed laboratory experiments, however, is critical to the success of such a challenging undertaking.
4. For coagulation and rapid mixing in water treatment, a future experimental study should investigate different injection points for the coagulant focusing, in particular, on the intersection of the mixer elements. The existing CFD model could easily be used to guide such an experiment.

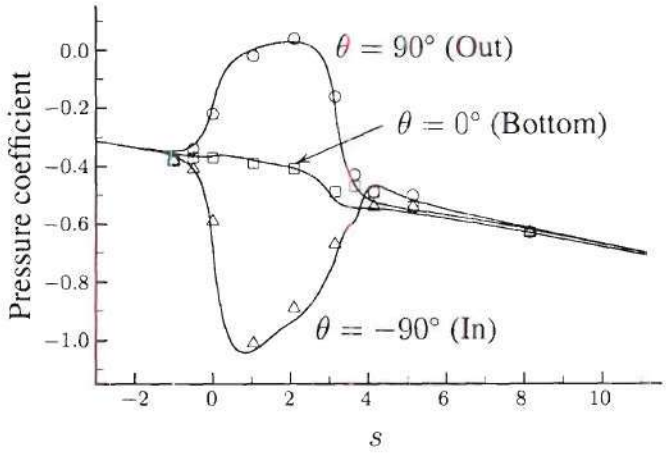

Figure 5.1 Predicted and measured pressure coefficient

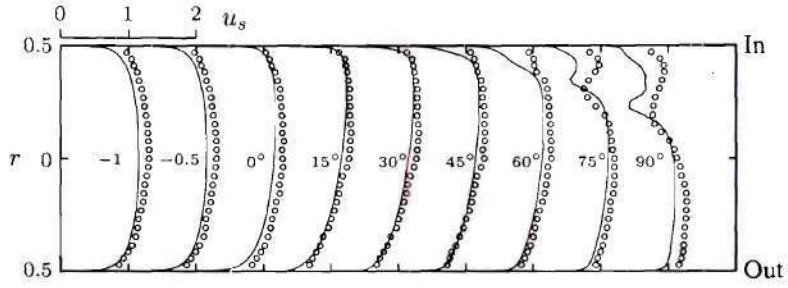

(a) Longitudinal velocity u_s on symmetry plane $z = 0$

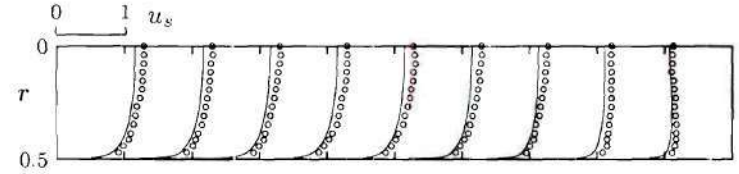

(b) Longitudinal velocity u_s on vertical plane $\theta = 0$

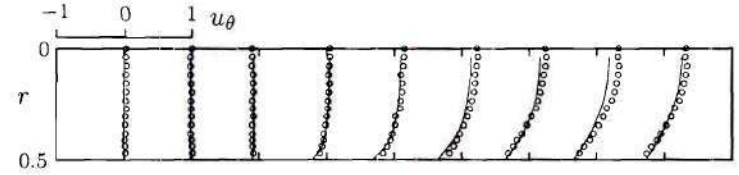

(c) Circumferential velocity u_θ on vertical plane $\theta = 0$

Figure 5.2 Velocity profiles within the bend and upstream of it

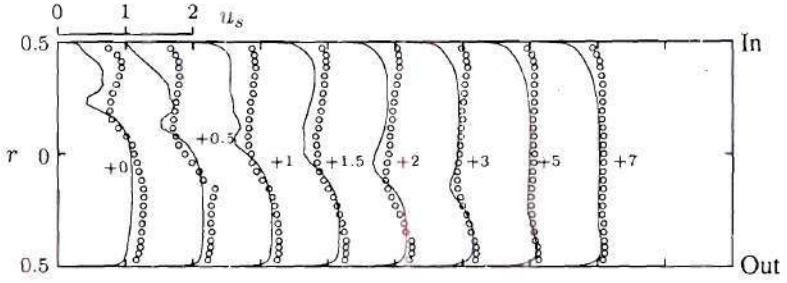

(a) Longitudinal velocity u_s on symmetry plane $z = 0$

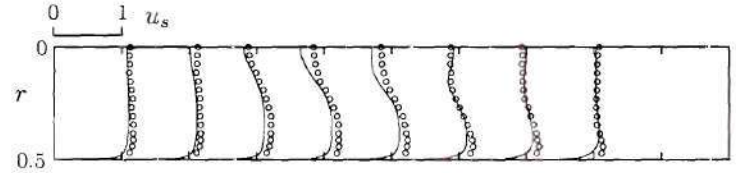

(b) Longitudinal velocity u_s on vertical plane $\theta = 0$

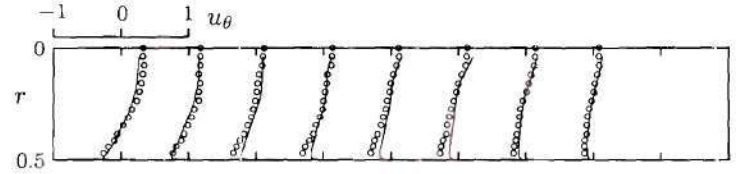

(c) Circumferential velocity u_θ on vertical plane $\theta = 0$

Figure 5.3 Velocity profiles downstream of the bend

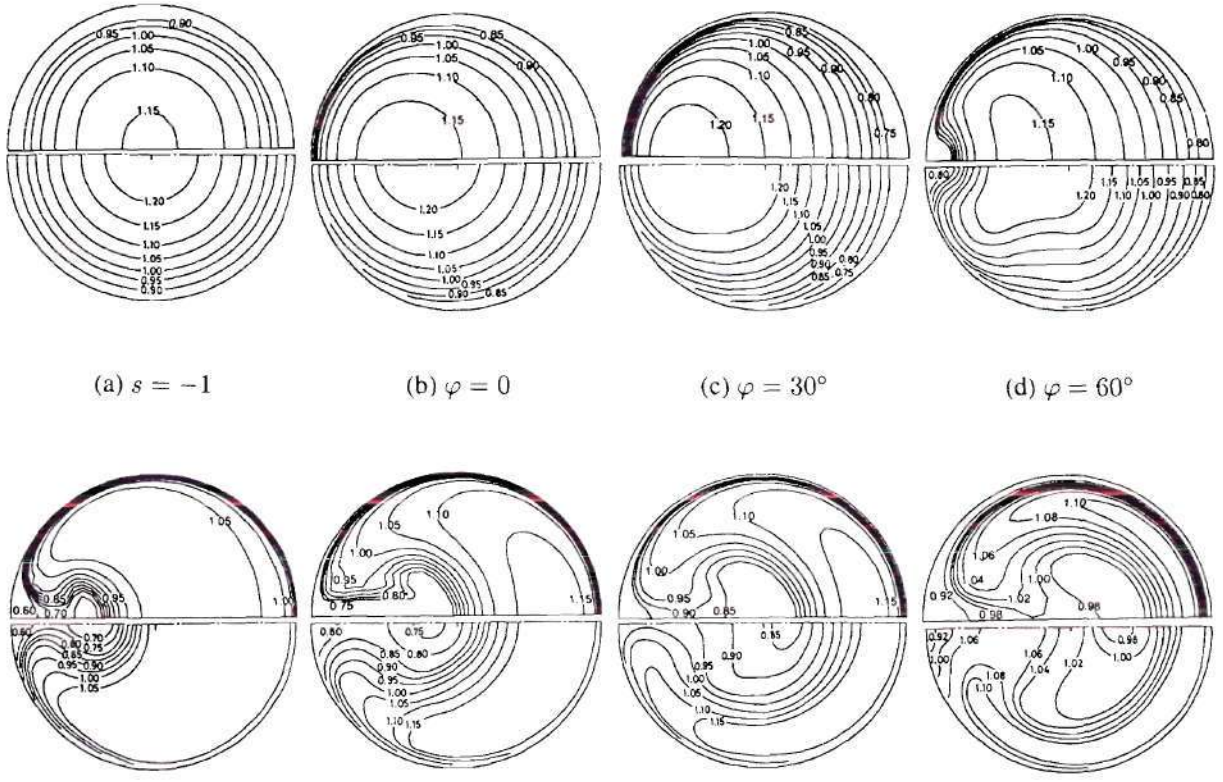

(a) $s = -1$ (b) $\varphi = 0$ (c) $\varphi = 30°$ (d) $\varphi = 60°$

(e) $\varphi = 90°$ (f) $s = \pi + 1$ (g) $s = \pi + 2$ (h) $s = \pi + 5$

Figure 5.4 Contours of the longitudinal velocity u_s with predictions in the top semi-circles and the measurements in the bottom ones

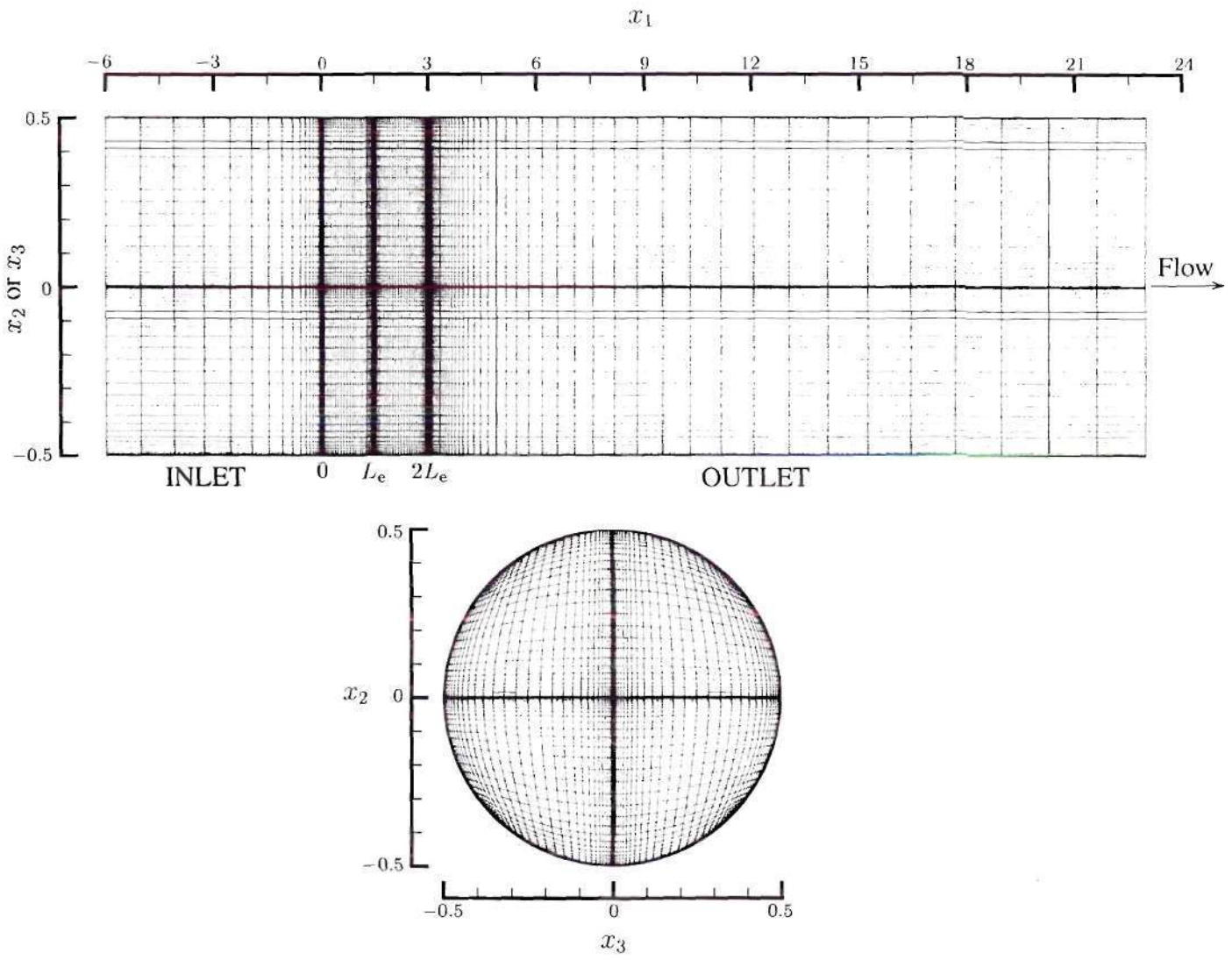

Figure 5.5 Computational grid for the turbulent flow predictions. The top of the figure shows a longitudinal cross-section that has been untwisted to emphasize the clustered grid near the leading and trailing edge of the elements. The bottom of the figure shows a transverse cross-section to emphasize the clustered grid near the sides of both elements.

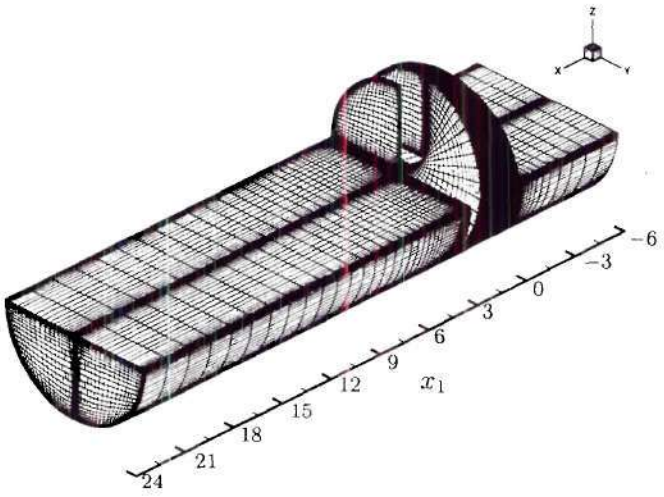

(a) One-half of the grid.

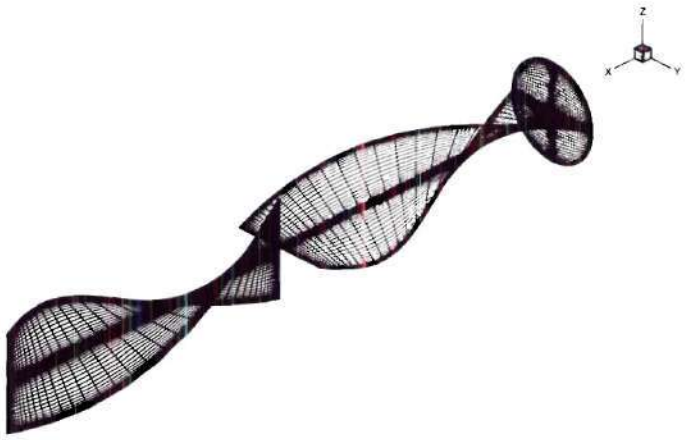

(b) Close-up of the two elements.

Figure 5.6 Three-dimensional picture of the computational grid with only one-half of the domain shown for clarity. The whole domain was used in the simulations.

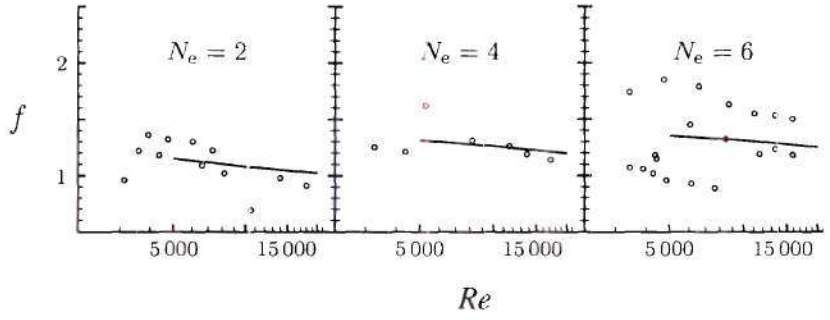

Figure 5.7 Friction factor comparison of predictions (lines) and experiments (circles) for different numbers of elements

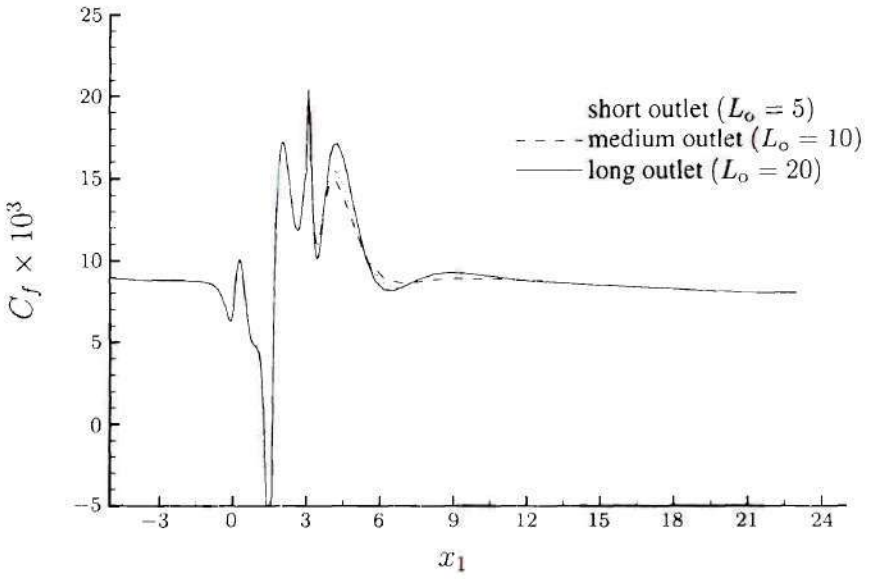

Figure 5.8 Effect of the outlet length on the skin-friction coefficient C_f at a point near the pipe wall plotted versus the longitudinal coordinate x_1

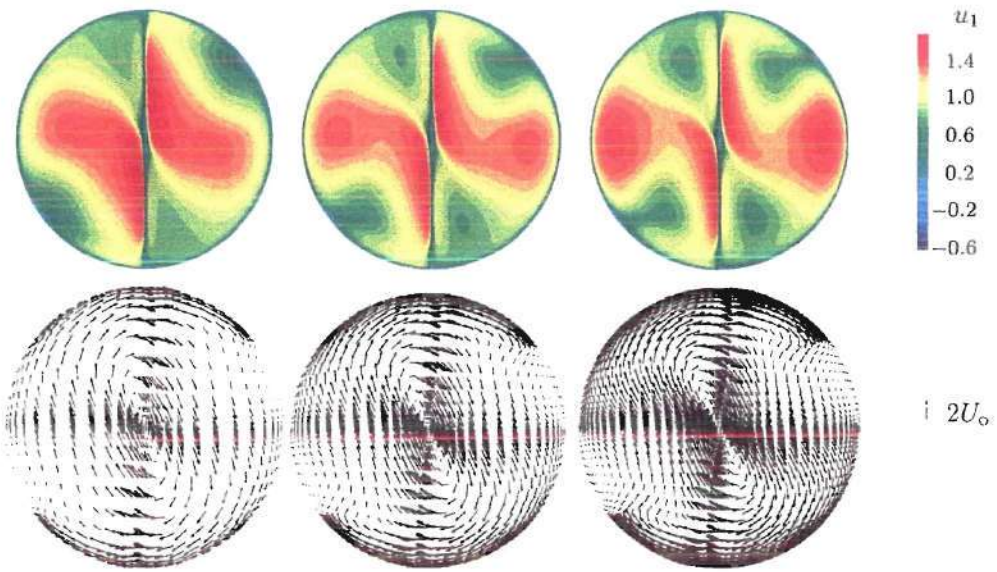

Figure 5.9 Effect of grid resolution on the flowfield. All three cross-sections are located at the exit of the two-element mixer at $Re = 10\,000$. The top row shows contours of the mean longitudinal velocity; the bottom row shows vectors of the mean transverse velocity.

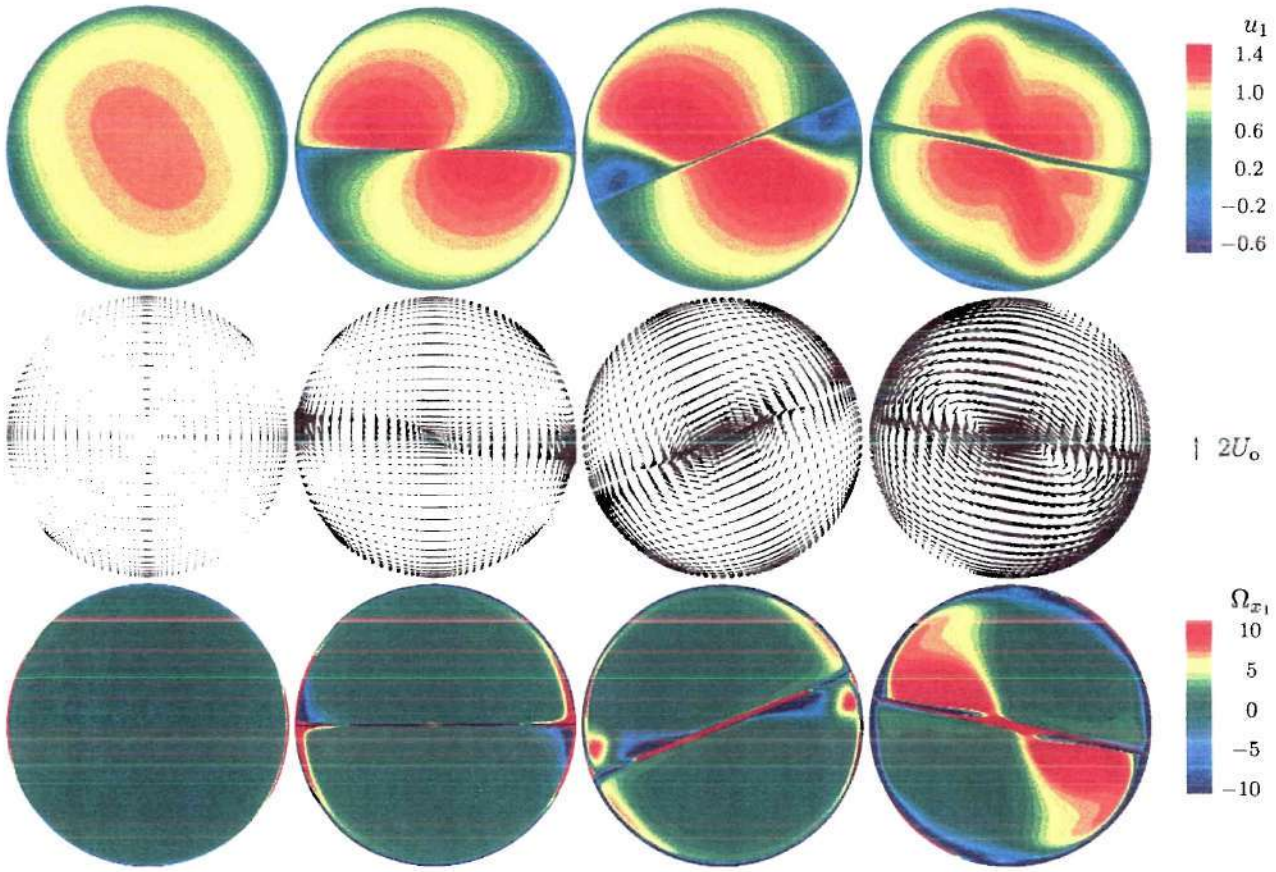

Figure 5.10 Flowfield upstream of and within first element for a simulation at $Re = 10\,000$ and two elements. The top row shows contours of the mean longitudinal velocity u_1; the middle row shows vectors of mean transverse velocity u_2 and u_3; and bottom row shows contours of the mean longitudinal vorticity Ω_{x_1}.

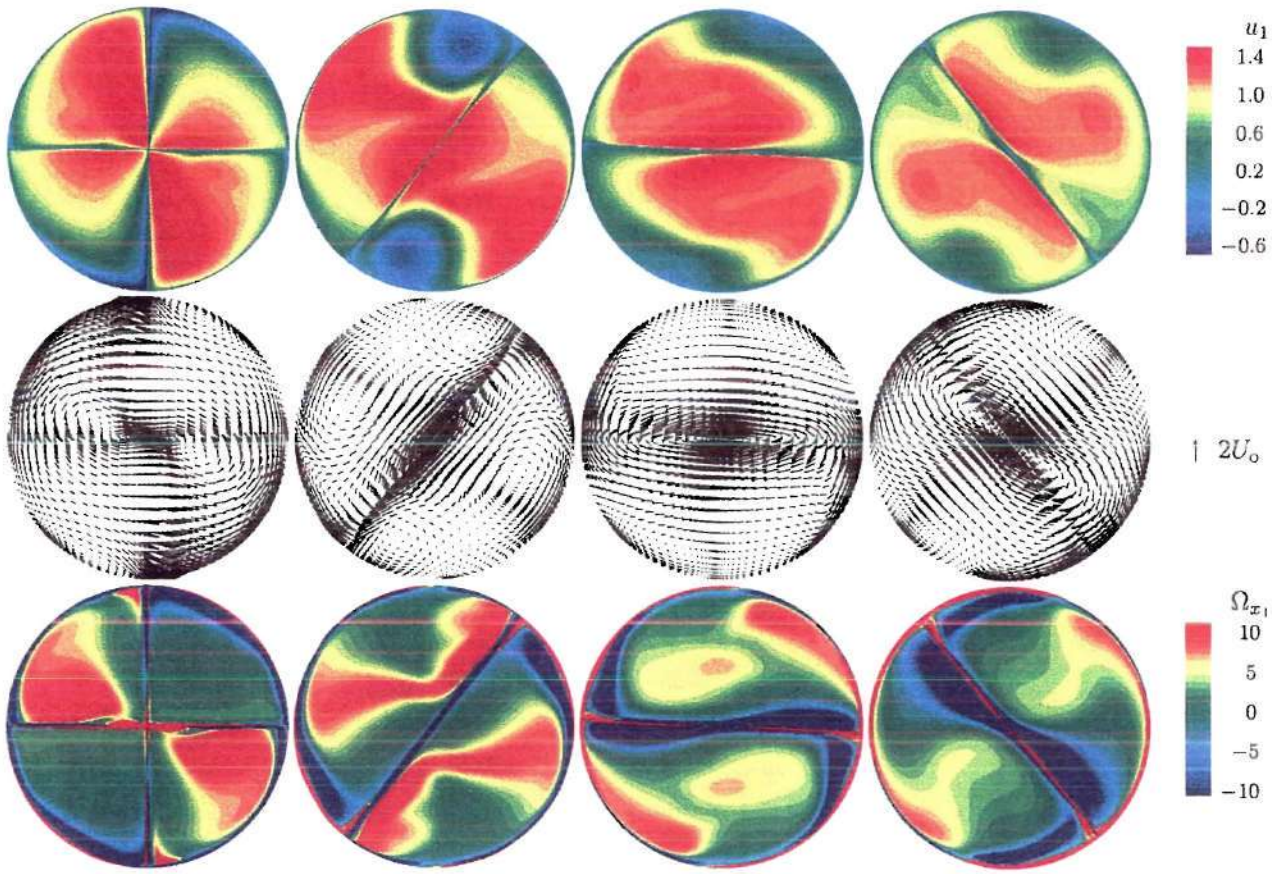

Figure 5.11 Flowfield within the second element for a simulation at $Re = 10\,000$ and two elements. The top row shows contours of the mean longitudinal velocity u_1; the middle row shows vectors of mean transverse velocity u_2 and u_3; and the bottom row shows contours of the mean longitudinal vorticity Ω_{x_1}.

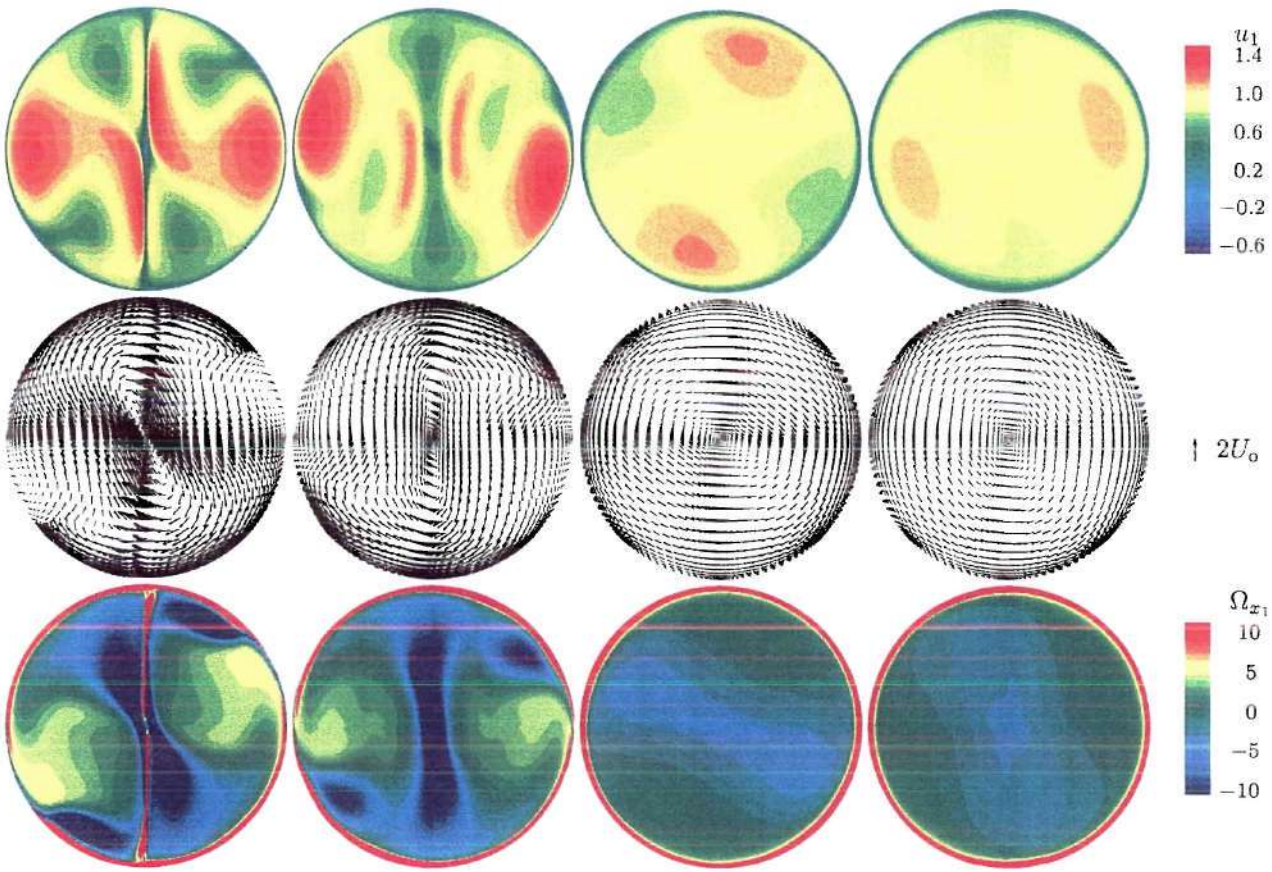

(a) $x_1 = 3.003$ (b) $x_1 = 3.262$ (c) $x_1 = 11.060$ (d) $x_1 = 12.082$

Figure 5.12 Flowfield downstream of the mixer elements for a simulation at $Re = 10\,000$ and two elements. The top row shows contours of the mean longitudinal velocity u_1; the middle row shows vectors of the mean transverse velocity u_2 and u_3; and the bottom row shows contours of the mean longitudinal vorticity Ω_{x_1}.

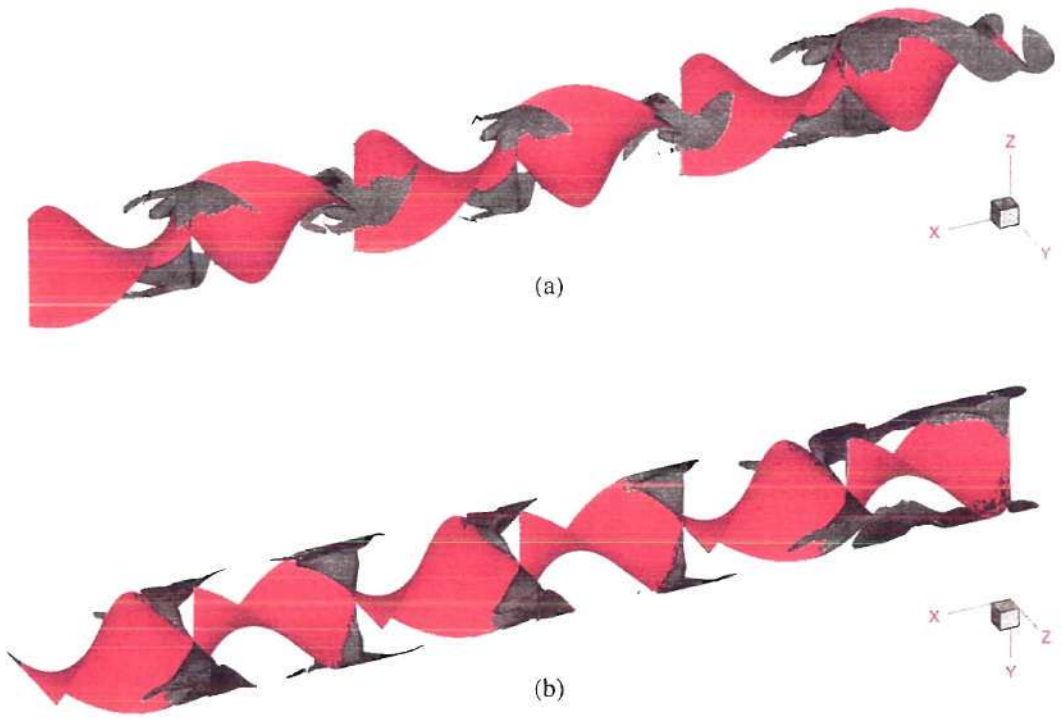

Figure 5.13 Regions of reverse flow ($u_1 < 0$) in a six-element mixer at $Re = 20\,000$. The bottom plot (b) is rotated 90° about the longitudinal direction.

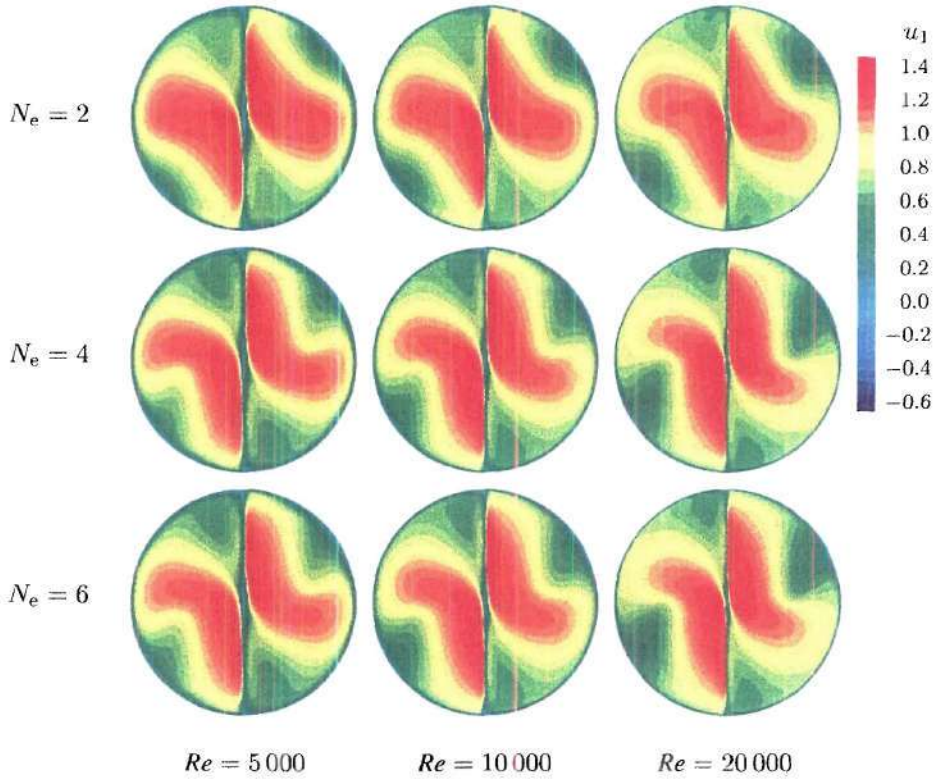

Figure 5.14 Effect of the number of elements on the mean longitudinal velocity for a range of Reynolds numbers. Each cross-section is located at the trailing edge of the last element.

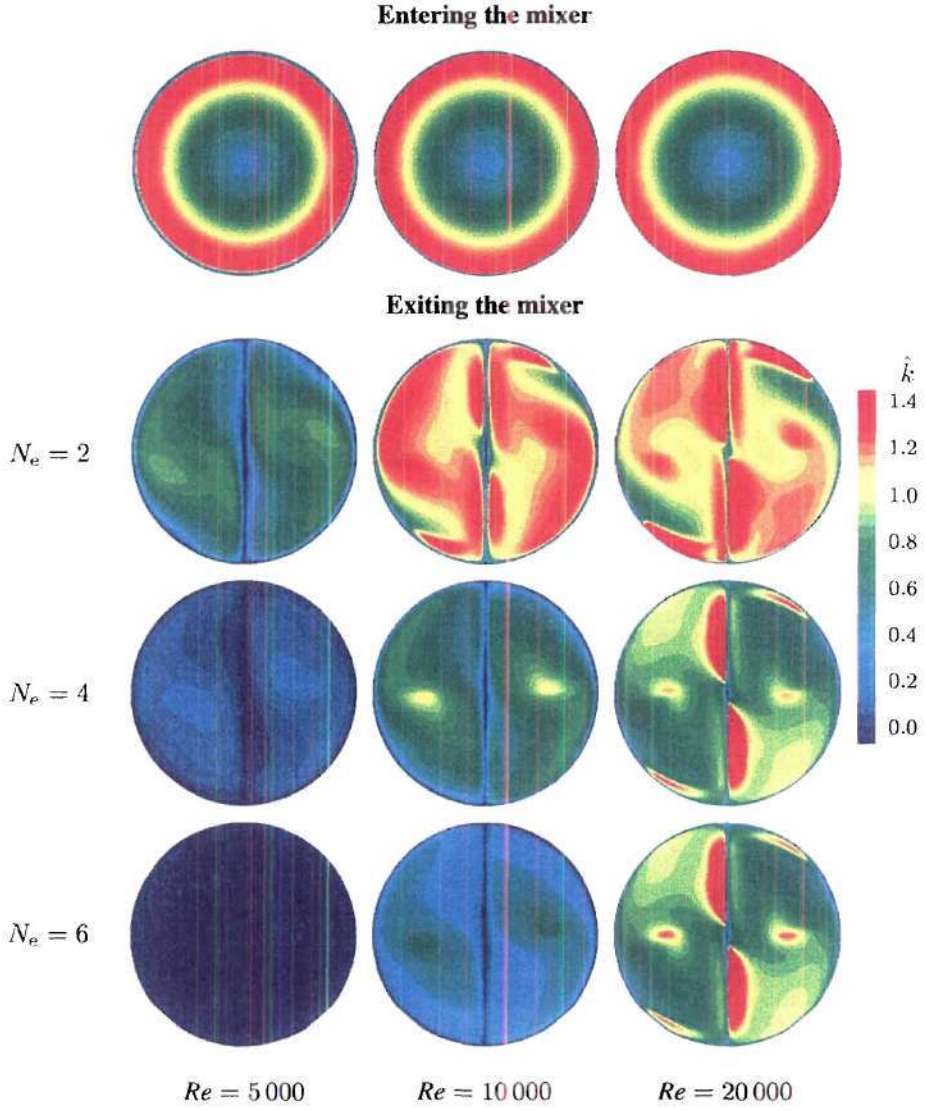

Figure 5.15 Effect of the number of elements on the turbulence kinetic energy for a range of Reynolds numbers. The top row of three contours is the normalized turbulence kinetic energy entering each mixer for each of the three Reynolds numbers. Each of the bottom nine cross-sections is located at the trailing edge of the last element.

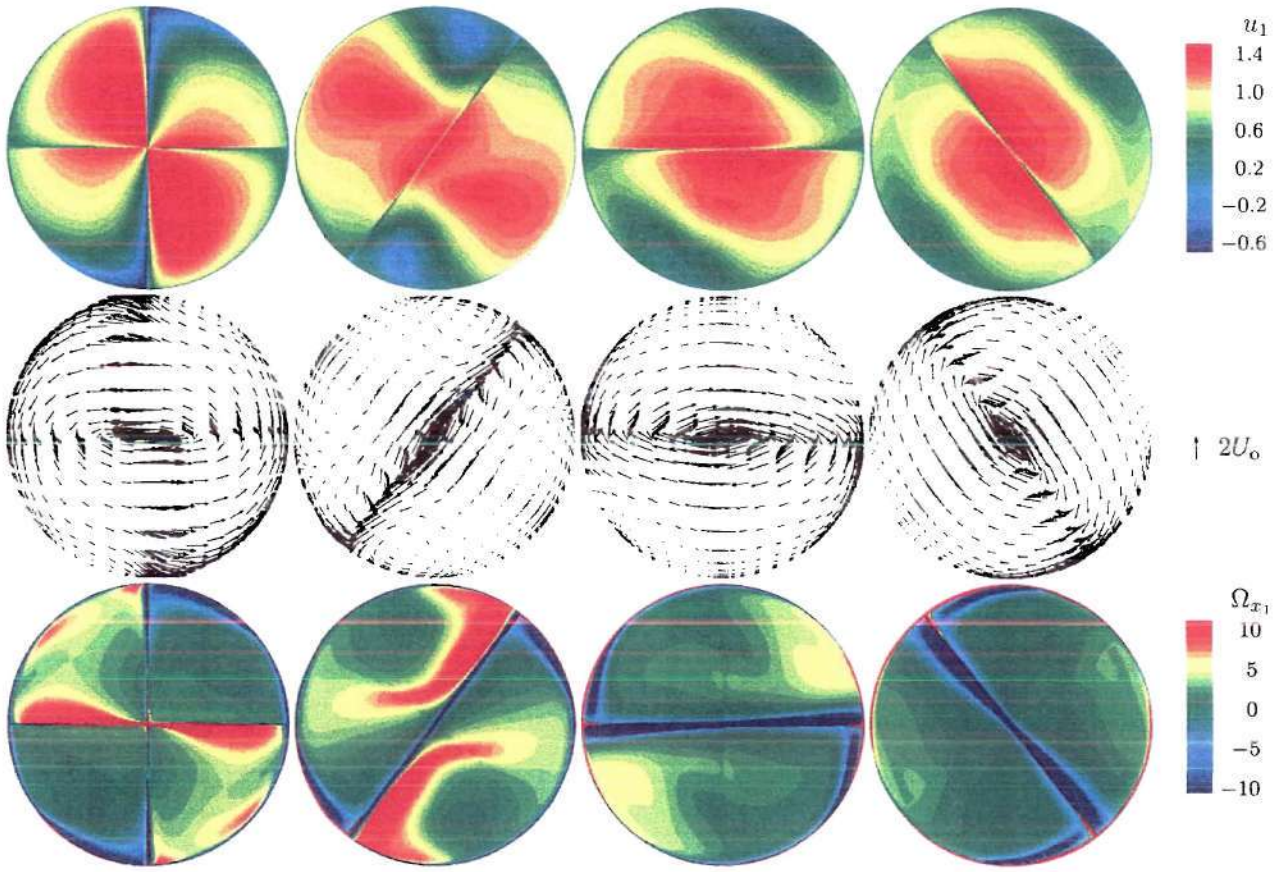

(a) $x_1 = 1.5 = L_e$ (b) $x_1 = 1.816 \approx 1.2L_e$ (c) $x_1 = 2.250 = 1.5L_e$ (d) $x_1 = 2.684 \approx 1.8L_e$

Figure 5.16 Flowfield within the second element for a simulation at $Re = 100\,000$ and two elements. The top row shows contours of the mean longitudinal velocity u_1; the middle row shows vectors of mean transverse velocity u_2 and u_3; and the bottom row shows contours of the mean longitudinal vorticity Ω_{x_1}.

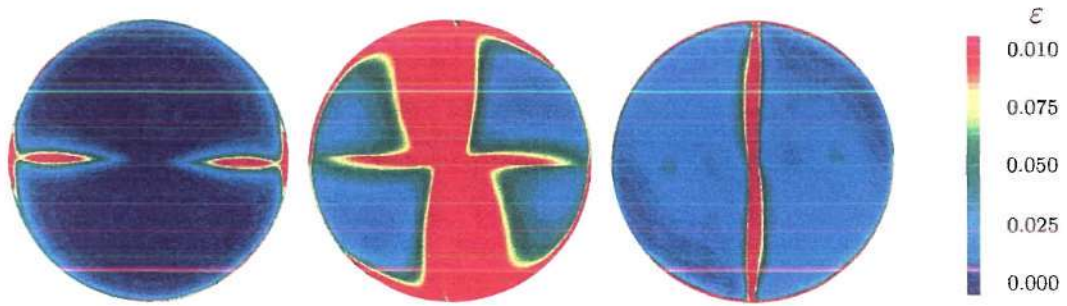

(a) $x_1 = -0.027$ (b) $x_1 = 1.526 \approx L_e$ (c) $x_1 = 3.004 \approx 2L_e$

Figure 5.17 Distribution of turbulence energy dissipation in a two-element, helical static mixer at $Re = 100\,000$.

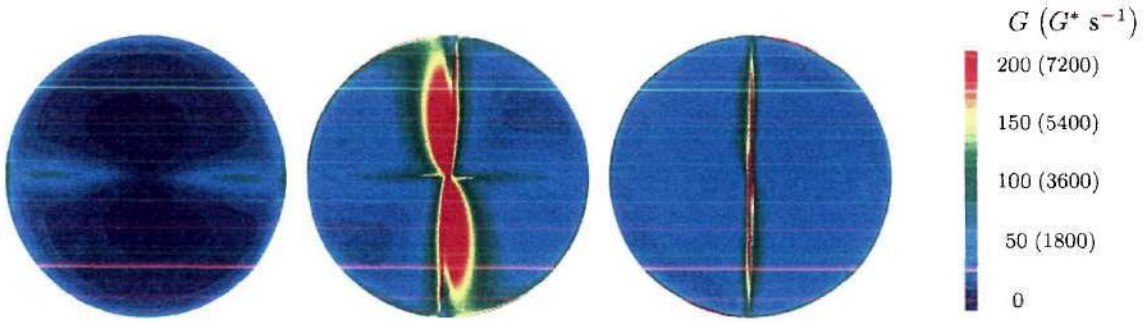

(a) $x_1 = -0.027$ (b) $x_1 = 1.526 \approx L_e$ (c) $x_1 = 3.004 \approx 2L_e$

Figure 5.18 Distribution of local G-value in a two-element, helical static mixer at $Re = 100\,000$.

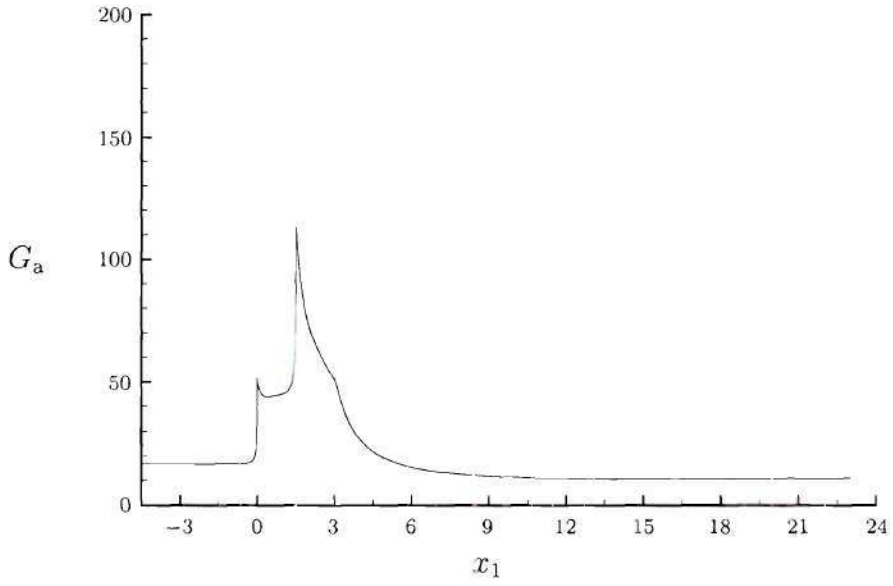

Figure 5.19 Average local G-value for $Re = 100\,000$ plotted versus the longitudinal coordinate. To obtain G_a in units of s^{-1}, multiply by 36.

Page missing from thesis

CHAPTER 6
CONCLUSIONS

OVERVIEW

This report presents the results of a multifaceted study on the use of static mixers for coagulation and disinfection in drinking water treatment. The research combined pilot-scale testing of several static mixers for coagulant mixing (Chapter 2); bench-scale testing of static mixers for inactivation of *Cryptosporidium parvum* (Chapter 3); and integrated these empirical studies with the development of a new disinfection model (Chapter 4) and a computational fluid dynamics model (Chapter 5) for predicting the complex flowfield in a static mixer. The conclusions specific to each facet of the study are presented in the individual chapters of this report. The following is a listing of the major conclusions from each part of the research project, and it also includes a synthesis of the conclusions from the different chapters as they relate to one another.

The recommendations for future work are noted at the end of each chapter and are specific to the topics discussed in that chapter. Therefore, they are not described in this concluding chapter.

STATIC MIXERS FOR COAGULATION

Four different static mixers were tested at the pilot scale to evaluate performance in coagulation and assess the effects of static mixer geometry, differences due to number of elements, and differences due to the diameter and head losses generated. The static mixers evaluated were: (1) Kenics helical static mixer (KMS), (2) Koch SMV mixer (SMV), (3) TAH Spiral mixer (Spiral), and the TAH Stata-tube mixer (Stata-tube). The performance of one of these mixers was also evaluated in comparison with a backmixer, and four of the mixers were compared with turbulent flow mixing in a pipe with no elements (empty pipe). The following conclusions are drawn from the pilot-plant experiments:

1. Under sweep coagulation chemical conditions with alum, all of the static mixers and the backmixer were very effective for rapid mixing based on settled-water turbidity, filtered-water turbidity, and filtered-water particle counts.
2. On the basis of streaming current measurements, filtered-water turbidities, and filtered-water particle counts, the KMS mixer performed as well as or better than the backmixer and the empty pipe for almost all the raw water, chemical, and mixing conditions tested.
3. For direct filtration or flotation plants where charge neutralization conditions and pinpoint floc are desired, the KMS mixer reduced the necessary alum doses by 20 to 30% as compared to the backmixer.
4. A comparison of static mixers with an empty pipe indicated that as scale increased (from 1 to 2 inches in diameter), the Reynolds number decreased from 10,500 to 2,200 and the static mixer maintains effective mixing while the empty pipe did not perform as well as the static mixer. This suggests that at higher diameters (greater than 2 inches) a static mixer is necessary for efficient mixing of coagulants.
5. The experiments on mixing intensity changes with number of elements suggests that there is a minimum mixing intensity required for treatment and additional elements only cause increases in detention time and head loss. This minimum number appears to be three or four. The CFD model studies indicate that the number of elements has only a small effect on mean flowfield but a dramatic effect on turbulence kinetic energy leaving the mixer. The highest turbulence kinetic energy at Reynolds numbers of 5,000 to 20,000 occurs at the exit from a two-element mixer indicating that a larger number of elements may not be useful.

INACTIVATION OF *CRYPTOSPORIDIUM PARVUM* USING STATIC MIXERS

In these studies, a new technique for measuring the inactivation (viability) of *Cryptosporidium parvum* oocysts using Madine Darby Canine Kidney (MDCK) cells was explored. This technique was used to determined the effectiveness of mixing of chlorine-based disinfectants in bench-scale experiments with 0.5-inch diameter static mixers. Six sets of experiments were completed with two- and six-element helical mixers, the Omega mixer, the Stata-tube mixer and an

empty-pipe mixer at Reynolds numbers of 3,000 to 3,500. The following conclusions are drawn from these studies, which were completed at the Centers for Disease Control and Prevention, Atlanta, Ga.

1. The MDCK cell culture method for testing infectivity of *Cryptosporidium parvum* oocysts is useful, reproducible, and gives an accurate measure of infectivity.
2. There was no discernible difference among the two-element helical mixer, the Omega mixer, and the empty-pipe mixer. All three mixers had less than 0.8 log inactivation of *Cryptosporidium parvum* at a free chlorine $C \times T$ value of approximately 1000 mg·min/L at pH 6.0 and temperature of 22°C. The general trend of the data indicated an increase in log inactivation from 0 to 0.8 as $C \times T$ increased from 0 to 1000 mg·min/L.
3. In contrast to the limited inactivation of the two-element helical mixer, the six-element disinfection experiments showed an inactivation of 1.85 log units of oocysts at a $C \times T$ value of 945 mg·min/L. The pH and temperature were 6.0 and 22°C respectively. The general trend of the data showed an increasing inactivation with $C \times T$ values. These results are useful for fundamental reasons and have application for water supply systems with very long transmission lines for chlorine-disinfected water.
4. The results of increased inactivation with the six-element helical mixer as compared to the two-element mixer are in contrast to the results of the coagulation studies as well as the CFD modeling studies that indicated very little difference between the two- and six-element mixers. Additional research is necessary to explain these contrasting results.
5. The Hom model fitted to the data (pH=6.0, temperature=22°C) for the six-element helical mixer gave the following empirical equation:

$$\log\left[\frac{N_o}{N}\right] = 3.28 \times 10^{-6} c^{3.26} t^{1.23}$$

where N_o = initial concentration of *Cryptosporidium parvum* oocysts
N = final concentration of *Cryptosporidium parvum* oocysts
c = chlorine concentration (mg/L)
t = contact time (minutes).

A nomograph based on the Hom model to determine log inactivation at various '*ct*' values was developed.

6. Experiments with static mixing of chlorine and changes in pH indicated the expected result that for both long and short contact times, chlorine at pH 6 was more effective at inactivating oocysts than at pH 7 or 8.
7. Limited experiments, with chlorine dioxide at pH 8 and temperature of 20°C, indicated that a slight increase in log inactivation (from 0.23 to 0.41) occurred in a six-element static mixer when the contact time increased from less than a minute to 30 minutes. The results were not significantly different for an empty pipe or a batch mixer.
8. Limited experiments with dual disinfectants (chlorine followed by monochloramines) were completed at pH 8 and temperature of 20°C to assess synergistic effects of disinfection of oocysts. The results indicated a small increase (0.12 logs) in inactivation due to synergism.

The six-element helical mixer has been shown to be particularly effective for inactivation of *Cryptosporidium parvum* oocysts at large $C \times T$ values. However, caution should be exercised in interpreting and applying these results, since the studies were performed in laboratory grade water buffered to pH 6 under controlled temperature conditions. Additional research to confirm the validity of these results with typical filtered water from treatment plants; in which chemical, biological, and particle interactions can occur; need to be completed.

A NEW MODEL OF MIXING AND DISINFECTION OF *CRYPTOSPORIDIUM PARVUM*

A new physicochemical model of the disinfection process was developed from a description of the inactivation of *Cryptosporidium* oocysts by a disinfectant based on five separate but interrelated steps or phases: (1) the chemical speciation of the disinfectant; (2) the distribution of disinfectants; (3) the distribution of pathogens; (4) the mass transfer of the disinfectant through the surface of the pathogen; and (5) the inactivation within the pathogenic organism. The new model is applied to two ideal reactors: a completely mixed batch reactor, which is an idealization

model is applied to two ideal reactors: a completely mixed batch reactor, which is an idealization of the traditional backmixer, and a plug-flow dispersion reactor, which is an idealization of static mixers. Parameters for the new model were determined using existing experimental data for both types of reactors and for two disinfectants, ozone and chlorine. The following conclusions may be drawn from the model development and the testing of its validity.

1. Predictions from the model are consistent with available experimental data as well as the Chick-Watson and Incomplete Gamma Hom model.
2. Oocyst inactivation calculated from the model, for the completely mixed batch reactor and the static mixer treated as a plug-flow dispersion reactor, compared reasonably well with experimental data generated from the MDCK cell culture testing (see Chapter 3).
3. The new model can easily be extended to incorporate the formation and breakup of pathogen clumps and can be applied to chlorine contact tanks, which are modeled with various plug-flow dispersion characteristics.
4. The usefulness of the model, which is still in its early stages of development, is that it provides a fundamental conceptual basis that can be coupled with a computational fluid dynamics model to predict disinfection efficiency in a real-world disinfection reactor.

COMPUTATIONAL FLUID DYNAMICS AND THE FLOWFIELD IN HELICAL STATIC MIXERS

A three-dimensional, computational fluid dynamics (CFD) model was developed to simulate the flowfield in helical static mixers to study the role of mixing in the processes of coagulation and disinfection. The CFD model was then applied to study the physics of flow in various helical static mixer configurations over a range of flow rates. A total of 22 different simulations (or runs) were performed with the model for flow Reynolds numbers (*Re*) from 5,000 to 100,000. For the CFD model, the Reynolds-averaged Navier–Stokes (RANS) equations were solved for computational grids with 0.37 to 2.59 million nodes on a supercomputer with one run requiring approximately 1 gigabyte of memory. The model was validated with published

experimental measurements of turbulent flow in a 90° pipe bend. The following conclusions may be drawn from the simulations completed with the CFD model.

1. The numerical model is capable of predicting the mean-flow characteristics of complex three-dimensional flows with sufficient accuracy for engineering simulations.
2. The flow in helical static mixers is highly three-dimensional and dominated by intense, counter-rotating, longitudinal vortices. A swirling, three-dimensional wake persists for several diameters (greater than tens of diameters) downstream of the mixer before fully developed pipe flow occurs.
3. A previously unknown feature of the flow in helical static mixers is the presence of pockets of reversed flow near the leading and trailing edges of the mixer elements. The size of the reversed-flow pockets shrunk substantially at *Re* of 100,000 as compared to lower Reynolds numbers. These regions of reversed flow could significantly affect mixing efficiency because such regions can prevent transport across the mixer cross-section.
4. A study of the number of elements (2, 4, and 6) on the flowfield and turbulence quantities showed that the number of elements has only a small effect on the mean flowfield but a dramatic effect on the turbulence kinetic energy leaving the mixer. These results suggest that the highest turbulence energy in the flow exiting the mixer occurs with two elements and increasing the number of elements has a stabilizing (laminarization) effect on the flow. The increasing laminarization suggests that a static mixer with more than 3 or 4 elements does not substantially improve (turbulent) mixing. The results of the coagulation experiments (Chapter 2) are consistent with this conceptual result, but the disinfection experiments with *Cryptosporidium* seems to be enhanced with six elements as compared to two elements (Chapter 3). Additional experimental and computational research needs to be completed to explain these contradictory results.
5. The stabilizing effect of the elements on the incoming turbulent flow could have obvious significant implications on the overall mixing efficiency of helical static mixers. In fact, if flow laminarization occurs within the range of Reynolds number suggested by the model ($Re \approx 5{,}000$ to 20,000), then great care must be exercised when inter-

preting results from static mixers in pilot plants where the Reynolds numbers are closer to the range where laminarization occurs as compared to full-scale plants. The Reynolds number in the full-scale plants are of the order of 10^6.

6. The CFD model can be used to obtain reliable predictions of pressure drop across the static mixer as a function of Reynolds number and number of mixer elements. The model can also be used to compute average local *G*-values (velocity gradients) and illustrate the variation of these *G*-values across and along the mixer.

Page missing from thesis

REFERENCES

Amirtharajah, A. 1978. Design of Rapid Mix Units. *Water Treatment Plant Design*. Edited by R.L. Sanks, Boston, Butterworth–Heinemann.

Amirtharajah, A. 1981. Initial Mixing. In *Proc. AWWA Conference: Coagulation and Filtration: Back to the Basics*. Denver, Colo.: AWWA.

Amirtharajah, A. 1988. Some Theoretical and Conceptual Views of Filtration. *Jour. AWWA,* 80 (12):36–46.

Amirtharajah, A., M.M. Clark, and R.R. Trussell, eds. 1991. *Mixing in Coagulation and Flocculation.* Denver, Colo.: AWWARF and AWWA.

Amirtharajah, A. and S.C. Jones. 1996. Mixing for Coagulation: Organic Polymers, Static Mixers, and Modeling. In *Chemical Water and Wastewater Treatment IV*. Edited by H.H. Hahn, E. Hoffman, and H. Ødegard. Berlin: Springer–Verlag.

Amirtharajah, A. and K.M. Mills. 1982. Rapid Mix Design for Mechanisms of Alum Coagulation. *Jour. AWWA,* 74(4):210–216.

Amirtharajah, A. and C.R. O'Melia. 1990. Coagulation Processes: Destabilization, Mixing, and Flocculation. In *Water Quality and Treatment*. 4th ed., Edited by F.W. Pontius. New York: McGraw-Hill.

Amirtharajah A. and S.L. Trusler 1986. Destabilization of Particles by Turbulent Rapid Mixing. *ASCE Jour. of Environmental Engineering*, 112(6):1085–1108.

APHA, AWWA, and WEF (American Public Health Association, American Water Works Association, and Water Environment Federation). 1995. *Standard Methods for the Examination of Water and Wastewater.* 21st ed. Washington, DC: APHA.

Arrowood, M.J. and K. Donaldson. 1996. Improved Purification Method for Calf-Derived *Cryptosporidium parvum* Oocysts Using Discontinuous Sucrose and Cesium Chloride Gradients. *Jour. of Eukaryote Microbiology,* 43(5):89.

Atherholt, T.B., M.W. LeChevallier, W.D. Norton, and J.S. Rosen. 1998. Effect of Rainfall on *Giardia* and *Cryptosporidium*. *Jour. AWWA,* 90(9):66–80.

AWWA and ASCE (American Water Works Association and American Society of Civil Engineers). 1998. *Water Treatment Plant Design*. 3rd ed. Washington, DC: McGraw-Hill.

AWWA and AWWARF (American Water Works Association and American Water Works Association Research Foundation). 1996. *Water Utility Database*. Denver, Colo.: AWWA.

AWWA (American Water Works Association) Coagulation Committee. 1989. Committee Report: Coagulation as an Integrated Water Treatment Process. *Jour. AWWA*, 81(10):72–78.

Baldyga J. and J.R. Bourne. 1984a. A Fluid Mechanical Approach to Turbulent Mixing and Chemical Reaction. Part I: Inadequacies of Available Methods. *Chemical Engineering Communications*, 28:231–241.

Baldyga J. and J.R. Bourne. 1984b. A Fluid Mechanical Approach to Turbulent Mixing and Chemical Reaction. Part II. Micromixing in the Light of Turbulence Theory. *Chemical Engineering Communications*, 28:243–258.

Baldyga J. and J.R. Bourne. 1984c. A Fluid Mechanical Approach to Turbulent Mixing and Chemical Reaction. Part III. Computational and Experimental Results for the New Micromixing Model. *Chemical Engineering Communications*, 28:259–281.

Baldyga J. and J.R. Bourne. 1989a. Simplification of Micromixing Calculations. I. Derivation and Application of New Model. *The Chemical Engineering Jour.*, 42:83–92.

Baldyga J. and J.R. Bourne. 1989b. Simplification of Micromixing Calculations. II. New Applications. *The Chemical Engineering Jour.*, 42:83–101.

Baldyga J., J.R. Bourne, and S.J. Hearn. 1997. Interaction Between Chemical Reactions and Mixing on Various Scales. *Chemical Engineering Science*, 52(4):457–466.

Berkman, P.D. and R.V. Calabrese. 1988. Dispersion of Viscous Liquids by Turbulent Flow in a Static Mixer. *AIChE Jour.*, 34(4):602–609.

Bourne, J.R. and P. Dell'Ava. 1987. Micro- and Macromixing in Stirred Tank Reactors of Different Sizes. *Chemical Engineering Research and Design*, 65(3):180–185.

Bourne, J.R., O.M. Kut, and J. Lenzner. 1992. An Improved Reaction System to Investigate Micromixing in High-Intensity Mixers. *Industrial Engineering Chemistry Research*, 31:949–958.

Bourne, J.R., J. Lenzner, and S. Petrozzi. 1992. Micromixing in Static Mixers: An Experimental Study. *Industrial and Engineering Chemistry Research*, (31)4:1216–1222.

Bourne, J.R. and H. Maire. 1991. Micromixing and Fast Chemical Reactions in Static Mixers. *Chemical Engineering and Processing*, 30(1):23–30.

Bradshaw, P. 1971. *An Introduction to Turbulence and its Measurement*. Oxford, Pergamon.

Bradshaw, P. 1987. Turbulent Secondary Flows. *Annual Review of Fluid Mechanics*, 19:53–74.

Brocard D., L. Vandeventer, N. Pizzi, and S. Sarrouh. 1998. Optimization of Tank Design Using CFD Modeling. In *Proc. of the Sixteenth Annual AWWA Water Quality Technology Conference*. Denver, Colo.: AWWA.

Brouckaert C.J., N.E. Fortmann, and C.A. Buckley. 1998. A Computational Fluid Dynamics Investigation of a Secondary Clarifier. In *Proc. WISA Biennial Conference*. Cape Town, South Africa: Water Institute of Southern Africa.

Burfoot, D. and P. Rice. 1983. Heat Transfer and Pressure Drop Characteristics of Short Lengths of Swirl Flow Inducers Interspaced Along a Circular Duct. *Chemical Engineering Research and Design,* 61(4):253–258.

Burke, J.C. 1996. Effectiveness of Static Mixers for Enhanced Coagulation. Master's Special Research Problem. Georgia Institute of Technology, Atlanta, Ga.

Camp T.R. and P.C. Stein. 1943. Velocity Gradients and Internal Work in Fluid Friction. *Jour. of the Boston Society of Civil Engineers*, 30(4):219–237.

Chang, S.L. 1970. Modern Concept of Disinfection. *Disinfection*. ASCE (American Society of Civil Engineers). New York. 635–681.

Chappell, C.L., M. Marshall, G. Widmer, P.C. Okhuysen, and C.R. Sterling. 1999. Cryptosporidium parvum (Gentoype 2) Isolates Vary in their Capacity to Infect Cultured Enterocytes and Animal Models. In *Proc. of the International Symposium on Waterborne Pathogens*. Milwaukee, Wis.: AWWA.

Chiu, K., D.A. Lyn, P. Savoye, and E.R. Blatchley. 1999. Integrated UV Disinfection Model Based on Particle Tracking. *ASCE Jour. Environmental Engineering*, 125(1):7–16.

Clancy, J.L., T.M. Hargy, M.M. Marshall, and J.E. Dyksen. 1998. UV Light Inactivation of *Cryptosporidium* Oocysts. *Jour. AWWA*, 90(9):92–102.

Clark, M.M. 1985. Critique of Camp and Stein's RMS Velocity Gradient. *ASCE Jour. of Environmental Engineering*, 111(6):741–754.

Clark, M.M. 1986. Scale-up of Laboratory Flocculation Results. In *Proc. AWWA Annual Conference*. Denver, Colo.: AWWA.

Clark, M.M. 1987. Effect of Micromixing on Product Selectivity. In *Proc. AWWA Annual Conference*. Denver, Colo.: AWWA

Clark, M.M., R.M. Srivastava, and R. David. 1993. Mixing and Aluminum Precipitation. *Environmental Science and Technology*, 27(10):2181–2189.

Clark, M.M., R.M. Srivastava, J.S. Lang, R.R. Trussel, L.J. McCollum, D. Bailey, J.D. Christie, and G. Stolarik. 1994. *Selection and Design of Mixing Processes for Coagulation*. Denver, Colo.: AWWARF and AWWA.

Cleasby, J.L. 1984. Is Velocity Gradient a Valid Turbulent Flocculation Parameter? *ASCE Jour. of Environmental Engineering*, 110(5):875–897.

Cleasby, J.L. 1990. Filtration. In *Water Quality and Treatment*. 4th ed. Edited by F.W. Pontius. New York: McGraw-Hill.

Cleasby, J.L., A.H. Dharamarajah, G.L. Sindt, and E.R. Bauman. 1989. *Design and Operation Guidelines for Optimization of the High-Rate Filtration Process: Phase I Report*. Denver, Colo.: AWWARF and AWWA.

Cockx, A., Z. Do-Quang, A. Liné, and M. Roustan 1999. Use of Computational Fluid Dynamics for Simulating Hydrodynamics and Mass Transfer in Industrial Ozonation Towers. *Chemical Engineering Science*, 54(21):5085–5090.

Cockx, A., A. Liné, M. Roustan, Z. Do-Quang, and V. Lazarova. 1997. Numerical Simulation and Physical Modeling of the Hydrodynamics in an Air-Lift Internal Loop Reactor. *Chemical Engineering Science*, 52(21–22):3787–3793.

Craun, G.F., S.A. Hubbs, F. Frost, R.L. Calderon, and S.H. Via. 1998. Waterborne Outbreaks of Cryptosporidiosis. *Jour. AWWA*, 90(9):81–91.

Daniel, P.A., N. Dumoutier, V. Mandra, N. Tambo, and T. Kamei. 1996. Pathogenic Protozoa in Raw and Drinking Water: Occurrence and Removal (*Giardia*, *Cryptosporidium*, etc.). *Water Supply*, 14(3/4):387–401.

Delichatsios, M.A. and R.F. Probstein. 1975. Coagulation in Turbulent Flow: Theory and Experiment. *Jour. of Colloid and Interface Science*, 51(6):394–405.

Despommier, D.D., R.W. Gwadz, and P.J. Holez. 1995. *Parasitic Diseases*. 3rd ed. New York: Springer-Verlag.

Devenport, W.J. and R.L. Simpson. 1990. Time-Dependent and Time-Averaged Turbulence Structure Near the Nose of a Wing-Body Junction. *Jour. of Fluid Mechanics*, 210:23–55.

Do-Quang, Z. and J.M. Laîné. 1997. Advanced Design of Ozonation Contactor for Drinking Water Treatment. Use of Computational Fluid Dynamics Modeling for Reactor Performance Evaluation. In *Proc. AWWA Annual Conference*. Denver, Colo.: AWWA.

Ducoste, J.J. 1996. The Effect of Tank Size and Impeller Type on Turbulent Flocculation. Ph.D. diss., University of Illinois, Urbana-Champaign.

Ducoste, J.J. and M.M. Clark. 1998. The Influence of Tank Size and Impeller Geometry on Turbulent Flocculation: II. Model. *Environmental Engineering Science*, 15(3):225–235.

Ducoste, J.J. and M.M. Clark. 1999. Turbulence in Flocculators: Comparison of Measurements and CFD Simulations. *AIChE Jour.*, 45(2):432–436.

Edzwald, J.K., M.B. Kelley, H.J. Dunn, G.S. Kaminski, and J.P. Malley. 1996. Control of Cryptosporidium by Coagulation, Floatation, and Filtration. In *Proc. of the 25th Annual AWWA Water Quality Technology Conference*. Boston: AWWA.

Emelko, M.B., P.M. Huck, and R.M. Slawson. 1999. Optimizing Filter Removal of Viable and Inactivated Cryptosporidium During Challenge Periods. In *Proc. of the International Symposium on Waterborne Pathogens*. Milwaukee, Wis.: AWWA.

Engler Jr, J.A., M.M. Bishop, I. Crossley, and A.M. McEnteggart. 1998. Computational Fluid Dynamics: A Valuable Tool in Clearwell Design Optimization and Analysis. In *Proc. AWWA Annual Conference*. Denver, Colo.: AWWA.

Fayer. 1995. Effect of Sodium Hypochlorite Exposure on Infectivity of *Cryptosporidium parvum* Oocysts for Neonatal BALB/c Mice. *Applied Environmental Microbiology*, 61(2):844–846.

Finch, G.R., E.K. Black, and L.L. Gyürék. 1995. Ozone and Chlorine Inactivation of *Cryptosporidium*. In *Proc. of the 23rd Annual AWWA Water Quality Technology Conference*. Denver, Colo.: AWWA.

Finch, G.R., E.K. Black, L.L. Gyürék, and M. Belosevic. 1993. Ozone Inactivation of *Cryptosporidium parvum* in Demand-Free Phosphate Buffer Determined by In Vitro Excystation and Animal Infectivity. *Applied Environmental Microbiology*, 59(12):4203–4210.

Finch, G.R., R.J. Liyange, and M. Belosevic. 1995. Effect of Chlorine Dioxide on *Cryptosporidium* and *Giardia*. In *Chlorine Dioxide: Drinking Water, Process Water, and Wastewater Issues*. Third International Symposium. New Orleans, L. American Water Works Research Foundation, Chemical Manufacturers Association, and the U.S. Environmental Protection Agency.

Fogel, D., J. Isaac-Renton, R. Guasparini, W. Moorehead, and J. Ongerth. 1993. Removal of *Giardia* and *Cryptosporidium* by Slow Sand Filtration. *Jour. AWWA,* 85(11):77–84.

Fox, K.R. and D.A. Lytle. 1996. Milwaukee's Crypto Outbreak: Investigation and Recommendations. *Jour. AWWA,* 88(9):87–94.

Freud, S. 1999. How to Balance Disinfection and Disinfection By-Product Goals when Starting Up Expansions. In *Proc. of the 27th Annual AWWA Water Quality Technology Conference.* Tampa, Fla.: AWWA.

Geisser, D.F. and S.R. Garver. 1977. High Rate Disinfection: Chlorine vs. Chlorine Dioxide. *ASCE Jour. Environmental Engineering Division,* 103(12):1089–1103.

Godfrey, J.C. 1992. Static Mixers. In *Mixing in the Process Industries*. Edited by N. Harnby, M. F. Edwards, and A. W. Nienow. Oxford: Butterworth-Heinemann.

Godfrey, J.C. and A. Amirtharajah. 1991. Mixing in Liquids. In *Mixing in Coagulation and Flocculation*. Edited by A. Amirtharajah, M.M. Clark, and R.R. Trussell. Denver, Colo.: AWWARF.

Gimbel, R., G. Logsdon, H. Kiuru, H.P. Vazquez, L. Contento, J. Bachur, A.M. Ingallinella, G. Sanguinetti, Y.S. Lin, J.W. Rong, S.J. Ying, L.X. Mei, T.H. Kao, J.L Su, H. Kiuru, G. Randon, J. Clasen, J. Willemsen-Zwaagstra, L.J. Hem, M. Sandu, C. Berevoianu, G. Racoviteanu, V. Onderikova, D.J. Nozaic, F. Ribas, J.A. Etxebarria, and J.C. Edge. 1998. Removal of Micro-Organisms by Clarification and Filtration Processes. *Water Supply,* 16(1/2):203–238.

Godfrey, J.C. 1992. Static Mixers. In *Mixing in the Process Industries*. 2nd ed. Edited by N. Harnby, M.F. Edwards, and A.W. Nienow. Oxford: Butterworth–Heinemann.

Graber, S.D. 1994. A Critical Review of the Use of the *G*-Value (RMS Velocity Gradient) in Evironmental Engineering. *Developments in Theoretical and Applied Mechanics*, 17:533–556.

Graber, S.D. 1997. Discussion of "Design of Flocculating Baffled Channel". *ASCE Jour. of Environmental Engineering,* 123(12):1269.

Graber, S.D. 1998. Discussion of "Influence of Strain-Rate on Coagulation Kinetics". *ASCE Jour. of Environmental Engineering*, 124(10):1028.

Grace, C.D. 1971. 'Static Mixing' and Heat Transfer. *Chemical and Process Engineering,* 52(7):57–59.

Grayman, W.M., R.A. Deininger, A. Green, P.F. Boulos, R.W. Bowcock, and C.C. Goodwin. 1996. Water Quality and Mixing Models for Tanks and Reservoirs. *Jour. AWWA*, 88(7):60–73.

Grayman, W, L. Rossman, R. Deininger, C. Arnold, C. Smith, J. Smith, and R. Schnipke. 1998. Improving Mixing in Distribution Storage Facilities. In *Proc. AWWA Annual Conference*. Denver, Colo.: AWWA.

Gyürék, L.L. 1997. Ozone and Chlorine Inactivation of *Cryptosporidium* in Water. Ph.D. diss., University of Alberta, Edmonton, Alta.

Gyürék, L.L. and G.R. Finch. 1998. Modeling Water Treatment Chemical Disinfection Kinetics. *ASCE Jour. of Environmental Engineering,* 124(9):783–793.

Gyürék, L.L, G.R. Finch, and M. Belosevic. 1997. Modeling Chlorine Inactivation Requirements of *Cryptosporidium parvum* Oocysts. *ASCE Jour. Environmental Engineering,* 123(9):865-875.

Gyürék, L.L., L.R.J. Liyanage, M. Belosevic, and G.R. Finch. 1996. Disinfection of *Cryptosporidium parvum* Using Single and Sequential Application of Ozone and Chlorine Species. In *Proc. of the 24th Annual AWWA Water Quality Technology Conference.* Boston, Mass.: AWWA.

Haas, C.N., J. Joffe, U. Anmangandla, J.G. Jacangelo, and M. Heath. 1996. Water Quality and Disinfection Kinetics. *Jour. AWWA,* 88(3):95–103.

Haas, C.N. 1990. Disinfection. In *Water Quality and Treatment.* 4th ed. Edited by F.W. Pontius, Washington, DC: McGraw-Hill.

Haas, C.N., K. Longley, and T. Selfridge. 1990. High-rate Coliform Disinfection of Stormwater Overflow. *Research Jour. Water Pollution Control Federation,* 62(3):282–287.

Hagstrom, J., G. Crozes, S. Reddy, M.M. Clark, and C. Burns. 1998. Modeling and Enhancement of Disinfection Contactor Hydromechanics Using Computational Fluid Dynamics. In *Proc. AWWA Annual Conference.* Denver, Colo. AWWA.

Hahn, H.H. and W. Stumm. 1968. Kinetics of Coagulation with Hydrolized Al(III). *Jour. of Colloid and Interface Science,* 28:133.

Hannoun, I.A., P.F. Boulos, and E.J. List. 1998. Using Hydraulic Modeling to Optimize Contact Time. *Jour. AWWA*, 90(8):77–87.

Hardy, S.A. 1999. Effectiveness of Static Mixers for Disinfection of *Cryptosporidium* Oocysts. Master's thesis. Georgia Institute of Technology, Atlanta, Ga.

Hardy, S.A., A. Amirtharajah, and M.J. Arrowood. 1999. Inactivation of *Cryptosporidium* Oocysts Using Static Mixers and Cell Culture Infectivity Assay. In *Proc. of the International Symposium on Waterborne Pathogens.* Milwaukee, Wis.: AWWA.

Heindel, H. 1999. Bench-Scale Examination of the Effects of Static Mixers on the Disinfection of *Cryptosporidium parvum.* Master's thesis. Georgia Institute of Technology, Atlanta, Ga.

Huang, J.Y.C., R. Warriner, and N.S.N. Ni. 1985. Pilot Tests of Chlorination Facility for Disinfecting Secondary Effluent. *Jour.* Water Pollution and Control Federation, 57(4):777–784.

Jaffer, S.A and P.E. Wood. 1998. Quantification of Laminar Mixing in the Kenics Static Mixer: An Experimental Study. *Canadian Jour. of Chemical Engineering,* 76(6):516–521.

Jakubowski, W., S. Boutros, W. Faber, R. Fayer, W. Ghiorse, M. LeChevallier, J. Rose, S. Schaub, A. Singh, and M. Stewart. 1996. Environmental Methods for *Cryptosporidium. Jour. AWWA,* 88(9):107–121.

James Montgomery Consulting Engineers. 1985. *Water Treatment Principles and Design.* New York. John Wiley and Sons.

Jones, S.C. 1999. Static Mixers for Water Treatment: A Computational Fluid Dynamics Model. Ph.D. diss., Georgia Institute of Technology, Atlanta, Ga.

Joshi, P., K.D.P. Nigam, E.B. Nauman. 1995. The Kenics Static Mixer: New and Proposed Correlations. *The Chemical Engineering Jour.,* 59:265–271.

Kabatek, J. P. Ditl, and V. Novak. 1989. Helax - A New Type of Static Mixer - Operation Characteristics and Comparison with Other Types. *Chemical Engineering and Processing,* 25(2):59–64.

Kaltenbach, H.J., M. Fatica, R. Mittal, T.S. Lund, and P. Moin. 1999.Study of Flow in Planar Asymmetric Diffuser Using Large-Eddy Simulation. *Jour. of Fluid Mechanics*, 390:151–185.

Karoui, A., H. Frederic, N. LeSauze, J. Costes, and J. Bertrand. 1998. Determination of the Mixing Performance of Sulzer SMV Static Mixers by Laser Induced Fluorescence. *Canadian Jour. of Chemical Engineering,* 76(6):522–526.

Karr, P.R., A. Amirtharajah, and S.C. Jones. 1997. Algal Blooms and Organics: A Case Study for Enhanced Coagulation. In *Proc. AWWA Annual Conference*. Denver, Colo.: AWWA.

Kawamura, S. 1991. *Integrated Design of Water Treatment Facilities*. New York: John Wiley and Sons.

Kelley, M.B., P.K. Warrier, J.K. Brokaw, K.L. Barrett, and S.J. Komisar. 1995. A Study of Two Army Installation Drinking Water Sources and Treatment Systems for the Removal of Giardia and Cryptosporidium. In *Proc. of the 25th Annual AWWA Water Quality Technology Conference*. Denver, Colo.: AWWA.

Kim, J., P. Moin, and R.D. Moser. 1987. Turbulence Statistics in Fully Developed Channel Flow at Low Reynolds Number. *Jour. of Fluid Mechanics*, 177:133.

Klute, R. and A. Amirtharajah. 1991. Particle Destabilization and Flocculation Reactions in Turbulent Pipe Flow. In *Mixing in Coagulation and Flocculation*. Edited by A. Amirtharajah, M.M. Clark, and R.R. Trussell. Denver, Colo.: AWWARF.

Korich, D.G., J.R. Mead, M.S. Madore, N.A. Sinclair, and C.R. Sterling. 1990. Effects of Ozone, Chlorine Dioxide, Chlorine, and Monochloramine on *Cryptosporidium parvum* Oocysts Viability. *Applied Environmental Microbiology*, 56(5):1423–1428.

Kramer, T.A. 1997. The Modeling of Coagulation Kinetics in Complex Laminar Flow. Ph.D. diss., University of Illinois at Urbana–Champaign.

Kramer, T.A. and M.M. Clark. 1997. Influence of Strain-Rate on Coagulation Kinetics. *ASCE Jour. of Environmental Engineering*, 123(5):444–452.

Krane, S.A. and G.J. Sutter. 1962. Statistical Methods for Assuring Precision of Microscopic Counts. Technical Note 6-62-1, Contract No. DA-42-007-CML-557. Dugway, UT:U.S. Army Chemical Corps.

Krebs, P., D. Vischer, and W. Gujer. 1995. Inlet-Structure Design for Final Clarifiers. *ASCE Jour. of Environmental Engineering*, 121(8):558–564.

Krusé, C.W., K. Kawata, V.P. Oliveri, and K.E. Longley. 1973. Improvement in Terminal Disinfection of Sewage Effluents. *Water and Sewage Works*, 120(6):57–64.

Latimer, R.J. 1998. Pilot Scale Comparison of Static Mixers and Backmix Reactors for Coagulation. Master's Special Research Problem. Georgia Institute of Technology, Atlanta, Ga.

Laufer, J. 1954. The Structure of Turbulence in Fully Developed Pipe Flow. Tech. Rep. 1174, NACA.

Le, H., P. Moin, and J. Kim. 1997. Direct Numerical Simulation of Turbulent Flow Over a Backward-Facing Step. *Jour. of Fluid Mechanics*, 330:349–374.

LeChevallier, M.W., W.D. Norton, and R.G. Lee. 1991. Occurrence of *Giardia* and *Cryptosporidium* spp. in Surface Water Supplies. *Applied Environmental Microbiology,* 57(9):2610.

LeChevallier, M.W. and W.D. Norton. 1995. *Giardia* and *Cryptosporidium* in Raw and Finished Water. *Jour. AWWA,*. 87(9):54.

LeChevallier, M.W., H. Arora, D. Battigelli, and M. Abbaszadegan. 1996. Chlorine Dioxide for Control of *Cryptosporidium* and Disinfection By-Products. In *Proc. of the 24th Annual AWWA Water Quality and Technology Conference.* Boston, Mass.: AWWA.

Lecjaks, Z., I. Machac, and J. Šír. 1987. Pressure Loss in Fluids Flowing in Pipes Equipped with Helical Screws. *International Chemical Engineering,* 27(2):205–209.

Letterman, R.D., J.E. Quon, and R.S. Gemmell. 1973. Influence of Rapid Mixing Parameters on Flocculation. *Jour. AWWA,* 74(4):210–216.

Li, H., G.R. Finch, N. Neumann, and M. Belosevic. 1998. Inactivation of *Cryptosporidium* by Chlorine Dioxide at 1°C. In *Proc. of the 26th Annual AWWA Water Quality and Technology Conference.* San Diego, Calif.: AWWA.

Li, W. 1999. Physicochemical Modeling of the Disinfection Process for *Cryptosporidium parvum* Oocysts. Master's Special Research Problem, Georgia Institute of Technology, Atlanta, Ga.

Lin, F.-B. and F. Sotiropoulos. 1997a. Assessment of Artificial Dissipation Models for Three-Dimensional Incompressible Flow Solutions. *ASME Jour. of Fluids Engineering*, 119(2):331–340.

Lin, F.-B. and F. Sotiropoulos. 1997b. Strongly-Coupled Multigrid Method for 3-D Incompressible Flows Using Near-Wall Turbulence Closures. *ASME Jour. of Fluids Engineering*, 119(2):314–324.

Ling, F. H, and X. Zhang. 1994. Chaotic Mixing in the Kenics Static Mixer. *Advances in Computational Methods in Fluid Dynamics*. 196:367–374. New York: ASME (American Society of Mechanics Engineers).

Lisle, J.T. and J.B. Rose. 1995. *Cryptosporidium* Contamination of Water in the USA and UK: A Mini Review. *Jour. Water SRT—AQUA,* 44(3):103–117.

Liyanage, L.R., G.R. Finch, and M. Belosevic. 1997. Effect of Aqueous Chlorine and Oxychlorine Compounds on *Cryptosporidium parvum* Oocysts. *Environmental Science and Technology,* 31(7):1992–1994.

Liyanage, L.R.J., L.L. Gyürék, M. Belosevic, and G.R. Finch. 1996. Effect of Chlorine Dioxide Preconditioning on Inactivation of *Cryptosporidium* by Free Chlorine and Monochloramine: Process Design Requirements. In *Proc. of the 24th Annual AWWA Water Quality and Technology Conference*. Boston, Mass.: AWWA.

Longley, K.E. 1978. Turbulence Factors in Chlorine Disinfection Efficiency. *Water Research,* 12(10):813–822.

Longley, K.E., V.P. Olivieri, C.W. Krusé, and K. Kawata. 1974. Enhancement of Terminal Disinfection of a Wastewater Treatment System. In *Virus Survival in Water and Wastewater Systems*. Edited by J.F. Malina Jr. and B.P. Sagik. Austin, Texas: Center for Research in Water Resources.

Luo, C. 1997. Distribution of Velocities and Velocity Gradients in Mixing and Flocculation Vessels: Comparison Between LDV Data and CFD Predictions. Ph.D. diss., New Jersey Institute of Technology, Newark.

Lyn, D.A., K. Chiu, and E.R. Blatchley III. 1999. Numerical Modeling of Flow and Disinfection in UV Disinfection Channels. *ASCE Jour. Environmental Engineering*, 125(1):17–26.

McDonough, R.J. 1992. In *Mixing in the Process Industries*. Edited by N. Harnby, M. F. Edwards, and A. W. Nienow. Oxford: Butterworth-Heinemann.

McKenna, C.J., D.E. Humble, and K.L. Hobson. 1986. Static Mixer Performance for Chlorine Mixing. In *Proc. of the 59th Annual Water Pollution Control Federation Conference*. Los Angeles, Calif.: WPCF.

Metcalf and Eddy. 1991. *Wastewater Engineering. Treatment, Disposal and Reuse*. New York: McGraw-Hill.

Meyer, T., R. David, A. Renken, and J. Villermaux. 1988. Micromixing in a Static Mixer and an Empty Tube by a Chemical Method. *Chemical Engineering Science,* 43(8):1955–1960.

Moin, P. and J. Kim. 1997. Tackling Turbulence with Supercomputers. *Scientific American*, 276(1):62–68.

Monk, R.D.G. and R.R. Trussell. 1991. Design of Mixers for Water Treatment Plants: Rapid Mixing and Flocculators. In *Mixing in Coagulation and Flocculation*. Edited by A. Amirtharajah, M.M. Clark, and R.R. Trussell. Denver, Colo.: AWWA RF.

Monk R.D.G. and J.F. Willis. 1987. Designing Water Treatment Facilities. *Jour. AWWA,* 79(2):45–57.

Morris, J.C. 1970. Disinfectant Chemistry and Biocidal Activities. ASCE (American Society of Civil Engineers). New York. 609–634.

Moser, R.D., J. Kim, and N.N. Mansour. 1999. Direct Numerical Simulation of Turbulent Channel Flow up to $Re_\tau = 590$. *Physics of Fluids*, 11(4):943–945.

Mutsakis M. and R. Rader. 1986. Static Mixers Bring Benefits to Water/Wastewater Operations. *Water Engineering and Management,* 133(11):30–34.

Mutsakis M., F.A. Streiff, and G. Schneider. 1986. Advances in Static Mixing Technology. *Chemical Engineering Progress,* 133(11):42–48.

Newkirk, D.D. and R.R. Trussell. 1991. Pilot-Plant Studies for Design and Operation. In *Mixing in Coagulation and Flocculation.* Edited by A. Amirtharajah, M.M. Clark, and R.R. Trussell. Denver, Colo.: AWWARF.

O'Melia, C.R. 1972. Coagulation and Flocculation. In *Physicochemical Processes for Water Quality Control.* Edited by W.J. Weber. New York: Wiley-Interscience.

Ongerth, J.E. and J.P. Pecoraro. 1995. Removing Cryptosporidium Using Multimedia Filters. *Jour. AWWA,* 87(12):83–89.

Pahl, M.H., and E. Muschelknautz. 1982. Static Mixers and Their Applications. *International Chemical Engineering,* 22(2):197–205.

Parker, J.F.W. and H.V. Smith. 1993. Destruction of Oocysts of *Cryptosporidium Parvum* by Sand and Chlorine. *Water Research,* 27(4):729–731.

Parker, J.F.W., G.F. Greaves, and H.V. Smith. 1993. The Effect of Ozone on the Viability of *Cryptosporidium parvum* Oocysts and a Comparison of Experimental Methods. *Water Science and Technology,* 27(3/4):93–96.

Peeters, J.E., E.A. Mazas, W.J. Masschelein, I.V.M. deManturana, and E. Debacker. 1989. Effect of Disinfection of Drinking Water with Ozone or Chlorine Dioxide on Survival of *Cryptosporidium parvum* Oocysts. *Applied Environmental Microbiology,* 55(6):1519–1522.

Pickup, R.W. and J.R. Saunders. 1996. *Molecular Approaches to Environmental Microbiology,* Hertfordshire, U.K.: Ellis Horwood.

Pontius, F.W. 1998. New Horizons in Federal Regulation. *Jour. AWWA,* 90(3):38–50.

Pontius, F.W. 2000. Regulations in 2000 and Beyond. *Jour. AWWA*, 82(3):40–54.

Pontius, F.W. and J.L. Clancy. 1999. ICR Crypto Data: Worthwhile or Worthless? *Jour. AWWA,* 91(9):14–22.

Ransome, M.E., T.N. Whitmore, and E.G. Carrington. 1993. Effect of Disinfectants on the Viability of *Cryptosporidium Parvum* Oocysts. *Water Supply*, 11(1):103-117.

Rauline, D., P.A. Tanguy, J.M.L. Blévec, and J. Bousquet 1998. Numerical Investigation of the Performance of Several Static Mixers. *The Canadian Jour. of Chemical Engineering,* 76:527–535.

Reddy, S., R. Joost, and R. McCleery. 1998a. Designing Ozone Contactors for the City of Arlington, Texas Using Computational Fluid Dynamics. In *Proc. AWWA Annual Conference*. Denver, Colo.: AWWA.

Reddy, S., J. Russell, R. Narasimhan, and C. Burns. 1998b. Improving Clearwell Design Using Computational Fluid Dynamics. In *Proc. AWWA Annual Conference*. Denver, Colo.: AWWA.

Rose, J.B. 1990. Occurrence and Control of *Cryptosporidium* in Drinking Water. In Drinking Water Microbiology. Edited by G.A. McFeter. New York: Springer-Verlag.

Rose, J.B., A. Cifrino, M.S. Madore, C.P. Gerba, C.R. Sterling, and M.J. Arrowood. 1986. Detection of *Cryptosporidium* from Wastewater and Freshwater Environments. *Water Research,* 18(10):233–239.

Rose, J.B., C.P. Gerba, and W. Jakubowski. 1991. Survey of Potable Water Supplies for *Cryptosporidium* and *Giardia. Environmental Science and Technology,* 25(8):1393.

Rowen J. and D. Behm. 1993. Fatal Neglect. *Milwaukee Jour.*. September 19-26.

Ruffell, K.M., J.L. Rennecker, and B.J. Marinas. 1998. Inactivation Kinetics of Cryptosporidium parvum Oocysts with Chlorine Dioxide. In *Proc. of the 26th Annual AWWA Water Quality and Technology Conference*. Denver, Colo.: AWWA.

Saffman, P.G. and J.S. Turner. 1956. On the Collision of Drops in Turbulent Clouds. *Jour. of Fluid Mechanics*, 1(16):16–30.

Sawyer, C.N., P.L. McCarty, and G.F. Parkin. 1994. *Chemistry for Environmental Engineering*. 4th ed. New York: McGraw-Hill.

Schuler, P.F., M.M. Ghosh, and S.N. Boutrous. 1988. Comparing the Removal of *Giardia* and *Cryptosporidium* Using Slow Sand Filtration and Diatomaceous Earth Filtration. In *Proc. of the AWWA Annual Conference*. Denver, Colo.: AWWA.

Schulgen, B.F. 1995. Effectiveness of Static Mixers for Coagulation in Water Treatment. Master's thesis. Georgia Institute of Technology, Atlanta, Ga.

Schulgen, B.F., A. Amirtharajah, and S.C. Jones. 1996. Effectivness of Static Mixers for Coagulation in Water Treatment. In *Proc. of the AWWA Annual Conference.* Denver, Colo.: AWWA.

Schutz, J. 1988. Agitated Thin-Film Reactors and Tubular Reactors With Static Mixers for a Rapid Exothermic Multiple Reaction. *Chemical Engineering Science,* 43(8):1975–1980.

Shah, N.F. and D.D. Kale. 1991. Pressure Drop for Laminar Flow of Non-Newtonian Fluids in Static Mixers. *Chemical Engineering Science,* 46(8):2159–2161.

Šir J. and Z. Lecjaks. 1982. Pressure Drop and Homogenization Efficiency of a Motionless Mixer. *Chemical Engineering Communications,* 16:325–334.

Skeens, B.M. 1999. Pilot Scale Evaluation and Comparison of Static Mixers for Coagulation in Water Treatment. Master's thesis. Georgia Institute of Technology, Atlanta, Ga.

Smith, H.V., L.J. Robertson, and J.E. Ongerth. 1995. Cryptosporidiosis and Giardiasis: the Impact of Waterborne Transmission. *Jour. Water SRT—AQUA,* 44(6):258–274.

Solo-Gabriele, H. and S. Neumeister. 1996. US Outbreaks of Cryptosporidiosis. *Jour. AWWA,* 88(9):76–86.

Sotiropoulos, F. 2000. Progress in Modeling 3-D Shear Flows Using RANS Equations and Advanced Turbulence Closures. In *Advances in Fluid Mechanics Series*. Southampton, United Kingdom: Computational Mechanics Publications, forthcoming.

Sotiropoulos, F. and V.C. Patel. 1992. Flow in Curved Ducts of Varying Cross-Section. IIHR Report 358, Iowa Institute of Hydraulic Research.

Sotiropoulos, F. and V.C. Patel. 1994. Prediction of Turbulent Flow Through a Transition Duct Using a Second-Moment Closure. *AIAA Jour.*, 32(11):2194–2204.

Sotiropoulos, F. and Y. Ventikos. 1998. Flow Through a Curved Duct Using Nonlinear Two-Equation Turbulence Models. *AIAA Jour.*, 36(7):1256–1262.

Sotiropoulos, F., A. Chrisochoides, and T.W. Sturm. 1999. Prediction of Bridge-Abutment Flows Using Advanced Turbulence Closures. In *Proc. ASCE International Water Resources Engineering Conference*. New York. ASCE.

Speziale, C.G. 1998. Turbulence Modeling for Time-Dependent RANS and VLES: A Review. *AIAA Jour.*, 36(2):173–184.

Sreenivasan, K.R. and P.J. Strykowski.1983. Stabilization Effects in Flow Through Helically Coiled Pipes. *Experiments in Fluids*, 1:31–36.

States, S., K. Stadterman, L. Ammon, P. Vogel, J. Baldizar, D. Wright, L. Conley, and J. Sykora. 1997. Protozoa in the Water: Sources, Occurrence, and Treatment. *Jour. AWWA,* 89(9):74–83.

Sudo, K., M. Sumida, and H. Hibara. 1998. Experimental Investigation on Turbulent Flow in a Circular-Sectioned 90-Degree Bend. *Experiments in Fluids*, 25:42–49.

Swertfeger, J., D.H. Metz, J. DeMarco, A. Braghetta, and J.G. Jacangelo. 1999. Effect of Filter Media on Cyst and Oocyst Removal. *Jour. AWWA,* 91(9):90–100.

Ta, C.T. 1998. Computational Fluid Dynamic Tools for Treated Water Reservoir Mixing Studies. In *Proc. AWWA Water Quality Technology Conference*. Denver, Colo.: AWWA.

Taweel, A.M.A. and L.D. Walker. 1983. Liquid Dispersion in Static In-Line Mixers. *Canadian Jour. of Chemical Engineering,* 61:527–533.

Taylor, G.I. 1929. The Criterion for Turbulence in Curved Pipes. *Proc. Royal Society of London Series A*, 124:243–249.

Turkel, E., R.C. Swanson, V.N. Vatsa, and J.A. White. 1991. Multigrid for Hypersonic Viscous 2-D and 3-D Flows. AIAA Paper 91–1572, American Institute of Aeronautics and Astronautics.

Van der Walt, J.J. 1998a. The Application of Computational Fluid Dynamics in the Calculation of Local *G*-Values in Hydraulic Flocculators. In *Proc. WISA Biennial Conference*. Cape Town, South Africa: Water Institute of Southern Africa.

Van der Walt, J.J. 1998b. Is a Sedimentation Tank Really That Simple? In *Proc. WISA Biennial Conference*. Cape Town, South Africa: Water Institute of Southern Africa.

Webster, D.R. 1994. An Experimental and Computational Study of Flow Instability in a Helical Coil. Ph.D. diss., University of California at Berkeley.

Webster, D.R. and J.A.C. Humphrey. 1993a. Experimental Observations of Flow Instability in a Helical Coil. *ASME Jour. of Fluids Engineering*, 115(3):436–443.

Webster, D.R. and J.A.C. Humphrey. 1993b. Questions in Fluid Mechanics—Reverse Transition Phenomena in Helically Coiled Pipes. *ASME Jour. of Fluids Engineering*, 115(2):191,192.

WEF (Water Environment Federation) and ASCE (American Society of Civil Engineers). 1991. *Design of Municipal Wastewater Treatment Plants*. Vol. 2, Alexandria, Va.: WEF and ASCE.

White, C.M. 1929. Streamline Flow Through Curved Pipes. *Proc. Royal Society of London Series A*, 123:645–663.

White, G.C. 1972. *Handbook of Chlorination*. New York: Van Nostrand Reinhold.

White, G.C. 1978. *Disinfection of Wastewater and Water for Reuse*. New York: Van Nostrand Reinhold.

Wilcox, D.C. 1994. Turbulence Modeling for CFD. La Cañada, Calif.: DCW Industries.

Wu, X. and K.D. Squires. 1998. Numerical Investigation of the Turbulent Boundary Layer Over a Bump. *Jour. of Fluid Mechanics*, 362:229–271.

You, X., M.J. Arrowood, M. Lejkowski, L. Xie, R.F. Schinazi, and J.R. Mead. 1996. A Chemiluminescence Immunoassay for Evaluation of *Cryptosporidium parvum* Growth In Vitro. *FEMS Microbiology Letters,* 136:251–256.

Page missing from thesis

ABBREVIATIONS

A	reactant in generic fast chemical reaction
a	fitting parameter in sigmodial model
A_f	surface area of the pathogen clumps
APHA	American Public Health Association
AWWA	American Water Works Association
AWWARF	American Water Works Association Research Foundation
α	parameter in five-phase model or turbulence closure coefficient
α^*	turbulence closure coefficient
B	reactant in generic fast, consecutive chemical reaction
b	fitting parameter in sigmodial model
BM	backmixer
BGMK	Buffalo Green Monkey Kidney cells
BSA	bovine serum albumin
β^*	turbulence closure coefficient
β_1	turbulence closure coefficient
℃	degrees centigrade
C_{Cl}	total chlorine concentration
C_d	concentration of disinfectant
ΔC	concentration difference across the interface
C_{bulk}	concentration of the disinfectant in the bulk fluid
C_{inner}	concentration of the disinfectant on the inside of the pathogen clump
C_p	number concentration of pathogens or pressure coefficient
C_p^0	is the initial number concentration of pathogens
C_d^0	is the initial disinfectant concentration
C/L	carbon per liter

$C \times T$	concentration of disinfectant (mg/L) times detention time (minutes)
CDC	Centers for Disease Control and Prevention
CFD	computational fluid dynamics
ξ	transport species in generic transport equation
D	pipe diameter
d	particle diameter or fitting parameter in sigmodial model
DBP	disinfection by-product
D/DBP	disinfectant/disinfection by-product
DISS	dissipation term in generic transport equation
DNS	direct numerical simulation
DPD	N,N-diethyl-p-phenylenediamine
δ	thickness of the interface
e	ratio of working volume to total volume in static mixer
E_d	rate of direct dissipation
E_d	dimensionless concentration of disinfectant
E_p	dimensionless concentration of pathogens
E_{inner}	dimensionless inner concentration of disinfectant
EWSTR	Enhanced Surface Water Treatment Rule
exp	exponential function
ε	turbulence energy dissipation
ε_d	apparent eddy diffusivity of the disinfectant
ε_p	apparent eddy diffusivity of the pathogens
η	Kolmogorov microscale
°F	degrees Fahrenheit
f	friction factor
FAS	ferrous ammonium sulfate

FDS	flux-difference splitting
ft	feet
G	root-mean-squared velocity gradient
$\bar{G}$	average G-value
g	gram
g	acceleration due to gravity
GAC	granular activated carbon
gal	gallons
gpm	gallons per minute
Δh	head loss
HCT-8	Human Enterocyte cells
$\mathbf{I}$	the identity matrix
IEM	interaction exchange with the mean
IEWSTR	Interim Enhanced Surface Water Treatment Rule
IgH	Incomplete Gamma Hom model
in	inch
$\mathbf{J}_d$	mass flux of disinfectant relative to average velocity
$\mathbf{J}_p$	mass flux of pathogens relative to average velocity
K_1	reaction rate constant
K_2	reaction rate constant
K_s	overall lumped coefficient for the five-phase process model
K_f	interfacial mass transfer coefficient
K_p	lumped parameter for pathogens
K_r	dimensionless rate constant for the inactivation reaction
k	turbulence kinetic energy

$\hat{k}$	normalized turbulence kinetic energy
$(k_a)_i$	turbulence kinetic energy averaged over the inlet of the static mixer
k_d	disinfectant constant
k_p	pathogen constant
k_1	rate constant for generic fast, consecutive chemical reaction
k_2	rate constant for generic fast, consecutive chemical reaction
L	liter
L	total length of static mixer
lb	pounds
LES	large eddy simulation
L_e	length of mixer element
log	logarithm base 10
ln	logarithm base e
m	fitting parameter for Hom model
MCL	maximum contaminant level
MDCK	Madine Darby Canine Kidney cells
mg	milligram
mgd	million gallons per day
min	minute
mL	milliliter
mm	millimeter
μ	dynamic viscosity
μL	microliter
μm	micrometer
μS/cm	microsiemens per centimeter
N	normal
N	final concentration of organisms

n	fitting parameter for Hom model
$\mathbf{N}_d$	mass flux of disinfectant relative to fixed coordinate system
N_f	flux through the interface
$N_{f,d}$	flux of the disinfectant through the interface
N_e	number of elements
N_o	initial concentration of organisms
$\mathbf{N}_p$	mass flux of pathogens relative to fixed coordinate system
N_{tot}	total number of nodes in computational grid
NOM	natural organic matter
nm	nanometer
ntu	nephelometric turbidity unit
ν	kinematic viscosity
ν_t	eddy or turbulent viscosity
Ω_{x_1}	axial vorticity
ω	specific dissipation of turbulence kinetic energy
P	mean pressure
P_d	production
Pe_d	Peclet number for the disinfectant
Pe_p	Peclet number for the pathogens
Po	power
P_{ref}	reference pressure
Δp	pressure drop
PROD	production term in generic species transport equation
Φ	average rate of energy dissipation
Q	flow rate

R	intermediate product in generic fast, consecutive chemical reaction
RANS	Reynolds-averaged Navier–Stokes
R_d	reaction rate of the disinfectant
R_p	reaction rate of the pathogens
Re	Reynolds number
Re_t	turbulent Reynolds number
rpm	revolutions per minute
R_r	rate of the inactivation reaction
ρ	fluid density
ρ_p	density of the *Cryptosporidium* oocyst
S	final product in generic fast, consecutive chemical reaction
s	second or longitudinal distance along the centerline of the 90° bend
SCD	streaming current detector
σ	turbulence closure coefficient
σ^*	turbulence closure coefficient
σ_ξ	diffusion coefficient for ξ
t	time
t_d	detention time in static mixer
TOC	total organic carbon
T-PBS	tissue culture phosphate buffer saline
TVD	total variation diminshing
θ	dimensionless length or azimuthal direction
U	mean (bulk) velocity
$\mathbf{U}$	mean velocity vector
$\widetilde{\mathbf{U}}$	instantaneous velocity vector
$\mathbf{u}'$	fluctuating part of the velocity
$\overline{\mathbf{u}'\mathbf{u}'}$	Reynolds stresses

USEPA	United States Environmental Protection Agency
UV	ultraviolet
V	volume
V_m	working volume in static mixer
V_t	total volume in static mixer
WEF	Water Environment Federation
WTP	water treatment plant
x	log *Cryptosporidium* inoculated
$\mathbf{x}$	position vector
x_o	fitting parameter in sigmodial model
Y	fitting parameter
y	fraction of views positive for *Cryptosporidium*
y_o	fitting parameter in sigmodial model
$y+$	dimensionless distance from the wall of the pipe